

# UC Santa Cruz

## UC Santa Cruz Electronic Theses and Dissertations

### Title

Hybrid Optofluidic Biosensors

### Permalink

<https://escholarship.org/uc/item/7xk3h3nh>

### Author

Parks, Joshua W.

### Publication Date

2016

Peer reviewed|Thesis/dissertation

UNIVERSITY OF CALIFORNIA  
SANTA CRUZ

**HYBRID OPTOFLUIDIC BIOSENSORS**

A dissertation submitted in partial satisfaction  
of the requirements for the degree of

DOCTOR OF PHILOSOPHY

in

ELECTRICAL ENGINEERING

by

**Joshua W. Parks**

December 2016

The Dissertation of Joshua W. Parks is approved:

---

Professor Holger Schmidt, Chair

---

Professor Joel Kubby

---

Professor Clair Gu

---

Tyrus Miller  
Vice Provost and Dean of Graduate Studies

Copyright © by

Joshua W. Parks

2016

All rights reserved

## Table of Contents

1	Introduction .....	1
2	Background .....	5
2.1	Fluorophores and Fluorescence .....	5
2.2	Fluorescent Reporters: Nucleic Acid Stains and Molecular Beacons .....	8
2.3	ARROW Fundamentals .....	12
2.3.1	Deriving the ARROW Condition .....	13
2.3.2	ARROW Device Fabrication .....	16
2.3.3	Fluorescence Based ARROW Detection .....	20
2.4	PDMS Prototyping and Fabrication .....	24
3	Enhancement of ARROW Optofluidic Biosensors via Thermal Annealing .....	29
3.1	Post Processing Low Temperature Thermal Annealing .....	32
3.2	Optical Characterization of Annealed ARROW Structures .....	32
3.2.1	Optical Confinement and Loss in Solid-core Waveguides .....	32
3.2.2	Transmission Changes in Connected Solid- and Liquid-core Waveguides 36	
3.2.3	Repeatability of Waveguide Improvements .....	39
3.3	Optofluidic Sensor Chip Improvement Upon Thermal Annealing .....	41
4	Passive Hybrid Optofluidic Integration .....	44
4.1	Device Fabrication and Hybrid Integration .....	46
4.2	Flow Properties of Hybrid Optofluidic Systems .....	51



4.3	On-Chip Mixing, Labelling and Detection of Single DNA.....	52
4.4	Microfluidic Sample Distribution to Multiple ARROW Waveguides .....	57
4.4.1	Positive Pressure Driven Flow in Hybrid Systems.....	59
4.4.2	Passive Control of Fluid Velocity in Hybrid Systems .....	61
4.5	Microparticle Filtering and Distribution.....	62
5	Active Hybrid Optofluidic Integration.....	67
5.1	Microfluidic Automaton Fabrication and Control.....	68
5.2	Integration of Microfluidic and Optofluidic Layers .....	71
5.3	On-chip Fluid Control and Mixing Using an Active Hybrid Optofluidic System .....	72
5.4	Detailed Control Analysis of the Hybrid System .....	74
5.5	Automated Single Nucleic Acid Detection .....	74
5.6	Automated Nucleic Acid Isolation and Detection.....	77
6	Detection of Clinically Relevant Biomolecules.....	82
6.1	Optofluidic analysis system for amplification-free, direct detection of Ebola infection.....	83
6.1.1	Systematic design of a hybrid optofluidic system for detection of single clinical nucleic acids .....	83
6.1.2	Automated pre-concentration of Ebola nucleic acids .....	85
6.1.3	Automated and specific detection of single, clinical ebola nucleic acids	87
6.2	MMI Based Wavelength Division Multiplexing for Optofluidic Detection of Single Virus Detection.....	91

6.2.1	Multimode Interference Waveguides (MMIs) .....	92
6.2.2	Optofluidic MMI Biosensor Architecture.....	96
6.2.3	Virus sample preparation .....	98
6.2.4	Multiplex virus fluorescence detection setup and experiment.....	99
6.2.5	Multiplexed single virus detection with single color labeling .....	100
6.2.6	Multiplexed single virus detection with combinatorial labeling.....	103
6.2.7	WDM Biosensing Analysis Considerations.....	107
7	Flexible PDMS optofluidic waveguide platform with multi-dimensional reconfigurability and functionality .....	113
7.1	Fabrication of multilayer flexible optofluidic platforms .....	114
7.2	Loss in PDMS Waveguides.....	116
7.3	Comparison of PDMS and ARROW Detection Chips.....	122
7.5	PDMS Optofluidic Waveguide Chips with Multi-dimensional Reconfigurability.....	127
7.5.1	Dynamically Reconfigurable PDMS MMI Waveguide .....	128
7.5.2	Lightvalve Architecture for Simultaneous Control of Fluid and Light	131
7.5.3	Lightvavle Trap with Single Bioparticle Analysis Capability .....	136
8	Conclusions and Outlook .....	139
9	Appendixes.....	141
10	Bibliography .....	182

## List of Figures

<b>Fig. 2.1   Organic dye properties: Cy3 and Cy5 dyes as examples.</b> .....	6
<b>Fig. 2.2   Binding modes of nucleic acid stains.</b> .....	8
<b>Fig. 2.3   YO and YOYO intercalating dye properties.</b> .....	9
<b>Fig. 2.4   Molecular Beacons for Nucleic Acid Detection.</b> .....	11
<b>Fig. 2.5   Generic ARROW Structure and Wavevector Diagram.</b> .....	13
<b>Fig. 2.6   Fabrication workflow for solid- and liquid-core ARROWs. (Dimensions not precisely to scale)</b> .....	17
<b>Fig. 2.7   ARROW Detection Geometry. a</b> ARROW fluorescence 3D view with butt coupled excitation and collection optical fibers. <b>b</b> Cross-sectional view of the excitation volume with an antibody labeled virus being excited. ....	20
<b>Fig. 2.8   Fluorescence Detection on an ARROW Chip. a</b> Bulk fluorescence detection of 22.5 nM Cy5 dye. <b>b</b> Detection of single fluorescent 100 nm Fluospheres (488 nm excitation, $c_{\text{fluosphere}} = 4 \times 10^7$ particles/mL). ....	21
<b>Fig. 2.9   Common geometries of pneumatically addressable PDMS microvalves.</b> The push-down valve is shown end-on while the membrane and lifting gate valves are shown from the side for clarity. ....	25
<b>Fig. 2.10   General multilayer PDMS device fabrication workflow.</b> .....	27
<b>Fig. 3.1   Reduction of tantalum oxide photoluminescence in thin films via thermal annealing. Note the red line indicates as-grown film photoluminescence.</b> .....	29

**Fig. 3.2 | Physical effects of thermal annealing on ARROW structures. a,**  
 Tantalum oxide thin film (100 nm) “star” cracking after 700 °C annealing. **b,**  
 Cross-sectioned liquid- to solid-core waveguide intersection with a large crack  
 caused by annealing. \*\*\*Secondary feature is an artifact of focused ion beam  
 milling ..... 30

**Fig. 3.3 | Scanning electron microscope (SEM) image (left) and schematic  
 representation (right) of a 4 μm wide solid-core ARROW ridge waveguide  
 sitting on a silicon pedestal..... 31**

**Fig. 3.4 | Effects of annealing on solid-core waveguide light propagation. a,** Top  
 down image of light confinement within an ARROW ridge waveguide before  
 (top) and after annealing (bottom). **b,** Integrated mode intensity output of a 1 cm  
 long as-grown (top) and annealed (bottom) solid-core waveguide. Intensity  
 within the core of the waveguide is shaded dark blue. **c,** Transmission  
 measurements for cut-back solid core waveguides. As-grown waveguides (open  
 blue squares) have a fitted loss coefficient  $\alpha_{AG} = 1.63 \text{ cm}^{-1}$  (dashed line).  
 Annealed waveguides (closed red circles) have a fitted loss coefficient  $\alpha_A =$   
 $0.471 \text{ cm}^{-1}$  (solid line). Both fits have  $r^2 > 0.99$ ..... 33

**Fig. 3.5 | Finite difference method simulations of a solid-core ARROW  
 waveguide before and after annealing. a,** SEM image of a solid-core  
 waveguide facet with silicon substrate, ARROW layers, low refractive index  
 $\text{SiO}_2$  ( $n_L = 1.46$ ), and high refractive index  $\text{SiO}_2$  DUL ( $n_{DUL} = 1.47$ ) labeled as 1-  
 4, respectively. **b,** Modal simulations (top, colored) and experimental images

(bottom, grayscale) for as-grown and annealed ridge waveguides. All white scale bars represent 5  $\mu\text{m}$ . ..... 34

**Fig. 3.6 | Simulation of optical transmission through connected solid- and liquid-core waveguides. a,** Side view images of simulated transmission through waveguide systems. The annealing simulation has homogenous refractive index in the solid-core waveguide while the as-grown waveguide has a DUL. ARROW lengths are 2 mm. **b,** Transmitted optical power for different solid-core waveguide lengths (as indicated in **a**). ..... 36

**Fig. 3.7 | Wavelength dependent improvement of full ARROW sensor chip transmission.** Improvement is measured across (**a**) and through (**b**) the liquid-core waveguide. Insets show schematics of the transmission experiments. .... 38

**Fig. 3.8 | Full ARROW sensor chip transmission data** (see inset for experiment schematic, transmission includes two solid-core sections intersected by a liquid core channel). As-grown (AG) waveguide transmission is presented, followed by cycles of annealing (A) and 4-hour water treatments (W). Appended numbers to A and W indicate annealing/water treatment number. Mode images are alternately presented below and above the transmission data for each treatment. The axis on the right side is normalized transmission with as-grown transmission equaling 1. .... 40

**Fig. 3.9 | ARROW sensor chip annealing induced improvement. a,** Orthogonally collected background (error bars are standard deviation of the background signal). **b,** Bulk fluorescence signal of 22 nM Cy5. **c,** Detection of 100 nm single

FluoSpheres,  $c_{FI} = 4 \times 10^7 \text{ mL}^{-1}$ . The left 0.5 seconds of **c** is signal from an as-grown chip and the right 0.5 seconds is signal obtained after annealing.

Representative peaks are marked with arrows. Note that all experiments were conducted with the geometry represented in the inset of **a**..... 41

**Fig. 4.1 | Schematic depiction of hybrid optofluidic integration of microfluidic sample preparation (top) and optical analysis (bottom) layers.** ..... 44

**Fig. 4.2 | Passive hybrid optofluidic integration.** **a**, Expanded view of PDMS integration with an ARROW optofluidic chip. Insets are scanning electron microscope (SEM) images of optical intersections. **b**, Assembled device with fluidic connections – the scale bar in the upper right represents 1 cm. .... 46

**Fig. 4.3 | Optical experimental setup for detection using a hybrid optofluidic system.**..... 50

**Fig. 4.4 | On-chip mixing and detection of fluorescent microspheres.** **a**, Dual fluorescence measurement of PDMS-mixed microspheres. The inset represents a higher resolution time trace demonstrating the chromatic separation of the signals. Regions A (0-60 s) and B (60-80 s) signify durations of the experiment in which the system was un-pumped and pumped, respectively. The dashed green line represents the transition between regions A and B. **b**, FCS analysis of the 670 nm fluorescence signal before (A) and during (B) pumping. .... 52

**Fig. 4.5 | On-chip labeling and detection of single  $\lambda$ -DNA.** **a**, Time dependent fluorescence trace of on-chip mixed, labelled, and detected single  $\lambda$ -DNA molecules. The dashed black lines represent  $3\sigma$  (three times the standard

deviation of the noise) and the inset displays single detection events. **b**, Experimental FCS trace of detected  $\lambda$ -DNA molecules (squares) and respective theoretical fit (line). ..... 55

**Fig. 4.6 | Distribution of fluorescent microspheres to dual liquid-core**

**waveguides. a**, PDMS Distribution with dual liquid-core waveguide detection. Signals were detected from liquid-core waveguide 1 (**b**) and 2 (**c**) separately while the same PDMS distribution device fluidically controlled both channels. **d**, FCS analysis of both time trace signals – local maxima are marked..... 58

**Fig. 4.7 | Investigation of Variable Flow Velocities in a Distributed Hybrid**

**Optofluidic Platform**..... 60

**Fig. 4.8 | Passive Control of Microfluidic Flow Velocity.** Velocity is controlled by

changing the fluid reservoir position with respect to the fluid outlet. The dashed line is a linear fit with  $r^2 = 0.998$ . ..... 61

**Fig. 4.9 | Microfluidic particle sorter and distributor. a**, Mask layout of the PDMS

sorter and distributor. **b**, Zoom-in view of the particle size sorter section. **c**, Zoom-in view of the filtering membrane and the corrugated walls inside the inlet channel. **d**, Microscope image of the fabricated PDMS filtering membrane slit. .... 62

**Fig. 4.10 | PDMS filtering and distribution with dual liquid-core waveguide**

**detection.** Signals were detected from liquid-core waveguide 1 and 2 with input flow rate at  $\sim 2 \mu\text{l}/\text{min}$ . ..... 64

**Fig. 5.1 | Automaton microfluidic processor schematic.** Pneumatic features are represented in red and fluidic features are represented in black. Black X's at the end of channels represent a punch in the fluidic and pneumatic layers while red X's represent a punch only in the pneumatic layer. Valves are numbered 1-11 for later assay reference. Inlets are considered by their valve number (1-3) while outlets are considered to be waste (11) and output (10), respectively. .... 68

**Fig. 5.2 | Generic 3 valve peristaltic pumping scheme.** Valves that have negative pressure applied (or are open/lifted and filled with fluid) are indicated by a filled red valve while those that are closed are represented by an empty red circle with underlying fluidic layer structure. **a**, valve 1 is opened to be filled with fluid. **b**, the fluid is moved further into the pump by opening valve 2. Once valve 1 is closed in **c**, the pump volume is determined by the size of the middle valve. Valve 3 is opened in **d** to move the fluid along and finally valve 2 is closed in **e**, and valve 3 is closed to complete the single pumping cycle (closing of valve 3 not shown)..... 69

**Fig. 5.3 | Two valve mixing schematic.** Once valves 1 and 4 are filled with solutions to be mixed **a**, valve 3 is opened in **b** to draw fluid in from both 1 and 4. Valve 1 is closed (**c**) and valve 2 is opened (**d**) to distribute the mixing fluid into valves 2-4. Once valve 4 is closed (**e**), the process is reflectively repeated to further mix the solutions (**f-h**)..... 70

**Fig. 5.4 | Automaton control box and operating connections. a**, Custom control box complete with a PC connected DAQ, which is in turn wired to a switchboard



controlling the operation of pneumatic solenoid valves. **b**, Control tubing from the solenoid valves connects to the acrylic manifold, allowing for individual operation of the automaton microvalves. A magnet TEC and fluid reservoirs (pipet tips) are pictured for completeness. .... 70

**Fig. 5.5 | Hybrid integration of automaton and ARROW chips principle and implementation. a**, Schematic of hybrid optofluidic device and connections; **b**, photograph of assembled device. The white scale bar in b represents 1 cm. .... 71

**Fig. 5.6 | Demonstration of the hybrid system's basic functionality: sealed connection and particle mixing. a**, Bead movement inside the ARROW chip as actuated by automaton with color coded directions of forward (white) and reverse (orange) pumping; **b**, corresponding fluorescence signal showing four microbeads repeatedly being moved past excitation spot; **c**, simultaneous detection of fluorescent beads and dye-labeled proteins that were mixed in automaton layer. The different laser excitation wavelengths are indicated; the HeNe laser used to excite the proteins is turned on at  $t=70\text{sec}$ . .... 72

**Fig. 5.7 | Systematic control of fluid flow in an automated hybrid optofluidic biosensor.** Note that in the top images, the view is along the excitation waveguide (within the liquid-core waveguide) and the excitation volume is indicated by a red oval. Arrows above the images indicate pumping in the forward (Automaton to ARROW, green) and reverse (red) direction. Stopped flow is indicated by an x. Dark blue in the images represents fluorescent protein solution while light blue represents non-fluorescent solution. .... 75

**Fig. 5.8 | Automated single nucleic acid detection and analysis.** **a**, Filling and emptying cycles of the automated system. **b**, Fluorescence detection of single  $\lambda$ -DNA molecules well above the  $3\sigma$  level. **c**, FCS analysis and fit of 10-60 seconds of **a**..... 76

**Fig. 5.9 | Advanced functionality: viral nucleic acid detection using on-chip solid-phase extraction and detection.** **a**, Solid phase nucleic acid pull-down assay - (I) Prepared "pull-down" magnetic beads and (II) nucleic acid target are mixed on automaton (III); washed magnetic particles are sent to the ARROW chip (IV). Particle detection for **b** negative (pull-down non-cognate)—see I—and **c** positive (pull-down cognate) nucleic acid samples—see IV. Single bead signals are marked by arrows in the figure inset..... 79

**Fig. 6.1 | Solid-phase extraction assay used for target isolation and detection. The dashed box indicates the steps that were implemented on the automaton chip.**..... 84

**Fig. 6.2 | Automated preconcentration and detection of synthetic Ebola nucleic acids.** **a**, Particles to be concentrated: target oligomers are bound to pull-down recognition sequence on magnetic microbeads; molecular beacons specifically bind to target and cause beads to fluoresce; **b**, particle fluorescence counts detected on ARROW chip before preconcentration step and **c** after preconcentration on automaton. A 335x concentration increase is observed. .... 85

**Fig. 3 | Amplification-free detection of Ebola virus on optofluidic chip.** **a**, segments of digitized fluorescence counts above background showing

concentration-dependent numbers of single RNAs; **b**, concentration-dependent particle counts for off-chip (open squares) and using the automaton (solid circles) sample preparation. Negative controls (SUDV, MARV) did not create any counts (note the broken vertical scale). Dashed line: Predicted particle count determined from initial concentration and experimental parameters (tested sample volume, excitation and detection mode areas, liquid-core channel cross section). The lowest two concentrations for on-chip sample prep were reached by 50x and 460x preconcentration steps, respectively..... 88

**Fig. 6.4 | Fluorescence concentration series in the analog detection regime demonstrating linear signal detection over six orders of magnitude (line: linear fit)..... 90**

**Fig. 6.5 | Example electromagnetic modes in generic multimode slab waveguide of width  $W_M$ ..... 93**

**Fig. 6.6 | Wavelength division multiplexing for single virus detection. a**, Schematic view of multi-mode interference (MMI) waveguide intersecting a fluidic microchannel containing target particles. Targets are optically excited as they flow past well-defined excitation spots created by the MMI; fluorescence is collected by the liquid-core waveguide channel and routed into solid-core waveguides (red); **b**, Scanning electron micrograph of MMI-based optofluidic chip (Inset: photograph of 1 cm by 1 cm chip, showing two fluidic reservoirs holding microliters of sample volume); **c**, Photographs of multi-spot excitation patterns created in fluidic channel filled with fluorescent liquid. The entire

visible spectrum is covered by independent channels (405 nm/11 spots, 453/10, 488/9, 553/8, 633/7, 745/6). (The original black and white color scale was rendered in the actual excitation colors; the wavelengths used for the virus assays are highlighted by white, dashed boxes)..... 96

**Fig. 6.7 | Three-color multiplex virus detection.** **a**, Representative fluorescence signal emitted by single H1N1 virus excited at 488nm showing 9 distinct peaks spaced by  $\Delta t_B$ ; **b**, Corresponding single-particle autocorrelation signal. Multiple peaks are observed at multiples of  $\Delta t_B$ ; dashed line: fit to underlying flow-limited correlations. **c**, Single-particle autocorrelation for 3 virus types after subtraction of flow-based contribution. The peak positions depend strongly on excitation spot number (arrows mark the 5<sup>th</sup> peak for each virus type). **d**, Segment of fluorescence from virus mixture excited at all three colors. Events are identified using single-particle autocorrelations. All but one identified signals (99.2%) agree with manual inspection of events. .... 101

**Fig. 6.8 | Analysis of single virus fluorescence signals.** **a**, Sketch of fluorescently labeled H3N2 virus, responding to excitation at 745 nm; **b**, fluorescence signal from single H3N2 virus showing six peaks with average spacing  $\Delta t_{DR}$ ; **c**, corresponding processed signal using shift-multiply algorithm with  $\Delta t_{DR}$  showing dramatically increased SNR. .... 104

**Fig. 6.9 | Two-color combinatorial detection of single viruses.** **a**, schematic view of labeling scheme for the three influenza types and their resulting single-virus fluorescence signals; the H2N2 virus shows a mixture of six and nine peaks

upon blue and dark red excitation; **b**, bar histograms of signals after shift-multiply processing at  $\Delta_B$  and  $\Delta_{DR}$ . Singly labeled viruses appear in only one  $\Delta t$  channel, while the double labeled virus creates signal in both color channels. 105

**Fig. 6.10 | Comparison of single and multiple peak autocorrelations.** **a**, The 20 second trace seen on the left yields the autocorrelation seen on the right. **b**, Single peak spanning  $\sim 5$  ms with 5 ms of adjacent background yields the much more pronounced autocorrelation seen on the right. Note that the binning size (0.01 ms) is presented here to demonstrate the noisiness of the signal before autocorrelation. .... 107

**Fig. 6.11 | Shift multiply peak finding analysis.** **a**, Data trace displaying three different regions of signal, color coded for different laser excitations, i.e. 488, 633, and 745 nm left to right. **b**, Output of the shift multiply algorithm (Eq. 6.8) with the signal from **a** being the  $F(t)$  input,  $N = 6$ , and  $\Delta t$  equaling the noted values. Note that a circle on a peak indicates that the signal for that particle reached its  $S(t)$  maximum for the noted  $\Delta t$ . **c**, Histogram of peak  $S(\Delta t)$  maxima yielding three distinct distributions of  $\Delta t$  values representing the peaks from the portions of the different color traces. .... 109

**Fig. 6.12 | Single particle shift-multiply identification.** **a**, 10 ms signal traces for a blue, blue-dark red, and dark red particle, from left to right. **b**,  $S(t)$  matrixes for each respective particle at  $N=6$ . **c**,  $S(t)$  matrixes for each respective particle at  $N=9$ . Each data matrix is internally normalized and logarithmically plotted with a heat map color system (where colder colors are low values and warmer colors

are higher values). **d**, Single slice of each  $S(t)$  matrix along a  $\Delta t_B = 0.41$  ms and  $\Delta t_{DR} = 0.63$  ms for  $N=9$  and  $N=6$ , respectively. Note that these traces are indicated in **b** and **c** as rainbow colored (vertical) cross-sections. Also, the  $N=9$   $S(t)$  trace occupies the left portion of the graph while the  $N=6$   $S(t)$  is offset to the right side of the graph. **e**, Single slice of each  $S(t)$  matrix along a given time value that contains the maximum  $S(t)$ . These traces are indicated in **b** and **c** as maroon (horizontal) cross-sections. .... 110

**Fig. 7.1 | Fabrication of PDMS Waveguide Platforms.** A stepwise fabrication workflow is presented, with high index PDMS colored dark grey, low index PDMS in light gray, SU8 in purple, and silicon in black. Dashed lines indicate bonding surfaces. .... 115

**Fig. 7.2 | Simulated visible light loss of a PDMS capillary waveguide.** Parameters as follows:  $n_c = 1.33$ ,  $n_{cl} = 1.41$ ,  $d = 7 \mu\text{m}$ , and  $m = 0$  where applicable.  $\alpha_F$  (Fresnel) is plotted in blue,  $\alpha_A$  (Archambault) is plotted in red, and  $\alpha_{HM}$  (Haus-Miller) is plotted black. TE loss is plotted with solid lines and TM loss is plotted with dashed lines. .... 119

**Fig. 7.3 | Capillary waveguide loss trends with varying fabrication parameters.** Parameters as follows unless specifically varied:  $n_c = 1.33$ ,  $n_{cl} = 1.41$ ,  $d = 7 \mu\text{m}$ ,  $\lambda = 532$  nm, and  $m = 0$ . TE loss is plotted with solid lines and TM loss is plotted with dashed lines. .... 120

**Fig. 7.4 | Experimental loss of PDMS waveguides.** **a**, Solid-core waveguide mode image (top) and cutback loss (bottom). **b**, Liquid-core waveguide mode image

(top), cutback loss (bottom left) and confirmed loss measurement using top down fluorescence monitoring along the liquid-core channel. All measurements were conducted at 488 nm and error bars represent the standard deviation of three or more measurements. .... 121

**Fig. 7.5 | Excitation profiles of ARROW and PDMS waveguide chips. a,** Top down ARROW excitation profile (right) with a respective cross section (left) of the fluorescence profile. **b,** Top down PDMS excitation profile (right) with a respective cross section (left) of the fluorescence profile. Note that the measurements were taken at 488 nm excitation with 2  $\mu$ M Dylight 488. .... 122

**Fig. 7.6 | Comparison of ARROW and PDMS detection chip performance. a,** Top down images of ARROW (left) and PDMS (right) detection chips. Dark green arrows indicate laser excitation input, dark red arrows indicate signal collection output, and the light blue arrow indicates fluid flow. **b,** Deionized water background comparison of unannealed ARROW, PDMS, and annealed ARROW chips. **c,** Detection of 22.5 nM Cy5 fluorescent dye. **d,** Detection of  $d = 100$  nm yellow-green (505/515 nm – ex/em) Fluospheres®. In plots **b-d** unannealed ARROW chip signals are blue (denoted by I), PDMS chip signals are green (denoted by II), and annealed ARROW chip signals are red (denoted by III). 124

**Fig. 7.7 | Directly integrated waveguide detection chip and actively controlled microvalves. a,** Schematic (top) and actual (bottom) images of a complete chip. Note that the inlets and outlet are represented by white circles in the top image. In the bottom image, all three inlets are filled with food dye, while the outlet is

empty. The two middle valves of the microvalve array, as well as the peristaltic pump valves, are open (filled with food dye) for contrast. **b**, Zoom-in of the optical detection region (dashed black box in the bottom of **a**) showing the fluorescence detection geometry directly connected to an actively controlled microvalve. **c**, Particle detection during a 200 second automated, on-chip pumping program (8 second cycling rate), 488 nm excitation. Black scale bars represent 5 mm and 300  $\mu\text{m}$  in **a** and **b**, respectively. .... 126

**Fig. 7.8 | Example PDMS Waveguide Platform Microscope Images. a,**

Reconfigurable optofluidic MMI, empty, **b**, Lightvalve in its static state, empty, and **c**, Lightvalve trap, both empty (top) and filled and under optical excitation (bottom). The filling fluid for the lightvalve trap is a 3  $\mu\text{M}$  Dylight 488 solution and exhibits fluorescence when excited by 488 nm laser light, injected from the left solid-core waveguide. Note: all white scale bars represent 50  $\mu\text{m}$ . .... 127

**Fig. 7.9 | Dynamically tunable multispot optofluidic waveguide. a,**

Schematic side-view of the solid- and liquid-core waveguides. **b**, Liquid-core MMI waveguide system from top (left) and side (right) views. Fiber injected laser light propagates through the excitation solid-core waveguide and into the liquid-core waveguide with a static width of  $w_0$ . Air pressure yields a decrease in liquid-core waveguide width (bottom left, side view) while liquid flow increases waveguide width (bottom right, side view). **c**, Experimental (top, green) and simulated (bottom, orange) multispot waveguide pattern for a 50  $\mu\text{m}$  wide liquid-core waveguide. **d**, MMI length vs. spot number for 7 fabricated liquid-core



waveguide widths, 50-200  $\mu\text{m}$ , 25  $\mu\text{m}$  increment. **e**, Dynamic tuning of optofluidic waveguides by varying core refractive index,  $n_c$ . **f**, Width based dynamic tuning of optofluidic waveguides,  $w_0 = 50$  and  $100 \mu\text{m}$  for green circles and magenta squares. Positive pneumatic pressure points increase to the left, at 20, 40, and 60 PSI, while the liquid flow rate is 1 mL/min. Note: theoretical predictions using eq. (7.7) are represented as solid curves/lines in **d**, **e**, and **f**. 130

**Fig. 7.10 | Lightvalve architecture.** **a**, Schematic representation of the lightvalve architecture. Top-center—as fabricated lightvalve composed of three functional layers: layer I is the control layer; layer II is composed of a high refractive index waveguide core (dark grey) and a low refractive index mechanical membrane (light grey); layer III is the substrate layer. Top-left—lightvalve operated in push-down mode. Top-right—lightvalve operated in lift-up mode. The bottom row of images are respective counterparts to the upper row, rotated  $90^\circ$  about a vertical axis. Importantly, the control layer defines the lightvalve’s width ( $w_v$ ) and length ( $L_v$ ) as well as the maximum deflection of layer II via its height,  $h_c$ .  
 ..... 132

**Fig. 7.11 | Lightvalve Operation.** **a**, Lightvalve operation and respective effects on liquid and light flow. Note that light flow is tailorable/tunable in both lift-up and push-down modes (see parts **c** and **d**). **b**, Optical switching of the lightvalve operated in lift-up (bottom, blue) and push-down (red, middle). The top subplot (black) is a schematic pressure trace designating the applied control pressure at any given time. The left-hand y-axis (red labels) denotes the pressure applied

during push-down operation while the right-hand y-axis (blue labels) denotes the pressures applied in lift-up mode. **c**, Optical switching efficiency of lightvalves operated in lift-up mode. The error-bars represent the standard deviation of 20 switching cycles. **d**, Optical rejection of a lightvalve operated at various push-down pressures..... 133

**Fig. 7.12 | Spectral dependence of lightvalve transmission.** **a**, Lightvalve spectral dependence operated in lift-up ( $P = -7$  PSI) mode over the visible wavelength regime using a tunable laser source and APD ( $L_v = 100 \mu\text{m}$ ,  $w_v = 160 \mu\text{m}$ ). **b**, A separate lightvalve was measured during lift-up and push-down operation using a spectrometer ( $L_v = 500 \mu\text{m}$ ,  $w_v = 500 \mu\text{m}$ ). Pressures from top to bottom are 0 (black), 20 (red), -7 (light blue), and 60 (dark red) PSI..... 135

**Fig. 7.13 | Lightvalve particle trap.** **a**, Top-down schematic of lightvalve trap with excitation laser light entering the trapping region from a solid-core waveguide, while signal is collected, filtered, and detected from the opposite waveguide facet. The observation volume is indicated in the center of the lightvalve trap by a Gaussian blurred red bar and is distinctly smaller than trap volume which is characterized by the diameter ( $d$ ) of the trap. Pressure is applied to the control layer, indicated here by dashed black lines. **b**, Waveguide mode cross-sections, with the  $1/e^2$  widths in the vertical ( $h_{ex} = 9.9 \mu\text{m}$ ) and horizontal ( $w_{ex} = 8.2 \mu\text{m}$ ) directions, define the optical interrogation region. **c**, Autocorrelation curves for different numbers of particles trapped inside a lightvalve,  $d = 50 \mu\text{m}$ . Microscope images on the left are snapshots of fluorescent particles within the

excitation volume for each autocorrelation trace. **d**, Fluorescence signal of trapped, single *E. coli* bacteria. Illustrations above the fluorescence trace indicate when the trap is closed, containing a cell (bacterium cartoon), and when the trap is cycling (open lightvalve cartoon)..... 136

## Appendix A

**Fig. A.1 | T3RViewer.** See description for different functions..... 142

**Fig. A.2 | View peaks dialog box. V.1**, The amount of space around the peak can be changed using the peak window box. **V.2**, Each peak is assigned a peak number based on its time with respect to the other peaks. The scrollbar can be used to scroll through all the peaks. The peak time is listed in the upper left and the (unprocessed) data trace for the peak is plotted here. **V.3**, Shift-multiply time range and spot number designations (note the spot number is the number of spots in an MMI/multipeak, the number of shift-multiplies is one less than this number). **V.4**, Shift-multiply signal,  $S(t)$  for the peak in **V.2** at the noted  $\Delta t$  value. The scrollbar can be used to scroll through the different  $\Delta t$ 's. **V.5**, Plot of maximum signal for given  $\Delta t$ 's, i.e.  $S(\Delta t)$ . The blue trace is  $S(\Delta t) = \max(S(t, \Delta t))$ . The red trace is  $S(\Delta t) = S(t_{\max}, \Delta t)$ , where  $t_{\max}$  is set as the time at which  $S(t)$  is at its global maximum. **V.6**, Each individual peak and its data can be saved using the noted button..... 146

**Fig. A.3 | Autocorrelate peaks dialog box. A.1**, The same information is plotted here as is in **V.2**, that is the single peak data trace, with time and number,

unadulterated. **A.2**, Autocorrelation trace of the single peak (smoothed here), with red peaks **A.3**, marking the local secondary maxima in the trace..... 147

**Fig. A.4 | Multi-peak finder dialogue box. M.1**, Similar to **V.3**, the shift-multiply algorithm parameters can be defined here. The Calculate Product button produces a shift-multiply product matrix of the entire data trace in the histogram plot. **M.2**,  $S(t)$  plot for the entire data trace, at the specified  $\Delta t$ . The scrollbar is used to change the  $\Delta t$  slice of the matrix that is viewed. **M.3**, similar to the controls in **(13)**, the controls in the box are dictated as a shift-multiply selectivity,  $S(t)$  amplitude threshold, and peak minimum distance. The new parameter, M-spot Peak Window, designates the  $\Delta t$  range in which the program should consider all maxima as occurring from a single multi-peak shift-multiplication. **M.4**, Similar to **V.5**, the local and global maximum  $S(\Delta t)$  traces are plotted and browsable for each shift-multiply peak. **M.5**, Histogram containing each peak's  $\Delta t_{\max}$  (i.e.  $S_{\max} = S(t_{\max}, \Delta t_{\max})$ ) in the defined number of bins. **M.6**, Save the multi-peak finder processed information using this button. .... 148

**Fig. A.5 | Peak statistics dialogue box. S.1**, Histogram of peaks found in histogram plot, based on their peak intensities. **S.2**, Histogram of peaks found in histogram plot, based on their times. **S.3**, Average Gaussian fitting parameters for all peaks. Use this plot with caution. .... 149

## Appendix B

**Fig. B.1 | Reflection of an S polarized (TE) wave at a dielectric interface. .... 157**

<b>Fig. B.2   Reflection of an S polarized (TE) wave at a dielectric interface.</b> .....	158
<b>Fig. B.3   Electric field propagation across two interfaces.</b> .....	160
<b>Fig. B.4   arrowDesignv5.m main window.</b> Numbers are described throughout the textual explanation. ....	163
<b>Fig. B.5   Custom ARROW calculation dialogue box.</b> .....	164

## **Appendix C**

<b>Fig. C.1   5:1 PDMS spinning characteristics.</b> Note that as the spin time, spin speed, or dilution is increased, the results are achieved from left to right.....	170
<b>Fig. C.2   Control master mold casting assembly.</b> Plate 1 is the base rectangular plate that the master wafer sits on, plate 2 is the rectangular wafer window plate, allowing for PDMS pouring, and plate 3 is the rectangular polygon plate that is used for mechanical stability to prevent PDMS shrinkage during alignment/bonding. ....	173
<b>Fig. C.3   PDMS alignment stage.</b> Note that the acrylic plate will be a polygon plate (3) during the actual procedure. ....	174
<b>Fig. C.4   PDMS surface images after dicing with different razor blades.</b> The utility blade is a thick blade made for general purpose cutting while the other blades are commercial razor blades deisgned for shaving.....	176

## List of Tables

<b>Table 2.1   Experimental Parameters for Fluorescence Characterization of ARROW Devices</b> .....	23
<b>Table 4.1   General SU-8 Processing Parameters</b> .....	47
<b>Table 4.2   Comparison of PDMS manifold materials</b> .....	48
<b>Table 5.1   Zaire Ebola Virus Nucleic Acid Sequences</b> .....	77

## List of Acronyms and Notation Conventions

AG	As-grown, a descriptor for CMOS devices directly after their conventional fabrication.
APTES	(3-aminopropyl)triethoxysilane, a chemical used to coat plastic surfaces to enable plasma activation and bonding to PDMS.
ARROW	Antiresonant reflecting optical waveguide
BHF	Buffered hydrofluoric acid, used to isotropically etch glass.
BSA	Bovine serum albumin, typically used as a blocking agent to reduce non-specific binding.
CMOS	Complementary metal–oxide–semiconductor, an acronym generally used to describe semiconductors in pertinence to processing techniques
CWDM	Coarse wavelength division multiplexing
Cy	Cyanine (as in fluorescent dyes)
DNA	Deoxyribose nucleic acid.
DRIE	Deep reactive ion etching, a CMOS process used to etch materials while creating vertical sidewalls.
DUL	Distinct upper layer, a high index layer formed at the top of SiO <sub>2</sub> structures due to porosity and absorption of water.
DWDM	Dense wavelength division multiplexing
EBOV	Ebola virus
EDX	Energy dispersive x-ray, a means of determining material composition by looking at x-ray emission patterns upon electron bombardment.
FCS	Fluorescence correlation spectroscopy, a method of analyzing fluorescence signals employing mathematical autocorrelation with a well defined observation volume to determine molecular characteristics such as concentration and diffusion coefficients.

FDM	Finite difference method, a means of computationally simulating structures by discretizing defining functions at points in space.
FRET	Fluorescence resonant energy transfer, a process which occurs between donor and acceptor fluorescent dyes.
HOMO	Highest occupied molecular orbital
LOD	Limit of detection, the lowest detectable signal of a sensor system.
LUMO	Lowest unoccupied molecular orbital
MARV	Lake Victoria Marburg virus
MEMS	Micro-electro-mechanical systems
MMI	Multimode interference waveguide, a waveguide that supports more than one transverse mode that can be propagated simultaneously to construct optical inference patterns.
PDMS	Polydimethylsiloxane, a polymer used for rapid prototyping microfluidic devices
PDMS	Polydimethyl siloxane, a polymer material that is composed of base and curing agent, mixed with various ratios of base:curing agent (e.g. 10:1), to form a cured elastomer. This material is ideal for rapid prototyping of microfluidic devices.
PECVD	Plasma enhanced chemical vapor deposition, a means of depositing various materials onto a surface through gaseous-to-solid phase transitions.
RET	Resonant energy transfer, a non-radiative version of FRET.
S/B	Signal to background ratio, a metric for signal level over bulk background signal.
S/N	Signal to noise ratio, a metric for peak signal level over the standard deviation of the noise level.
SEM	Scanning electron microscope, a means of imaging samples with near nanometer resolution using a beam of collimated



	electrons.
SiO <sub>2</sub>	Silicon dioxide (commonly known as glass)
SUDV	Sudan virus
TIR	Total internal reflection
TIRF	Total internal reflection fluorescence, a means of exciting a fluorescent sample using the evanescent wave of propagating light.
T <sub>m</sub>	Melting temperature, used here to define the temperature at which two complementary nucleic acid strands are 50% dissociated.
WDM	Wavelength division multiplexing, a term canonically used to describe the process of propagating multiple wavelengths of light through an optical fiber to increase data throughput.
YO	Oxazole Yellow, an intercalating dye

%T	Percent transmission
C	Concentration
c <sub>v</sub>	Coupling coefficients of electromagnetic fields
D	Diffusion coefficient
d	Layer thickness
d <sub>c</sub>	Waveguide core thickness
F(t)	Time dependent fluorescence signal data trace.
FWHM	Full width half maximum
G(τ)	Autocorrelation function
h	Height of a channel/feature

$H(\tau)$	Autocorrelation fitting function
$h_c$	Control channel height
$h_{ex}$	Excitation mode $1/e^2$ height
ID	Inner diameter
$k_C$	Core propagation wavevector of a waveguide mode
$k_{TC}$	Transverse decomposition of $k_C$
L	Length of a channel/feature
LOD	Limit of detection, the lowest detectable signal of a sensor system.
$L_v$	Length of lightvalve
$L_\pi$	Beat length between the fundamental and first order mode (or the length of propagation at which the modes $v = 0$ and $v = 1$ are completely out of phase, e.g. $(\beta_0 - \beta_1)L_\pi = \pi$ ).
N	Number of excitation pattern (spot) replicas reproduced in an MMI.
$n_C$	Core refractive index of waveguide
$n_i$	Refractive index of an antiresonant layer
OD	Outer diameter
P	Pressure
$P_i$	Input optical power
$P_o$	Output optical power
R	Microfluidic channel flow resistance
R	Reflection coefficient
$S(t,\Delta t)$	Most generally a matrix describing the shift multiply output of a processed multippeak signal.

$t_i$	Thickness of an antiresonant layer
$T_m$	Melting temperature, used here to define the temperature at which two complementary nucleic acid strands are 50% dissociated.
$V_z$	Flow velocity
$w$	Width of a channel/feature
$W_e$	Effective width of a waveguide
$w_{ex}$	Excitation mode $1/e^2$ width
$w_v$	Width of lightvalve
$w_{xc}$	Spot size of the collection efficiency function in $x$ -direction (defined by the liquid-core waveguide mode)
$w_y$	Excitation beam $y$ dimension
$w_z$	Excitation beam $z$ dimension
$\alpha$	Optical waveguide loss
$\beta$	Mode propagation constant
$\Delta t$	The time difference between fluorescence peaks in multisport excitation fluorescence detection experiments.
$\eta$	Viscosity of a fluid
$\theta_c$	Propagation angle of a mode in a waveguide core
$\theta_i$	Angle of propagation or incidence angle
$\lambda$	Wavelength of electromagnetic waves
$\nu$	Order of a waveguide mode
$\tau$	Time lag
$\Psi$	Total electromagnetic field

$\psi_v$	Modal electromagnetic field
----------	-----------------------------

## **Abstract**

**Joshua W. Parks**

### **Hybrid Optofluidic Biosensors**

Optofluidics, born of the desire to create a system containing microfluidic environments with integrated optical elements, has seen dramatic increases in popularity over the last 10 years. In particular, the application of this technology towards chip based molecular sensors has undergone significant development. The most sensitive of these biosensors interface liquid- and solid-core antiresonant reflecting optical waveguides (ARROWs). These sensor chips are created using conventional silicon microfabrication. As such, ARROW technology has previously been unable to utilize state-of-the-art microfluidic developments because the technology used—soft polydimethyl siloxane (PDMS) micromolded chips—is unamenable to the silicon microfabrication workflows implemented in the creation of ARROW detection chips. The original goal of this thesis was to employ hybrid integration, or the connection of independently designed and fabricated optofluidic and microfluidic chips, to create enhanced biosensors with the capability of processing and detecting biological samples on a single hybrid system. After successful demonstration of this paradigm, this work expanded into a new direction—direct integration of sensing and detection technologies on a new platform with dynamic, multi-dimensional photonic re-configurability.

This thesis reports a number of firsts, including:

- 1,000 fold optical transmission enhancement of ARROW optofluidic detection chips through thermal annealing<sup>1</sup>
- Detection of single nucleic acids on a silicon-based ARROW chip<sup>2</sup>
- Hybrid optofluidic integration of ARROW detection chips and passive PDMS microfluidic chips<sup>2</sup>
- Hybrid optofluidic integration of ARROW detection chips and actively controllable PDMS microfluidic chips with integrated microvalves<sup>3</sup>
- On-chip concentration and detection of clinical Ebola nucleic acids<sup>4</sup>
- Multimode interference (MMI) waveguide based wavelength division multiplexing for detection of single influenza virions<sup>5</sup>
- All PDMS platform created from monolithically integrated solid- and liquid-core waveguides with single particle detection efficiency and directly integrated microvalves<sup>6</sup>, featuring:
  - Tunable/tailorable PDMS MMI waveguides
  - Lightvalves (optical switch/fluidic microvalve) with the ability to dynamically control light and fluid flow simultaneously
  - Lightvalve trap architecture with the ability to physically trap, detect, and analyze single biomolecules.

## Acknowledgements

This work was made possible by the support of my mentors, colleagues, collaborators, thesis committee, friends, and families. I am deeply grateful to all of them for their support. Among them, I would like to express direct appreciation for exceptional contributions. Firstly, I would like to thank my This work was made possible by the support of my mentors, colleagues, collaborators, thesis committee, friends, and families. I am deeply grateful to all of them for their support. Among them, I would like to express direct appreciation for exceptional contributions. Firstly, I would like to thank my advisor Professor Holger Schmidt for his direct and omnipresent support throughout my graduate career. As an exceedingly diligent and expert teacher, he guided me through my transition from biochemistry to electrical engineering. The hours of shared critical dialogue and mentoring have truly prepared me as an able minded scientist. I am also indebted to my collaborators at Brigham Young University and UC Berkeley who provided me with the fundamental expertise and physical equipment/samples that were used throughout this thesis. For that matter, I owe much of my success to the hard work and brilliant ideas of my colleagues and fellow graduate students at UC Santa Cruz. One graduate student in particular, my brother — Joe Parks, contributed intellectually and physically to many of the new works reported here. Without him, I would have accomplished half as much, with a quarter of the fun in between. From my first step, I've learned from you – thank you for your constant and bold striding into the unknown, my role-model, best friend, and brother. Last (and certainly not least), I would like to thank my

parents, Virgil and Kathy Parks. I recognize you've dedicated your lives to helping me achieve happiness and success, and I am unfathomably grateful for your selflessness. I love you both; thanks again for the frozen meals and unclogged sinks.



## 1 Introduction

Semiconductor computing technology has propelled human civilization into the 21<sup>st</sup> century with the capability to process information in less than a billionth of a second. The development of this technology has required considerable expansion of industrial infrastructure. The machines and techniques used therein are known as semiconductor processing (CMOS) technology. However, the abundance of Moore's law, requiring the doubling of feature density every two years, inherently required an industrial infrastructure that was continuously in flux. It is thus from the dregs of the CMOS industry that many technologies were born.

In 1967, Nathanson et al. utilized CMOS technology to create a resonant gate transistor, which married the orthogonal fields of mechanical sensors and semiconductor devices.<sup>7</sup> Little did they know, they had created the first of many devices that would become collectively known as micro-electro-mechanical systems (MEMS). Such systems would prove themselves industrially through applications such as car crash impact detectors<sup>8</sup>, video projector micro-mirrors<sup>9</sup>, and printer inkjet nozzles<sup>10</sup>.

The pervasion of CMOS technology into the sciences did not stop in MEMS – it seeped into biological sciences in the form of microfluidics—i.e. the handling of fluids in channels with micrometer dimensions. Relying heavily on CMOS processing techniques in addition to MEMS device architectures, conduction and manipulation of fluids on the micrometer scale became reality.<sup>11</sup> One particular application of conventional lithography, soft polydimethylsiloxane (PDMS) lithography, quickly

became the standard in microfluidics due to its ability to rapidly prototype devices<sup>12</sup>, create 3-dimensional fluidic channels<sup>13</sup>, and enable fluidic architectures with active flow control<sup>14</sup>. Microfluidic devices demonstrated abilities to miniaturize sample handling<sup>15</sup>, process biological materials<sup>16</sup>, and even analyze single cells<sup>17</sup>. Such device functionality gave rise to the idea that entire biological experiments could be conducted in a “lab-on-a-chip”.<sup>18</sup>

While lab-on-a-chip devices continued to develop into complete fluidic assays onto microfluidic chips, the readout mechanisms remained bulky in off-chip optical equipment. The drive for full miniaturization led to the development of optofluidics, or the fusion of microfluidics and optics.<sup>19</sup> Due to the planarity of the CMOS/MEMS technologies used to create microfluidics, many of the developed optofluidic platforms relied on optical waveguide technology. Such waveguides were based on one of two principles, total internal reflection (TIR) or wave interference.<sup>18</sup> The former, a direct product of Snell’s law, is achieved by filling microfluidic channels with high refractive index liquids.<sup>20</sup> This type of guiding is unfortunately limited when it comes to biosensing as the conventional biological solvent, water, has a lower refractive index than the vast majority of solid materials. While there are certain materials that meet Snell’s requirements for water based optofluidic TIR waveguides,<sup>21,22</sup> their fabrication is difficult and often leads to unstable devices. As such, a CMOS compatible anti-resonant device is the next best approach. Relying on anti-resonant reflecting optical waveguide (ARROW) technology, a device can be built with multi-layer reflectors forming the exterior walls of a fluidic waveguide.<sup>23</sup>

Thanks to tried and true semiconductor processing technology, direct integration of liquid filled ARROW waveguides is easily achievable with both ridge waveguides<sup>24</sup> and fiber optics<sup>25</sup>. Integrated solid- and liquid-core waveguides led to optofluidic devices with the ability to detect fluorescent analytes<sup>26</sup>, trap biological particles<sup>27</sup>, and filter optical excitation light<sup>28</sup>. It is clear that these advancements succeeded at integrating optics into microfluidic environments.

In spite of continuous advancement, the original dream of optofluidics—to directly marry optical technology with modern microfluidics—has fallen short of its potential. Most optofluidic devices have compromised automated sample processing for integrated optics. Conversely, true-to-form microfluidic analysis systems have become more complex in fluidic capabilities without expanding optical ones. Therefore, this thesis was aimed to directly combine microfluidic and optofluidic technology into a hybrid optofluidic biosensor that truly features the best of both worlds.

Organization of this thesis follows accordingly: chapter 2 will contain the information required to fundamentally understand molecular detection through the lens of ARROW optofluidic device design, fabrication, and implementation. Bimolecular processing and sample handling will be explained through the lens of PDMS microfluidic chip layout and manufacture. Chapter 3 will describe a crucial enhancement of ARROW optofluidic chips that allows for detection of single biomolecules. The first union of passive microfluidic devices with CMOS optofluidic detection chips will be presented in Chapter 4. Congruently, the integration of

programmable active microfluidics with ARROW detection technology will be presented in Chapter 5. The advantages of hybrid optofluidic integration are leveraged, culminating in the automated detection of clinically relevant biomolecules in Chapter 6. Finally, Chapter 7 will introduce a novel, flexible optofluidic waveguide platform, finally marrying solid- and liquid-core waveguides with active microfluidic technology, ultimately leading the way towards a true lab-on-chip device.

## 2 Background

Understanding hybrid optofluidic biosensors in their entirety requires a fundamental understanding of each of the components. In the following chapter I will attempt to describe these components insofar as their pertinence to biosensing, with emphasis on the aspects of the technologies used throughout this thesis. I will begin at the molecular level, describing light-matter interactions (e.g. fluorescence) and their application to biosensing. I will then lay the groundwork for understanding the antiresonant reflecting optical waveguide (ARROW) platform as well as PDMS microfluidic devices, from fabrication to implementation.

### 2.1 Fluorophores and Fluorescence

Organic fluorophores are the most widely used reporting molecules implemented in current-day biosensing. Historically, cyanine dyes tend to be the most widely used dyes in biological sciences. This adoption, although seemingly trivial, has had dramatic impact on industrial standards in regions such as optical filters, optical elements, and even laser excitation sources.

For demonstration, the case of Cy3 and Cy5 fluorescent dyes will be considered. As seen in Fig. 2.1 (left), Cy3 and Cy5 are very similar molecules with similar fluorescence properties. Ignoring their differences for now, the general case of fluorescence can be considered in the center plots of Fig. 2.1. Within these plots it can be seen that two sub-processes must occur for successful fluorescence: absorption and emission. Absorption occurs when an incident photon's energy ( $E_{\text{ex}} = hc/\lambda_{\text{ex}}$ ) is equal

to the energy difference between a molecule's relaxed,  $S_0$ , and excited,  $S_1$ , electronic states.

Upon absorption, an electron moves from state  $S_0$  to  $S_1$ . Emission occurs when an electron relaxes back to state  $S_0$  from  $S_1$ , regenerating a photon. If this explanation were the entirety of the truth, one would expect complete conservation of energy and equivalency of absorbed and emitted photons. However, a hallmark of fluorescence is that the energy of the emitted photon is slightly less than the absorbed one. Looking more closely at Fig. 2.1 (center), it can be seen that the electronic energy states (dark lines) are split into sub-states (light lines). This splitting is known as rotational/vibrational broadening, and occurs because molecular bonds are not strictly rigid. As the molecules relax between excited vibrational energy states, energy is lost as heat, resulting in the characteristically lower energy of emitted

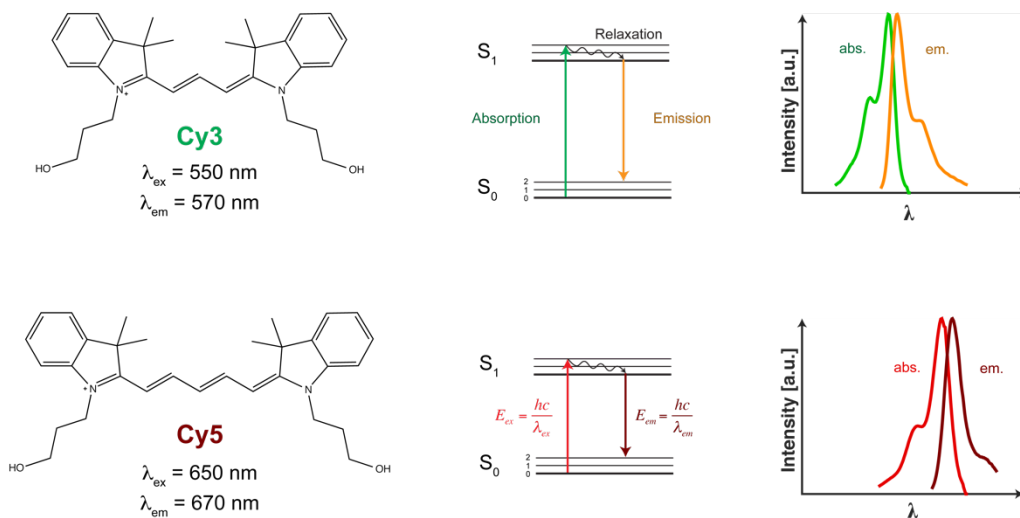


**Fig. 2.1 | Organic dye properties: Cy3 and Cy5 dyes as examples.**

photons (in comparison to absorbed ones). Furthermore, due to lax transition rules between vibrational and electronic states, it is possible to absorb/emit between a multitude of ro-vibration states, creating a continuum that leads to the broad spectra seen in Fig. 2.1 (right).

Now that the general properties of fluorescence are understood, it becomes important to understand the nuanced differences between Cy3 and Cy5 dyes. The highly conjugated molecules are represented as Kekulé structures in Fig. 2.1 (left) where carbons are at each line juncture and each line represents a pair of electrons. In both molecules, there is a noticeable pattern of alternating double and single bonds (lines). This leads to conjugation, or a continuous system of ( $\pi$ ) electrons. In fact, the electrons reside within molecular orbitals, which are linear combinations of the atomic orbitals of each compositional atom. Importantly, upon combination of  $N$  atomic orbitals,  $N$  molecular orbitals are created. Note that the molecular orbitals have split energies in comparison to the originally degenerate atomic orbitals due to the laws of quantum mechanics. Spectroscopists tend to call the highest occupied molecular orbital (HOMO) the  $S_0$  state and the lowest unoccupied molecular orbital (LUMO) the  $S_1$  state. It is interesting to see that the difference in energy between these states is different for Cy3 and Cy5. More specifically, Cy3 has an absorption wavelength of 550 nm while Cy5 absorbs at 650 nm (or decreased photon energy, i.e.  $E \propto 1/\lambda$ ). As the only difference in molecular structure is an added double bond in Cy5, it is clear that increased  $\pi$  conjugation decreases the amount of energy splitting

between  $S_0$  and  $S_1$  states. This results in a red-shifted absorption/emission spectrum for Cy5.

The purpose of the chemical difference between Cy3 and Cy5 is to manufacture different fluorescent wavelength dyes. However, this begs the question: is it possible to further modify the dyes in order to create alternate utility? For example, one important characteristic of molecular reporters in biosensing is that they can “sense” their chemical environments. There are two clear avenues to build this functionality into fluorescent reporters: further intelligent alteration of the dye’s chemical structure or alteration of its photo-physical environment. An example of each approach is presented in the form of nucleic acid stains and molecular beacons, respectively.

## 2.2 Fluorescent Reporters: Nucleic Acid Stains and Molecular

### Beacons

Nucleic acid stains can, in general, be either absorbent or fluorescent. Due to the nature of the work within this thesis, focus will be given to stains of the fluorescent nature. The utility in nucleic acid stains, unlike conventional

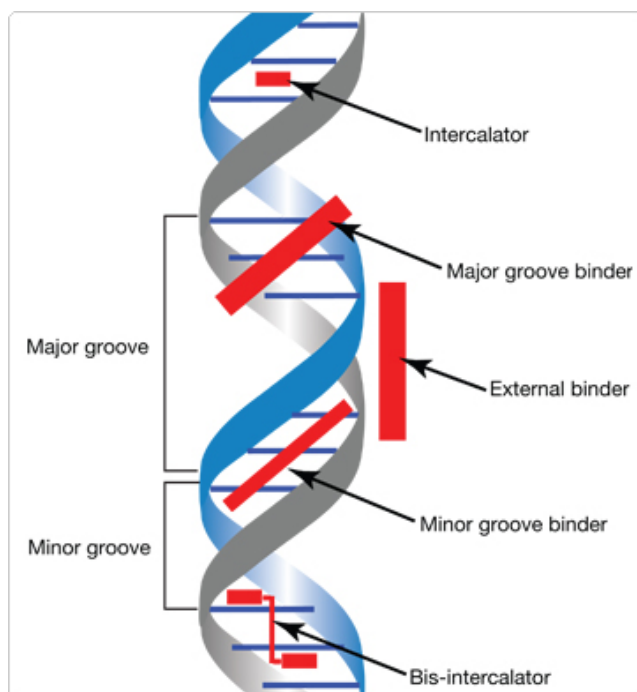
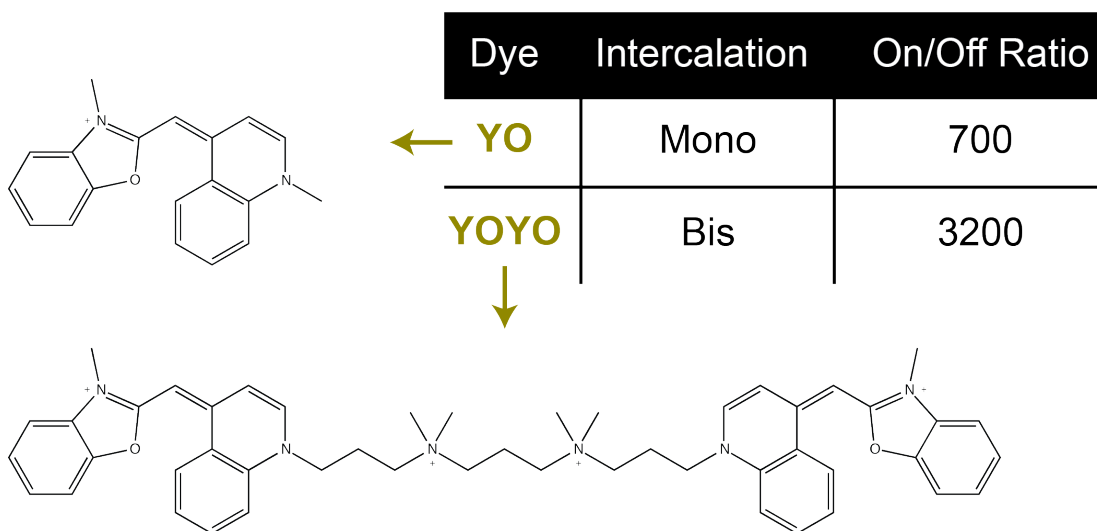


Fig. 2.2 | Binding modes of nucleic acid stains.



fluorophores, is that they emit very little fluorescence when not bound to nucleic acids, yielding very low background signals. Upon binding to a nucleic acid, the stain “turns on”, i.e. becomes much more fluorescent. While the mechanism of this “on-off” utility varies depending on the type of dye, the increase in fluorescence is typically generated by a stabilization of the fluorophores thanks to secondary and



**Fig. 2.3 | YO and YOYO intercalating dye properties.**

tertiary structures of nucleic acids, as illustrated in Fig. 2.2.<sup>29</sup>

For the purpose of exemplifying general properties of nucleic acid stains, two intercalators will be considered, oxazole yellow (YO) and its homologous dimer (YOYO).<sup>30</sup> Seen in Fig. 2.3, both fluorescent dyes exhibit regions of highly conjugated hydrocarbons as was the case in common fluorophores (see Section 2.1). As discussed previously, these highly conjugated structures are a hallmark of almost all organic fluorescent dyes. However, there is a subtle utility built implicitly into the monomeric YO dye: there is a propensity for isomerization and dimerization upon optical excitation, both of which significantly reduce the quantum efficiency of the

dye, and both of which are eliminated upon binding to nucleic acids.<sup>31</sup> For a representative picture of how these conformational changes are forbidden, see the intercalator and bis-intercalator binding modes in Fig. 2.2.

Another thing to note about the structures of YO and YOYO is that they are both highly positively charged. This is a common feature of essentially all nucleic acid stains as the biomolecule itself carries two negative charges per base pair. Due to charge shielding and steric hindrance, the intercalators presented here have the ability to bind every two and four base pairs for YO and YOYO, respectively. Herein lies the real power of nucleic acid stains: each nucleic acid can be labeled many times, without need for covalent modification of the target biomolecule. For example, a single nucleic acid of 10 kilobase pairs can have up to 5,000 YO intercalators or 2,500 YOYO intercalators.<sup>30</sup> This leads to incredibly large fluorescent signals that are easy to detect.

Unfortunately, nucleic acid stains themselves contain only the ability to turn off and on in a sequence agnostic fashion. In some applications, it is desirable or even necessary to have the ability to turn the reporting molecule off and on in the presence of specific nucleic acid sequences. In such applications, the ideal fluorescence reporter is a molecular beacon. A molecular beacon relies on two core technologies to function. The first technology is fluorescence resonance energy transfer, or FRET which requires two dyes: a donor dye and an acceptor dye. The donor dye has an absorption spectrum that overlaps with the excitation source. The acceptor dye has an absorption spectrum that overlaps with the emission spectrum of the donor dye. The

actual process of resonant energy transfer happens as follows: the donor dye absorbs a photon from the excitation source. If the donor and acceptor are in close proximity ( $< \sim 10$  nm), there is a distinct probability that resonant energy transfer will occur instead of fluorescence. Note that the probability scales linearly in a small dynamic range of distance, and then reaches close to unity at small distances. If FRET occurs between donor and acceptor, the donor will relax without fluorescing, and the acceptor itself will fluoresce. An example dye pair is Cy3 and Cy5 (see Fig. 2.1), with the former being the donor and the latter being the acceptor. Although this dye pair is well suited and characterized, it ultimately results in fluorescence (albeit at a higher wavelength), while the ideal case for molecular beacons would be a fluorescence/no fluorescence behavior, i.e. resonance energy transfer (RET), instead of FRET. As such, the implementation of non-fluorescent chromophores into molecular beacons became a standard.<sup>32</sup> Note that the selection of dye-quencher pairs can be an involved process.<sup>33</sup>

In addition to the characteristic dye-quencher pair, molecular beacons also have an implicit sequence specific sensor function. As seen in Fig. 2.4, the molecular beacon is composed of a dye, quencher, and interconnecting nucleic acid sequence



**Fig. 2.4 | Molecular Beacons for Nucleic Acid Detection.**

which typically has a deoxyribose backbone, i.e. DNA. The DNA sequence is designed such that the terminal ends (i.e. 3' and 5' ends, denoted as such due to the reactive backbone sugar bonds) have reverse complement sequences – reverse complement meaning if the 5' end of a beacon is AATGC then the 3' end sequence would be TTACG (with both sequences read from 5' to 3'). This design yields an energetically favorable intramolecular hybridization that puts the dye and quencher in close (non-fluorescing) proximity – a structure called a hairpin. This ~ 5 base pair structure, denoted the stem, is connected by the loop structure of the beacon. It is in the loop that the molecular specificity resides. Specifically, the loop is a reverse complement of a subsequence of the target nucleic acid. It is designed in length such that formation of a hybrid between the loop and target sequences is a lower free energy than the intramolecular stem formation. As such, in the presence of target, the molecular beacon preferentially forms a hybrid rather than an intramolecular hairpin. The hybrid formation separates the dye and quencher spatially, removing the RET interaction and allowing fluorescence to occur. Molecular beacons thus have the advantage of inherent specificity, with the retained ability to turn on and off. However, as the structure is rather complex and large in comparison to nucleic acid stains, it is difficult to multiply label single nucleic acid targets.

### **2.3 *ARROW Fundamentals***

Molecular labeling and reporting, a well established field, can be a very powerful biosensing tool when coupled with new detection technologies. More specifically, miniaturization of detection technology onto platforms that can fit in the palm of your

hand reduce sample volume and instrument complexity, while increasing detection efficiency. Developing such a platform, i.e. chip based technology, has been the major thrust of the Schmidt lab for over a decade. In contrast, the main focus of this thesis is based on the integration of chip based detection technology with chip based fluid processing technology. However, it is essential to first understand the fundamental concepts underlying the detection platform. At the heart of the detection technology is the antiresonant reflecting optical waveguide (ARROW) principle which will be described herein.

### 2.3.1 Deriving the ARROW Condition

ARROWs were originally developed to enable waveguiding in low index cores.<sup>34</sup> Specifically, conventional waveguides rely on total internal reflection to keep light inside a high refractive index core, however, in biosensing applications where liquid water is the solvent, it is not possible to freely choose the core refractive index. In contrast, it is possible dictate the photonic environment of the water, namely by cladding a liquid channel with antiresonant layers. Such cladding will allow for

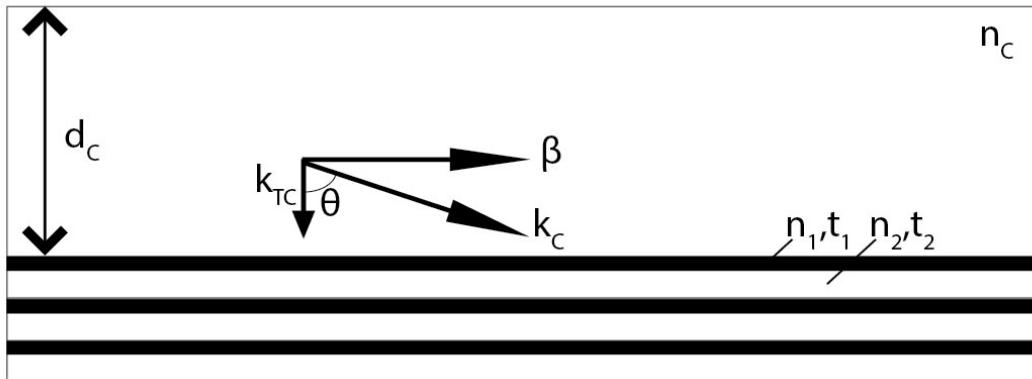


Fig. 2.5 | Generic ARROW Structure and Wavevector Diagram.

retention of optical light in a low index medium. Design of the layers is a careful and analytic process that is described below.

In order to develop an understanding of ARROWs, the structure seen in Fig. 2.5 will be carefully considered. First of all, the mode condition for this generic slab waveguide requires that the light can form a standing wave (mode) inside the core.

This can be expressed mathematically as

$$k_{TC}d_C = m\pi \quad m = 1,2,3 \dots \quad (2.1)$$

Although there are phase changes at reflection interfaces, depending both on polarization and refractive indexes, they cancel for a correctly defined structure and are thus omitted for clarity. Notice that  $k_{TC}$  is the transverse propagation wave vector (or the transverse decomposition of the core propagation vector  $k_C$ ). Furthermore, this equation states  $k_{TC}$  must have a phase change of  $m\pi$  over the thickness of the core,  $d_C$ . For the fundamental mode,  $m = 1$ , a propagation angle,  $\theta_C$ , can be solved for:

$$\begin{aligned} k_{TC}d_C &= \pi \\ k_C \cos(\theta_C)d_C &= \pi \\ \frac{2\pi n_C}{\lambda} \cos(\theta_C)d_C &= \pi \\ \cos(\theta_C) &= \frac{\lambda}{2n_C d_C} \end{aligned} \quad (2.2)$$

Using the Pythagorean Formula ( $\sin^2 + \cos^2 = 1$ ), we can equally state (2.2) as

$$\sin(\theta_C) = \sqrt{1 - \left(\frac{\lambda}{2n_C d_C}\right)^2} \quad (2.3)$$

Now that we have explicitly defined the propagation angle in terms of design parameters, the next step is to do the same for the  $i^{\text{th}}$  ARROW layer. As the name ARROW suggests, the layers are antiresonant and will consequently form destructive standing waves changing the condition from (2.1) to

$$k_{Ti}t_i = (2N - 1)\frac{\pi}{2} \quad N = 1,2,3 \dots \quad (2.4)$$

An interesting note: this is the vector relation of a quarter wave Bragg stack, further verifying the principle of antiresonance. Next, solving for  $t_i$  we find

$$t_i = \frac{(2N - 1)\lambda}{4n_i \cos(\theta_i)} \quad N = 1,2,3 \dots \quad (2.5)$$

Rewriting using the Pythagorean Formula

$$t_i = \frac{(2N - 1)\lambda}{4n_i \sqrt{1 - \sin^2(\theta_i)}} \quad N = 1,2,3 \dots \quad (2.6)$$

and noting that Snell's Law affords the following relation (with expansion for  $i > 1$ )

$$\sin(\theta_i) = \frac{n_c}{n_i} \sin(\theta_c) \quad (2.7)$$

we can rewrite (2.6) using (2.3) and (2.7) as

$$t_i = \frac{(2N - 1)\lambda}{4n_i \sqrt{1 - \left( \frac{n_c}{n_i} \sqrt{1 - \left( \frac{\lambda}{2n_c d_c} \right)^2} \right)^2}} \quad N = 1,2,3 \dots \quad (2.8)$$

Finally, simplifying the ARROW equation is found to be

$$t_i = \frac{(2N - 1)\lambda}{4n_i \sqrt{1 - \frac{n_c^2}{n_i^2} + \frac{\lambda^2}{4n_i^2 d_c^2}}} \quad N = 1,2,3 \dots \quad (2.9)$$

From this result, it is possible to gain insight into the physical dimensions of ARROW devices. More explicitly, for visible wavelengths, core dimensions of  $\sim 5$   $\mu\text{m}$ , and core refractive index around 1.33-1.46, first order ( $N = 1$ ) ARROW layer thicknesses are approximately hundreds of nanometers. Luckily, these thicknesses are achievable with optical grade smoothness using conventional semiconductor fabrication techniques.

### **2.3.2 ARROW Device Fabrication**

ARROW structures can be built to propagate multiple mode<sup>23</sup> or a primarily a single mode<sup>35</sup>. While the former has advantages insofar as ease of fabrication and direct fiber interfacing, it is only capable of detecting large fluorescent analytes such as cells.<sup>25</sup> On the other hand, coupling into the fundamental mode of ARROWs confines light in small waveguides (4-5  $\mu\text{m}$  in critical dimensions) yielding very high optical intensities and also reduces spurious background sources. Such advantages are very desirable for chip-based fluorescence sensors, and will be fully borne out in the following section. Currently, it is important to understand the geometry and fabrication of single mode ARROW devices as a stepping stone to understand the technology as a whole.

ARROW devices, aptly dubbed, require antiresonant layers to function. Uncoincidentally, the fabrication of sensor devices begins with the deposition of ARROW layers onto a silicon substrate as seen in Fig. 2.6a. It is clear that both solid-core and liquid-core waveguide fabrication begin on the same plane, above the deposited ARROW layers. Note that current ARROW sensors employ industrially



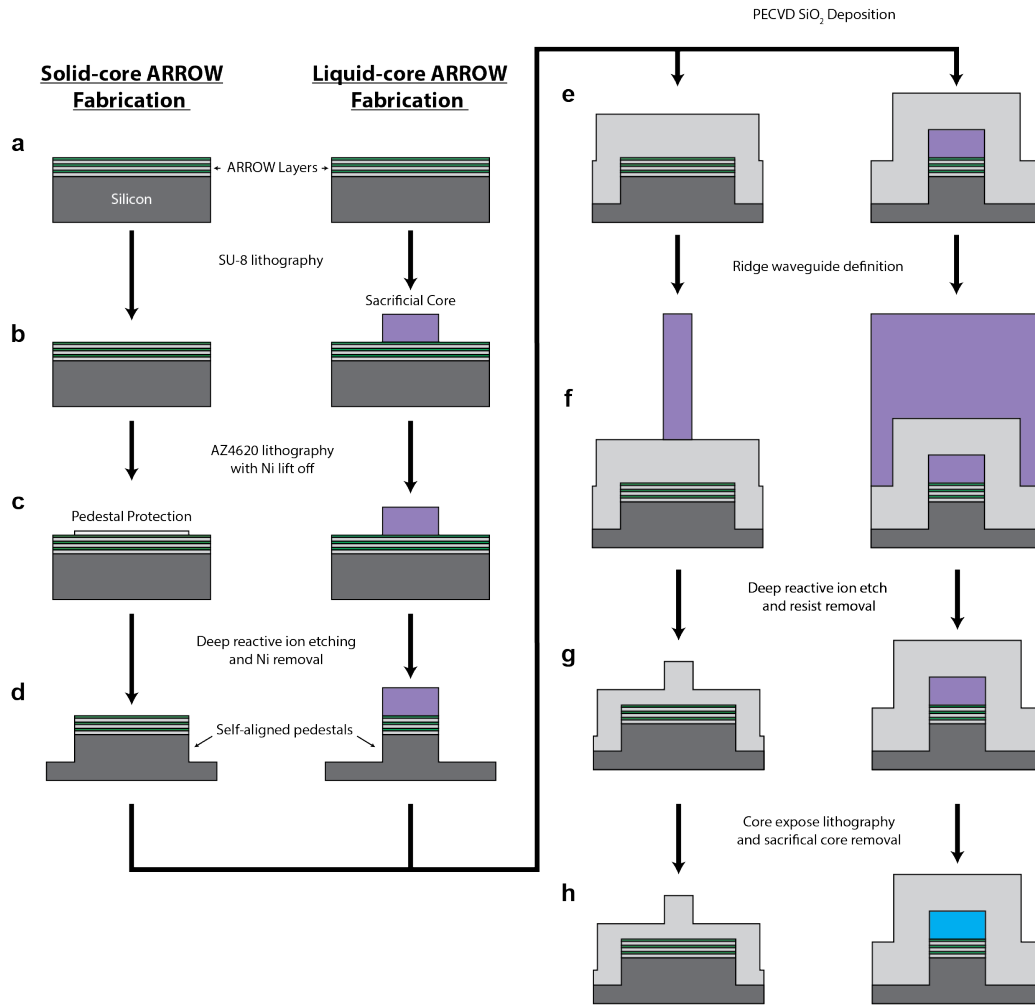


**Fig. 2.6 | Fabrication workflow for solid- and liquid-core ARROWs. (Dimensions not precisely to scale)**

deposited tantalum and silicon oxide layers (Evaporated Coatings, Inc.). The choice of these layers is based on their optical quality (transparency and low photoluminescence) in the visible regime.<sup>36–38</sup> After this step, a 20 nm silicon dioxide (SiO<sub>2</sub>) layer (adhesion promotion) and a 100 nm chrome “pre-core” layer (downstream etch stop) are deposited. These steps are omitted in Fig. 2.6 for clarity.

The first step of defining waveguide geometry is definition of the sacrificial core (a place holder that will later be etched to form the liquid-core waveguide), see

Fig. 2.6b. Accomplished through SU-8 lithography, sacrificial core dimensions are typically defined as  $5 \times 12 \mu\text{m}$ . In the vertical dimension, a  $\sim 5 \mu\text{m}$  limit is reached in attempts of mitigating multimode device behavior through mode matching to optical fiber.<sup>39</sup> While tapers can be used in the horizontal direction to mitigate multimode behavior<sup>40</sup>, a  $\sim 12 \mu\text{m}$  limit is imposed because of aspect ratio limitations (i.e. hollow channels begin to collapse at larger dimensions and also support more high order modes). Furthermore, while maintaining single-mode behavior, small waveguide dimensions reduce background signal in fluorescence experiments and also yield higher excitation intensities.

Next, lithography (employing positive resist AZ4620) in conjunction with nickel lift off procedures defines a ridge protection region as a preamble to the following fabrication step (Fig. 2.6c). That is, in the next step, a deep reactive ion etcher (DRIE) is used to anisotropically etch the ARROW layers and subsequent silicon to form isolated pedestals upon which waveguides can be fabricated.<sup>41</sup> Note that the pedestals formed in Fig. 2.6d are considered “self-aligned” because the features themselves define the etch mask, as opposed to an independent etching step.<sup>42</sup>

Plasma enhanced chemical vapor deposition (PECVD) is then used to conformally cover the wafer in approximately  $6 \mu\text{m}$  of  $\text{SiO}_2$ , as illustrated in Fig. 2.6e. Oxide deposition can be precluded by growth of another set of ARROW layers,<sup>35</sup> however, these layers tend to degrade waveguide intersection transmission

performance and do not significantly affect the optical loss of liquid-core ARROW waveguides.<sup>43</sup>

Solid-core ridge waveguides are then formed using a combination of SU-8 lithography and DRIE. These steps are depicted in Fig. 2.6f and g. There are a couple important things to notice in these steps. First, a rather thick (~15  $\mu\text{m}$ ) layer of SU-8 has to be used to protect the waveguide features (both liquid-core and soon to be solid-core waveguides). Such a thick etch stop is needed because there is poor selectivity for the DRIE between SU-8 and  $\text{SiO}_2$ . This thickness is an inherent limitation in lateral resolution for waveguide feature definition. Secondly, the alignment of this photolithographic step critically protects the liquid-core waveguide and aligns both excitation and collection solid-core waveguides to liquid-core waveguide. As such, this lithography step is one of the most crucial steps in the fabrication process.

Finally, the liquid-core waveguides are formed in the following steps: a core expose lithography step is used to isolate the oxide above the ends of each liquid-core channel. The oxide is then removed down to the chrome etch stop layer through use of buffered hydrofluoric acid (BHF). Once the oxide is removed, the sacrificial SU-8 core is exposed and can be etched using an optimized piranha etching formula over the course of approximately one week.<sup>44</sup> The final resulting solid- and liquid-core waveguides are shown in Fig. 2.6h (on the left and right, respectively).

### 2.3.3 Fluorescence Based ARROW Detection

ARROW devices have been used in a variety of application including particle trapping<sup>27,40,45,46</sup>, SERS detection<sup>47</sup>, atomic spectroscopy<sup>48–50</sup>, optical filtering<sup>51,52</sup>, and nanopore detection<sup>53–55</sup>. However, one of the most important applications of the ARROW device is its use as biomolecular detection system. More specifically, the ability to fabricate intersecting solid- and liquid-core waveguides yields itself readily to the formation of an orthogonal waveguide geometry, and inherently a chip based fluorescence detection system.<sup>24</sup>

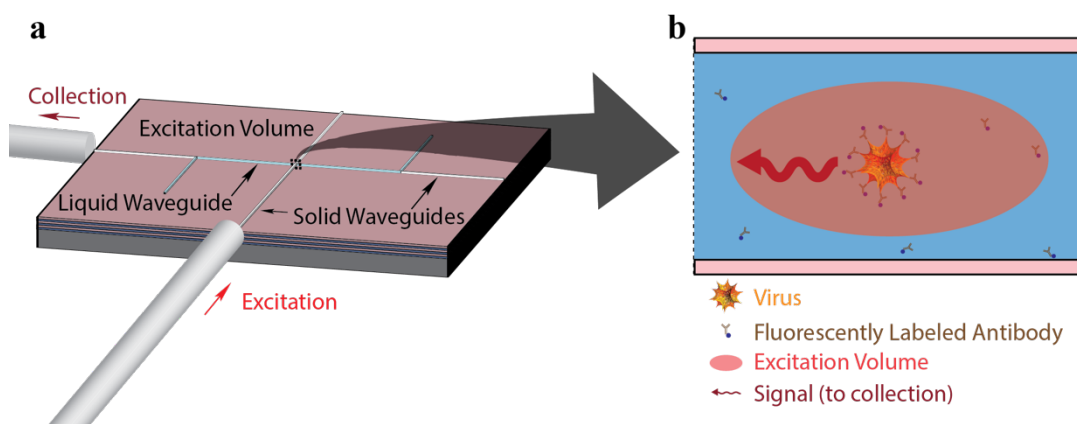


**Fig. 2.7 | ARROW Detection Geometry. a**, ARROW fluorescence 3D view with butt coupled excitation and collection optical fibers. **b**, Cross-sectional view of the excitation volume with an antibody labeled virus being excited.

As discussed above, fluorescence in the biological sciences is usually achieved through absorption and emission of light from organic fluorophores. Fluorescence thus requires two components for an instrument to be a viable fluorimeter – a method of optical excitation and a means of collecting the stimulated fluorescence signal. The approach in ARROW chips is to employ waveguides in both processes. The geometry, illustrated in Fig. 2.7a, involves intersecting ARROWs.

First, an excitation solid-core waveguide is fiber butt coupled to a laser excitation source. The laser light travels down the solid-core waveguide and passes through the orthogonal liquid-core waveguide creating an optical excitation volume. The excitation volume, illustrated in red in Fig. 2.7b, is defined by the solid-core waveguide mode. Any fluorescent analyte (with correct absorption properties) traveling through the excitation volume will be excited by the input laser light. However, due to the limitations of the collection volume, which is defined by the liquid-core waveguide mode, not all excited particles will be detected. By convoluting the excitation volume (roughly an elliptical cylinder) with the liquid-core waveguide mode, the observation volume can be determined. Any particles within the observation volume will be detected, provided they emit enough fluorescence signal.

As far as fluorescence goes, there are two regimes of detection: bulk fluorescence detection and single particle fluorescence detection. Bulk implies residence of multiple analytes within the observation volume at any given time while single particle detection implies an average of less than one particle in the observation volume per unit time. Representative data is presented in Fig. 2.8. More

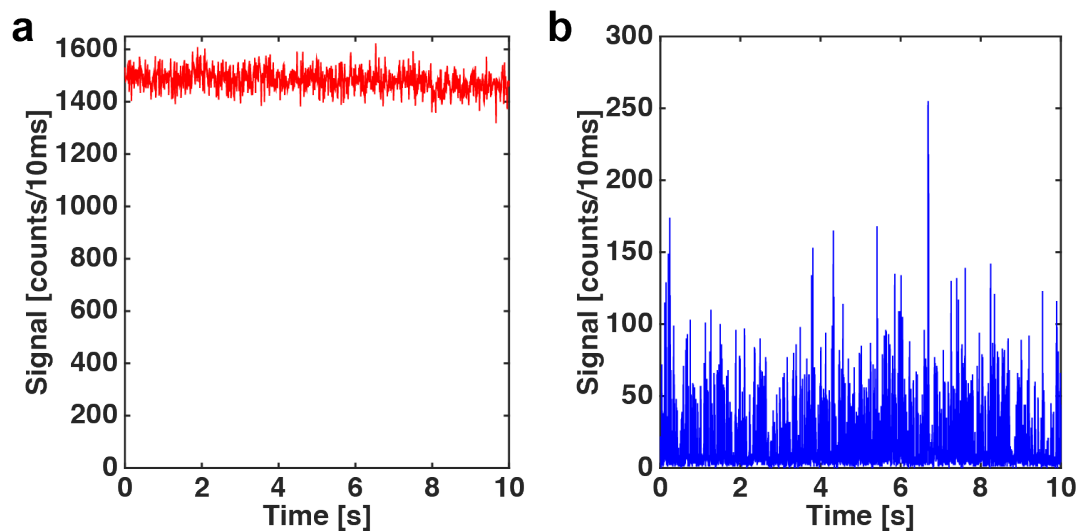


**Fig. 2.8 | Fluorescence Detection on an ARROW Chip. a.** Bulk fluorescence detection of 22.5 nM

specifically, Fig. 2.8a demonstrates bulk detection of 22.5 nM dye. Qualitatively, it is bulk detection because the signal does not reach the background level between each fluorescence incident (note single dye detection is not currently feasible, rather, the readout is the average fluorescence intensity). Quantitatively, the experiment demonstrates bulk detection as the concentration of dye, 22.5 nM, is well above the limit of  $\sim 10$  pM where there is on average one molecule per excitation volume,  $\sim 100$  fL (the dimensions here are approximate as they depend on the particular chip/waveguide mode geometry). On the other hand, Fig. 2.8b clearly shows multiple single particle detection events where the signal returns to baseline before the next particle signal begins. This makes sense as the concentration  $4 \times 10^7$  particles/mL (or 66 fM), is well below the single particle concentration limit. It is important to note that in the case of exceedingly fast flow velocity (i.e. the flow velocity multiplied by the detector acquisition time is much greater than the width of the excitation volume) the observation volume is in fact enlarged in the direction of flow. In other words, a single bin in the fluorescence trace can contain multiple times the volume of fluid in a single excitation volume. It is thus advisable to keep the concentration of analytes much lower (orders of magnitude) than the single particle detection limit when using external flow initiation, e.g. vacuum, positive pressure, electric field, as the readout here is the detection of individual peaks.

The importance of these simple fluorescence experiments is not their novelty (as they have been conducted on ARROW chips in multiple published works); rather, the importance of simple bulk and particle detection is in their function as a metric.

More specifically, Fig. 2.8 shows a bulk signal of about 1500 photons/10ms for 22.5 nM Cy5 and fluorescence spikes for 100 nm fluospheres at an average of 50 photons/10ms peak signal. While these numbers are a decent metric in themselves for comparison to other ARROW detection chips, there is a multitude of other considerations that must be addressed before an analytical comparison can occur. In addition to analyte composition and concentration the following experimental properties must be accounted for in an equal comparison: optical filter configuration, excitation laser power, optical setup light collection efficiency, liquid flow velocity, data analysis binning size, the number of excitation spots, and most importantly, the chip background. In the above experiment the parameters were as follows in Table 2.1.

**Table 2.1 | Experimental Parameters for Fluorescence Characterization of ARROW Devices**

<b>Parameter</b>	<b>Red Channel (Bulk Dye Detection)</b>	<b>Blue Channel (Single Particle Detection)</b>
<b>Optical Filters</b>	660BP40 (through 600nm dichroic)	513BP17 (reflected 600nm dichroic)
<b>Optical Excitation</b>	$P_{in-633nm} = 1.8 \text{ mW}$	$P_{in-488nm} = 1.8 \text{ mW}$
<b>Excitation Waveguide</b>	Single-mode operation	Single-mode operation
<b>Collection Efficiency</b>	$CE_{Red} = 75\%$	$CE_{Blue} = 70\%$
<b>Flow Velocity</b>	$v_{flow} = 2 \text{ mm/s}$	$v_{flow} = 2 \text{ mm/s}$
<b>Data Binning</b>	10 ms	10 ms
<b>Background</b>	$1 \pm 1 \text{ photon/10ms}$	$7 \pm 3 \text{ photons/10ms}$
<b>Analyte</b>	22.5 nM Cy5	$4 \times 10^7 \text{ mL}^{-1}$ 488 nm 100nm Fluospheres
<b>Signal</b>	$S_{bulk} = 1500 \text{ cts/10ms}$	$S_{peak} = 50 \text{ cts/10ms}$
<b>Figure-of-merit</b>	S/B = 1,500	S/N = 7

It is clear that there are many factors to control for a sound and direct comparison of chips between users/labs, however, for single user chip comparison on a consistent experimental setup, there is a simple means of comparing optofluidic

chips. The direct means of comparing chips/wafers is through signal-to-background (S/B) or signal-to-noise (S/N) comparisons. Specifically, when using the same setup and same dye/particles (essentially controlling all of the above factors), it possible to simply take a signal measurement and background measurement for each chip and directly compare their S/B and S/N ratios. This metric is considerably more accurate than simple liquid-core waveguide transmission tests as it directly measures chip detection efficiency. As an example, the chip used in Fig. 2.8 has a bulk S/B ratio of 1,500 for the red channel and an average S/N ratio of 7 on the blue channel. Here, the background is taken as the average signal with a water filled chip while the noise is taken as the standard deviation of the background signal. Note that for bulk measurements where the average signal level is important, S/B ratio is the relevant figure of merit, whereas, in particle measurements where detection of peaks is important, S/N ratio is the most important. In both categories the chip used above performed exceedingly well and can be used as a metric for further device characterization.

## ***2.4 PDMS Prototyping and Fabrication***

Silicon-based ARROW chips have been significantly optimized for fluorescence detection, however, due to their solid structure, they are unable to control/process fluids on-chip. One technology that has been significantly used in this regard (fluid handling) is elastomeric microfluidics.<sup>56</sup> Although there are many polymers used in conventional microfluidics<sup>57</sup>, polydimethylsiloxane (PDMS) has become the most ubiquitous due to its ease of use, low-cost, and ability to rapidly



prototype.<sup>12,58</sup> Furthermore, by stacking PDMS layers, it is possible to form topologically complex 3-dimensional microfluidic networks.<sup>13</sup> An immediate adaptation of this 3D architecture is in the creation of addressable microvalves.

While microvalves come in many shapes and sizes<sup>14</sup>, the academically adopted standard is an addressable valve that is actuated via off-chip pneumatics. The original pneumatic PDMS microvalve was fabricated in a so-called “push-down” geometry.<sup>59</sup> Depicted on the left of Fig. 2.9, push-down valves are open under atmospheric pressure because the hemispherical channel is unobstructed. When positive pressure is applied to the control (upper) layer, the fluid channel (blue) collapses and flow is

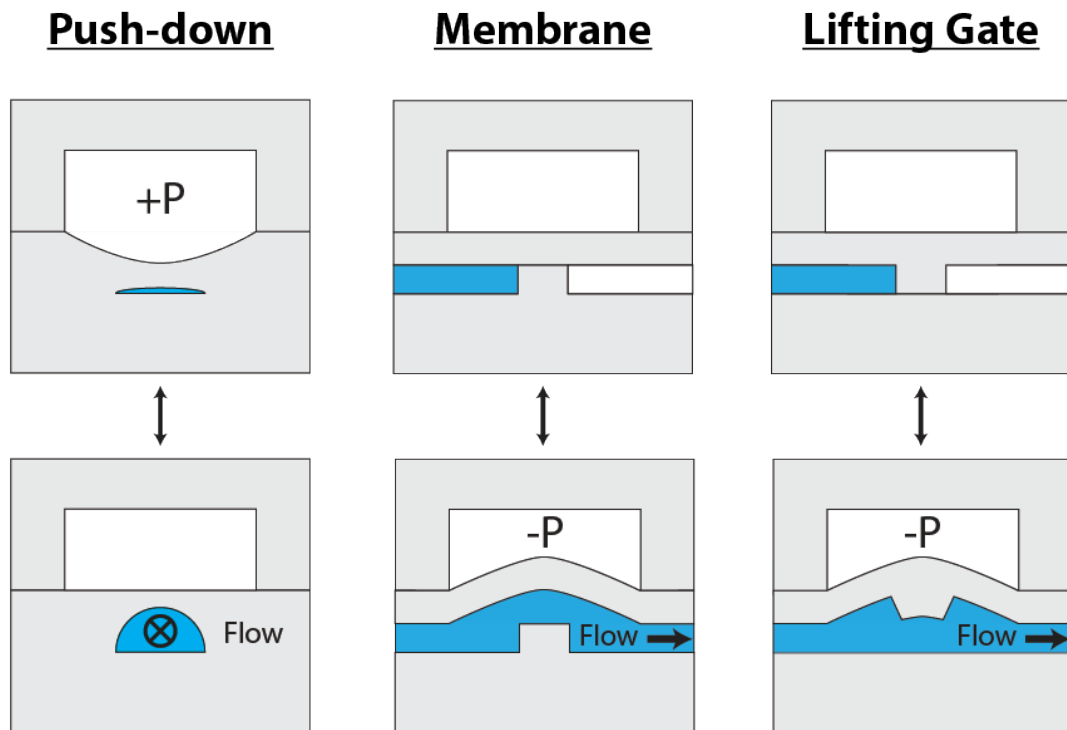


**Fig. 2.9 | Common geometries of pneumatically addressable PDMS microvalves.** The push-down valve is shown end-on while the membrane and lifting gate valves are shown from the side for clarity.

blocked. Note, it is important for the flow channel to be hemispherical (as opposed to rectangular) in this geometry in order for the valve to completely close during actuation. The advantages of this technology in comparison to the other pneumatic valve architectures are that the alignment step between the upper and lower layer is easy, there is no need for a free-standing membrane, and there is no gating structure upon which analytes can get caught on. On the other hand, this structure requires mixed lithography to form different channel geometries and the requisite hemispherical channel obviates the possibility of integrated optical structures.

The middle and right most pneumatic valve geometries in Fig. 2.9 are very similar in structure. Each contains a gate structure for blocking fluid flow in the passive position (opposite of the push-down valve, which is open in the non-actuated position). Both valves are then actuated by applying negative pressure to deform the membrane and create a continuous fluid path. The membrane valve is composed of featured upper and lower materials with an un-patterned membrane in the center of the device.<sup>60</sup> This is in contrast to the lifting gate architecture which has a featured upper and membrane layer with an featureless base layer.<sup>61,62</sup> Each of these geometries has its advantages. The membrane valve is very amenable to glass microfluidics and the introduction of different materials to form the internal membrane. On the other hand, the lifting gate valve removes the gate from the fluid path and thus creates more streamlined fluid flow, which particles are less likely to become stuck in. Furthermore, when reversibly bound, lifting gate devices can be repeatedly used on patterned substrates for a variety of assays.<sup>63</sup>

Despite their differences, the above microvalves are all fabricated in similar ways. As all of the devices used in this thesis are lifting gate geometry, the fabrication outline specific to this technology will be discussed herein. Furthermore, a more detailed fabrication procedure will be presented concerning PDMS waveguide/optofluidic structure formation in Chapter 7, so the description here will be brief.

In general, microfluidic features are conventionally transcribed using CAD software. The works presented in this thesis were created using AutoCAD as this commercial software is free to students. Once the features have been defined digitally, they are printed either on a Mylar transparency—when feature size limits don't shrink below 10  $\mu\text{m}$ —or are laser printed on a chrome mask with  $\sim 1 \mu\text{m}$  precision. Note the latter technology is only avoided because of dramatically increased cost and production times. From this point, the masks are treated identically and used in conventional lithography. Depicted in Fig. 2.10,

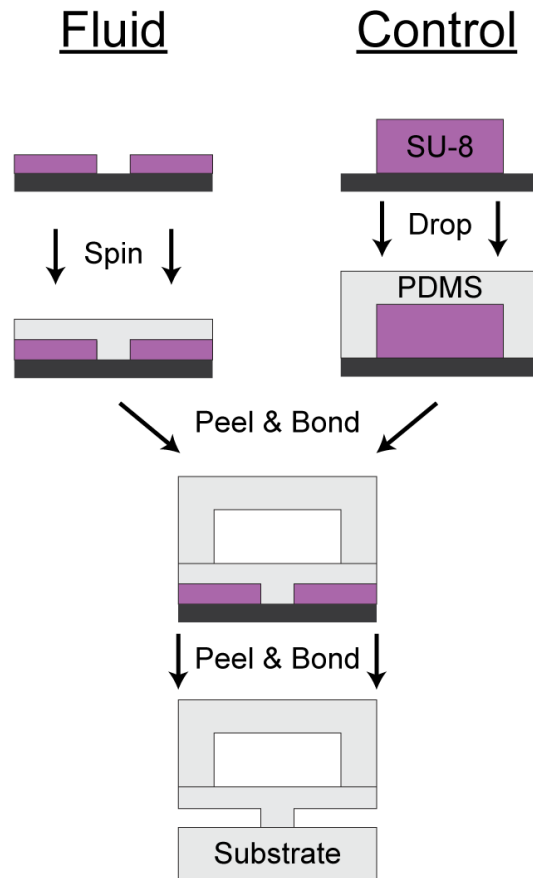


**Fig. 2.10 | General multilayer PDMS device fabrication workflow.**

simultaneous fabrication of fluid and control layers begins with formation of SU-8 master molds. Note that control and fluid features can be defined with dramatically different lateral dimensions as well as thickness. The fluid layer is formed by spin casting a thin ( $\sim 100 \mu\text{m}$ ), continuous membrane on the master mold while the control layer is simply drop casted to an appropriate thickness ( $\sim 3 \text{ mm}$ ) to support the physical stability of the device. After curing, the control layer is peeled from the master mold and pneumatic access ports are punched using a disposable biopsy punch. Both the fluid membrane (still attached to the master mold) and control layer are plasma treated, aligned, and brought into contact to permanently bond the two together. Finally, the dual-layer structure is then peeled from the fluidic master mold, punched for access to fluid channels, plasma treated, and bonded to a desired substrate.

### 3 Enhancement of ARROW Optofluidic Biosensors via Thermal Annealing

ARROW photonic biosensors have been undergoing optimization for more than a decade. Published improvements include layer optimization,<sup>42</sup> waveguide intersection transmission optimization,<sup>64</sup> waveguide geometry optimization,<sup>40</sup> on-chip optical background filtering,<sup>28,52</sup> signal-to-noise enhancement strategies,<sup>65</sup> and chip background reduction.<sup>37</sup>

One idea to further lower optical background was to anneal tantalum oxide ARROW thin films as a means to reduce spurious recombination centers and photoluminescence.<sup>38</sup> As seen in Fig. 3.1, the idea was successful when implemented

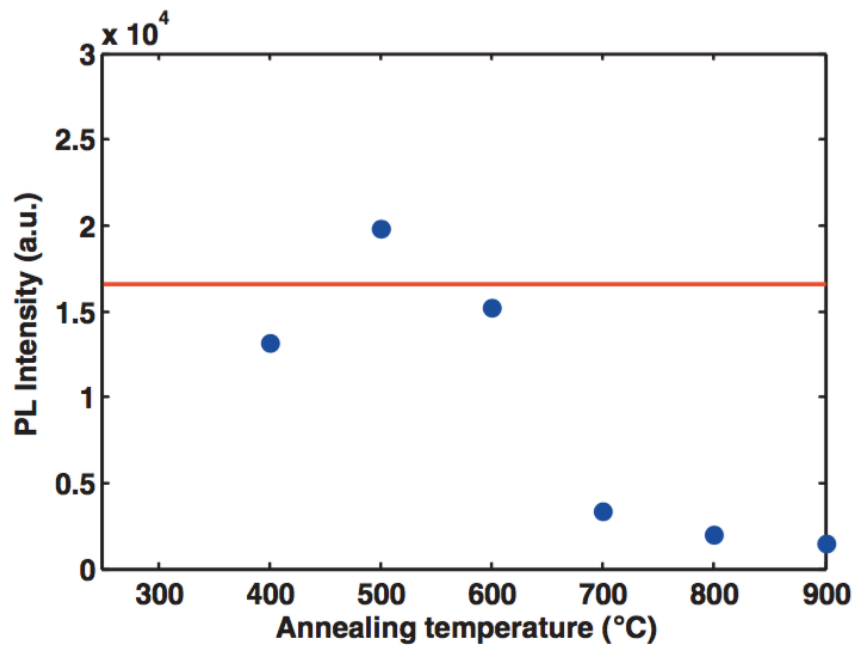
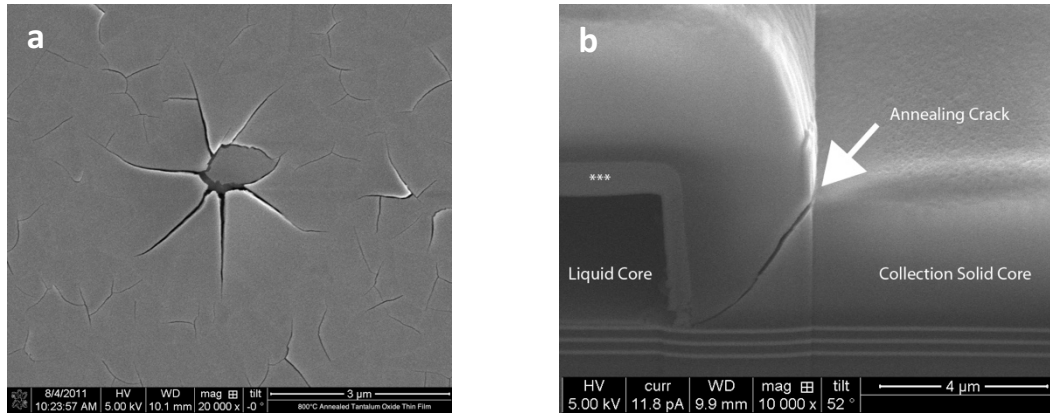
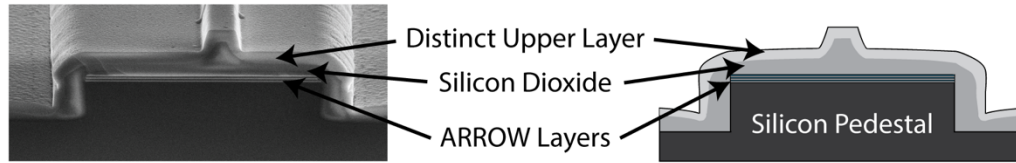


Fig. 3.1 | Reduction of tantalum oxide photoluminescence in thin films via thermal annealing. Note the red line indicates as-grown film photoluminescence.



**Fig. 3.2 | Physical effects of thermal annealing on ARROW structures. a,** Tantalum oxide thin film (100 nm) “star” cracking after 700 °C annealing. **b,** Cross-sectioned liquid- to solid-core waveguide intersection with a large crack caused by annealing. \*\*\*Secondary feature is an artifact of focused ion beam milling.

on free standing tantalum oxide films (backscattered photoluminescence was measured with a 632.8 nm excitation source) for temperatures above 700 °C, annealed for at least 2 hours. Optical imaging and scanning electron microscopy of the annealed waveguides demonstrated that cracking was occurring during annealing. Furthermore, imaging of individual annealed ARROW layers showed that cracking was occurring due to a crystalline phase transition at higher ( $> 700$  °C) temperatures. Both of these effects, illustrated in Fig. 3.2, should have led to poor optical guiding, however they did not have significant negative effects. On the contrary, waveguide transmission was dramatically increased upon annealing. Furthermore, lowering the annealing temperature to 300 °C mitigated most cracking while still dramatically improving optical transmission. The interrogation of this curious annealing effect led to the work in the following chapter and the largest improvement in ARROW chip performance to date.<sup>1</sup>



**Fig. 3.3 | Scanning electron microscope (SEM) image (left) and schematic representation (right) of a 4  $\mu\text{m}$  wide solid-core ARROW ridge waveguide sitting on a silicon pedestal.**

Specifically, in this chapter, I show that a distinct upper layer (DUL) with increased refractive index in the  $\text{SiO}_2$  ridge waveguides of ARROW devices is formed during fabrication. This layer, illustrated in Fig. 3.3, causes significant degradation of optical chip quality, concerning both power transmission and mode shape. I further demonstrate that low temperature thermal annealing eliminates the DUL and its effects. After annealing, silicon dioxide ridge waveguides have dramatically increased confinement within the core, leading to substantially lower optical propagation losses and improved solid- to liquid-core waveguide coupling efficiencies. Finite difference method (FDM) simulations support experimental results showing that optical field localization within the DUL causes high loss, both in propagation and waveguide to waveguide coupling. Repeated cycles of boiling (in water) and thermal annealing of silicon dioxide waveguides suggest that water absorption into the porous oxide is the cause of the DUL. Finally, I report dramatic signal improvements for fluorescence particle detection in orthogonal beam geometry produced by thermal annealing of optofluidic detection chips. Although the effects presented here were observed over multiple renditions of ARROW chips, the data reported herein corresponds to treatments of ZA5, SP2, and MA15 wafers.

### **3.1 Post Processing Low Temperature Thermal Annealing**

It is important to note that throughout the remainder of the chapter, annealing refers to a specific post processing of as-grown ARROW chips. This procedure was consistently conducted as follows: low temperature thermal annealing was performed in an annealing furnace at atmospheric pressure (normal air atmosphere) by placing diced chips from a wafer onto a ceramic plate (Thermo-Fisher). The furnace was programmed to ramp from room temperature to 300°C over 4 hours (to avoid rapid thermal expansion and cracking of SiO<sub>2</sub> layers), maintain a 300°C temperature for 8 hours, and ramp down to room temperature over no less than 4 hours (subject to dissipative cooling). Note that while 300°C was the lowest temperature exhibiting exhibiting positive effects for 8 hour anneals, further optimization of the annealing procedure is certainly possible.

### **3.2 Optical Characterization of Annealed ARROW Structures**

#### **3.2.1 Optical Confinement and Loss in Solid-core Waveguides**

First, we determined that thermal annealing has significant effects on the properties of PECVD-grown solid-core SiO<sub>2</sub> ridge waveguides. As seen in Fig. 3.4a, as-grown ARROWs exhibited considerable lateral divergence of butt-coupled laser light, spreading quickly over a distance of ~250 μm before being laterally confined by the silicon pedestal. When annealed following the procedure described above, lateral optical confinement underneath the 4 μm wide ridge is dramatically improved. In order to quantify the increase in lateral confinement upon annealing, the optical mode profile was imaged at the waveguide facet. As seen in Fig. 3.4b, an as-grown



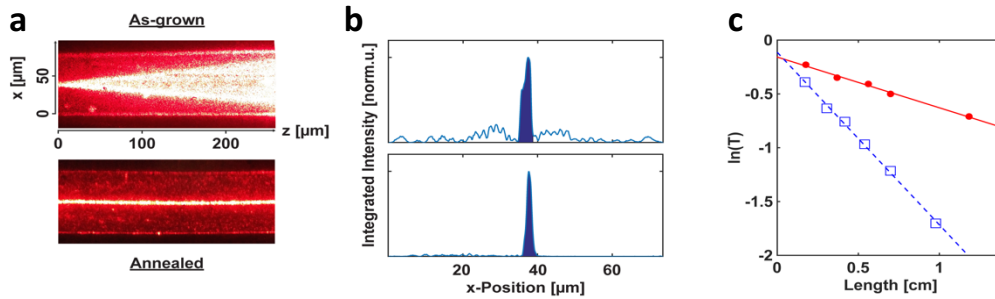


**Fig. 3.4 | Effects of annealing on solid-core waveguide light propagation.** **a**, Top down image of light confinement within an ARROW ridge waveguide before (top) and after annealing (bottom). **b**, Integrated mode intensity output of a 1 cm long as-grown (top) and annealed (bottom) solid-core waveguide. Intensity within the core of the waveguide is shaded dark blue. **c**, Transmission measurements for cut-back solid core waveguides. As-grown waveguides (open blue squares) have a fitted loss coefficient  $\alpha_{AG} = 1.63 \text{ cm}^{-1}$  (dashed line). Annealed waveguides (closed red circles) have a fitted loss coefficient  $\alpha_A = 0.471 \text{ cm}^{-1}$  (solid line). Both fits have  $r^2 > 0.99$ .

ARROW chip has poor lateral confinement—34% within the ridge core, after 1 cm of propagation. Note that the mode intensity was integrated in the vertical (y) direction to obtain the plots seen in Fig. 3.4b. Upon annealing, the confinement of the ARROW increases to 84% within the ridge core, a nearly 2.5-fold improvement. There is an apparent discrepancy in core confinement between Fig. 3.4a and Fig. 3.4b as-grown samples. This is explained by the fact that the loss of widely spread modes is higher than that of the fundamental ridge modes and thus appears more prominently in the top-down view of Fig. 3.4a. In addition, the images in Fig. 3.4a cover a propagation distance of  $\sim 250 \mu\text{m}$ , while the mode images in Fig. 3.4b were taken at 1 cm length, where a significant portion of the unconfined light had already been lost.

In order to obtain the waveguide loss for the light confined within the 4  $\mu\text{m}$  ridge, two adjacent solid-core waveguides were separated and subjected to a cut-back analysis. Note that output optical intensity was focused through an iris, collecting intensity propagating within the core and 10  $\mu\text{m}$  to either side. The results displayed

in Fig. 3.4c show that the annealed ARROW had an optical loss coefficient ( $\alpha_A = 0.47 \text{ cm}^{-1}$ ) over three times lower than that of an as-grown ARROW ( $\alpha_{AG} = 1.63 \text{ cm}^{-1}$ ). We also note that as we are selecting the intensity within the core for this measurement, the as-grown sample exhibits the lower limit of its loss coefficient. If included, the more divergent/lossy light outside of the ridge core would contribute to a higher loss value.

Finite difference method (FDM) optical modeling was used to further investigate the difference between as-grown and annealed solid-core waveguides. The

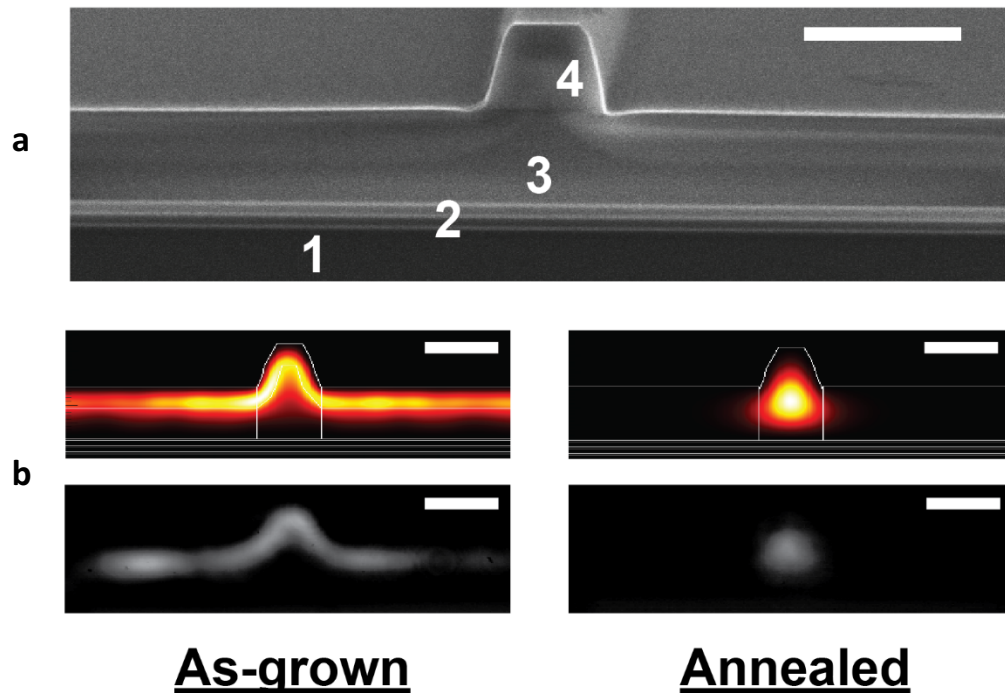


**Fig. 3.5 | Finite difference method simulations of a solid-core ARROW waveguide before and after annealing. a,** SEM image of a solid-core waveguide facet with silicon substrate, ARROW layers, low refractive index  $\text{SiO}_2$  ( $n_L = 1.46$ ), and high refractive index  $\text{SiO}_2$  DUL ( $n_{DUL} = 1.47$ ) labeled as 1-4, respectively. **b,** Modal simulations (top, colored) and experimental images (bottom, grayscale) for as-grown and annealed ridge waveguides. All white scale bars represent  $5 \mu\text{m}$ .

sample dimensions were extracted from the SEM cross-section of a solid-core waveguide shown in Fig. 3.5a. While the silicon substrate, ARROW layers, and ridge waveguide profile matched their design specifications, the presence of a distinct upper layer, DUL (designated 4), is readily apparent and follows the ridge profile with a thickness of  $\sim 2 \mu\text{m}$ . Energy-dispersive X-ray (EDX) analysis confirmed the presence of this layer, and showed that the DUL had markedly higher oxygen content. Specifically, the bulk oxide had an expected 2:1 ratio of oxygen to silicon while the DUL had a 2.8:1 ratio of oxygen to silicon. This increase in oxygen content can be explained by water absorption. In accordance with literature data concerning water absorption into a porous  $\text{SiO}_2$  layer, the DUL was set to have a higher refractive index ( $n_4 = 1.47$ ) than the lower  $\text{SiO}_2$  layer ( $n_3 = 1.46$ ).<sup>66</sup> With this inclusion, modal simulations of as-grown waveguides match experimentally determined patterns, as seen in Fig. 3.5b (left) for a 3 mm long ARROW waveguide. Furthermore, when the mode profile is simulated with a homogeneous  $\text{SiO}_2$  layer ( $n_3 = n_4 = 1.46$ ), the fundamental ridge mode is primarily excited. Fig. 3.5b (right) shows that after annealing, the ARROW chip has a mode matching that of a ridge waveguide fundamental mode. The simulated  $1/e^2$  fundamental mode width for the given waveguide structure— $3.6 \mu\text{m}$ —is in very good agreement with the measured width— $3.3 \mu\text{m}$ . Furthermore, the simulated modes presented in Fig. 3.5 have confinement factors (relative intensity within the ridge width) of 43% and 89% for as-grown and annealed, respectively. This is in excellent agreement with the experimentally observed confinement factors of 41% and 89%. We also note that even though the

sample presented in Fig. 3.5 is different than that of Fig. 3.4, there is relative agreement between the data.

There is some variability amongst as-grown ARROW chip performances due to fabrication inhomogeneities as well as the uncontrolled nature of water absorption, which inherently gives rise to varying DUL dimensions. Although the as-grown structure in Fig. 3.5b exhibits no fundamental ridge mode (in simulation or experiment), thinner DULs exhibit hybrid fundamental modes, while the thinnest DULs simply exhibit an upward shift of the fundamental mode. However, all tested chips exhibit a fundamental mode after annealing.

### 3.2.2 Transmission Changes in Connected Solid- and Liquid-core Waveguides

#### Waveguides

While annealing significantly improves modal confinement and loss in solid-core only waveguides, a more complete study of full optofluidic devices, that are

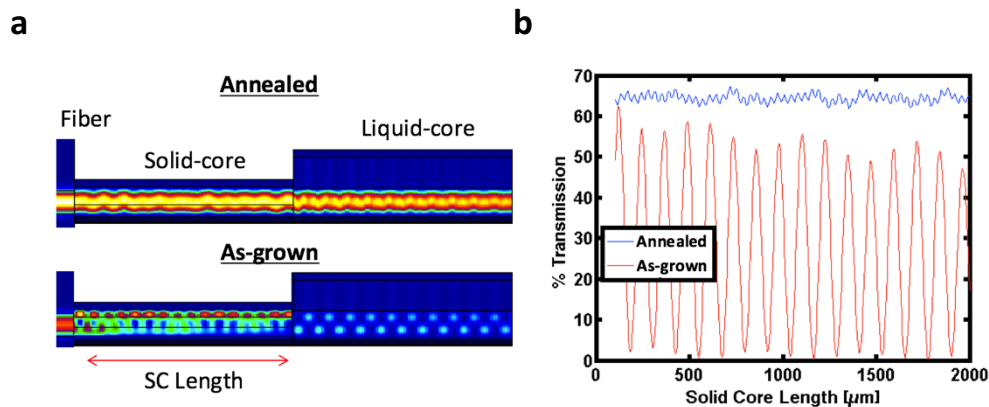


**Fig. 3.6 | Simulation of optical transmission through connected solid- and liquid-core waveguides.** **a**, Side view images of simulated transmission through waveguide systems. The annealing simulation has homogenous refractive index in the solid-core waveguide while the as-grown waveguide has a DUL. ARROW lengths are 2 mm. **b**, Transmitted optical power for different solid-core waveguide lengths (as indicated in **a**).

composed of connected solid- and liquid-core waveguides, is needed. To this end, similar simulations to those seen in Fig. 3.5 were conducted. More specifically, as seen in Fig. 3.6a, a fiber fundamental mode was used to couple light into a solid-core ARROW structure with (bottom, as-grown) and without (top, annealed) a DUL in the transverse dimension. It is clear simply from these images that a strong beat pattern occurs in the as-grown sample solid-core waveguide while the annealed solid-core waveguide exhibits nearly fundamental mode behavior. When the output of the solid-core waveguide is connected to a liquid-core ARROW, the effect of the mode beating becomes more prominent. In detail, due to the small number of low-loss modes a liquid-core ARROW supports, it acts as an aperture for optical transmission. Seen in Fig. 3.6b, the optical transmission of connected, annealed liquid- and solid-core ARROWs is fairly constant for different solid-core lengths as there is minimal mode beating in the solid-core waveguide and coupling into low order liquid core modes is consistent. However, an as-grown solid-core waveguide has significant mode beating and consequently only couples into low order ARROW modes for specific length solid-core waveguides, resulting in inconsistent total optical transmission.

In order to supplement simulation findings, the optical transmission of combined solid-/liquid-core waveguide systems were measured over the majority of the visible light spectrum using a white light source.<sup>67</sup> We first examine transmission *across* a short, 12  $\mu\text{m}$  wide, liquid-core waveguide. This reveals changes in the coupling efficiency across solid/liquid-core interfaces. Fig. 3.7a shows the improvement factor generated by dividing the chip's transmission spectra before and

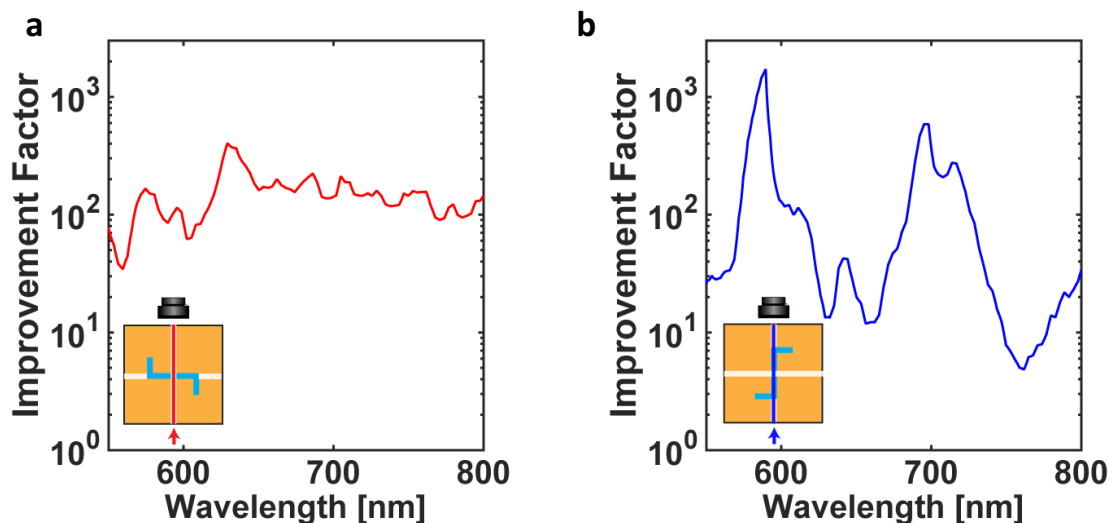


**Fig. 3.7 | Wavelength dependent improvement of full ARROW sensor chip transmission.** Improvement is measured across (a) and through (b) the liquid-core waveguide. Insets show schematics of the transmission experiments.

after annealing. It is clear that the transmission of solid-/liquid-core ARROW samples improves considerably throughout the visible light spectrum. These large improvements cannot be explained by the reduced solid-core waveguide loss alone. Instead, they are due to increased transmission across the two solid-to-liquid-core waveguide intersections. This is also evident with the top-down observation that scattering at solid/liquid intersections was much brighter in as-grown samples than in annealed ones. Previous work has demonstrated the importance of ARROW intersection optimization for increased optical transmission.<sup>68</sup> In particular, the solid-core waveguide thickness decreases at the interface with the liquid core due to the finite conformality of the PECVD process. This crevice reduces coupling into the liquid-core waveguide<sup>68</sup> which is much more pronounced for the DUL modes in the as-grown sample that are propagating near the top of the solid-core waveguide.

Next, we investigated transmission *through* a long (4 mm) liquid-core waveguide section. This study addresses additional changes due to multi-mode

propagation in the liquid-core waveguide. Fig. 3.7b shows a large and more spectrally varying transmission improvement due to annealing. Modeling—i.e. FDM simulation of connected solid- and liquid-core waveguides—reveals two contributions to the transmission improvement spectrum. First, the solid- to liquid-core transmission at the interface improves from 15% for the as-grown DUL sample to 96% for the annealed sample due to poor spatial overlap between the solid-core DUL and liquid-core waveguide modes. Secondly, an additional propagation effect arises from beating between the modes in the multi-mode 12  $\mu\text{m}$  wide liquid core.<sup>69</sup> Depending on the ratio of liquid-core length and period of the beat note, spectral variations in the coupling between the solid- and liquid-core waveguides arise. This results in the observed transmission variations seen in Fig. 3.7b and is confirmed by simulations.

### ***3.2.3 Repeatability of Waveguide Improvements***

The effect of repeated exposure to water absorption on transmission and mode patterns of a full ARROW sensor chip with intersecting solid- and liquid-core waveguides was tested by subjecting the devices to multiple use cycles. The first point in Fig. 3.8 represents the transmission of an as-grown (AG) ARROW chip. The relatively low initial optical throughput is greatly improved (> 30x) by the first annealing treatment (A1). In addition, the optical mode profile for an as-grown waveguide is localized in the DUL (inset), suggesting the presence of absorbed water and high refractive index that was introduced during fabrication. Conversely, the annealed waveguide shows excellent modal confinement and throughput, suggesting the elimination of water and homogenization of  $\text{SiO}_2$  refractive index. The chip was

next subjected to a typical cleaning procedure, i.e. a 4-hour boil in water (W1). The transmission decreases dramatically ( $> 100\times$ ) upon boiling and the mode re-localizes into the DUL due to the reabsorption of water. The annealing and water boiling processes were repeated for two more cycles, with similar changes in transmission and mode images. While transmission is always improved directly after annealing, there is a long-term decay in transmission with increasing number of annealing steps

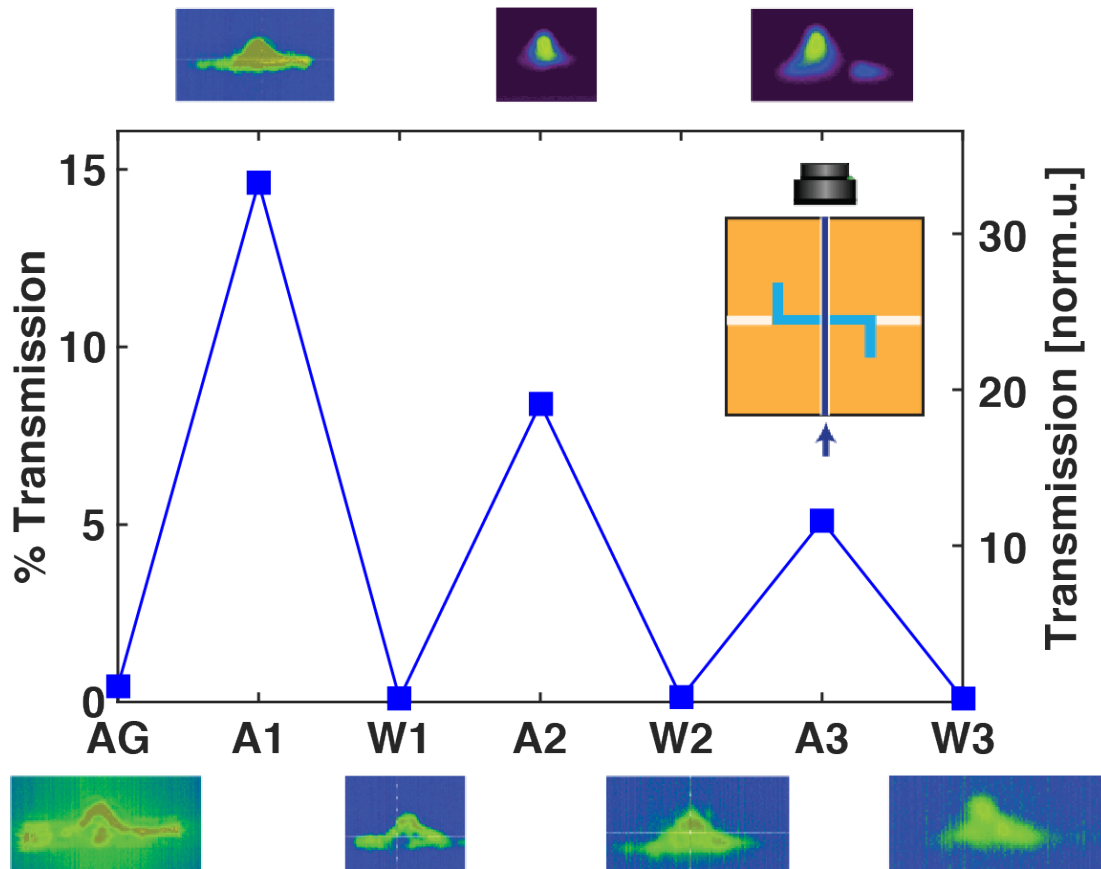


**Fig. 3.8 | Full ARROW sensor chip transmission data** (see inset for experiment schematic, transmission includes two solid-core sections intersected by a liquid core channel). As-grown (AG) waveguide transmission is presented, followed by cycles of annealing (A) and 4-hour water treatments (W). Appended numbers to A and W indicate annealing/water treatment number. Mode images are alternately presented below and above the transmission data for each treatment. The axis on the right side is normalized transmission with as-grown transmission equaling 1.



(A1-3). This is attributed to slight cracking that occurs after multiple annealing cycles, which can be eliminated by further optimization of the annealing conditions.

### 3.3 Optofluidic Sensor Chip Improvement Upon Thermal

#### Annealing

Finally, we address the impact of the waveguide improvement on single particle fluorescence detection in ARROW chips. For particle sensing, an orthogonal excitation/collection geometry is implemented (Fig. 3.9a, inset). Optical particle sensing measurements were performed similar to previously described work.<sup>70</sup> But coupled laser light was used to excite analytes via a solid-core excitation waveguide (2 mW input power). This waveguide perpendicularly intersects a liquid-core ARROW in which fluorescent dye/particles were flowing (see Fig. 3.9a inset). Excited fluorescence signals from these analytes then propagated along the liquid-core waveguide, into the collection solid-core waveguide (through a liquid- to solid-

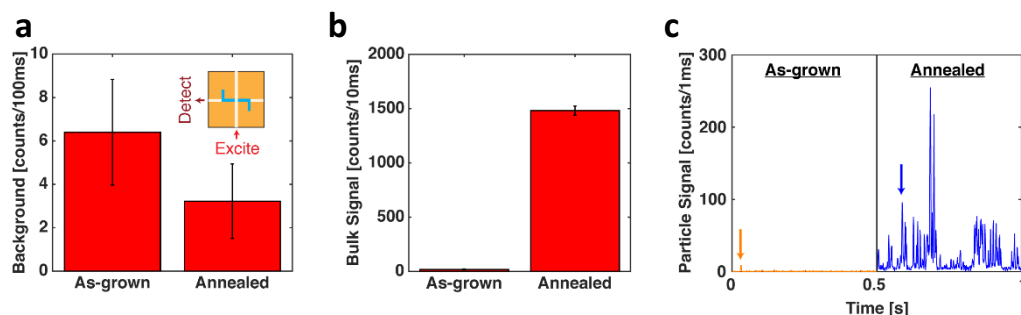


**Fig. 3.9 | ARROW sensor chip annealing induced improvement. a**, Orthogonally collected background (error bars are standard deviation of the background signal). **b**, Bulk fluorescence signal of 22 nM Cy5. **c**, Detection of 100 nm single FluoSpheres,  $c_{Fl} = 4 \times 10^7 \text{ mL}^{-1}$ . The left 0.5 seconds of **c** is signal from an as-grown chip and the right 0.5 seconds is signal obtained after annealing. Representative peaks are marked with arrows. Note that all experiments were conducted with the geometry represented in the inset of **a**.

core waveguide intersection), after which it was collected by a microscope objective, filtered by a bandpass filter, and focused onto a single-photon avalanche photodiode. Fig. 3.9a shows a two-fold reduction of orthogonally collected background noise upon annealing (633 nm excitation, channel filled with water). This background reduction is attributed to better light confinement within the solid-core excitation waveguide core (see Fig. 3.4a), which leads to less photoluminescence generation and light scattering at waveguide intersections. Next, we measured the signal intensity for bulk detection of fluorescence from 22 nM Cy5 dye solution. The detected signal shown in Fig. 3.9b improved by 83x for annealed chips in excellent agreement with Fig. 3.7 due to the improved mode coupling across the two liquid/solid-core waveguide interfaces. Combined with the background enhancement, we observe a total chip signal to background ratio (SBR) enhancement of 166x. These improvements are fully borne out in single particle detection, seen in Fig. 3.9c, using 100 nm FluoSpheres ( $c_{FI} = 4 \times 10^7 \text{ mL}^{-1}$ ) excited by a 488 nm laser. The much improved chip performance resulted in a dramatic increase in the number of detected particles detected over a 40 second experiment from 3 particles for an as-grown ARROW chip to 314 particles after annealing. The variation of the height of the fluorescence peaks within each individual trace is due to different positions of the particles within the cross section of the fluid channel and is typical for ARROW-based single particle detection.<sup>71</sup> Fluorescence correlation spectroscopy (FCS) was used to determine flow velocity, and in conjunction with channel dimensions, the volume transport. Multiplying the volume transport by the concentration of particles

gives an expected number of detected particles. The annealed ARROW detection chip had a 96.6 % detection efficiency, while the as-grown chip detected only 2.52 % of expected particles.

We have demonstrated the presence of a high-index distinct upper layer (DUL) in PECVD grown SiO<sub>2</sub> ARROW ridge waveguides. This layer causes an abnormal localization of the primary waveguide mode within the DUL, leading to poor lateral light confinement, high propagation losses, and reduced mode coupling across intersections between liquid- and solid-core waveguides. Optical simulations present evidence that the DUL has higher refractive index, which is the cause of light guiding in that region.

We directly linked water absorption in SiO<sub>2</sub> to these degradation mechanisms in waveguide performance. Upon low temperature thermal annealing, negative effects such as poor mode localization, high propagation/intersection losses, and high background are eliminated. Furthermore, full ARROW sensor chip sensitivity is dramatically improved for detecting both bulk dye and single fluorescent nanoparticles. In summary, low temperature thermal annealing removes water from SiO<sub>2</sub> films, homogenizing its refractive index and consequently improves ARROW chip performance. This is particularly important for the detection of clinically relevant biomolecules. As such, the work in this chapter lays the necessary groundwork for biomolecular detection throughout the rest of this thesis.

## 4 Passive Hybrid Optofluidic Integration

The original motivation for a lab-on-a-chip was to unite as many functions in a single chip-scale device as possible.<sup>72</sup> Typically, this includes both chemical or biological sample preparation and optical or electronic sample analysis. This presents considerable challenges since the materials that have been optimized for these tasks—polymers and glass for sample preparation; semiconductors for optoelectronic detection—are very different. In addition, the growing need for genomic and proteomic molecular analysis at low concentrations and volumes such as in single-cell analysis requires extremely high sensitivities.<sup>73</sup>

The growing area of optofluidics<sup>19,74,75</sup> offers a path towards accomplishing these goals by combining microfluidics and integrated optics in a single lab-on-chip system. It has been pointed out early on<sup>19,76</sup> that one particularly attractive optofluidic approach would involve the vertical integration of dedicated fluidic and optical layers, each optimized independently and suitably interfaced with the other.

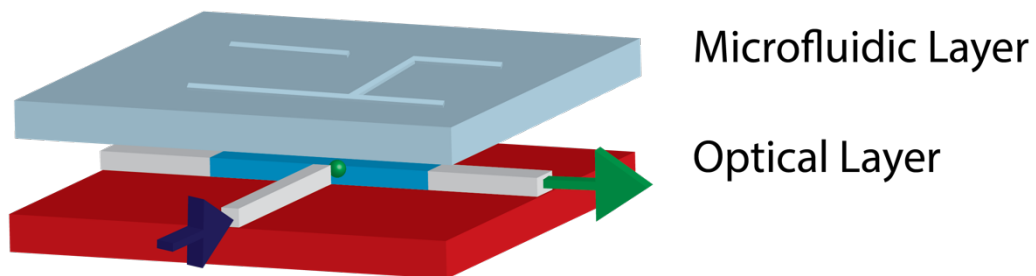


**Fig. 4.1 | Schematic depiction of hybrid optofluidic integration of microfluidic sample preparation (top) and optical analysis (bottom) layers.**

In the following two chapters, we introduce the concept of hybrid optofluidic integration that combines the strengths of microfluidic sample handling in PDMS microchannels with single particle optical detection sensitivity in silicon-based liquid-core waveguide chips. Its core features are reconfigurability via a non-permanent interface, small dead volume, optical planarity that allows for vertical integration as shown in Fig. 4.1, and single-particle optical sensitivity afforded by the use of liquid-core antiresonant reflecting optical waveguides (ARROWs).<sup>34,77-79</sup> In this chapter, the integration is noted as “passive” because the PDMS microfluidic chips do not have moving/pneumatically-switchable microvalves. In addition, fluid flow is initiated off chip, i.e. not by on-chip peristaltic pumps.

The key steps for preparing a complex biological sample based on whole blood, saliva, etc. for on-chip optical analysis include the removal of large matrix components that could clog the waveguide channels, labeling with target-specific optical markers, and distribution into multiple optical channels for multiplex detection. In this chapter, I demonstrate the compatibility of all three canonical functions (mixing/labeling, filtering, distribution) with analysis on an ARROW chip and characterize the fluid transport properties of the integrated device. Specifically, I implement for the first time the combination of on-chip labeling of  $\lambda$ -DNA, followed by single molecule DNA detection in the optical layer. This assay indicates that amplification-free detection of nucleic acids starting with raw sample material is feasible. Other experiments include microparticle mixing and detection with control of fluid velocity, sample distribution with multiplex detection, and finally particle

sorting with multiplexed detection. The work in this Chapter is based on previously published work.<sup>2</sup>

#### 4.1 Device Fabrication and Hybrid Integration

ARROW devices were fabricated as described in Section 2.3.2, however, for completeness, a brief description of the devices used in this experiment will be included. Optimized SiO<sub>2</sub> (refractive index  $n = 1.47$ ) and Ta<sub>2</sub>O<sub>5</sub> ( $n = 2.107$ ) ARROW

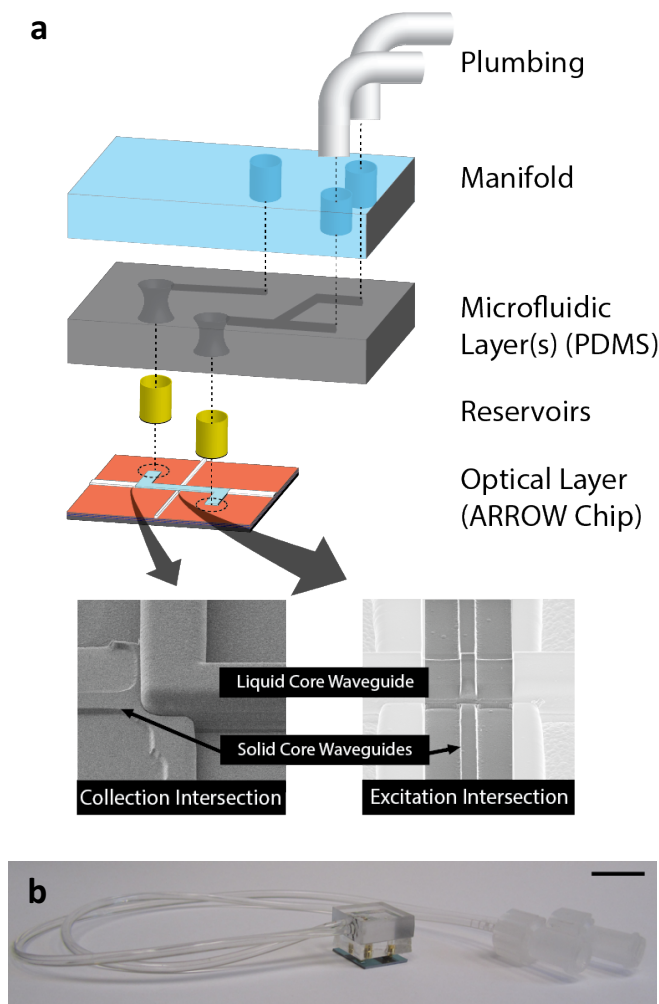


**Fig. 4.2 | Passive hybrid optofluidic integration. a,** Expanded view of PDMS integration with an ARROW optofluidic chip. Insets are scanning electron microscope (SEM) images of optical intersections. **b,** Assembled device with fluidic connections – the scale bar in the upper right represents 1 cm.

layers were deposited by Evaporated Coatings Inc. on a silicon wafer. The layers were deposited in an alternating fashion, starting with SiO<sub>2</sub>, at thicknesses of 265/102/265/102/265/102 nm. The liquid-core waveguide was defined lithographically to nominal cross-section dimensions of 12×5 μm (width × height). An SiO<sub>2</sub> thin film overcoat of 6 μm thickness was used to create the channel. Solid-

core ridge waveguides for delivery and collection of optical signals were formed in the top oxide overcoat via reactive ion etching with a width of 4  $\mu\text{m}$  and etch depth of 3  $\mu\text{m}$ . The layout of the final “ARROW Chip” is shown in Fig. 4.2a (footprint 8 $\times$ 8 mm). Scanning electron microscope images are presented for both the excitation and collection intersection between the liquid- and solid-core waveguides.

Channels for the microfluidic layer were formed in PDMS using conventional soft lithography (see Section 2.4). Master molds for channels of 30  $\mu\text{m}$  height and widths from 13 to 200  $\mu\text{m}$  were lithographically defined using SU-8 negative photoresist. General processing parameters for different SU-8 formulations are cited in Table 4.1 (Appendix C gives a detailed fabrication processing recipe for SU-8 master mold and PDMS replica fabrication). PDMS elastomer and curing agent were mixed in a 10:1 ratio and degassed for one hour, after which the mixture was poured onto the silanized SU-8 master and baked for one hour at 60  $^{\circ}\text{C}$ .

**Table 4.1 | General SU-8 Processing Parameters**

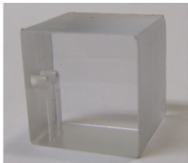


	<b>SU-8 2015</b>	<b>SU-8 2025</b>	<b>SU-8 2150</b>
<b>Spin Speed</b>	4000 RPM	2000 RPM	1500 RPM
<b>Soft Bake (65/95/65<math>^{\circ}\text{C}</math> [min])</b>	1/5/1	5/5/5	5/40/5
<b>Exposure Dose</b>	120 $\text{mJ}/\text{cm}^2$	155 $\text{mJ}/\text{cm}^2$	300 $\text{mJ}/\text{cm}^2$
<b>Post Exposure Bake (65/95/65<math>^{\circ}\text{C}</math> [min])</b>	6/6/7	6/6/7	6/15/7
<b>Spray Development</b>	8 s	20 s	90 s
<b>Hard Bake (65/200/65<math>^{\circ}\text{C}</math> [min])</b>	1/5/1	1/5/1	1/5/1

Manifold, or access, layers—as seen in Fig. 4.2a—were bonded according to material type. For access layers made of glass or PDMS, the manifold and microfluidic PDMS layers were bonded using a 30 W oxygen plasma treatment for 30

seconds. For polycarbonate access layers, a preliminary APTES treatment was used to activate the surface before oxygen plasma bonding.<sup>80</sup> A comparison of the different substrate/manifold layers is presented in Table 4.2. Due to the ease of fabrication, bonding, and use, in most cases PDMS manifolds are the most desirable choice for rapid prototyping.

To perform the hybrid integration between a PDMS microfluidic device and an ARROW optofluidic chip, we implemented an approach using metal reservoirs (2 mm outer diameter, Fire Mountain Gems) that were inserted into holes punched into the PDMS layer. The natural concavity of the punch holes results in an excellent airtight seal with the reservoirs. Subsequently, epoxy was applied to the lower reservoir edges, and finally the entire device was assembled by lowering the fluidic chip onto the optical chip using a micromanipulation stage. At this point, the epoxy

**Table 4.2 | Comparison of PDMS manifold materials**

	<b>Polycarbonate</b>	<b>PDMS</b>	<b>Glass</b>
<b>Bonding</b>	-15 min sonication isopropanol -30 sec. 60W oxygen plasma -5% v/v APTES soak (20 min – 1hour @ 70°C)* -30 sec. 30W plasma	- Tape clean - 30 sec. 17W oxygen plasma	-15 min sonication isopropanol/acetone - 30 min. bake @ 60°C -30 sec. 30W oxygen plasma
<b>Pros/Cons</b>	+ Side access + Good indust. interfacing - Difficult Bonding - High precision pieces	+ Easy bonding + Easy fabrication + Good optical clarity - Top access only - Poor indust. interfacing	+ Easy bonding + Good optical clarity - Top access only - No press-fit - Fragile
<b>Images</b>			



was allowed to cure overnight to ensure device stability. It is important to note that the PDMS layer is not in contact with the ARROW chip and thus optical guiding properties are inherently conserved. Furthermore, while the PDMS-reservoir interface is stable under very high pressures, it is also reconfigurable due to the lack of permanent adhesive. In other words, after the device has been completed, the PDMS microfluidic assembly can be removed/replaced by simply pulling it off, leaving the aligned reservoirs in place. An alternative, more permanent approach using a punched 200  $\mu\text{m}$  thin PDMS gasket layer to replace the reservoirs was also tested. In that case, the gasket layer was plasma-bonded to both the top of the ARROW chip and the bottom of the microfluidic PDMS layer. This bonding method surprisingly formed a leak free seal around SAP<sup>41</sup> ARROW structures. Specifically, red food dye was pumped through the hybrid system using a syringe pump, exiting the ARROW channel without observable leaks anywhere in the system. However, this approach is permanent and less amenable to laboratory research; as such, results presented in the remainder of this work were obtained using the non-permanent reservoir interface.

Control of liquid flow through the integrated device was realized externally using custom Luer lock syringe based actuators. Tygon tubing was used to connect the PDMS microfluidic chip to a 1 mL Luer lock syringe. Both ends of the tubing were press-fit, providing a strong seal while retaining re-configurability. Finally, the syringe was immobilized in a custom mount and a micrometer screw was used to actuate flow in mixing and distribution experiments. For experiments that required a

more controlled velocity, a syringe pump was used to actuate flow (Pump 11 Elite, Harvard Apparatus).

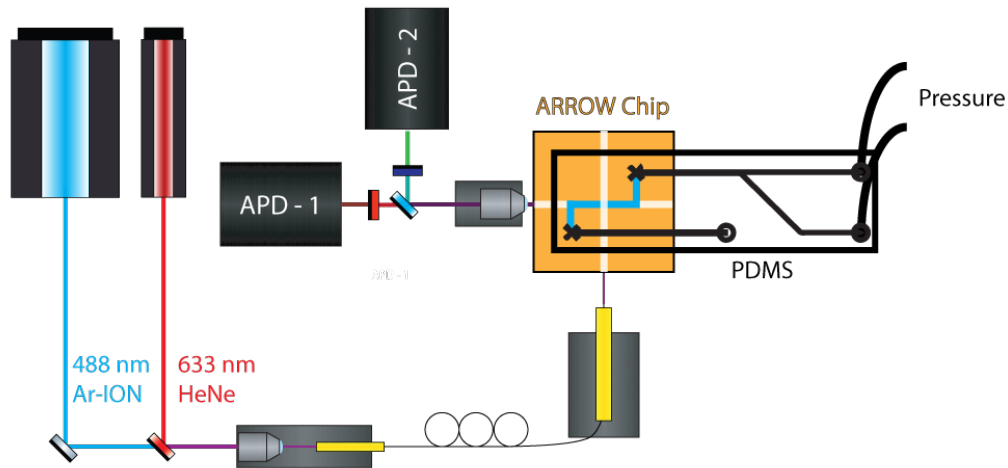


**Fig. 4.3 | Optical experimental setup for detection using a hybrid optofluidic system.**

The detection setup implemented for optical particle analysis with fluidic control is seen in Fig. 4.3. An excitation laser (632.8 nm HeNe laser or 488 nm Ar-ion laser) was coupled into single mode fiber, which was in turn butt coupled into the ARROW chip with optical access from 3 sides as seen in Fig. 4.3. The waveguide output power was monitored straight across the chip to ensure stable coupling. Fluorescence signals were collected from the collection waveguide by a microscope objective, spectrally separated by a dichroic mirror (3RD640LP, 3<sup>rd</sup> Millennium), filtered for background (blue and red fluorescence filtered by 513BP17, Semrock and 660BP20, Omega, respectively), and sent to single photon avalanche photodiodes (SPAPDs).

Here I note an important formulation used throughout the thesis that keeps materials from clogging/sticking in microfluidic channels: experimental solutions

contained 0.1 mg/mL BSA (New England BioLabs) and 0.05% Tween20 (Fisher) as dynamic surfactants to inhibit aggregation and wall binding. Sodium azide was added at a final concentration of 5  $\mu\text{M}$  to all solutions to retain biological purity.

## **4.2 Flow Properties of Hybrid Optofluidic Systems**

As the cross-sectional dimensions of the microfluidic and liquid-core waveguide channels are dramatically different, we first consider the flow properties of the integrated device. The fluidic resistance of a micro-channel is well approximated (less than 1% error for aspect ratios over 2) by the following equation<sup>81</sup>

$$R = \frac{12\eta L}{wh^3(1 - 0.630 h/w)} \quad (4.1)$$

where  $\eta$  is the viscosity of the fluid,  $L$  is the length,  $w$  is the width of the channel, and  $h$  is the height. By substituting the dimensions of PDMS ( $75 \times 30 \mu\text{m}$ ,  $L = 8 \text{ mm}$ ) and ARROW liquid-core waveguide ( $12 \times 5 \mu\text{m}$ ,  $L = 4 \text{ mm}$ ) channels, fluidic resistances of  $R_{\text{ARROW}} = 43.48 \text{ cP}/\mu\text{m}^3$  and  $R_{\text{PDMS}} = 0.0635 \text{ cP}/\mu\text{m}^3$  are calculated. It is clear the resistance of the ARROW chip is about 700 times that of the PDMS channels. As the resistance scales linearly with channel length, a PDMS channel would need to be  $\sim 5 \text{ m}$  long to match the impedance of typical ARROW chips. This implies that for typical chip dimensions, the fluidic resistance will always be dominated by the ARROW optical device layer, particularly since this simplified model does not account for the  $90^\circ$  bends in the ARROW liquid-core waveguide that further increase the resistance. Here we note the robustness of the reservoir bonding method to withstand large impedance mismatches and pressure differentials while remaining reconfigurable. For example, the maximum flow speed achieved was approximately 3

cm/s (as measured by top down video tracking of particles) corresponding to a flow rate of 0.108  $\mu\text{L}/\text{min}$ . Accordingly, the pressure drop across the device (calculated from flow rate multiplied by fluidic resistance) was 78.3 kPa, and no leakage was observed.

### 4.3 On-Chip Mixing, Labelling and Detection of Single DNA

Microfluidic solution processing requires many steps, and one of the most important of these steps is mixing. Consequently, the first design presented involves the junction of two PDMS channels leading to a single inlet on the optofluidic ARROW chip – i.e. a mixer, as shown in Fig. 4.3. Here, two separate solutions of fluorescently labeled microspheres were introduced via the different inlets (1:500 dilution of 1  $\mu\text{m}$  FluoSpheres<sup>®</sup>, Invitrogen). One inlet was pumped with crimson microspheres (625/645 nm excitation/emission) while the other inlet was pumped with yellow-green microspheres (505/515 nm).

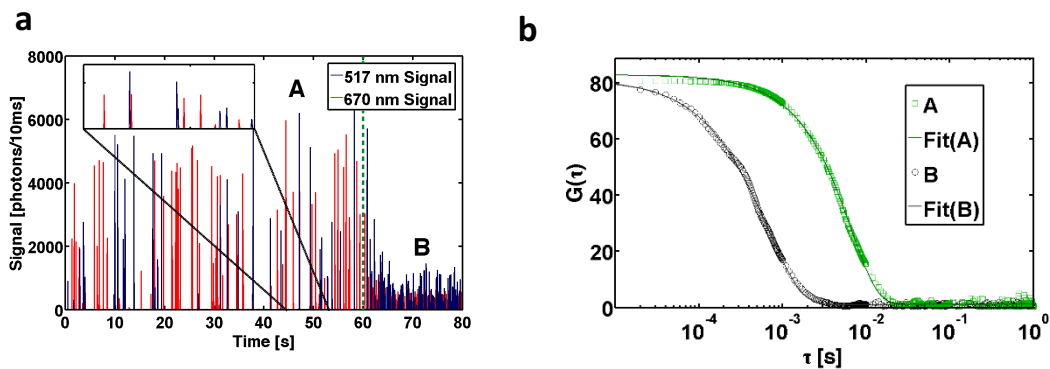


**Fig. 4.4 | On-chip mixing and detection of fluorescent microspheres.** **a**, Dual fluorescence measurement of PDMS-mixed microspheres. The inset represents a higher resolution time trace demonstrating the chromatic separation of the signals. Regions A (0-60 s) and B (60-80 s) signify durations of the experiment in which the system was un-pumped and pumped, respectively. The dashed green line represents the transition between regions A and B. **b**, FCS analysis of the 670 nm fluorescence signal before (A) and during (B) pumping.

The resultant time dependent fluorescence signal detected from the ARROW chip is presented in Fig. 4.4a, which shows several important features. First, fluorescent peaks—representing single particles moving past the excitation spot—are present in both the blue (517 nm) and red (670 nm) detection channels. The absence of cross talk and the uncorrelated nature of the two fluorescence channels are exemplified in the inset. Note that the first peak in the inset is on the red channel and the second peak is in the blue channel. This demonstrates the feasibility of the hybrid optofluidic integration: sample solutions can be moved leak-free through the combined device while optical analysis with single-particle detection sensitivity is preserved. This is one of the principal results of this work.

Moreover, fluidic control over the mixing process is also preserved: at around 60 seconds, pressure was applied to the pumping syringes to induce faster particle transport. As a result, the optical trace shows a distinct change in both the rate and amplitude of particle signals, signified here by the transition from region A to region B. The detection rate increases due to the larger number of particles during segment B, and the amplitude decreases due to the shorter time each particle spends in the optical excitation volume.

In order to further characterize the change in the signal upon pumping, the 670 nm fluorescence trace was subjected to fluorescence correlation spectroscopy (FCS) analysis, as seen in Fig. 4.4b. The signals between 0 and 60 seconds of Fig. 4.4a were used to generate autocorrelation trace A, while the signals between 60 and 80 seconds were used to generate trace B. The fit associated with each of these plots was

calculated using a previously described model that accounts for both diffusion and flow<sup>82</sup>, and matches the data very well. Specifically, a flow corrected, chip-based autocorrelation fit was defined to be

$$H(\tau) = \frac{1}{\pi^{3/2} w_{xc} w_y w_z \langle C \rangle} \left[ 1 + \frac{4D\tau}{w_{xc}^2} \right]^{-1/2} \left[ 1 + \frac{4D\tau}{w_y^2} \right]^{-1/2} \times \left[ 1 + \frac{4D\tau}{w_z^2} \right]^{-1/2} e^{-\left( \frac{(V_z \tau)^2}{w_z^2 + 4D\tau} \right)} \quad (4.2)$$

with  $w_{xc}$  being the spot size of the collection efficiency function in  $x$ -direction (defined by the liquid-core waveguide mode);  $w_y$ ,  $w_z$  are spot sizes of the excitation beam in  $y$ - and  $z$ -direction, respectively (defined by the excitation waveguide mode);  $\langle C \rangle$  is the local concentration of particles;  $D$  is the diffusion coefficient of molecules;  $V_z$  is the flow velocity in  $z$ -direction;  $\tau$  is the lag time. Note, in this formalism, the ARROW chip lies in the  $xz$ -plane, with excitation (solid-core waveguide) and collection (liquid-core waveguide) beam propagation in  $x$ - and  $z$ -directions, respectively.

For both traces in Fig. 4.4b, we find  $G(0) \sim 80$ , corresponding to nearly equal concentrations of  $4.42 \times 10^7$  (trace B) and  $4.32 \times 10^7$  particles/mL (trace A), in reasonable agreement with the nominal manufacturer concentration of  $2.7 \times 10^7$  particles/mL. The corresponding fitted values for the flow speed are  $670 \mu\text{m/s}$  and  $5,200 \mu\text{m/s}$ , respectively.

Beyond proof of principles using fluorescent microspheres lies the realm of biosensing. A key step in a fluorescence bioassay is labeling the target with an optical marker. To this end, the raw sample must be brought in contact with the label. Here,

we demonstrate mixing of  $\lambda$ -DNA with intercalating SYBR Gold fluorescent dye in the microfluidic layer, followed by detection of single, labeled  $\lambda$ -DNA molecules in the optical layer. Molecules were then excited with 488 nm laser light and detected as depicted above. Using an experimental geometry similar to Fig. 4.3,  $\lambda$ -DNA (New England Biolabs) and SYBR Gold (Invitrogen) are input into separate inlets on the microfluidic layer. In this layer, the two channels meet, the solutions mix, and are sent to the inlet of the optical layer for analysis.

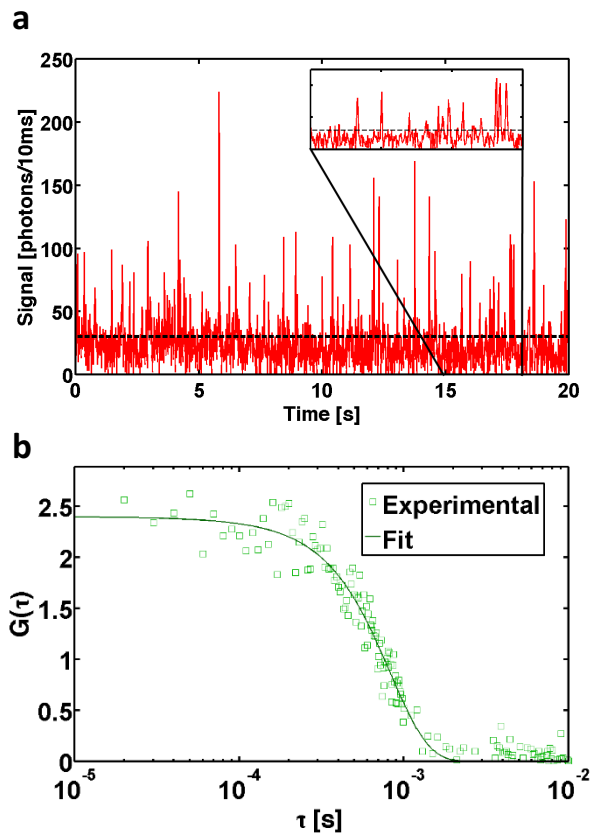


**Fig. 4.5 | On-chip labeling and detection of single  $\lambda$ -DNA.** **a**, Time dependent fluorescence trace of on-chip mixed, labelled, and detected single  $\lambda$ -DNA molecules. The dashed black lines represent  $3\sigma$  (three times the standard deviation of the noise) and the inset displays single detection events.

**b**, Experimental FCS trace of detected  $\lambda$ -DNA molecules (squares) and respective theoretical fit (line).

A resultant time dependent fluorescence trace obtained by excitation with a 488 nm laser is presented in Fig. 4.5a. The dashed horizontal line shows the threshold level above background – defined here as  $3\sigma$  (three times the standard deviation) of a SYBR Gold control signal. Fluorescence peaks representing single  $\lambda$ -DNA molecules are present throughout the time trace – well above the noise threshold. The inset of Fig. 4.5a shows a zoom-in displaying individual fluorescence signals. Differences in signal strengths between individual nucleic acids are caused by an inhomogeneous labeling efficiency and the spatially dependent velocity<sup>81</sup> (Poiseuille flow) and collection efficiency<sup>79</sup> of the liquid-core waveguide. However, as this is a direct counting experiment of single nucleic acids above a background threshold, the variation in signal strengths does not affect the assay.

$\lambda$ -DNA time traces were subjected to fluorescence correlation spectroscopy (FCS) analysis. The experimental autocorrelation plot shown in Fig. 4.5b is presented along with a fitted curve, and matches the data very well. For this FCS trace,  $G(0)$  is fit to approximately 2.4, corresponding to a concentration of 8.8 pM that is in reasonable agreement with the nominal diluted concentration of 12.5 pM, confirming the detection of single nucleic acids. Furthermore, the fitted value for flow speed is 6.8 mm/s further verifying the ability of the device to withstand high fluid velocities and respective pressures.



## **4.4 Microfluidic Sample Distribution to Multiple ARROW**

### **Waveguides**

On-chip sample distribution is another important component of a lab-on-chip device as it enables multiplex detection in several ARROW channels and increases fluidic throughput. In this work, we implement a 1-in-2 splitter in the PDMS layer in order to distribute sample analyte from a single inlet into two optofluidic channels as seen in Fig. 4.6a. The particular dual liquid-core ARROW chip used in this experiment (SPA3-D6-E6) has two solid-core waveguides that are excited simultaneously (see Fig. 4.6a and red arrows in Fig. 4.6b,c insets) to yield a double Gaussian excitation profile for direct determination of the flow velocity (see below). These excitation waveguides extend across the entire chip and thereby provide simultaneous optical excitation of both liquid-core waveguides. For the collection of fluorescence signals, an objective was aligned sequentially to the top and bottom collection waveguides as illustrated in Fig. 4.6. After injecting crimson microspheres via a single PDMS input, 632.8 nm HeNe light was used to excite the analytes.

Both data traces in Fig. 4.6 have characteristic doublets indicative of a double Gaussian excitation. The maximum signal for each doublet is lower in Fig. 4.6b than that in Fig. 4.6c because the excitation light experiences some attenuation between the first and second liquid channels. We note this is a result of lossy propagation and intersection scattering, both of which have no effect on single particle detection.<sup>79</sup> Such losses result in respectively smaller fluorescence signals in the channel more distant from the excitation source. For this same reason, the imperfections in the

double Gaussian signals of Fig. 4.6c—caused by leakage of excitation light in the cladding of solid-core waveguides—are not apparent in Fig. 4.6b. Further analysis

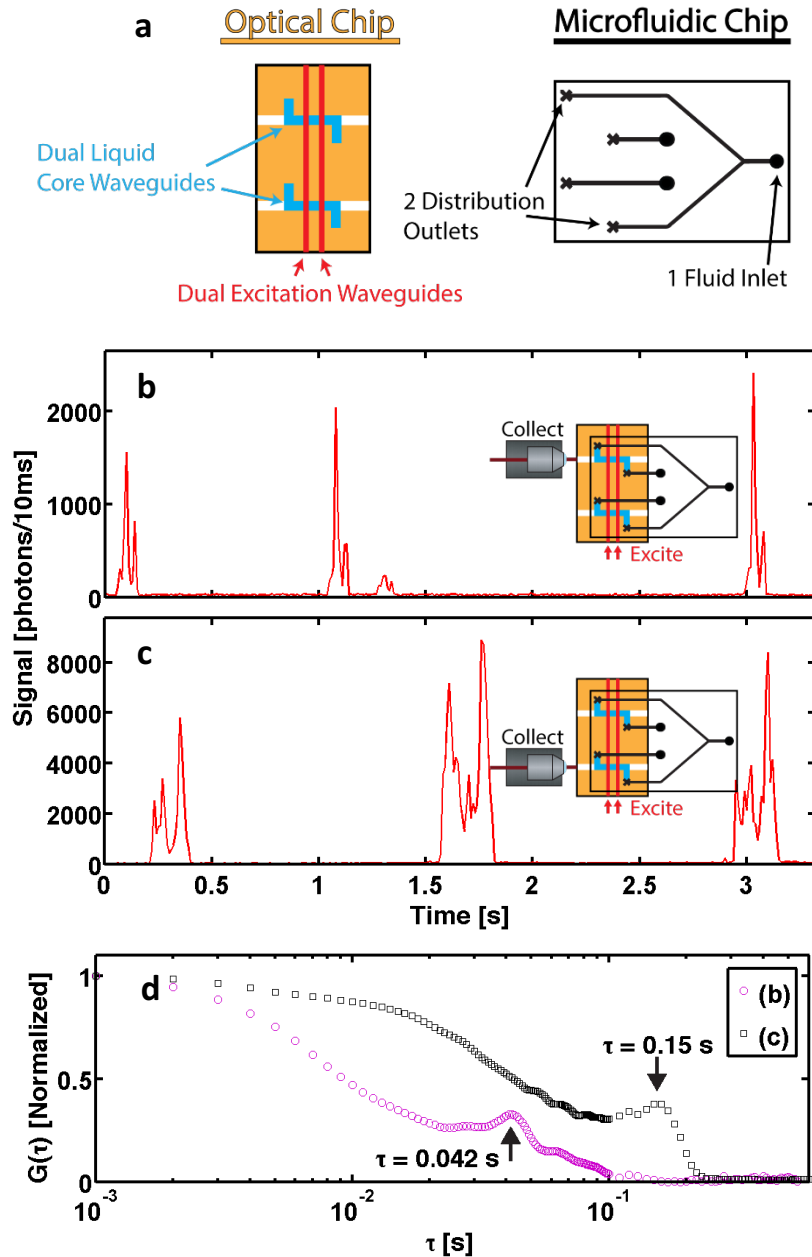


**Fig. 4.6 | Distribution of fluorescent microspheres to dual liquid-core waveguides.** **a**, PDMS Distribution with dual liquid-core waveguide detection. Signals were detected from liquid-core waveguide 1 (**b**) and 2 (**c**) separately while the same PDMS distribution device fluidically controlled both channels. **d**, FCS analysis of both time trace signals – local maxima are marked.

shows that the first peak of each doublet in Fig. 4.6b, and the second of each doublet in Fig. 4.6c, are larger in amplitude than their respective partners due to uneven power distribution between the excitation waveguides, and the fact that injection into the ARROW channel occurs from opposite ends (see Fig. 4.6). Finally, as the spacing between the maxima of the two excitation waveguides is well defined, an easy, direct, and accurate velocimetry analysis can be performed. By taking the spacing of the excitation waveguides (25  $\mu\text{m}$ ) and dividing it by the temporal spacing of each doublet, the magnitude of the velocity was determined to be 600  $\mu\text{m/s}$  for particles in Fig. 4.6b and 170  $\mu\text{m/s}$  for particles in Fig. 4.6c. Similarly, upon performing FCS analysis on these traces, there is a local maximum at lags equal to the time between peaks—as seen in Fig. 4.6d—that is in excellent agreement with the direct measurement, thus confirming this technology as an accurate flow sensor. The difference in flow velocities is attributed to a hole in the epoxy sealing one of the ARROW chip-reservoir interface. This highlights the possibility of differential control of the channel velocities via a pressure release system or channel dimensions that produce different fluidic resistance. Even without differential control, this is the first presentation of multiplexed liquid-core waveguide detection with a single optical source.

#### ***4.4.1 Positive Pressure Driven Flow in Hybrid Systems***

A further investigation into the difference of flow velocities seen in Fig. 4.6 can be conducted using the throughput data for this particular experiment. As mentioned above, the difference in flow velocity was attributed to leaking in the epoxy bonds

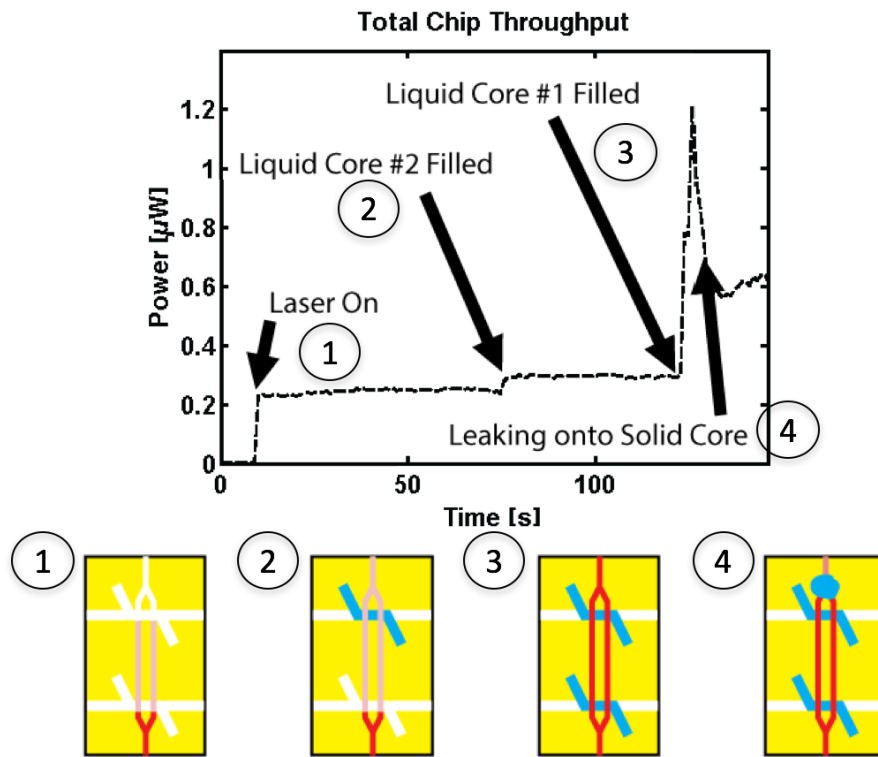


**Fig. 4.7 | Investigation of Variable Flow Velocities in a Distributed Hybrid Optofluidic Platform.**

between the ARROW chip and one of the metal reservoirs. Illustrated in Fig. 4.7, when the chip is initially totally unfilled (1), there is significant optical loss at both solid-to-liquid-core waveguide intersections, depicted as a loss of red color (laser excitation). At around 75 s, the back (#2) liquid-core waveguide fills with fluid and the through transmission increases (2). Upon filling the front liquid-core waveguide (#1), the transmission increases again (3). However, shortly thereafter, the seal to liquid-core #2 begins to leak and water on top of the solid-core waveguide reduces optical transmission (4). Note that the presence of liquid on the solid-core waveguide was noted after the experiment, further confirming the cause of flow velocity differences between the liquid-core channels.

#### 4.4.2 Passive Control of Fluid Velocity in Hybrid Systems

Pumping fluids through microfluidic systems can cause burst seals and is difficult to control due to high channel impedances. However, there is a less discussed, reproducible means of accurately controlling flow velocity in hybrid optofluidic systems. Specifically, when the inlet of a closed and filled system is connected to a reservoir of solution that is open to atmospheric pressure, hydrostatics dictates fluid flow. That is, if the end of fluid reservoir is above (at a higher altitude than) the outlet of the chip, fluid will flow from the reservoir to the chip. Conversely, if the reservoir is below the outlet of the chip, then fluid will flow in reverse. This relationship was realized experimentally in Fig. 4.8. The flow velocity, tracked using fluorescent microspheres, is linearly related to the vertical displacement between the fluid reservoir and chip outlet. Furthermore, the flow velocity is reversible and well controlled over a large range of flow velocities. Notably, the range of velocities

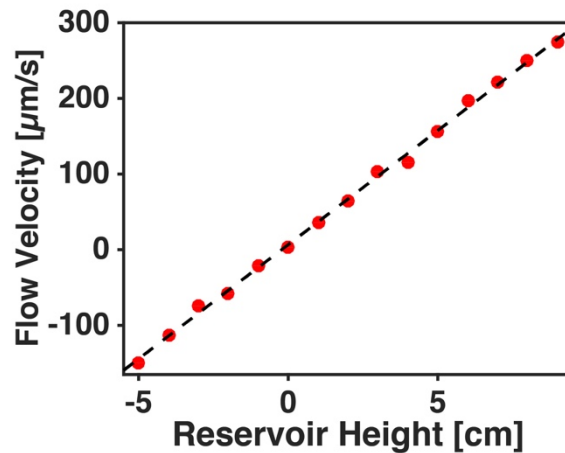


**Fig. 4.8 | Passive Control of Microfluidic Flow Velocity.** Velocity is controlled by changing the fluid reservoir position with respect to the fluid outlet. The dashed line is a linear fit with  $r^2 = 0.998$ .

includes the origin, meaning that this technique can be used to stop flow in microfluidic systems, and passively halt particles for interrogation/manipulation.

#### 4.5 Microparticle Filtering and Distribution

Control of flow in microfluidic systems is essential for proper function; another step that is quintessential for microfluidic assays is size-based particle filtering and selection. In our hybrid optofluidic system, such a step is critical to prevent particles such as cells or cell fragments of more than a few microns diameter from clogging the small channels of the ARROW chip. Furthermore, this purification step is a necessary component of many biological assays.

Fig. 4.9a shows the mask layout of the sorter which we combined with a 1-in-2 distributor section as described above. Fig. 4.9b and Fig. 4.9c show the zoom-in view of the sorter which consists of a corrugated wall in the input channel and a micro-slit filtering membrane separating the inlet/waste and outlet channel.<sup>83</sup> A

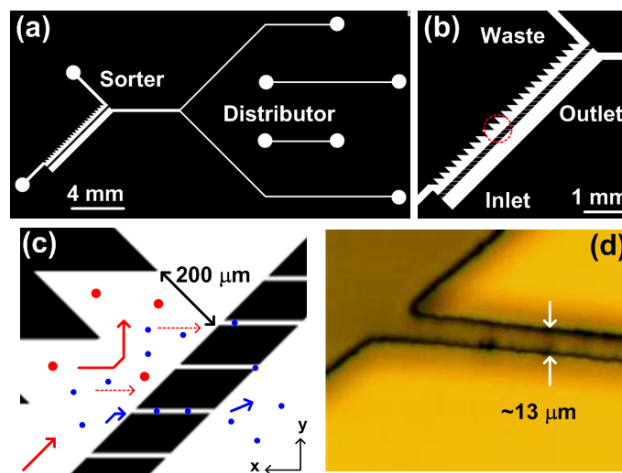


**Fig. 4.9 | Microfluidic particle sorter and distributor.** **a**, Mask layout of the PDMS sorter and distributor. **b**, Zoom-in view of the particle size sorter section. **c**, Zoom-in view of the filtering membrane and the corrugated walls inside the inlet channel. **d**, Microscope image of the fabricated PDMS filtering membrane slit.

particle mixture (diameters 1 and 15  $\mu\text{m}$ ) is injected from the inlet channel. The mixed solution generally travels from the inlet of the sorter to outlet. The corrugated wall in the input channel helps to deflect the particles towards the filtering membrane by creating a two-dimensional flow (the flow direction is indicated by red and blue arrows in Fig. 4.9c) and thus creates another pressure gradient in the x-y plane (indicated by red-dashed arrows in Fig. 4.9c). Particles smaller than the slit opening pass through the membrane and enter the outlet channel for secondary processing (which in this case means distribution into the two ARROW channels for fluorescence detection). Particles with larger sizes than the slit opening will continue to flow forward to the waste output, as illustrated in Fig. 4.9c. The gap between the corrugated wall and the filtering membrane was chosen to be 200  $\mu\text{m}$ . Fig. 4.9d shows a microscope image of the fabricated PDMS filtering membrane. The fabricated filtering slit width is 13  $\mu\text{m}$  in order to block 15  $\mu\text{m}$  particles. For a commercialized mylar photolithography mask, we are able to transfer a filtering slit down to  $\sim 6$   $\mu\text{m}$  wide which is limited by the commercial printer. With laser-defined chrome masks, submicron resolution is achievable. Such resolution is sufficient to block larger sized components of biological samples from clogging the ARROW channel – an example of which is filtering red blood cells from whole blood.

For this experiment, a detection scenario similar to that seen in Fig. 4.6 was implemented. Two notable differences include a single excitation waveguide and the use of a syringe pump. After injecting a mixture of 1  $\mu\text{m}$  (Invitrogen) and 15  $\mu\text{m}$

(Polysciences) diameter microspheres via the PDMS layer into the ARROW chip, a 488 nm Ar-ion laser was used to excite the filtered particles.

Fig. 4.10 shows the detected fluorescence signal from ARROW channels 1 and 2 with the input flow rate of the sorter set to 2  $\mu\text{l}/\text{min}$ . The particle injection rates inside the ARROW channels were recorded as 0.33 particle/s and 0.37 particle/s for channel 1 and 2, respectively. Note the ARROW chip inlets are completely sealed and the flow velocities in each channel are very similar.

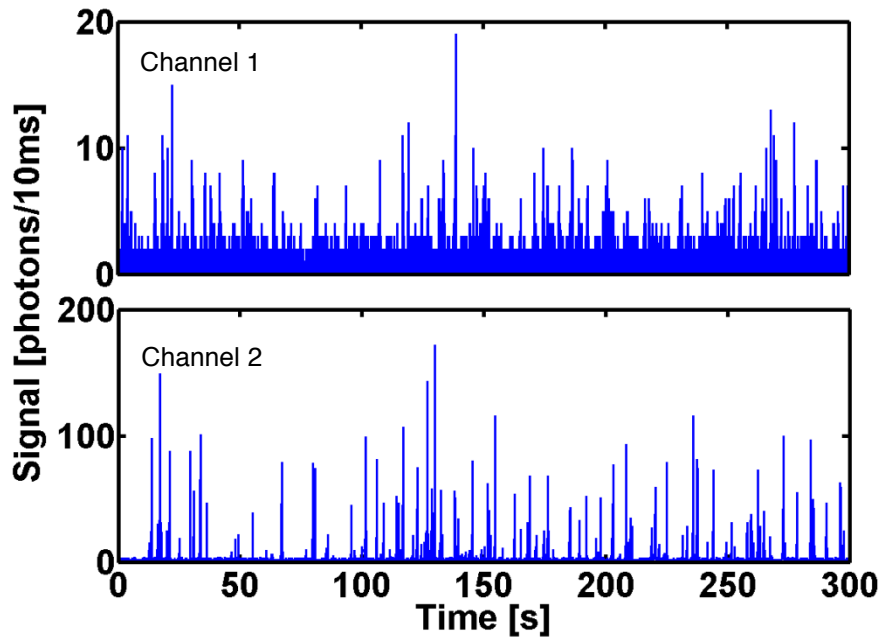


**Fig. 4.10 | PDMS filtering and distribution with dual liquid-core waveguide detection.** Signals were detected from liquid-core waveguide 1 and 2 with input flow rate at  $\sim 2 \mu\text{l}/\text{min}$ .

The large microbeads were prevented from reaching the ARROW channel with 100% efficiency. In order to determine the sorting efficiency for 1  $\mu\text{m}$  particles, aliquots of experimental solution were subjected to flow cell cytometry. The prepared 1  $\mu\text{m}$  particle concentration was measured to be  $3.25 \times 10^7$  particles/ml. The 1  $\mu\text{m}$



particle concentration collected at the waste output during the experiment was found to be  $2.37 \times 10^7$  particles/ml. Therefore, the sorting efficiency for the 1  $\mu\text{m}$  particles is 33.5%. This value can be increased by repeated cycling through the sorter section and by optimizing the dimensions of the sorter section, such as the period of the corrugated wall, the angle of the slits, and the gap distance.

In this chapter I have introduced a method for hybrid integration of dedicated fluidic sample processing and high sensitivity optical analysis in a single optofluidic system. Vertical integration using non-permanent, reconfigurable interfacing via reservoirs provides a means of retaining optical viability of liquid-core ARROW waveguides while allowing for closed integration with microfluidic PDMS layers. The interfacing provides excellent sealing even at high pressures despite large fluidic impedance mismatches between the optical and microfluidic layers. Three capabilities that will form part of a complete chip-scale bioanalysis device—fluidic mixing, distribution, and filtering—were presented. In particular, the combination of fluorescent dye labelling with fluorescence detection of single  $\lambda$ -DNA molecules was demonstrated.

The independence of the fluidic layer design will allow for future hybrid integration with more complex microfluidic technologies based on actively controlled valves.<sup>59,62,84</sup> These examples of integrated sample processing and detection are important steps towards complete Lab-on-Chip analysis. They point towards the possibility of comprehensive molecular analysis such as amplification-free nucleic acid testing using small input volumes of biologically and chemically complex

sample material. However, this passive approach limits the system in a few ways. First, due to the need for off-chip flow control, the system remains bulky. Furthermore, nanoliter precision of distributed fluid volumes is difficult (sometimes impossible) with off-chip flow control. Finally, due to the passive/static nature of the above describe system, there is no implicit re-configurability. That is, a single system can only perform a single function (until the PDMS layer is physically replaced). All of these pitfalls can be overcome using active microfluidics with switchable microvalves. As such, the integration of active hybrid optofluidic systems is presented in the following chapter.

## 5 Active Hybrid Optofluidic Integration

Passive integration, presented in Chapter 4, of soft microfluidic devices and silicon optofluidics requires off-chip fluid control (e.g. through syringe pumps). Moreover, this architecture is completely static (i.e. their fluid paths cannot be reconfigured on the fly). As such, integration of microfluidic chips with addressable microvalve systems—such as those shown in Fig. 2.9—solve both of these shortcomings.

In the following chapter I present a significant advance to optofluidic integration by introducing a hybrid system that combines an *actively controlled* microfluidic layer with an optical sensing chip with single particle fluorescence detection sensitivity. Active control is achieved by employing an interconnected array of nanoliter microvalves called an automaton.<sup>61,62</sup> This technology allows for complex sample processing steps and reconfigurable operation that can implement multiple functions in sequence via customized software control. The optofluidic chip, on the other hand, is able to detect fluorescence from single biomolecules.<sup>79,82</sup> We demonstrate the functional integration of the microfluidic automaton with an optofluidic chip and the implementation of sample preparation steps required for nucleic acid analysis used in genomic studies and disease detection based on single particle fluorescence detection in flow. Specifically, we show on-chip mixing of multiple fluorescent agents as well as sequence-specific solid-phase extraction and detection of synthetic viral nucleic acid targets.

## 5.1 Microfluidic Automaton Fabrication and Control

Lifting gate microvalves and pumps are the core components of the programmable microfluidic automaton portion of the system.<sup>62</sup> Although the general fabrication of microfluidic valving structures is presented in Section 2.4, a brief description of the devices used later in this chapter is presented herein. Note that the fabrication of the ARROW chips used in this work follow Section 2.3.2 closely, and were specifically from the ZA6 wafer.

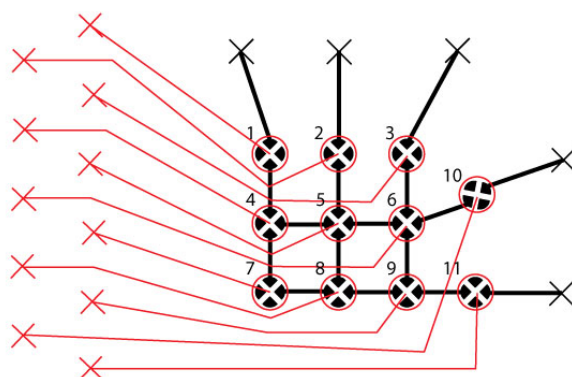


**Fig. 5.1 | Automaton microfluidic processor schematic.** Pneumatic features are represented in red and fluidic features are represented in black. Black X's at the end of channels represent a punch in the fluidic and pneumatic layers while red X's represent a punch only in the pneumatic layer. Valves are numbered 1-11 for later assay reference. Inlets are considered by their valve number (1-3) while outlets are considered to be waste (11) and output (10), respectively.

Each automaton is composed of three layers: a substrate, fluidic, and pneumatic layer. Both fluidic and pneumatic layers are made of PDMS, which were molded using conventional SU8 lithography.<sup>12,56</sup> In the case of the fluidic layer, a deformable membrane containing fluidic patterns was molded at a thickness of 300  $\mu\text{m}$  and a channel depth of 100  $\mu\text{m}$  by spin-coating the PDMS mixture (Sylgard 184, Dow Corning) at 350 rpm on the SU-8 2025 (MicroChem) master.<sup>85</sup> For the pneumatic

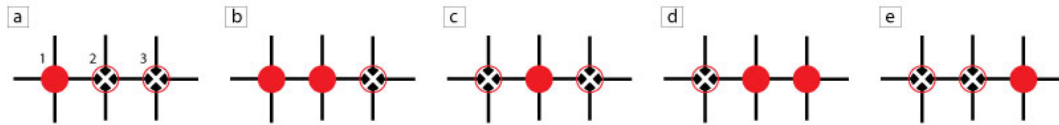


**Fig. 5.2 | Generic 3 valve peristaltic pumping scheme.** Valves that have negative pressure applied (or are open/lifted and filled with fluid) are indicated by a filled red valve while those that are closed are represented by an empty red circle with underlying fluidic layer structure. **a**, valve 1 is opened to be filled with fluid. **b**, the fluid is moved further into the pump by opening valve 2. Once valve 1 is closed in **c**, the pump volume is determined by the size of the middle valve. Valve 3 is opened in **d** to move the fluid along and finally valve 2 is closed in **e**, and valve 3 is closed to complete the single pumping cycle (closing of valve 3 not shown).

layer, a 3 mm thick PDMS replica was created on the SU8 master mold by pouring and subsequent degassing. Once baked for 2 hours at 60 °C, the pneumatic layer was peeled from the master. Inlets/outlets (2mm diameter) were punched, followed by alignment and bonding to the top of the fluidic layer by oxygen plasma activation (30 W for 30 seconds, PETS). A UV-ozone treatment was used to reversibly bond the assembled two-layer PDMS device to the substrate glass slide.<sup>86</sup> The device architecture is clearly outlined in Fig. 5.1. For a cross section of an individual valve, refer to Fig. 2.9 (right – lifting gate). Prior to use, the automaton was filled with 10 mg/mL bovine serum albumin (BSA) and incubated for 15 minutes in order to minimize nonspecific adsorption to the channel walls.

For external pressure control of the valves, the automaton was connected to a control box (system described below) via a custom acrylic manifold consisting of two clamping pieces of plastic that made conformal connections to the pneumatic and substrate layers of the automaton. Furthermore, 3 mm diameter air ports (designed to be aligned with pneumatic layer exits) were available for press fit connection to 3 mm outer diameter tygon tubing (EW-95702-01, Cole Palmer). This tubing was in turn

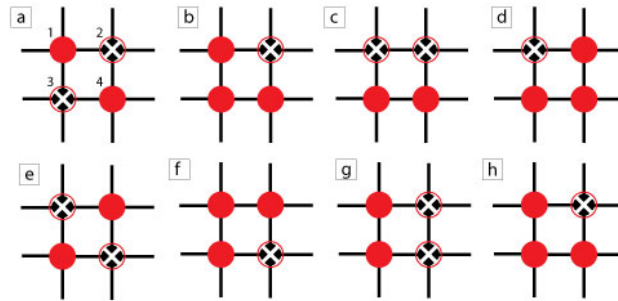


**Fig. 5.3 | Two valve mixing schematic.** Once valves 1 and 4 are filled with solutions to be mixed **a**, valve 3 is opened in **b** to draw fluid in from both 1 and 4. Valve 1 is closed (**c**) and valve 2 is opened (**d**) to distribute the mixing fluid into valves 2-4. Once valve 4 is closed (**e**), the process is reflectively repeated to further mix the solutions (**f-h**).

connected to solenoid valves (S070M-6DC-32, ADI), which were electrically controlled via a switchboard (ULN2803, Elexol), data acquisition board (NI USB 6501, National Instruments), and a custom Labview program.<sup>87</sup> Note that when three valves are operated in series, they form a peristaltic pump as seen in Fig. 5.2. An array of four valves can be used as a mixer in multiple ways. For example, mixing of the contents of two valves can be conducted as seen in Fig. 5.3. The control system is

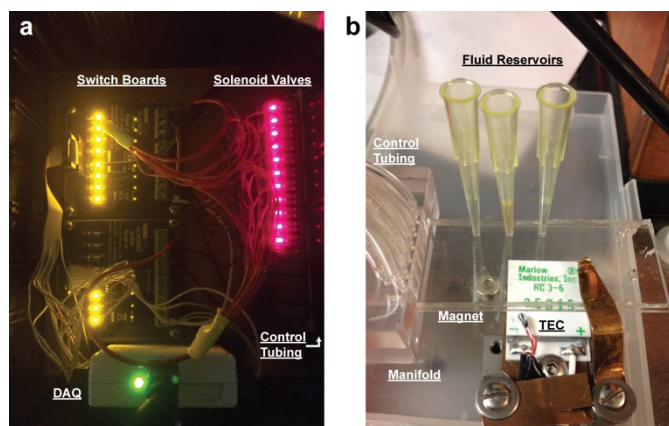


**Fig. 5.4 | Automaton control box and operating connections.** **a**, Custom control box complete with a PC connected DAQ, which is in turn wired to a switchboard controlling the operation of pneumatic solenoid valves. **b**, Control tubing from the solenoid valves connects to the acrylic manifold, allowing for individual operation of the automaton microvalves. A magnet TEC and fluid reservoirs (pipet tips) are pictured for completeness.

depicted in Fig. 5.4a, and the operatable automaton is shown in Fig. 5.4b.

## 5.2 Integration of Microfluidic and Optofluidic Layers

Fig. 5.5 shows the integration of the active microfluidic fluid handling (automaton) layer and the on-chip optical detection (ARROW chip) layer. The ARROW optofluidic chip and microfluidic automaton were connected as follows: first, a cylindrical brass connector of 2 mm outer diameter (OD) was glued to the ARROW liquid-core waveguide chip inlet. A stretchable 1.5 mm inner diameter (ID) piece of tygon tubing was then placed around the connector. Finally, a 2 mm OD, 130  $\mu\text{m}$  ID tygon tubing was press fit into the tygon adapting tubing at one end and the 2 mm OD, 130  $\mu\text{m}$  ID tygon tubing was press fit into the tygon adapting tubing at one end and the 2 mm OD, 130  $\mu\text{m}$  ID tygon tubing was press fit into the tygon adapting tubing at the other, creating a perfect seal, as seen in Fig. 5.5b. This setup provides full reconfigurability (i.e. fluidic and optical chips can be swapped out for different experimental tasks) while adding only a small amount of dead volume on the order of 5  $\mu\text{L}$ .

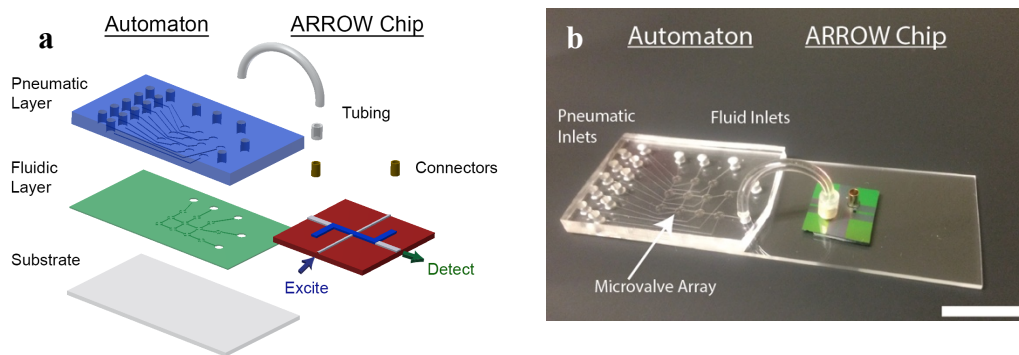


**Fig. 5.5 | Hybrid integration of automaton and ARROW chips principle and implementation. a**, Schematic of hybrid optofluidic device and connections; **b**, photograph of assembled device. The white scale bar in b represents 1 cm.

### 5.3 On-chip Fluid Control and Mixing Using an Active Hybrid Optofluidic System

We first demonstrate functional connections and fluidic control between these two components (Automaton and ARROW) with very dissimilar fluidic resistances (see Fig. 5.5). To this end, an inlet of the automaton was filled with a solution containing 1  $\mu\text{m}$  Tetraspeck fluorescent spheres (diluted to  $1 \times 10^8$  particles/mL), which was in turn introduced into the hybrid system via automaton pump actuation (see Fig. 5.2).<sup>84,88</sup> Alternating forward and reverse automaton pumping programs (20 seconds in length, 600 ms/pump cycle) repeatedly moved fluorescent microbeads through the optical excitation volume as illustrated in Fig. 5.6a. The optical experimental setup was previously illustrated in Fig. 4.3.

As the particles move through the excitation volume, they produce characteristic fluorescence signals such as those seen in Fig. 5.6b. Upon reversing the pumping direction, the same particles are redetected as confirmed by direct, top-down

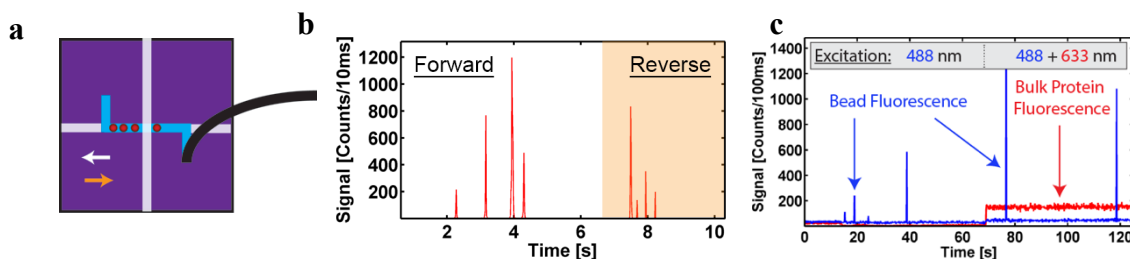


**Fig. 5.6 | Demonstration of the hybrid system's basic functionality: sealed connection and particle mixing.** **a**, Bead movement inside the ARROW chip as actuated by automaton with color coded directions of forward (white) and reverse (orange) pumping; **b**, corresponding fluorescence signal showing four microbeads repeatedly being moved past excitation spot; **c**, simultaneous detection of fluorescent beads and dye-labeled proteins that were mixed in automaton layer. The different laser excitation wavelengths are indicated; the HeNe laser used to excite the proteins is turned on at  $t=70\text{sec}$ .



observation using a microscope. The reverse signal has different respective peak heights due to Brownian motion of the beads and the resulting position change in the observation volume.<sup>71</sup> This experiment clearly demonstrates the ability of the hybrid optofluidic system to controllably transfer analytes between the interconnected chips with their drastically different fluidic impedances (see Section 4.2 for impedance details).

The next level of functional complexity is to implement dynamic sample preparation capabilities in the automaton layer, followed by optical detection on the single particle level in the ARROW chip. To this end, mixing functionality—required for important reactions such as labeling, lysing, and dilution—was shown by filling separate inlets of the automaton with Dylight 633 nm labeled antibody (diluted to 50 nM, Thermo) and streptavidin coated Dragon Green (excitation 480 nm) 220 nm diameter polystyrene spheres (diluted to  $1 \times 10^6$  particles/mL, Bangs Labs). These solutions were then mixed by pre-programmed actuation sequences of the microvalve array, as described in Section 5.1. The mixing process here is dependent on both convective and diffusive mass transport, whereas straight channels rely only on the latter.<sup>84</sup> This enables faster mixing with identical efficiency as that of an off-chip experiment.<sup>89</sup> Once the solution was pumped into the ARROW device, an external vacuum—attached to the exit connector of the ARROW chip—was used to drive the flow, resulting in the data traces seen in Fig. 5.6c. For approximately 70 seconds, the sample was excited solely with 488 nm light. In this portion of the trace, only single particle events are detected in the blue fluorescence trace. After 70 seconds,

excitation light was incident from both HeNe and Argon lasers (633 and 488 nm) resulting in simultaneous bulk fluorescence (due to the constant presence of multiple fluorescent antibodies in the excitation volume at any given time) and peaks (representing single nanospheres) in the red and blue fluorescence traces, respectively.

#### **5.4 Detailed Control Analysis of the Hybrid System**

In order to further characterize the hybrid system, a more systematic and reproducible analysis of the fluidic control was conducted. Specifically, the ARROW chip was filled with deionized water and then connected to the Automaton which was filled with 50 nM antibody (dye labeled for 633 nm, see above). The solution was pumped into the ARROW yielding high fluorescence signal seen in Fig. 5.7. When the automated on-chip pumping is stopped, the fluorescence decreases due to photobleaching. As the residual dye in the channel flows back through the excitation volume, the fluorescence returns to the high signal level. However, the output reservoir was initially filled with water. As such, once the residual content of the channel has been removed, water flows into the excitation volume yielding background fluorescence levels. This process is repeated reproducibly over multiple cycles (three shown here).

#### **5.5 Automated Single Nucleic Acid Detection**

Two inlets of the Automaton microfluidic device were connected to separate reservoirs of 1x SYBR Gold and 300 pM lambda DNA ( $\lambda$ -DNA). The fully assembled automated hybrid optofluidic system was then set to run a mixing and

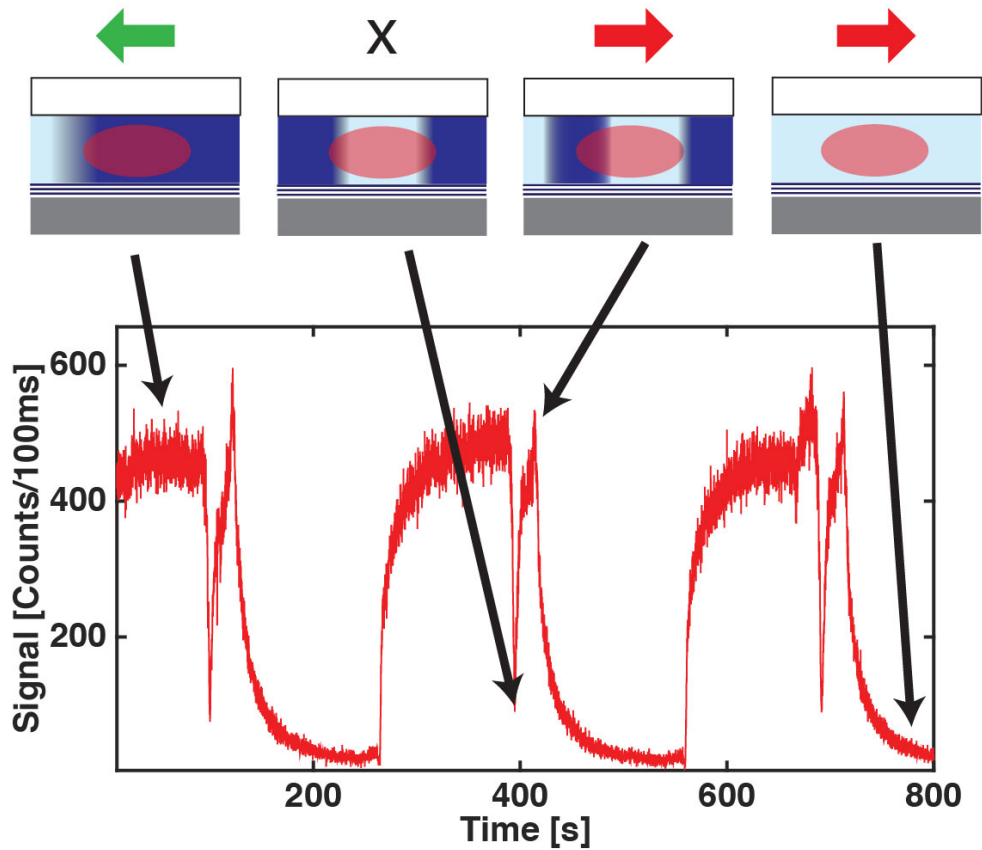


**Fig. 5.7 | Systematic control of fluid flow in an automated hybrid optofluidic biosensor.** Note that in the top images, the view is along the excitation waveguide (within the liquid-core waveguide) and the excitation volume is indicated by a red oval. Arrows above the images indicate pumping in the forward (Automaton to ARROW, green) and reverse (red) direction. Stopped flow is indicated by an x. Dark blue in the images represents fluorescent protein solution while light blue represents non-fluorescent solution.

dispensation program followed by a removal program and subsequent re-dispense.

The respective collected fluorescence data is presented in Fig. 5.8a. Note that the experimental trace contains three regions, an initial detection (forward flow) program, a cleaning program (during which the ARROW chip is emptied—as monitored via through power), and finally another detection program.

Introduction of fluid into the ARROW liquid core waveguide causes a change in the fluorescence signal (red trace in Fig. 5.8a) due to the presence of fluorescent

analytes. The molecules here are individual labeled  $\lambda$ -DNA molecules, where Fig. 5.8b is provided to clearly show individual fluorescence peaks. The molecular fluorescence is at a signal/noise of 3-4, notably above the  $3\sigma$  (three times the standard deviation) background fluorescence of SYBR Gold, here indicated by a horizontal dashed black line. Further inspection of Fig. 5.8a shows that during the cleaning cycle—starting at 100 seconds—the fluorescence signal disappears due to the emptying of the ARROW chip. Re-initiation of the detection program at 215 seconds yields the telltale reemergence of fluorescence signal due to the presence of SYBR Gold stained  $\lambda$ -DNA.

The fluorescence time trace from 10 to 60 seconds was post-experimentally subjected to FCS analysis with a previously described fitting algorithm (see Section 4.3). Experimental data and the respective fit are presented in Fig. 5.8c. By fixing the diffusion coefficient to its published value of  $0.008 \mu\text{m}^2/\text{s}$ ,<sup>90</sup> the concentration and flow speed were determined to be 199 pM and 84  $\mu\text{m}/\text{s}$  respectively. The concentration is in reasonable agreement with the expectation value of 150 pM (the stock is diluted in half during the intercalation process).

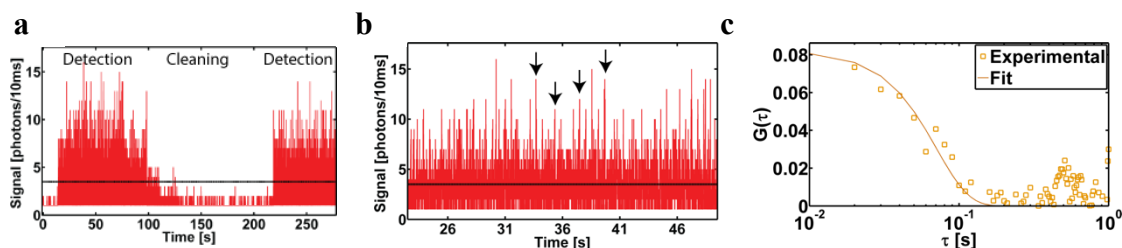


**Fig. 5.8 | Automated single nucleic acid detection and analysis.** **a**, Filling and emptying cycles of the automated system. **b**, Fluorescence detection of single  $\lambda$ -DNA molecules well above the  $3\sigma$  level. **c**, FCS analysis and fit of 10-60 seconds of **a**.

## 5.6 Automated Nucleic Acid Isolation and Detection

Once control, mixing, and distribution had been demonstrated, a more complex biological assay for sequence-specific nucleic acid extraction and detection was developed that takes full advantage of the active fluid control. The nucleic acid of interest was chosen here to be a protein-coding region of Zaire Ebola Virus (GeneBank ID AY354458.1), see Table 5.1 for sequence details. This target region was chosen to be specific to the virus and of synthesizable length. A hairpin molecular beacon<sup>32</sup> (see Section 2.2 for design details) was designed to recognize a portion of the target nucleotide. The beacon was designed to have thermodynamically higher stability when bound to the target oligonucleotide (simulated melting temperature from target  $T_{m,t} = 61.6$  °C vs. intramolecular hairpin formation of  $T_{m,h} = 42.6$  °C). Finally, a biotinylated “pull-down” oligonucleotide was designed to hybridize to a different portion of the target sequence and function as a means of separating target oligonucleotide from complex sample mixtures. All synthetic oligonucleotides were purchased from Integrated DNA Technologies.

**Table 5.1 | Zaire Ebola Virus Nucleic Acid Sequences.**

	Length (nt.)	Sequence
<b>Pull-down</b>	15 (6917- 6931)	5'-BiotinTEG/AAAGGAGCAATACCA-3'
<b>Target</b>	100 (6931- 6832)	5'-GTG AGG TTT TTT TTA GTT TCC CAG AAG GCC CAC TCC CCG ATT GTT GTA TCA ATT TCG GGG TTG ACC TTC CAA ATT AGT TTT CCC GTG GTA TTG CTC CTT T-3'
<b>Beacon</b>	32 (6900- 6923)	5'-/TYE665/ CGCATGGGCCTTCTGGGAACTAAAAAATGCG /IAbRQSp/-3'

In preparation for the on-chip assay, pull-down magnetic beads were created.<sup>91,92</sup> It is noted that off-chip, amplification free imaging of captured nucleic acids has been shown on magnetic beads.<sup>93</sup> An aliquot (0.1mg) of MyOne T1 streptavidin coated magnetic beads (Invitrogen) was washed three times with 1xT50 (10 mM Tris-HCl pH 8.0, 50 mM NaCl) and incubated with 100 picomoles of biotinylated pull-down oligonucleotide for 2 hours at room temperature on a rotary mixer. Next, a magnet was used to retain the magnetic beads during a 4x washing cycle with 1xT50, after which the sample was resuspended in 100  $\mu$ L of 1xT50 (with 2 mM sodium azide) and stored for later use. Fig. 5.9a shows the complete sequence of the strain-specific solid-phase extraction protocol to label and isolate the target viral nucleic acids. Part I of the figure illustrates the magnetic beads coated with the pull-down sequences. In a second preparation step, beacon and target oligonucleotides were hybridized at a concentration of 1  $\mu$ M by heating to 95 °C for 5 minutes in a dry bath (MyBlock), followed by subsequent cooling to room temperature (Fig. 5.9a, part II).

On-chip, the assay was conducted as illustrated in Fig. 5.9a (steps III, IV). First, three inlets of the automaton were filled with the pull-down bead solution ( $\sim 1 \times 10^7$  beads/mL), oligonucleotide mixture (target or non-target oligonucleotide with molecular beacon, each at a concentration of 1  $\mu$ M), and 1xT50 buffer, respectively.

Each valve actuation ( $\sim 125$  nL) then corresponds to dispensation of about 1,250 microspheres or 125 femtomoles of each nucleic acid. Single valve volumes of the pull-down and beacon-target solutions were circularly mixed for 30 seconds in the

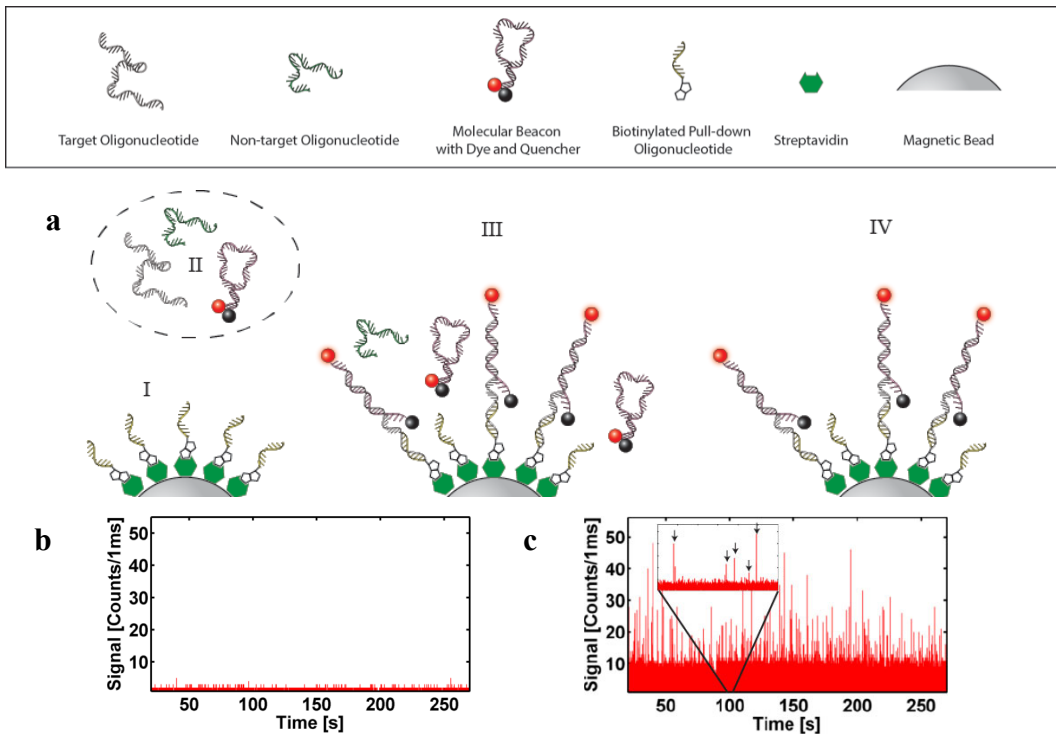


**Fig. 5.9 | Advanced functionality: viral nucleic acid detection using on-chip solid-phase extraction and detection.** **a**, Solid phase nucleic acid pull-down assay - (I) Prepared "pull-down" magnetic beads and (II) nucleic acid target are mixed on automaton (III); washed magnetic particles are sent to the ARROW chip (IV). Particle detection for **b** negative (pull-down non-cognate)—see I—and **c** positive (pull-down cognate) nucleic acid samples—see IV. Single bead signals are marked by arrows in the figure inset.

microvalve array. The specific Automaton program was written as follows – variations of pumping (as seen in Fig. 5.2) were used to fill valves 5 and 6 with nucleic acid mixture and pull-down beads, respectively, which were then mixed in a similar fashion to Fig. 5.3 using valves 5,6,8, and 9 (valve numbers are indicated in Fig. 5.1). The solution was then pumped to valve 7 where a magnet was attached to the bottom of the substrate to pull down magnet beads and bound target. Analytes that were not pulled down were then washed off using buffer from inlet 1 via a long peristaltic pump using valves 1,4,7,8,9, and 11. The retained solution containing only labeled target nucleic acids is shown in part IV of Fig. 5.9a. The process was repeated

until enough beads were accrued for analysis in the space of valve 7. Upon removal of the magnet, beads were re-suspended and sent to the output using valves 1,4,7,8,9,6, and 10. This entire cycle takes 60 seconds for processing.

Signal traces for experiments containing non-target oligonucleotide plus beacon (negative control) and beacon-target hybrids are shown in Fig. 5.9b and c, respectively. It is clear that the magnetic beads, under negative control conditions (Figure 3b)—no target or completely non-complementary contaminating oligos, in this case a 100 nt H1N1 synthetic oligonucleotide—yield on average 3 counts/ms per particle. In contrast, beads that are subjected to mixing with beacon bound targets have an average signal of 15 counts/ms per particle (up to a maximum of 50 counts/ms per particle), corresponding to a signal-to-noise ratio of 5 and allowing for specific detection of the viral target. As ARROW devices have single nucleic acid sensitivity (see Section 4.3), the limit of detection (LOD) of this devices is dependent only on the counting time of the assay. These results demonstrate the ability of the hybrid optofluidic system to process and extract small volumes (about 5  $\mu$ L) of target nucleic acid material with sequence specificity. Note this volume can be dramatically increased and is discussed in the following chapter. It is notable that the signal for target-beacon bound beads is high for each individual bead. Therefore, it would be possible to further reduce the sample volume, and thus the number of fluorescent targets per bead.

In summary, I have presented a hybrid chip-scale system combining automated microfluidic processing with highly sensitive on-chip optical detection. Actively



controlled manipulation of fluidic volumes is necessary to carry out the complex sample preparation tasks required for realistic molecular diagnostic tests. We implemented this active control using programmable microvalve arrays and demonstrated that these can be fluidically coupled to a liquid-core waveguide analysis layer. In addition to basic functions such as reversible pumping, valving, and mixing processes, we implemented an assay for molecular diagnosis of viral nucleic acids from complex solutions. The target nucleic acids were extracted and isolated in the microfluidic layer and optically detected in the optofluidic layer. The simultaneous miniaturization of both fluidic and optical components thus allows for highly sensitive and specific detection of a wide range of test volumes (i.e. nL to mL), containing small numbers of target molecules in complex biological fluids. This finding is leveraged in the next chapter for the automated detection of single, clinical viral nucleic acids.

## 6 Detection of Clinically Relevant Biomolecules

Any integrated diagnostic platform has two aims: (1) processing biological samples, and (2) detection of the processed analytes. The first aim can be handled entirely using microfluidic devices.<sup>16,94</sup> Using active microfluidics—or polydimethylsiloxane (PDMS) chips that can pump their own fluids—one can miniaturize and automate the process.<sup>60,95</sup> The second aim can be accomplished using optofluidic chips, i.e. chips that can guide both light and fluids. Our group has demonstrated that single virus sensitivity is possible on silicon optofluidic devices using fluorescence based optical detection in waveguides.<sup>82</sup> The difficulty for a fully integrated chip is that aims (1) and (2) are achieved using soft (PDMS) and hard (crystalline silicon) materials, respectively, which are difficult to functionally integrate. In Chapters 4 and 5 I demonstrated the ability to marry silicon and PDMS based technologies into passive and active hybrid devices, respectively. In the following chapter I present an elegant solution for both aims (1) and (2). Specifically, I rely heavily on the findings in Chapter 5 to process and detect clinical Ebola virus. Thereafter, I expand on current ARROW technology by introducing a multimode interference waveguide (MMI) for multiplexed detection of single influenza viruses. The following discussions closely follow the results presented in our published works.<sup>4,5</sup>

## **6.1 Optofluidic analysis system for amplification-free, direct detection of Ebola infection**

The 2014 Ebola epidemic is the largest and deadliest in history. Affecting 10 countries worldwide, the West Africa outbreak has reported over 28,000 cases, ten times the amount of all other Ebola outbreaks combined.<sup>96</sup> Recognizing the possibility of a global Ebola pandemic illuminates the need for a rapid and cheap detection technology. Reverse transcriptase polymerase chain reaction (RT-PCR), the gold standard for nucleic acid detection, was the basis for RealStar<sup>®</sup> Filovirus Screening used during the outbreak, however, this detection technology required sophisticated instruments and trained users. ReEBOV Antigen Rapid Test is the second technology approved by the World Health Organization for diagnosing Ebola. While the antigen test requires less sophisticated equipment, it reports 8% higher false negatives and 15% higher false positives.<sup>97</sup> Both of the testing technologies require trained personnel to be exposed to contaminated bodily fluids. An integrated point-of-care device capable of safe, fast, cheap, and fully automated Ebola detection is presented herein. For motivation and explanation of the programmable microfluidics used throughout this chapter, refer to Chapter 5.

### **6.1.1 Systematic design of a hybrid optofluidic system for detection of single clinical nucleic acids**

Here, we report on the differentiated detection of Ebola virus using amplification-free, direct detection of single nucleic acids on a hybrid optofluidic

device. We demonstrate that this system has the requisite *sensitivity*, *dynamic range*, and *specificity* for a viable clinical assay.

The hybrid optofluidic system used in this work is nearly identical to that used in Chapter 5. Refer to Chapter 5, and specifically Fig. 5.5, for our approach to creating an integrated device that is capable of carrying out both sample preparation and amplification-free detection. The *sensitivity* required for amplification-free detection of single nucleic acids is provided by the optofluidic layer, i.e. the ARROW chip. The need for integrated biological sample processing and large *dynamic range* is satisfied by the microfluidic layer, which consists of an array of lifting gate microvalves (automaton).<sup>62,84</sup> This layer is created in PDMS (polydimethylsiloxane) using established soft lithography techniques (see Sections 2.4 and 5.1). Finally, the *specificity* for accurately identifying different viral targets is created by the solid-phase extraction assay shown in Fig. 6.1. We note that the extraction assay is very similar to the one described in Fig. 5.9 and the sequence design was conducted in a similar fashion to that seen in Table 5.1. The difference being that after washing off

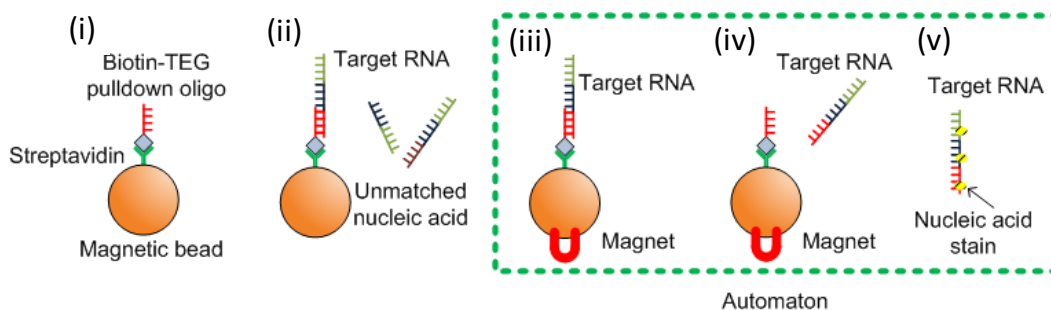


**Fig. 6.1 | Solid-phase extraction assay used for target isolation and detection. The dashed box indicates the steps that were implemented on the automaton chip.**

the non-matching nucleic acids and other random biomolecules (steps (i)-(iii)), the remaining targets are thermally released from the beads (step (iv)), resuspended in buffer solution, and fluorescently labeled with SYBR Gold nucleic acid stain (step (v)). About 5  $\mu\text{L}$  of this solution are then pumped through the ARROW chip for optical detection in under ten minutes. These preparation steps were carried out either entirely off-chip or on the automaton chip. The dashed box in Fig. 6.1 marks the steps that were implemented by the automaton in the present study.

### 6.1.2 Automated pre-concentration of Ebola nucleic acids

In addition to sample isolation, the automaton is also capable of facilitating a pre-concentration step that allows for extending the detection limit of the ARROW sensor to pre-symptomatic target concentrations below 1 pfu/mL. For an initial demonstration and characterization of this feature, we used 100-mer synthetic oligonucleotide targets, corresponding to the protein coding region of the Ebola virus (IDT Technologies). These were mixed off-chip with magnetic beads and molecular beacons, resulting in a solution containing magnetic beads with hundreds of

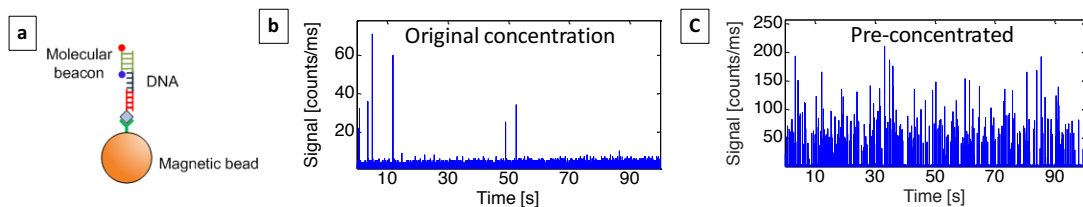


**Fig. 6.2 | Automated preconcentration and detection of synthetic Ebola nucleic acids.** **a**, Particles to be concentrated: target oligomers are bound to pull-down recognition sequence on magnetic microbeads; molecular beacons specifically bind to target and cause beads to fluoresce; **b**, particle fluorescence counts detected on ARROW chip before preconcentration step and **c** after preconcentration on automaton. A 335x concentration increase is observed.

fluorescently labeled targets as shown in Fig. 6.2a (see Section 5.6 for detailed design information). After diluting the beads in 3mL of buffer solution, this analyte was pumped through the ARROW chip by applying negative pressure to the outlet reservoir, enabling optical detection, either directly or after preconcentration on the automaton. During preconcentration, a permanent magnet was placed under one of the microvalves as the analyte was pumped over it, continuously pulling down magnetic beads. Finally, the beads extracted from 3mL of analyte were resuspended in  $\sim 5\mu\text{L}$  of solution in outlet 11 (see Fig. 5.1) for transfer to the ARROW chip and optical fluorescence analysis. The unconcentrated solution (Fig. 6.2b) shows only 7 particles (magnetic beads with labeled target) over the course of the test (5 min total). After preconcentration, a constant stream of hundreds of particles is detected over the same period (Fig. 6.2c), demonstrating highly efficient on-chip concentration. Individual signal levels vary somewhat due to differences in the position of the particles within the waveguide cross section which results in variations in the excitation and collection efficiencies in accordance with the optical mode profiles in the solid-core excitation and liquid-core collection waveguide.<sup>98</sup> Variations due to microbead aggregation could be excluded by control observations from the top with a CCD camera. After correcting for the different flow speeds in each experiment, which results in different volumes tested during the identical assay time, a concentration factor of 335 was determined.

### ***6.1.3 Automated and specific detection of single, clinical ebola nucleic acids***

With these capabilities in hand, we carried out an assay to demonstrate amplification-free detection of Ebola virus using this integrated system. In the first set of experiments, all sample preparation steps (see Fig. 6.1) were carried out off-chip. Supernatant of EBOV-infected Vero E6 cells was collected five days post infection. After inactivation, total RNA content was isolated for testing at a concentration of  $2.1 \times 10^5$  pfu/mL. Equivalent negative control samples of Sudan virus (SUDV,  $2.2 \times 10^5$  pfu/mL) and Lake Victoria Marburg virus (MARV,  $4.4 \times 10^6$  pfu/mL) were prepared. All concentrations were verified using PCR. In order to determine the dynamic range and limit of detection of our assay, these initial solutions were serially diluted, followed by the solid-phase extraction assay and the ARROW chip optical detection.

Single nucleic acids are identified by individual fluorescence peaks extending above a background level caused by free SYBR Gold dye. The detection threshold is defined as the maximum background level observed during a reference measurement with a dye-only solution of identical concentration immediately preceding the sample testing. Each signal exceeding this threshold is identified as an event and digitized, much like in single-photon counting. Fig. 3a shows the resulting digitized signal traces for three different target concentrations. Therefore, different concentrations are distinguished by the number of peaks per time as clearly seen in the figure. With single RNA sensitivity, any concentration can be detected as long a reliable number of counts are collected. Therefore, the limit of detection is determined by the assay time (here between 3 and 10 minutes) which defines the amount of sample liquid

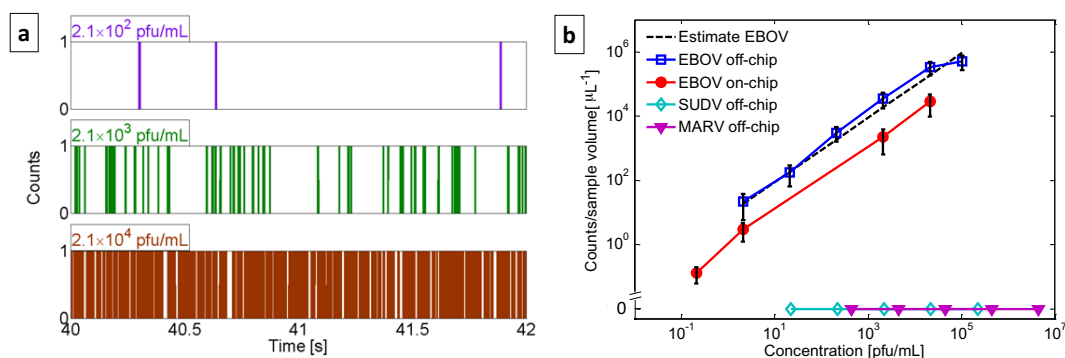


**Fig. 3 | Amplification-free detection of Ebola virus on optofluidic chip.** **a**, segments of digitized fluorescence counts above background showing concentration-dependent numbers of single RNAs; **b**, concentration-dependent particle counts for off-chip (open squares) and using the automaton (solid circles) sample preparation. Negative controls (SUDV, MARV) did not create any counts (note the broken vertical scale). Dashed line: Predicted particle count determined from initial concentration and experimental parameters (tested sample volume, excitation and detection mode areas, liquid-core channel cross section). The lowest two concentrations for on-chip sample prep were reached by 50x and 460x preconcentration steps, respectively.

tested and thus the maximum number of counts. Fig. 3b shows the concentration dependent number of counts per starting volume of clinical sample. First, we find that both negative controls, SUDV and MARV, produce zero counts at all tested concentrations and flat lines in Fig. 3b (Note the broken scale on the ordinate axis to visualize zero counts on an otherwise logarithmic scale). The positive EBOV sample, on the other hand, creates positive counts with the expected concentration dependence. Here, we first consider the case of off-chip sample preparation (blue line). A linear concentration dependence is observed over 6 orders of magnitude down to 2.1 pfu/mL below which there are too few targets in our tested sample volume of a few microliters. The dashed line is an estimated count rate based on the initial number of target RNA copies independently measured by PCR. This concentration is converted into a count rate using the flow speed in the ARROW channel (measured by FCS analysis of each fluorescence signal) and the ratio of the



liquid-core waveguide optical mode and the channel cross section area (only targets flowing within the mode area can be detected). We find excellent agreement between the expected and measured count rates within the experimental error, confirming the ability of the ARROW chip to both identify and quantify a target virus in clinical sample material by direct nucleic acid counting.

In order to demonstrate a pathway towards complete on-chip diagnosis, we implemented sample preparation steps (iii)-(v) in Fig. 1c (target extraction, washing, and fluorescent labeling) on the automaton. In addition, we added a preconcentration step to further improve the limit of detection of this assay. The result for integrated sample processing and detection is shown by the red line in Fig. 3b. Again, we observe a linear dependence of the measured signal on concentration over six orders of magnitude. Moreover, by using 50x and 460x preconcentration (i.e. starting volumes of 0.25 mL and 2.3 mL, respectively) on the automaton chip, we were able to push the limit of detection to 0.2 pfu/mL, comparable with PCR analysis<sup>99</sup>, covering the entire range of viral loads observed in typical hemorrhagic fever cases<sup>100</sup>, and more than four orders of magnitude lower than other chip-based approaches.<sup>101</sup> The overall count rate for on-chip processing is lower than in the off-chip preparation case due to some nucleic acid and bead loss in the automaton channels. While this did not prevent us from improving the sensitivity of the assay, this issue can be mitigated by optimizing the automaton layout with shorter connecting channels and the surface treatment using a different coating.<sup>102</sup>

In addition to single nucleic acid counting and preconcentration, the system is also capable of reliably detecting nucleic acids well above the single molecule concentration limit. In order to demonstrate the extension of our chip-based detection to the high concentration (more than 1 target on average in excitation volume) limit, we carried out a series of experiments using a synthetic 100-mer nucleic acid specific to Ebola virus. We fluorescently labeled these nucleic acid off chip using SYBR gold nucleic acid stain. SYBR gold dyes nucleic acids  $\sim 1$  dye/4bp, resulting in  $\sim 25$  fluorophores per target molecule. We prepared a serial dilution series of seven concentrations covering six orders of magnitude in concentration and measured the

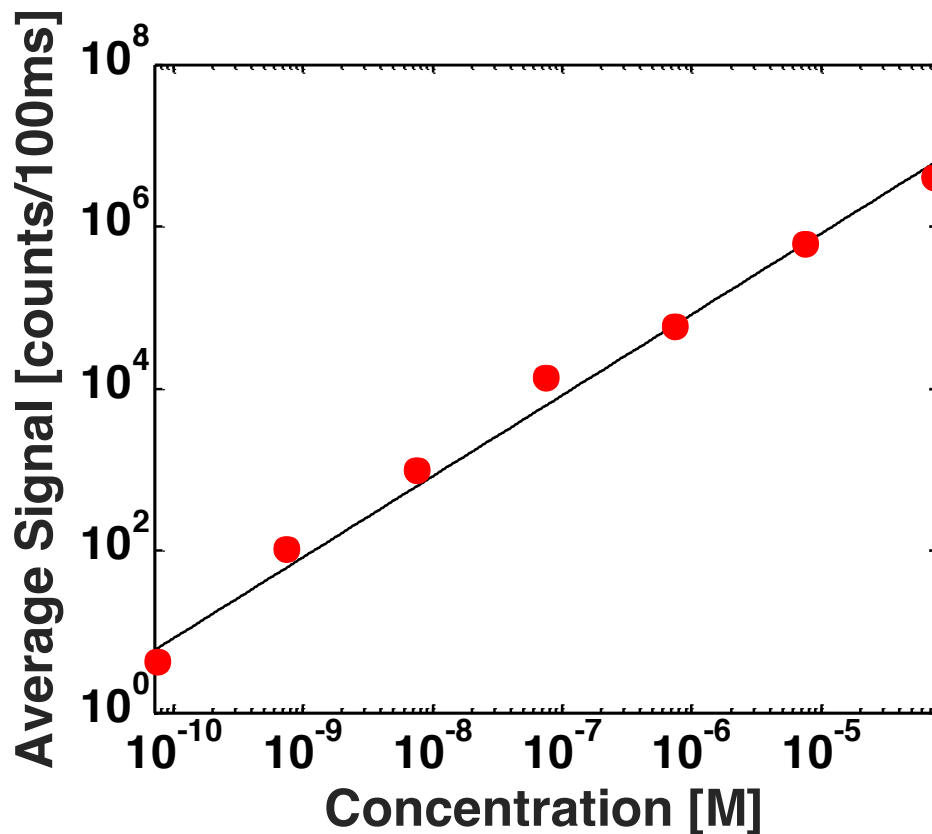


**Fig. 6.4 | Fluorescence concentration series in the analog detection regime demonstrating linear signal detection over six orders of magnitude (line: linear fit).**

average fluorescence signal of each sample in an ARROW chip as shown in Fig. 4.3 and Fig. 5.5. The results are shown in Fig. 6.4. We find a clear concentration dependence of the signal. The solid line is a linear fit, showing excellent linearity over the full concentration range. This demonstrates the ability for on-chip fluorescence detection of viral nucleic acids over six orders of magnitude in the high concentration limit and an overall dynamic range of at least 13 orders of magnitude.

In summary, we have demonstrated variant-specific identification and quantification of hemorrhagic fever infection in clinical samples using amplification-free counting of single nucleic acids. Both sample preparation and optical detection were implemented on-chip in a hybrid system with individually designed microfluidic and optofluidic layers. The system features excellent specificity, sensitivity and dynamic range. On-chip preconcentration was implemented to reach a limit of detection comparable to PCR. The demonstrated assay can be readily applied to other nucleic acid tests for infectious diseases or other applications. The high level of integration combined with reduced complexity makes this approach an attractive and user-friendly technology for point-of-use diagnosis, especially in resource-limited settings.

## **6.2 MMI Based Wavelength Division Multiplexing for Optofluidic Detection of Single Virus Detection**

The ability to overlay multiple electromagnetic waves in the same physical space by virtue of linear superposition is arguably at the root of modern communication as we know it. Originally implemented in the radio frequency regime,

this wavelength division multiplexing (WDM) principle was transferred to optical wavelengths in the visible and near infrared range which can be carried by a single, low-loss silica fiber.<sup>103</sup> Available in both coarse (CWDM) and dense (DWDM) varieties, terabits of data are now shuttled between a source and their destination using anywhere from four to over one hundred wavelengths.<sup>104,105</sup> Here, we transfer the WDM principle from data communications into a different realm, that of chip-based biomedical analysis where much can be gained by superimposing multiple colors in an optical waveguide, albeit for different reasons.

Specifically, we implement WDM on an optofluidic platform for on-chip analysis of single influenza viruses. In place of silica fiber as the physical carrier, we create a single waveguide structure that combines multiple spectral channels for fluorescence excitation of biological targets. Instead of temporally modulating each channel to transport information, we use this waveguide to produce wavelength-dependent spatial patterns in an intersecting fluidic channel. The spatial encoding of spectral information then allows for direct identification of multiple labeled targets with extremely high sensitivity and fidelity. The technique is demonstrated in two implementations for direct counting and identification of individual virus particles from three different influenza A subtypes – H1N1, H2N2, and H3N2 – at clinically relevant concentrations.

### ***6.2.1 Multimode Interference Waveguides (MMIs)***

In order to understand the concept of WDM for multiplexing, it is first essential to understand the underlying photonic architecture – namely, the multimode

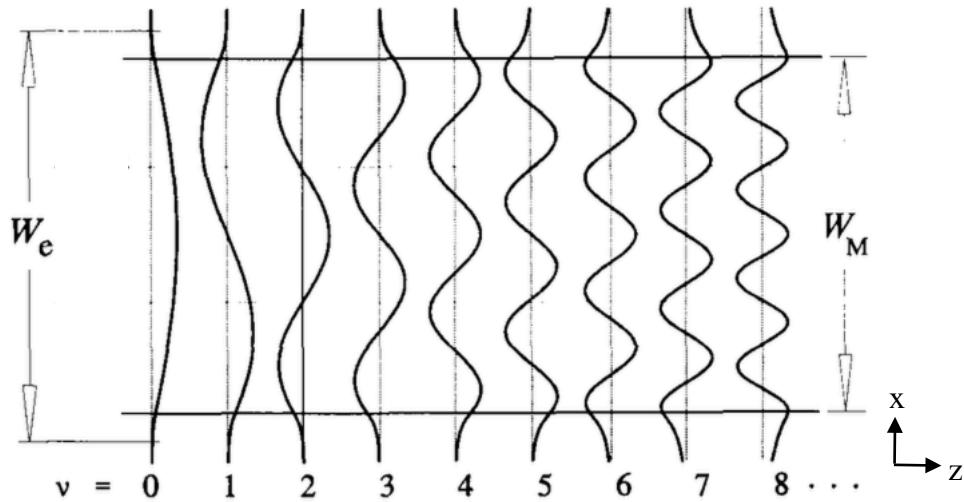


**Fig. 6.5 | Example electromagnetic modes in generic multimode slab waveguide of width  $W_M$ .**

interference waveguide (MMI). The subject was discussed in detail by Soldano and Pennings in 1995 and their analysis is presented briefly in this section.<sup>106</sup> For consistency, the notation from their analysis is adopted herein.

First we consider a generic multimode waveguide, i.e. a waveguide that has a width large enough to support multiple electromagnetic modes. The first 9 guided modes of an example slab waveguide of width  $W_M$  are presented in Fig. 6.5<sup>106</sup> (here,  $W_e$  is the effective width of the waveguide accounting for lateral penetration of the modes and  $v$  is the order of the mode presented). Note that this analysis assumes an index guiding waveguide where the core of the slab waveguide has a higher refractive index than the external cladding.

Each of the modes in a multimode waveguide, when excited independently, will present the same field pattern after any propagation distance (assuming no perturbations/intermodal coupling). However, in the case of a generic input field that

does not match a single waveguide mode, multiple modes will be excited.

Accordingly, the field at an arbitrary propagation distance,  $z$ , will be defined by the linear superposition of the coupled modes. Specifically, the propagation constant spacing (of the confined modes) defined as

$$(\beta_0 - \beta_\nu) \simeq \frac{\nu(\nu + 2)\pi}{3L_\pi} \quad (6.1)$$

will dictate the beating between the fundamental and higher order modes. Here,  $\beta$  is the propagation constant,  $\nu$  is once again the order of the mode, and  $L_\pi$  is the beat length between the fundamental and first order mode (or the length of propagation at which the modes  $\nu = 0$  and  $\nu = 1$  are completely out of phase, e.g.  $(\beta_0 - \beta_1)L_\pi = \pi$ ).

At the very beginning of the waveguide, where no propagation has happened, it is clear that the propagation constant spacing has no effect on the field pattern. As such, the total field pattern is directly dependent on the coupling between the input field and waveguide modes. The total field,  $\Psi$ , at the beginning of the waveguide is simply the sum of the individual mode fields,  $\psi_\nu$ , multiplied by their coupling coefficients,  $c_\nu$ ,

$$\Psi(y, 0) = \sum_{\nu=0}^{m-1} c_\nu \psi_\nu(y) \quad (6.2)$$

summing over the entire guided mode spectrum. Note that the coupling coefficients are simply derived from an overlap integral of the input field with each individual mode. Assuming implicit time dependence and accounting for

the phase factor of the first order mode, a position dependent total field can be derived as

$$\Psi(y, z) = \sum_{v=0}^{m-1} c_v \psi_v(y) \exp [i(\beta_0 - \beta_v)z] \quad (6.3)$$

now containing a propagation distance dependence,  $z$ . Finally, substituting Eq. 6.1, we find

$$\Psi(y, L) = \sum_{v=0}^{m-1} c_v \psi_v(y) \exp \left[ i \left( \frac{v(v+2)\pi}{3L\pi} \right) L \right] \quad (6.4)$$

where an evaluation distance  $L$  is now assumed. The second portion of the equation, i.e. the exponential, is considered the mode phase factor and describes how the modes will interfere. More specifically, when this phase factor is equal to 1 or -1 for all  $v$ , the input image is replicated (in the case of negative, the image is inverted across the central axis of the waveguide). This equality happens at

$$L = p(3L\pi) \quad p = 0,1,2 \dots \quad (6.5)$$

When this general case is reduced to a symmetric input centered at  $x = 0$ , the length at which  $N$  replicas of the input field are reproduced is 4 times shorter (due to the integer nature of  $v(v+2)$  for even  $v$ ) resulting in

$$L = \frac{p}{N} \left( \frac{3L\pi}{4} \right) \quad p = 0,1,2 \dots \quad (6.6)$$

which can be related to effective waveguide width,  $W_e$ , through consideration of wave vector relations and penetration depths (with  $p = 1$ )<sup>106</sup>, as

$$N \cdot \lambda = \frac{n_c W_e^2}{L}. \quad (6.7)$$

Note that 6.7 is a useful equation for designing MMI's in optofluidic WDM applications and will be implemented for the rest of this section.

### 6.2.2 Optofluidic MMI Biosensor Architecture

Fig. 6.6a<sup>5</sup> schematically shows the principle of WDM fluorescence detection on an optofluidic chip. A wide solid-core optical waveguide acts as a multi-mode interference (MMI) waveguide in which numerous waveguide modes with different propagation constants interfere as they propagate along the structure.<sup>106</sup> At propagation distances where the relative phases of these modes match up correctly, well-defined images (spot patterns), including self-images of the original input mode,

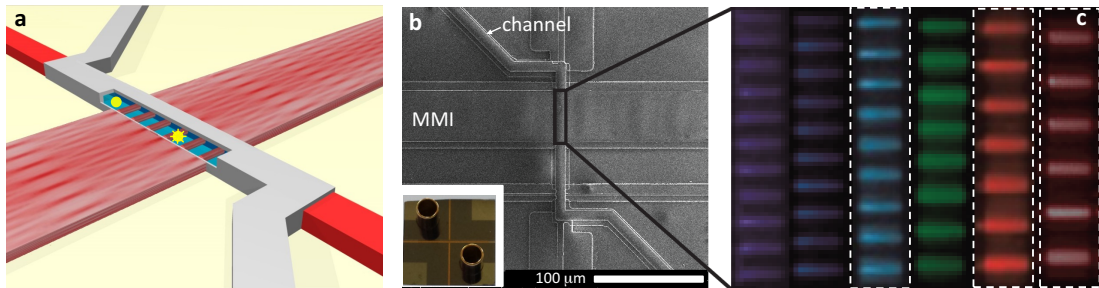


**Fig. 6.6 | Wavelength division multiplexing for single virus detection.** **a**, Schematic view of multi-mode interference (MMI) waveguide intersecting a fluidic microchannel containing target particles. Targets are optically excited as they flow past well-defined excitation spots created by the MMI; fluorescence is collected by the liquid-core waveguide channel and routed into solid-core waveguides (red); **b**, Scanning electron micrograph of MMI-based optofluidic chip (Inset: photograph of 1cm by 1cm chip, showing two fluidic reservoirs holding microliters of sample volume); **c**, Photographs of multi-spot excitation patterns created in fluidic channel filled with fluorescent liquid. The entire visible spectrum is covered by independent channels (405 nm/11 spots, 453/10, 488/9, 553/8, 633/7, 745/6). (The original black and white color scale was rendered in the actual excitation colors; the wavelengths used for the virus assays are highlighted by white, dashed boxes).



are created. Here, we design the MMI such that a fluidic microchannel intersects the waveguide at a position that corresponds to a well-defined, integer number of spots for multiple wavelengths. Fig. 6.6a<sup>5</sup> shows the example of six spots for excitation in the dark red (745 nm) spectral range. A particle labeled for excitation at this wavelength creates six signal emission peaks that are equally spaced in time if the particle flows through the channel at constant speed. Emitted photons are captured and routed to a detector if the channel also acts as a liquid-core optical waveguide.<sup>24,107</sup> This type of multi-spot excitation can be used to significantly enhance the signal-to-noise ratio of a fluorescence assay.<sup>108,109</sup> The SEM image in Fig. 6.6b shows the physical implementation of this concept - an optofluidic platform that combines solid-core and liquid-core antiresonant reflecting optical waveguides (ARROWs). The full chip, including fluidic reservoirs for introducing microliters of sample volume into the channel, is shown in the inset. Using single-mode waveguides, this platform has demonstrated single particle fluorescence detection sensitivity, e.g. for viruses<sup>82</sup> and nucleic acids (see Chapters 4 and 5).

The true power of the MMI approach, however, is to leverage the large available spectral bandwidth in a single photonic structure. This is evident if we consider that the product of spot number  $N$  and wavelength  $\lambda$  for a specific MMI is derived in Eq. 6.7, where  $W_e$  the effective MMI width (here: 100 $\mu$ m),  $n_c$  the effective refractive index of the MMI (here: 1.46), and  $L$  the MMI length (here: 3.4 mm) are all fabrication parameters. This allows us to implement on-chip WDM by creating physically different excitation patterns simultaneously from a single MMI. For the

device used in this study, we were able to produce six well-defined spot patterns across the visible spectrum using wavelengths ranging from 403nm (11 spots) to 745nm (6 spots). Fig. 6.6c shows all the excitation patterns created when the intersecting fluidic channel was filled with solutions containing fluorescent liquid (a 7<sup>th</sup> channel at 886 nm with five spots was also observed).<sup>110</sup> The number and spectral positions of these six channels are a perfect match to the absorption spectra of commercially available fluorescent dyes.<sup>111</sup> The differences in spot number and spacing are evident and constitute the basis for a new multiplex pathogen analysis technique. This multiplexing capability is ultimately limited by the finite absorption bandwidth of the dye labels which can lead to channel cross-talk if the absorption spectra overlap. However, six to seven channels can be used with proper design, enabling detection of dozens of targets using the combinatorial technique described below.

### **6.2.3 Virus sample preparation**

Three inactivated, whole influenza virus samples were purchased for testing –  $\beta$ -Propiolactone-inactivated A/PR/8/34 (H1N1) and UV-inactivated A/2/Japan/305/57 (H2N2) (Advanced Biotechnologies Inc.) as well as Formalin-inactivated A/Aichi/68 (H3N2) (Charles River). Viruses were dyed using NHS-activated Dylight fluorophores according to manufacturer instructions (Thermo Scientific). Briefly, virus samples were added to aliquots of dried Dylight dyes and allowed to incubate at room temperature for 2 hours. Samples were then separated from free dye using PD MiniTrap G-25 gel filtration columns (GE Healthcare). Fractions were collected

drop-wise (i.e. single drops were collected in separate Eppendorf tubes) and tested for fluorescent virus and free-dye background on a custom total internal reflection fluorescence (TIRF) microscope. Once identified, the viral fractions were aliquoted and flash-frozen via liquid nitrogen for later use. While manufacturer concentrations were reported, the variable dilution/fractionation process of gel filtration chromatography leads to an inability to directly account for virus concentration. However, TIRF-based measurements concluded that virus concentrations were on the order of femtomolar as observed by direct counting on the chip.

#### ***6.2.4 Multiplex virus fluorescence detection setup and experiment***

A detection setup was employed similar to that previously reported in Chapter 4. The optical setup implements three lasers, a 488 nm Ar-Ion laser, a 633nm HeNe laser, and a Ti:Sapphire laser tuned to 745 nm in cw mode. All three of the laser lines were coupled into a single mode fiber which then butt coupled into a narrow (4  $\mu\text{m}$ ) single-mode excitation solid-core waveguide on the ARROW optofluidic chip. The single-mode waveguide ends in the center of the 100  $\mu\text{m}$  wide and 3.4 mm long MMI waveguide. (For fabrication workflow, see Section 2.3.2; the ARROW samples used here were from the MA13 wafer.) In the MMI, multiple modes interfere with each other, creating equally separated spots at the liquid-core waveguide section. Fluorescently labeled viruses passing through the MMI excitation volume are subjected to the MMI pattern and thus produce multiple fluorescent signals per virus. These signals are captured by the liquid-core waveguide, transmitted into the collection solid-core waveguide, and are collected at the chip facet by an objective.

The signal is collimated, passed through a single penta-bandpass optical filter (FF01-440/521/607/694/809-25, Semrock) to eliminate the excitation wavelengths, and is finally detected by a single photon avalanche diode (Excelitas). No spectral filters to separate the emission colors are required (unlike Fig. 4.3).

### **6.2.5 Multiplexed single virus detection with single color labeling**

For the virus detection assays, three deactivated virus types were labeled with one or two of the selected fluorescent dyes and up to three of the channels shown in Fig. 6.6c were used. The viruses were mixed and a 5  $\mu$ l aliquot was pipeted into one of the reservoirs covering the ends of the fluidic channel (see inset of Fig. 6.6b). The solution was then pulled through the channel and past the MMI excitation areas using negative pressure applied to the second reservoir. Light from up to three lasers was coupled into single mode optical fiber and into a single-mode solid-core waveguide connecting the MMI to the edge of the chip. The excitation wavelengths (488, 633, and 745 nm) were chosen to create 9, 7, and 6 spots, respectively (see Fig. 6.6c). We implemented two multiplex assays and analyzed them with two different methods to demonstrate the capabilities of our approach. For the first assay, each of the three virus types was labeled with a different dye and all three excitation wavelengths were used.

Fig. 6.7a shows a representative fluorescence signal  $F(t)$  emitted from a single H1N1 virus at 488 nm excitation, collected along the liquid-core waveguide channel. Nine distinct peaks are clearly visible, illustrating both the high quality of the MMI pattern and the sensitivity of the optofluidic chip to single virus particles using only

waveguides for excitation and collection. The virus type can be identified visually by the number of peaks (here: nine), but more sophisticated analysis algorithms can be applied that are compatible with rapid and automated signal processing of large numbers of particles in a clinical setting. For this assay, we used single-particle autocorrelations for demultiplexing. A virus particle can be detected if its fluorescence intensity exceeds the maximum background level. This background is due to residual photoluminescence of the solid waveguide materials, which was

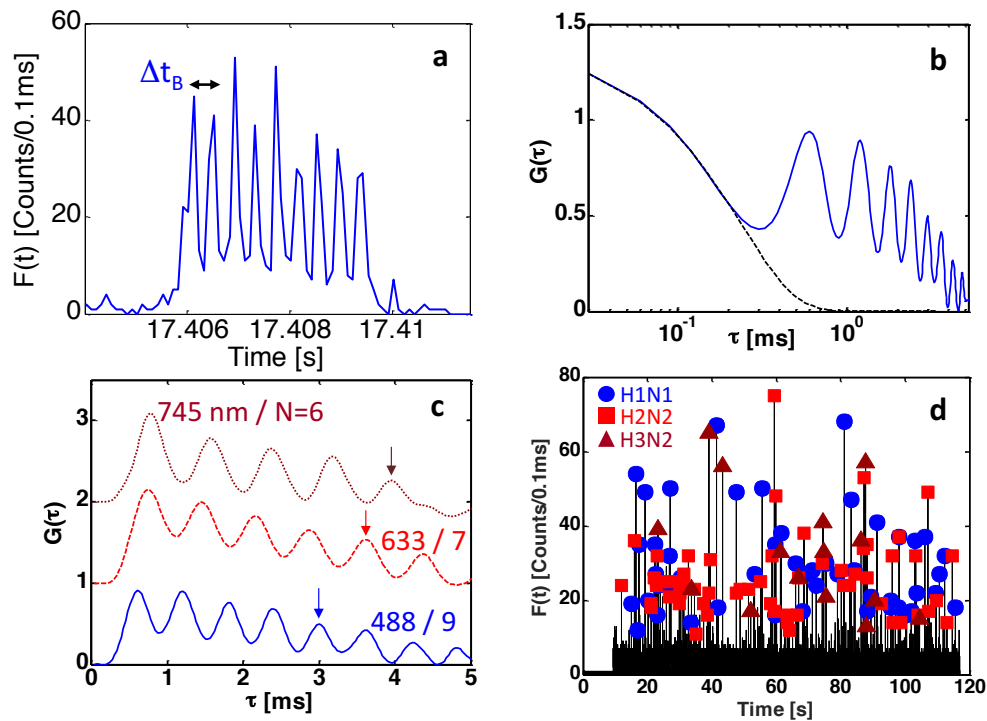


**Fig. 6.7 | Three-color multiplex virus detection.** **a**, Representative fluorescence signal emitted by single H1N1 virus excited at 488nm showing 9 distinct peaks spaced by  $\Delta t_B$ ; **b**, Corresponding single-particle autocorrelation signal. Multiple peaks are observed at multiples of  $\Delta t_B$ ; dashed line: fit to underlying flow-limited correlations. **c**, Single-particle autocorrelation for 3 virus types after subtraction of flow-based contribution. The peak positions depend strongly on excitation spot number (arrows mark the 5<sup>th</sup> peak for each virus type). **d**, Segment of fluorescence from virus mixture excited at all three colors. Events are identified using single-particle autocorrelations. All but one identified signals (99.2%) agree with manual inspection of events.

minimized by the choice of cladding material.<sup>38</sup> A user defined threshold is set, at or above which peaks are detected as viruses. Viruses are then identified by performing an autocorrelation of their respective signals. The detection threshold was set to 11 cts/0.1ms to ensure high confidence identification without false positives. Fig. 6.7b shows the autocorrelation signal  $G(\tau)$  corresponding to the event of Fig. 6.7a. As is typical for fluorescence correlation spectroscopy (FCS), a curve with an overall decay due to drift and diffusion is observed (dashed line).<sup>112</sup> Superimposed on this, however, we observe a number of distinct peaks that arise at integer multiples of the lag time  $\Delta t_B$  that correspond to the time it takes the particle to travel between excitation spots. Fig. 6.7c shows close-ups of the autocorrelations for each virus type in the region of these cross-correlation peaks. The drift-induced overall decay seen in Fig. 2b was subtracted from each trace. Corresponding peaks are clearly separated (see arrows for 5<sup>th</sup> peak) and allow for correct assignment of the virus. By using the delay time for the fifth peaks, we analyzed the fluorescence trace from a particle mixture over 120 s as shown in Fig. 6.7d. It is important to note that neither spectral separation nor filtering of the emitted light was needed. All spectral information was extracted from the temporally encoded detector signal. The symbols in Fig. 6.7d indicate the virus type identified using single particle autocorrelations. All but one event (0.8% false positive rate) were correctly assigned as verified by manual inspection of each signal for peak number and spacing. 73 events had peak intensities between the maximum background level and our threshold and were not assigned to a subtype (false negatives). We note that the individual fluorescence signal intensities

vary in the form of a Poisson distribution due to differences in the position of the particles within the waveguide cross section.<sup>55</sup> This produces variations in the excitation and collection efficiencies in accordance with the optical mode profiles in the solid-core excitation and liquid-core collection waveguide. Here, (15±2)% of all particles have peak intensities below the maximum background signal and are not detected, representing a false negative baseline. The virus concentrations were measured from the count rates and flow speed (H1N1: 3.2x10<sup>6</sup>/ml; H2N2: 2.0x10<sup>6</sup>/ml; H3N2: 8.9x10<sup>5</sup>/ml). This shows that we were able to carry out high-fidelity multiplex detection of single viruses at clinically relevant concentrations.<sup>113–115</sup> For the MMI used here (illuminated volume: 5µm x 12µm x 100µm = 6pL), limitations due to simultaneous presence of multiple targets in the excitation volume do not arise until concentrations exceed 1.67x10<sup>8</sup>/mL – well above the viral titer range of influenza and other diseases.<sup>113–116</sup>

### **6.2.6 Multiplexed single virus detection with combinatorial labeling**

3x multiplexing is already sufficient for some applications, but extended differentiation is often desired. Simply increasing the number of wavelengths quickly reaches a limit due to limited choice of fluorescent dyes and laser sources as well as overlapping emission spectra. A combinatorial approach, however, which assigns multiple labels to a target can be scaled up favorably. Here, we demonstrate combinatorial multiplexing using MMI excitation using two colors for identifying three virus types. To this end, the H2N2 virus was co-labeled with both blue and dark red dye as shown in Fig. 6.9a, while H1N1 (blue) and H3N2 (dark red) remained

singly labeled. Again, we analyzed a mixture of all three viruses, now simultaneously excited by two sources. We implemented a different signal processing algorithm to demultiplex the virus types. Fig. 6.8b shows the fluorescence signal  $F(t)$  from a single H3N2 virus.  $F(t)$  is shifted and multiplied with itself  $N-1$  times to create a processed signal

$$S(t, \Delta t) = \prod_{i=0}^{N-1} F(t - i \cdot \Delta t) \quad (6.8)$$

$S(t, \Delta t)$  will take on a large value only at the correct  $\Delta t$  value(s) for a given signal, allowing us to define two color channels when eqn. (1) is applied with  $\Delta t_B$  and  $\Delta t_{DR}$ , respectively. This shift-multiply algorithm also increases the signal-to-noise ratio of the particle detection.<sup>109</sup> The SNR improvement is evident in Fig. 6.8c which shows  $S(t, \Delta t)$  for the mixed signal of Fig. 6.8b at  $\Delta t_{DR}=0.63\text{ms}$  (dark red).

Fig. 6.9a shows the labeling and individual fluorescence signals from all three virus types under two-color excitation. Most notably, the signal for the double-labeled H2N2 changes and clearly shows a superposition of the 9-spot (488 nm) and 6-spot

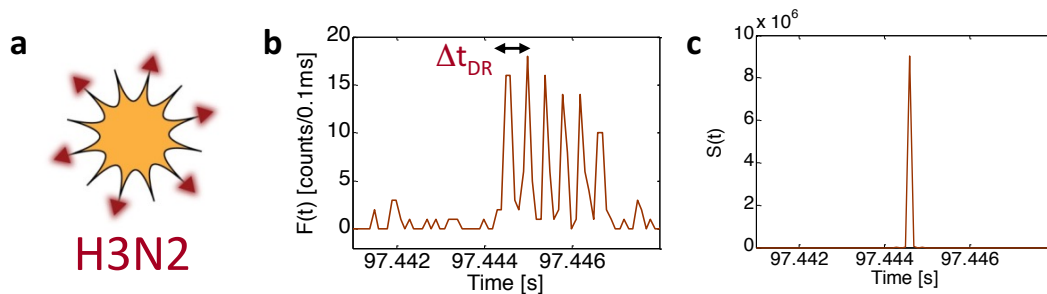


**Fig. 6.8 | Analysis of single virus fluorescence signals.** **a**, Sketch of fluorescently labeled H3N2 virus, responding to excitation at 745 nm; **b**, fluorescence signal from single H3N2 virus showing six peaks with average spacing  $\Delta t_{DR}$ ; **c**, corresponding processed signal using shift-multiply algorithm with  $\Delta t_{DR}$  showing dramatically increased SNR.



(745 nm) patterns. For further analysis, we first identified the average shift times  $\Delta t_B$  and  $\Delta t_{DR}$  for blue and dark red excitation using single color excitation. Then, each event of the mixed assay was analyzed using eqn. (1) at those  $\Delta t$  values. Fig. 4b shows that a blue-labeled H1N1 virus only shows appreciable  $S(t)$  at  $\Delta t_B$ . Likewise, an H3N2 virus shows strong signal in the  $\Delta t_{DR}$  channel. The double-labeled virus, however, shows large  $S(t)$  in both channels, demonstrating that we can successfully identify three different viruses with two colors.

Considering the multiplexing capability of such a system requires the use of

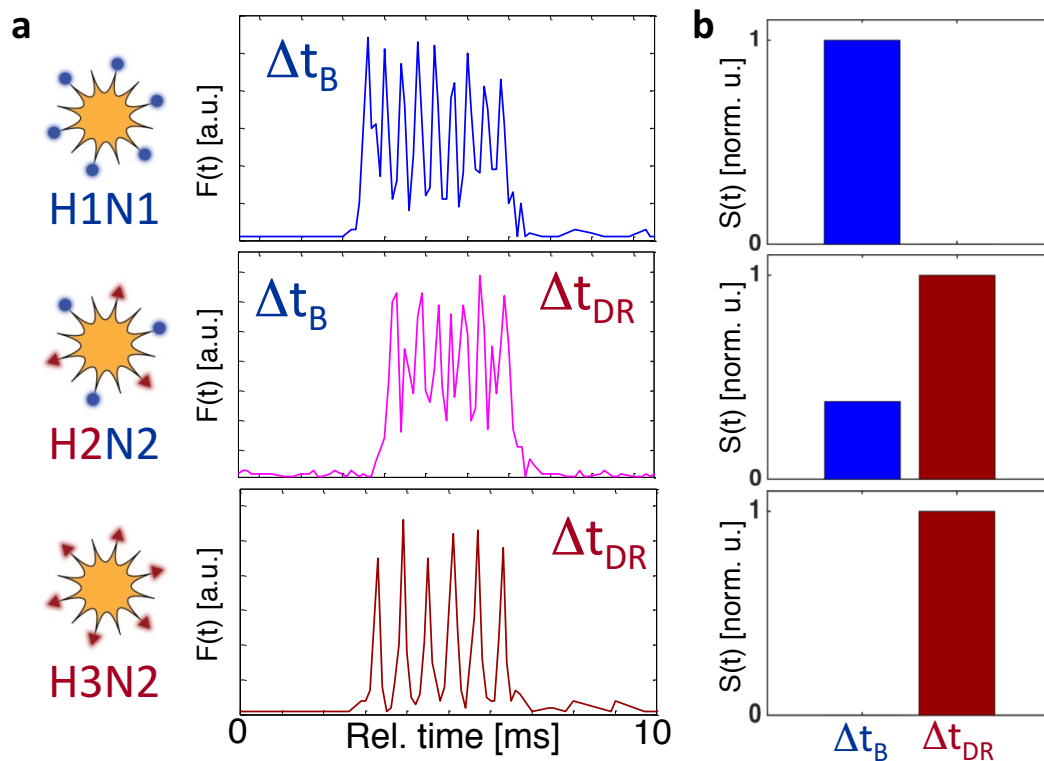


**Fig. 6.9 | Two-color combinatorial detection of single viruses.** **a**, schematic view of labeling scheme for the three influenza types and their resulting single-virus fluorescence signals; the H2N2 virus shows a mixture of six and nine peaks upon blue and dark red excitation; **b**, bar histograms of signals after shift-multiply processing at  $\Delta t_B$  and  $\Delta t_{DR}$ . Singly labeled viruses appear in only one  $\Delta t$  channel, while the double labeled virus creates signal in both color channels.

combinatorics. Specifically, one is faced with the problem of combinations with repetitions. For such a problem, the number of possibilities is described by the following equation:

$$\binom{r + p - 1}{r} = \frac{(r + p - 1)!}{r! (p - 1)!} \quad (6.9)$$

with  $p$  being the number of colors and  $r$  being number of fluorescent label sites.

However, for intensity independent combinatorics, (e.g. assuming a labeling of blue-blue-red being equivalent to blue-red-red) we can reach a maximum of  $2^p - 1$  multiplexing (with  $p$  again being the number of colors. For example, with three colors, we can distinguish seven targets. With four colors, 15x spectral multiplexing is possible, sufficient for the vast majority of diagnostic panels. The readout fidelity depends on the ratio of spot spacing (determined by the MMI width  $W_E$ ) and the individual spot width (determined by the width of the input single-mode waveguide  $W_i$ ) and can be further improved by increasing  $W_E/W_i$ . Moreover, multiple fluidic channels addressed with MMIs of different dimensions can further increase the multiplexing power. The multi-color labeling strategy can readily be extended to fluorescently labeled nucleic acids and antibodies specific to target surface proteins. The planar optical architecture also allows for further integration of a dedicated microfluidic layer for upstream sample processing and distribution (see Chapters 4 and 5) as well as techniques for focusing the particles in the center of the fluidic channel for optimized detection efficiency.<sup>27,55</sup>

### 6.2.7 WDM Biosensing Analysis Considerations

In addition to the high quality signals, a careful consideration of the signal processing method must be ensured for proper implementation of wavelength division multiplexing. As such, in this section I will present a rigorous representation and reasoning behind each of the previously mentioned analysis methods.

First, it is important to understand the reasons for using single peak autocorrelation, rather than autocorrelation of an entire data trace. The obvious reason is that in the case of a particle mixture, autocorrelation of different number of spots (i.e. different colored particles) will result in an ambiguous autocorrelation. However, this is not the only reason. Even in the case of single color/spot number detection, the

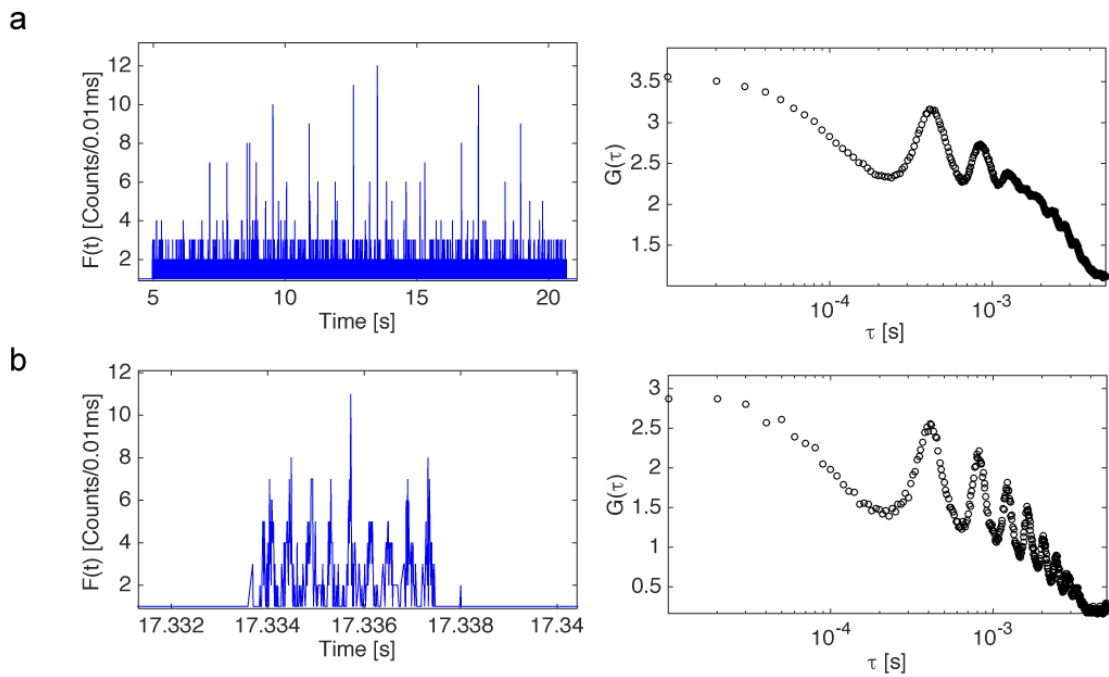


**Fig. 6.10 | Comparison of single and multiple peak autocorrelations. a,** The 20 second trace seen on the left yields the autocorrelation seen on the right. **b,** Single peak spanning  $\sim 5$  ms with 5 ms of adjacent background yields the much more pronounced autocorrelation seen on the right. Note that the binning size (0.01 ms) is presented here to demonstrate the noisiness of the signal before autocorrelation.

autocorrelation can become indistinct when multiple peaks are considered. Take for example Fig. 6.1, which considers single and multiple particle autocorrelations. It is clear that for the large number of particles in Fig. 6.1a, the autocorrelation yields a distinct secondary peak at  $\Delta t_B$  and its second integer multiple. However, the secondary autocorrelation peaks 3-7 are seen distinctly only in the single peak autocorrelation. The main reason for the smoothness of Fig. 6.1a (right) at higher time lags is that each of the particles experiences a slightly different velocity based on Poiseuille flow in laminar flow channels.<sup>71,81</sup> As such, the position of the  $\Delta t_B$  and its multiples are ill defined for large number of particles, leading to a distribution of values.

Velocity distributions in MMI based particle measurements can also be observed through shift-multiply analysis. More specifically, by shift multiplying a signal through the entire  $\Delta t$  space, it is possible to define  $\Delta t_{max}$ , or the shift time at which each particle signal gives the maximum  $S(t)$ . The results of such an analysis are shown in Fig. 6.11. In this proof of concept, a data trace was taken with single laser excitation during three different times. As such, each region of the data trace should have only a single color of particles (as indicated by the shaded boxes in Fig. 6.11a). The entire trace was then subjected to the shift-multiply algorithm with  $\Delta t$  ranging from 0.05-0.5 ms. The maximum  $S(\Delta t)$  value was then selected for each peak and the results were binned in Fig. 6.11c. A few things are clear in this analysis. First, peaks with  $\Delta t_B = 0.28$  are only detected within the blue region (likewise for  $\Delta t_R = 0.37$  ms and  $\Delta t_{DR} = 0.42$  ms), justifying particle identification through shift-multiply

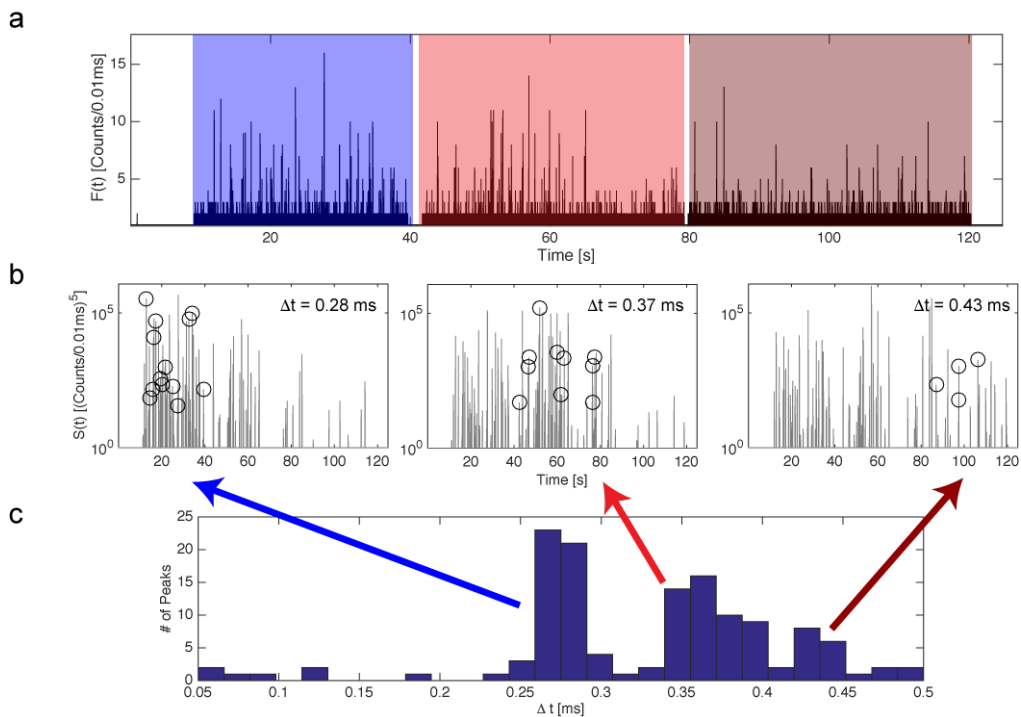


**Fig. 6.11 | Shift multiply peak finding analysis.** **a**, Data trace displaying three different regions of signal, color coded for different laser excitations, i.e. 488, 633, and 745 nm left to right. **b**, Output of the shift multiply algorithm (Eq. 6.8) with the signal from **a** being the  $F(t)$  input,  $N = 6$ , and  $\Delta t$  equaling the noted values. Note that a circle on a peak indicates that the signal for that particle reached its  $S(t)$  maximum for the noted  $\Delta t$ . **c**, Histogram of peak  $S(\Delta t)$  maxima yielding three distinct distributions of  $\Delta t$  values representing the peaks from the portions of the different color traces.

analysis. Secondly, not all of the peaks are highlighted in each  $S(t)$  trace indicating that  $S(\Delta t)$  for many of the particles did not maximize at the given  $\Delta t$ . This is exemplified in the Fig. 6.11c histogram as broadening of the three  $\Delta t$  distributions. Again it is noted that this is caused by varying particle velocities.

A more rigorous explanation of the shift-multiply particle selection algorithm can be described in context of single particle identification. Take for example the three particle traces in Fig. 6.12a. By eye it is very easy to identify the distinctive 9 and 6 spot patterns for the blue and dark-red viruses. The middle particle (in pink) is

more ambiguous, yet seems to be a combination of blue and dark red. It is possibly to

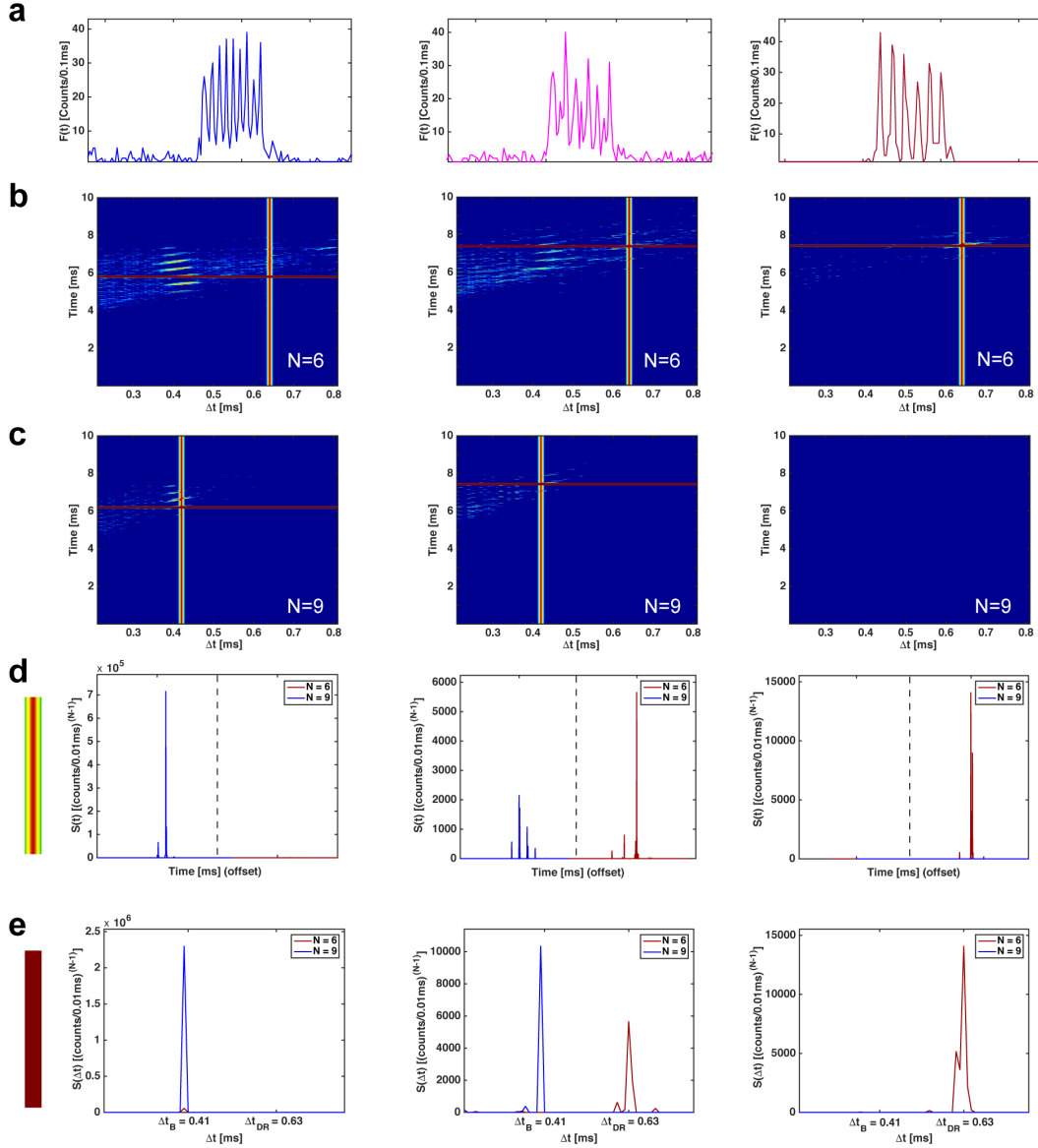


**Fig. 6.12 | Single particle shift-multiply identification.** **a**, 10 ms signal traces for a blue, blue-dark red, and dark red particle, from left to right. **b**,  $S(t)$  matrixes for each respective particle at  $N=6$ . **c**,  $S(t)$  matrixes for each respective particle at  $N=9$ . Each data matrix is internally normalized and logarithmically plotted with a heat map color system (where colder colors are low values and warmer colors are higher values). **d**, Single slice of each  $S(t)$  matrix along a  $\Delta t_B = 0.41$  ms and  $\Delta t_{DR} = 0.63$  ms for  $N=9$  and  $N=6$ , respectively. Note that these traces are indicated in **b** and **c** as rainbow colored (vertical) cross-sections. Also, the  $N=9$   $S(t)$  trace occupies the left portion of the graph while the  $N=6$   $S(t)$  is offset to the right side of the graph. **e**, Single slice of each  $S(t)$  matrix along a given time value that contains the maximum  $S(t)$ . These traces are indicated in **b** and **c** as maroon (horizontal) cross-sections.

programmatically define the identities of these particles through shift-multiply analysis. In Fig. 6.12b and Fig. 6.12c, each 10 ms data trace is now shift multiplied into a data matrix containing columns of  $S(t)$ , for different  $\Delta t$  values. Although it is possible to see color throughout the many of the graphs, it should be explicitly noted that these data matrixes have their color dimension plotted on a logarithmic heat map, because on a linear scale a single point typically dominates each matrix.

The matrixes in Fig. 6.12b and Fig. 6.12c provide a wealth of information that can be used to identify the particle color. As seen in Fig. 6.12d, in the case where  $\Delta t$ 's have been defined for each color particle,  $S(t)$  traces provide excellent information on the identification of the particle. It is clear from these traces that each particle identity can be correctly defined by simply creating a single slice of each  $S(t, \Delta t)$  matrix (namely the  $\Delta t_B$  and  $\Delta t_{DR}$  at  $N=9$  and  $N=6$ , respectively) and comparing the maximum of each trace. Note, for example, while there is some small amplitude in the  $S(t)$  trace at  $\Delta t_{DR}$  for the  $N=6$  matrix, there is no visible amplitude in Fig. 6.12d (left) as the maxima of the  $N=9$  slice is so much larger. The converse of this is displayed even more starkly for the dark red red particle on the right of Fig. 6.12. Note that the  $N=9$   $S(t, \Delta t)$  matrix is null, showing the power of shift multiplying a signal nine times that only contains six peaks. In the case of the blue-dark red particle, there is appreciable amplitude for both  $S(t)$  slices.

The need for creating an  $S(t)$  matrix is only borne out when  $\Delta t_B$  and  $\Delta t_{DR}$  are unknown. In this case, seen in Fig. 6.12e, the maximum value of each  $S(t, \Delta t)$  matrix is used to define the time slice to be considered. Once determined, this slice can then

be plotted for all considered  $\Delta t$  values. In the case of the blue particle (Fig. 6.12 left), the maximum  $S(t)$  value is actually achieved at a  $\Delta t$  value slightly smaller than  $\Delta t_B$ . Note, this once again exemplifies the outcome of different particle velocities. It is clear that this more general analysis can also be useful for correctly identifying particles, with similar outcomes of Fig. 6.12d. However, it is the combination this  $S(t, \Delta t)$  matrix method and  $\Delta t$  binning seen in Fig. 6.11 that yields the most sensitive discriminations such as those seen in Fig. 6.9. This analysis was conducted using a custom Matlab program that is described in Appendix A.

MMI-based wavelength division multiplexing is clearly ideal for on-chip bioanalysis, providing the missing element to turn an optofluidic chip with single molecule detection sensitivity into the basis for a powerful and versatile diagnostic instrument for a variety of bioparticles and biomarkers. Beyond that, the ability to encode different wavelengths into unique spatial light patterns opens the door to new avenues for integrated photonic and optofluidic devices, for example spectrally reconfigurable optical particle traps or distribution of different colors to different areas on a chip. Furthermore, while the work in the above chapter focused on the use of silicon fabricated MMIs with static architectures, it is possible to create flexible MMIs that have tunable optical properties for dynamic applications. Such an MMI device with widely adjustable properties will be the a main focus in the following chapter.



## **7 Flexible PDMS optofluidic waveguide platform with multi-dimensional reconfigurability and functionality**

The integration of photonic functions with non-solid media has made tremendous progress in recent years.<sup>74,75,117</sup> Such optofluidic integration is particularly attractive for creating reconfigurable optical devices and for taking lab-on-chip based approaches for biological and chemical analysis to new levels. Photonic elements that can be altered by introducing different fluids or changing device dimensions with applied pressure include lasers<sup>118–121</sup>, spectral filters<sup>52,76,122,123</sup>, lenses<sup>124</sup>, interferometers<sup>125,126</sup>, and optical switches<sup>20,127–129</sup>. Lab-on-chip style optofluidic analysis, on the other hand, has led to the development of waveguide-based biomolecular analysis down to the observation of single nucleic acids and viruses (see Chapters 4-6 and references).<sup>130,131</sup> Up to now, the most sensitive devices have predominantly taken a hybrid approach (Chapter 4 and reference<sup>132</sup>) in which microfluidic sample handling is done in PDMS chips while ultrasensitive optical detection is implemented in semiconductor based solid-state waveguides.

Here, we introduce a new optofluidic platform that provides optofluidic particle detection capability, advanced fluidic sample handling, and multi-modal photonic reconfiguration in a single chip. On-chip photonic devices are based on a combination of solid-core and liquid-core PDMS waveguides. The waveguides can be built with established multilayer soft lithography techniques and seamlessly connect with each other to form a wide variety of photonic layouts. Moreover, the layer structure is compatible with incorporation of fluidic microvalves to enable both optical tuning

and fluid control in a single device. Unlike previous implementations of PDMS waveguides, our cores are only  $\sim 7 \times 8 \mu\text{m}$  in cross section (unless otherwise noted), providing excellent mode matching to single-mode fiber, thus allowing for advanced photonic devices such as interferometers that rely on careful control over one or a few waveguide modes. Much of the discussion in this chapter follows closely from our previously published work.<sup>6</sup>

### **7.1 Fabrication of multilayer flexible optofluidic platforms**

The optofluidic chips were fabricated using standard SU-8 lithography. Seen in Fig. 7.1, the workflow involves parallel fabrication of waveguide valve and control layers.<sup>61,62</sup> The solid-core optical waveguides are fabricated by spinning 5:1 (base:curing agent) PDMS onto a  $7 \mu\text{m}$  tall silanized SU-8 master at 6000 RPM for 30 minutes. Note that this non-standard polymerization mixture creates a higher refractive index ( $n_{c-488} \approx 1.423$ ) than the manufacturer specified ratio of 10:1 ( $n_{c1-488} \approx 1.420$ ).<sup>133</sup> Furthermore, it is noted that PDMS creates an excellent waveguide material for the visible wavelength regime.<sup>134</sup> A 2-hour cure at  $60^\circ\text{C}$  ensures full polymerization of the waveguide core material. A subsequent 2 minute, 2000 RPM spin of 10:1 PDMS then creates a continuous membrane across the waveguide valve layer. In parallel, the control layer is fabricated by pouring and curing 10:1 PDMS on a silanized SU-8 master—with  $80 \mu\text{m}$  tall features. Ports are then punched into the control layer for pneumatic access, after which the bottom of the control layer and top of the waveguide/fluidic layer are activated via oxygen plasma, aligned on a custom alignment stage, and brought into contact, whereupon the bond is enhanced via a 2-

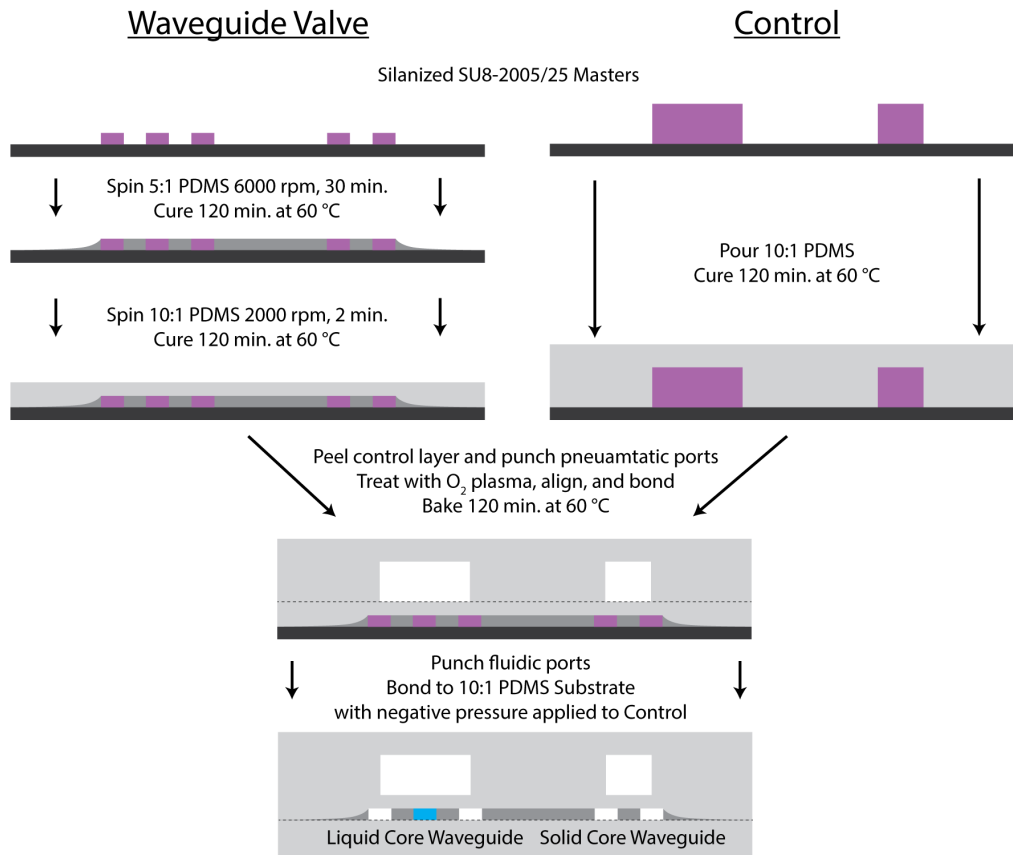


**Fig. 7.1 | Fabrication of PDMS Waveguide Platforms.** A stepwise fabrication workflow is presented, with high index PDMS colored dark grey, low index PDMS in light gray, SU8 in purple, and silicon in black. Dashed lines indicate bonding surfaces.

hour thermal activation. Next, ports are punched into the stack to allow fluidic access, followed by another bonding process. This step occurs with negative pressure applied to the pneumatic ports to prevent the bonding of waveguide valve layer to the substrate layer. In the case of single layer devices (i.e. tunable optofluidic MMI), only the left hand side of Fig. 7.1 is followed, replacing the 10:1 PDMS spin step with a drop casting of 10:1 PDMS. Waveguide chips were diced using commercial razor blades to ensure good facet quality for low optical coupling losses.<sup>135</sup>

## 7.2 Loss in PDMS Waveguides

The optical loss coefficient is arguably one of the most important parameters for any fabricated waveguide structure. To understand the loss of the waveguides in this work, one must first consider the structure of the waveguides themselves. For example, solid-core waveguides here are composed of a high refractive index material surrounded on all sides by lower index material. As such, the loss of the index guiding solid-core structures is limited to structural causes such as bends and surface roughness. However, in the case of the liquid core waveguides, the waveguides are inherently lossy (given that the core refractive index is less than that of the cladding, i.e.  $n_c < n_{cl}$ ). Note: if  $n_c > n_{cl}$  then the liquid core also behaves as an index guided waveguide. For lossy propagation, the liquid-core waveguide is composed quite differently in horizontal and vertical directions. In the horizontal direction, the liquid core waveguide is immediately clad by a higher index PDMS, however is ultimately clad by air, resulting in a pseudo index guiding structure (note that for such thin walled capillaries Fabry-Perot resonances are possible for very homogeneously defined structures,<sup>136</sup> however this effect was not observed and is not considered in this analysis).

On the other hand, in the vertical direction the liquid-core waveguide behaves as a lossy capillary waveguide due to the thickness of bounding PDMS walls (greater than 100  $\mu\text{m}$ , Fig. 7.1 not to scale). As such, it is possible to consider the capillary loss three different ways. The first (and simplest) approach, dubbed here “Fresnel loss”, considers the amount of light lost per interface reflection during waveguide

propagation. That is, as a ray propagates along the core of the waveguide, it will hit a PDMS wall and be reflected based on boundary considerations (Fresnel reflection) and will propagate through the core for another distance before repeating the process on the opposite sidewall. The number of reflections per distance propagation is based on the mode angle of the waveguide, defined by Eq. 2.1 and 2.2. In essence, the loss here is defined by the amount of light refracted out of the core, per reflection, per unit distance. Considered mathematically, the output power ( $P_o$ ) of a leaky waveguide is

$$P_o = P_i e^{-\alpha z}. \quad (7.1)$$

determined by the input power ( $P_i$ ) and the loss ( $\alpha$ ) of the waveguide over some propagation distance ( $z$ ). The derivative of this equation simplifies to the following

$$\begin{aligned} \frac{dP_o}{dz} &= -P_i \alpha e^{-\alpha z} \\ \frac{dP_o}{dz} &= -\alpha P_o \\ \alpha &= \frac{1 - R}{dz} \end{aligned} \quad (7.2)$$

where  $dP = -P_o(1-R)$  (or the power loss at a single reflection). If we consider that the propagation distance ( $dz$ ) is geometrically related to the thickness of the waveguide,  $d$ , and angle of propagation,  $\theta_i$ , then we find

$$\alpha_F = \frac{1 - R}{d \tan(\theta_i)}. \quad (7.3)$$

Finally substituting the findings from Eq. 2.2 (where  $m$  is simply the mode number),

$$\alpha = \frac{1 - R}{d \tan\left(\cos^{-1}\left(\frac{(m+1)\lambda}{2n_c d}\right)\right)}. \quad (7.4)$$

we find the first approximation (Fresnel approximation) for the loss in leaky waveguides. Note that implicit difference for TE and TM mode loss are built into the Fresnel reflectivity.

A more rigorous modal approach was conducted by Archambault et al. in 1993.<sup>137</sup> The lengthy derivation described therein is beyond the scope of this section and should be learned from the referred work. In short, the approach used in the referenced paper contains similar wave vector considerations for mode angle and thickness calculations demonstrated in Section 2.3.1, however when considering the loss, Archambault et al. use a perturbation approach based on the modal eigenvalue equation. For simplicity, the capillary loss equation found in the paper is repeated here with notation more consistent with this thesis:

$$\alpha_{A-TE} \approx \frac{\lambda^2 (m+1)^2}{n_1 \sqrt{n_{cl}^2 - n_c^2}} \cdot \frac{1}{d^3} \quad (7.5)$$

$$\alpha_{A-TM} \approx \frac{n_c^2}{n_{cl}^2} \cdot \alpha_{TE}$$

where an approximation has been made when the mode angle is very large (minimizing the transverse propagation wave vector) and/or the contrast between the core and cladding refractive indexes is proportionally large –mathematically stated  $k_{cl}^2 - k_c^2 \gg k_{TC}^2$ ).

Lastly, the loss can be approximated using a matrix formalism for propagation in layered media, described by Pochi Yeh.<sup>138</sup> Essentially, this formalism is a more rigorous approach of the Fresnel loss, that is applicable to layered media. For a detailed explanation of the derivation, see Appendix B. Using matrices to connect

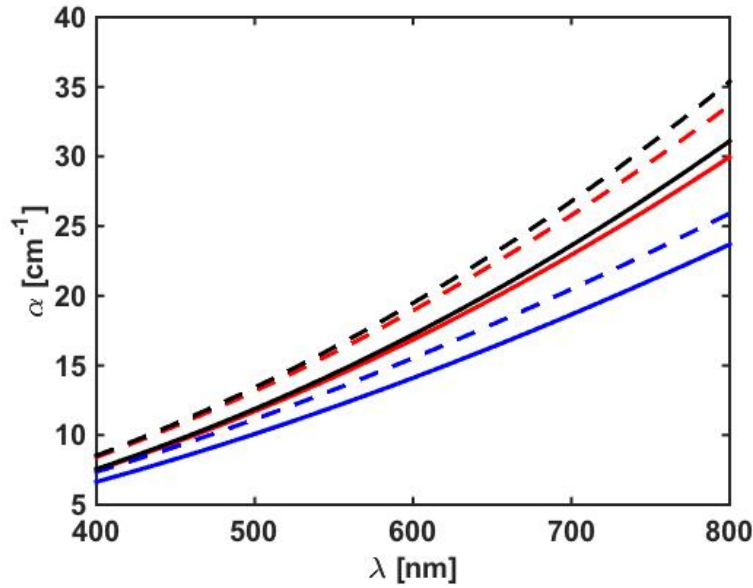


**Fig. 7.2 | Simulated visible light loss of a PDMS capillary waveguide.** Parameters as follows:  $n_c = 1.33$ ,  $n_d = 1.41$ ,  $d = 7 \mu\text{m}$ , and  $m = 0$  where applicable.  $\alpha_F$  (Fresnel) is plotted in blue,  $\alpha_A$  (Archambault) is plotted in red, and  $\alpha_{HM}$  (Haus-Miller) is plotted black. TE loss is plotted with solid lines and TM loss is plotted with dashed lines.

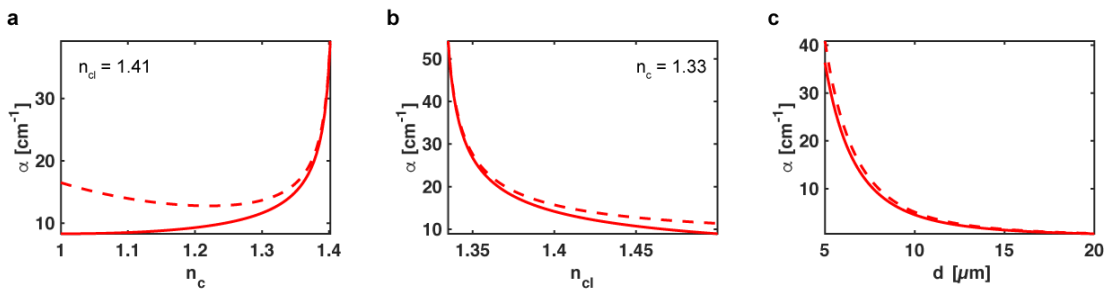
electric fields across dielectric interfaces, it is possible to come out with an “M” matrix that encompasses all reflection and transmission coefficients during propagation through a layered media. The matrix elements themselves can then be used to determine the overall reflection and subsequent waveguide loss. In order to find the loss, it is possible to employ a formula developed by Haus and Miller derived from the comparison of a steady state and initial value problem for a Fabry-Perot resonator,<sup>139</sup>

$$\alpha_{HM} = \frac{1 - R_1 R_2}{2d \tan(\theta_i) \sqrt{R_1 R_2}}$$

$$\alpha_{HM} = \frac{1 - R^2}{2dt \tan(\theta_i) R} \quad (7.6)$$

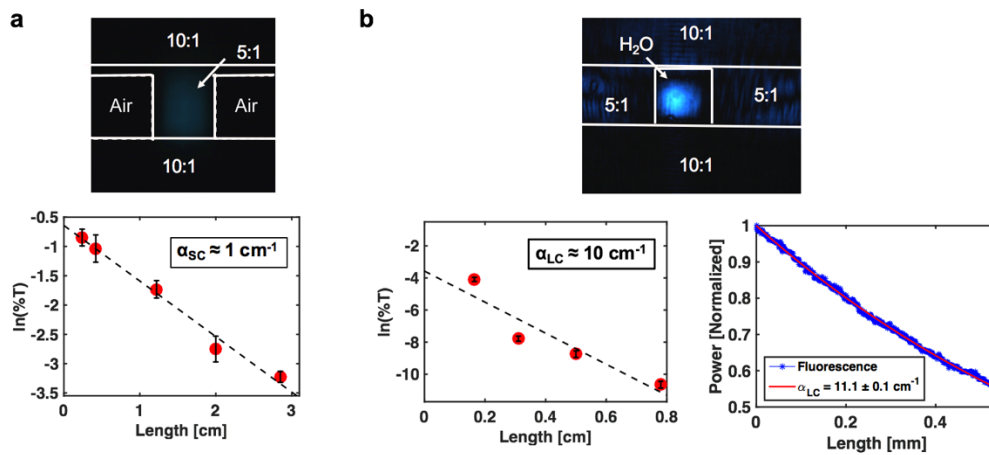
with the simplification (equality of the different slab waveguide boundaries;  $R_1 = R_2 = R$ ) arising due to the symmetry of the PDMS waveguide system. It is possible to use the reflection coefficient obtained from the Yeh matrix formalism in this equation to yield an approximation of the leaky waveguide loss. Plotting the Haus and Miller, Archambault, and Fresnel loss approximations, we find them all to be in good qualitative agreement – as seen in Fig. 7.2. Note that the Fresnel loss is slightly offset as the approximation deviates when the reflection coefficient(s) are not approximately equal to 1.<sup>140</sup> Considering the similarity of the Archambault and Haus-Miller approximations, in conjunction with the basic parameter set used in the Archambault approximation, further graphs will be represented with this approximation only for clarity.

Fig. 7.3 shows general trends in capillary waveguide loss. In summary, it is clear that as the core and cladding indexes approach equality, the loss approaches infinity (see Fig. 7.3a and b). When generally considered, this result seems reasonable as there will be no waveguide when the indexes match one another. Furthermore, an



**Fig. 7.3 | Capillary waveguide loss trends with varying fabrication parameters.** Parameters as follows unless specifically varied:  $n_c = 1.33$ ,  $n_{cl} = 1.41$ ,  $d = 7 \mu\text{m}$ ,  $\lambda = 532 \text{ nm}$ , and  $m = 0$ . TE loss is plotted with solid lines and TM loss is plotted with dashed lines.





**Fig. 7.4 | Experimental loss of PDMS waveguides. a**, Solid-core waveguide mode image (top) and cutback loss (bottom). **b**, Liquid-core waveguide mode image (top), cutback loss (bottom left) and confirmed loss measurement using top down fluorescence monitoring along the liquid-core channel. All measurements were conducted at 488 nm and error bars represent the standard deviation of three or more measurements.

important result that is immediately evident in all the loss formulas as well as Fig.

7.3c is that the waveguide loss and core dimension,  $d$ , are inversely related (cubically in the case of the Archambault approximation). One conclusion is certain from both

Fig. 7.2 and Fig. 7.3, the loss of small hollow PDMS waveguides is quite high and core lengths should be kept short in the case of leaky operation.

Fabricated devices were subjected to loss analysis for comparison to theoretical approximations. As seen in Fig. 7.4, the solid-core waveguide has a loss of  $1 \text{ cm}^{-1}$  that is revealed during cutback analysis (i.e. total transmission is monitored as the waveguide is cut back to different lengths). While this loss is very large in comparison to fiber waveguide losses (on the order of  $\text{km}^{-1}$ ) it is decent for chip based waveguides that are fabricated with a Mylar mask (as low resolution masks yield rough sidewalls and large scattering losses). On the other hand, the liquid-core capillary waveguide loss is an order of magnitude higher, resulting from the leaky

operation, and is in decent agreement with theoretical predictions ( $d = 7 \mu\text{m}$ ,  $\lambda = 488 \text{ nm}$ ,  $n_c = 1.33$  yields  $\alpha \approx 11 \text{ cm}^{-1}$ ). The larger experimental loss is likely due to non-fundamental mode coupling in such large waveguides.

### 7.3 Comparison of PDMS and ARROW Detection Chips

In addition to reasonable waveguide losses, optofluidic detection platforms require a well defined excitation volume. Top down fluorescence imaging in Fig. 7.5 reveals that PDMS optofluidic platforms confine light to well defined excitation regions, similar to well studied ARROW chips. Specifically, consider a solid-core waveguide (excited by laser light) intersecting a liquid-core channel filled with fluorescent dye (see Fig. 7.6a for a diagram). The emission of the fluorescent dye,

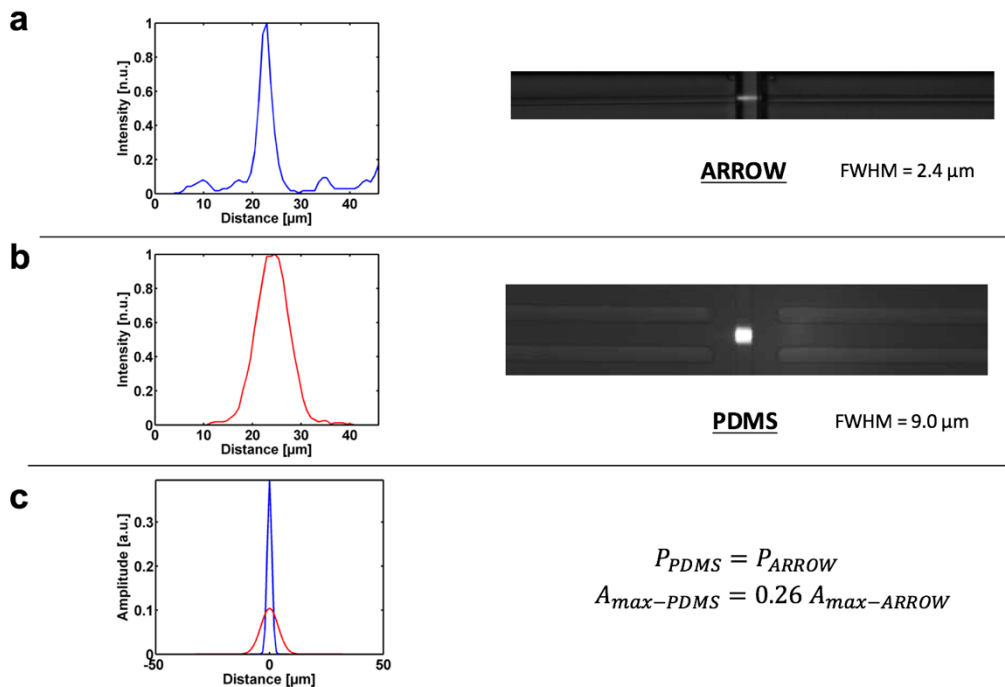


**Fig. 7.5 | Excitation profiles of ARROW and PDMS waveguide chips. a,** Top down ARROW excitation profile (right) with a respective cross section (left) of the fluorescence profile. **b,** Top down PDMS excitation profile (right) with a respective cross section (left) of the fluorescence profile. Note that the measurements were taken at 488 nm excitation with  $2 \mu\text{M}$  Dylight 488.

captured from the top by a custom compound microscope, reveals the excitation pattern created by the intersecting waveguide. In the case of the ARROW, a small rib-waveguide yields an excitation spot with a small full width half maximum (FWHM) of 2.4  $\mu\text{m}$ , whereas a rectangular PDMS excitation waveguide yields a spot with 9.0  $\mu\text{m}$  FWHM (note again that the PDMS dimensions in this case were limited to a minimum feature size of 10  $\mu\text{m}$  by Mylar mask printing specifications). When the total power of both excitation profiles is normalized, Fig. 7.5c clearly shows that an ARROW waveguide's excitation profile will have a peak amplitude nearly four times greater than that of a PDMS waveguide. This is important for particle detection measurements as fluorescence emission generally scales linearly with excitation intensity (excluding very high intensities).<sup>141–143</sup>

Ultimately, when comparing fluorescence sensors, the bottom line is signal to noise (S/N) and signal to background (S/B) ratios in conjunction with high accuracy. Demonstrated in Fig. 7.6b, the background of a PDMS detection chip (when filled with deionized water and excited with 488 nm laser light, see Fig. 7.6a) is higher than that of an as-grown or annealed ARROW chip. However, it is clear from Fig. 7.6c that while an as-grown ARROW is unable to detect 22.5 nM Cy5 dye, a PDMS waveguide chip detects approximately 7% of the signal that an annealed ARROW does. For bulk fluorescent measurements, flow velocity is important as stationary dyes tend to photobleach quickly under high intensity excitation. Accordingly, part of the signal discrepancy in Fig. 7.6c between the ARROW and PDMS chips can be attributed to the much lower flow velocity in the PDMS chip (190  $\mu\text{m/s}$ ) versus the

high flow velocity of the ARROW chips (3 mm/s). Finally, when detecting 100 nm nanospheres in Fig. 7.6d, it is clear that a few very small signals (average signal 8 counts/ms) are achieved on an as-grown ARROW chip, some relatively low signals (average signal 16 counts/ms) are detected on a PDMS chip, and many strong signals (average signal 74 counts/ms) are detected on an annealed ARROW chip. One interesting figure of merit is the particle detection efficiency. Specifically, the product of the liquid-core waveguide cross section dimensions, the flow velocity, experiment time, and particle concentration yields an expected number of particles. For an as-grown ARROW, the efficiency is at 5%, the PDMS chip is at 61%, and the annealed ARROW is at 93%.

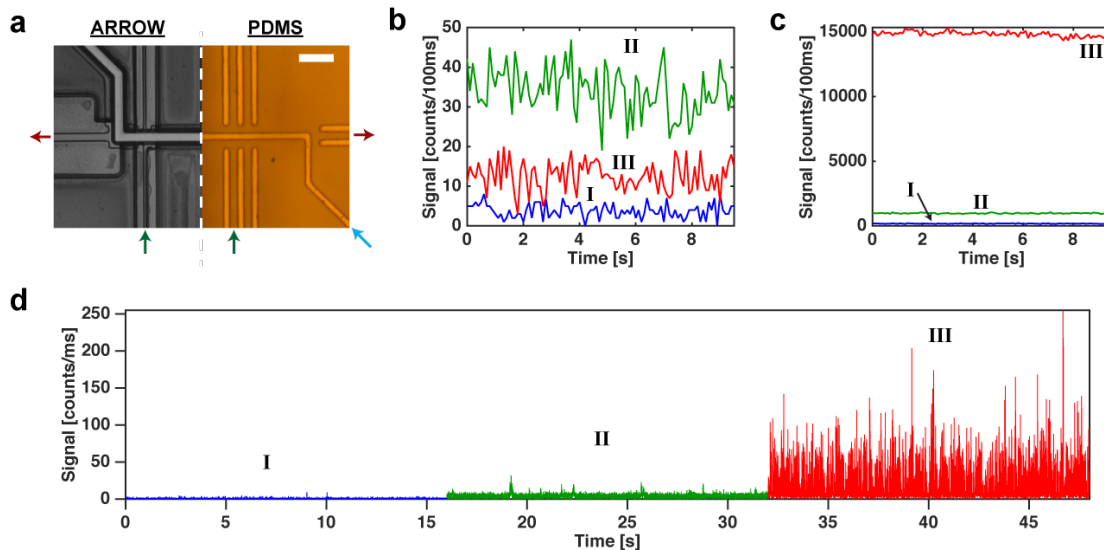


**Fig. 7.6 | Comparison of ARROW and PDMS detection chip performance.** **a**, Top down images of ARROW (left) and PDMS (right) detection chips. Dark green arrows indicate laser excitation input, dark red arrows indicate signal collection output, and the light blue arrow indicates fluid flow. **b**, Deionized water background comparison of as-grown ARROW, PDMS, and annealed ARROW chips. **c**, Detection of 22.5 nM Cy5 fluorescent dye. **d**, Detection of  $d = 100$  nm yellow-green (505/515 nm – ex/em) Fluospheres<sup>®</sup>. In plots **b-d** as-grown ARROW chip signals are blue (denoted by I), PDMS chip signals are green (denoted by II), and annealed ARROW chip signals are red (denoted by III).

It is clear that the annealed ARROW chip is by far the most sensitive detection platform amongst the three tested in Fig. 7.6. Interestingly, the PDMS detection chip is quite competitive, with performance often within the same order of magnitude as the annealed ARROW chip. These results are in fact promising for PDMS waveguide chips as particle sensors, especially considering the low development time (< 1year), lower excitation intensity (see Fig. 7.5), and poor feature resolution of the Mylar masks used to create the PDMS waveguide chips in these experiments.

#### ***7.4 Direct Integration of an Optofluidic Waveguide Detection Chip with Actively Controlled Microfluidic Valves***

When considering the works in Chapter 5 in conjunction with those in the previous sections to this chapter, it seems that the obvious next step is a direct integration of active (on-chip controllable microvalves) microfluidics with a waveguide detection chip. The chip architecture, presented in Fig. 7.7, is composed of both optical detection and microfluidic processing units. Seen in Fig. 7.7a, microfluidic processing is handled by a two-dimensional array of 7 interconnected microvalves. In conjunction with a 3-valve peristaltic pump, fluid can be transported from any of the three inlets through the optical interrogation region. Pneumatic ports are used to separately actuate all of the microvalves by applying negative and positive pressure to open and close the valves, respectively. The waveguide system comprising the optical detection area is magnified in Fig. 7.7b.

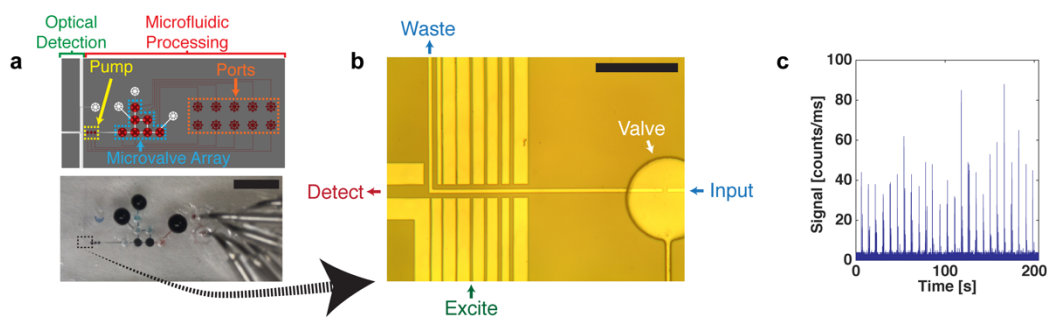


**Fig. 7.7 | Directly integrated waveguide detection chip and actively controlled microvalves. a,** Schematic (top) and actual (bottom) images of a complete chip. Note that the inlets and outlet are represented by white circles in the top image. In the bottom image, all three inlets are filled with food dye, while the outlet is empty. The two middle valves of the microvalve array, as well as the peristaltic pump valves, are open (filled with food dye) for contrast. **b,** Zoom-in of the optical detection region (dashed black box in the bottom of **a**) showing the fluorescence detection geometry directly connected to an actively controlled microvalve. **c,** Particle detection during a 200 second automated, on-chip pumping program (8 second cycling rate), 488 nm excitation. Black scale bars represent 5 mm and 300  $\mu\text{m}$  in **a** and **b**, respectively.

The devices capabilities were tested by conducting a particle distribution and detection experiment. The chip was initially filled with deionized water. One of the inlet reservoirs was then emptied and refilled with a solution containing 1  $\mu\text{m}$  Fluospheres (488 nm excitation) at a concentration of  $3.1 \times 10^6$  particles/mL. The chip was then connected (via syringe needles) to a custom control box (see Section 5.1) for programmed pneumatic actuation and placed into a custom optical setup for fluorescence detection (as illustrated Fig. 7.7a). Microspheres were systematically moved from the inlet, through the optical excitation volume, and to the waste by programmed peristaltic pumping. The data collected in Fig. 7.7c shows fluorescence detection of microspheres. Microspheres are only pumped through the optical excitation region when the valve closest to the detection region is being actuated. In all other cases, the nearest valve is statically closed and the optical detection region is isolated from microfluidic pumping and free of microspheres due to the low

concentration and lack of flow. This results in fluorescence signals (from a series of single spheres per cycle) with the periodicity of the full pumping cycle time (8 seconds).

## **7.5 PDMS Optofluidic Waveguide Chips with Multi-dimensional Reconfigurability**

While the direct integration of PDMS waveguide detection and actively controlled microvalves is a culmination of the works presented in this thesis, it is also possible to use the architectures described in this chapter to design and construct optofluidic devices with built-in reconfigurability. The images presented in Fig. 7.8 are examples of the reconfigurable devices that will be presented through the remainder of this chapter. Briefly, a reconfigurable/tailorable MMI waveguide is shown in Fig. 7.8a and has direct application to the work presented in Section 6.2. A new “lightvalve” architecture, shown in Fig. 7.8b has the ability to control light and liquid flow simultaneously. Finally, the lightvalve trap shown in Fig. 7.8c can act as a physical trap and optical interrogator of single biomolecules. We note that all of these



**Fig. 7.8 | Example PDMS Waveguide Platform Microscope Images.** **a**, Reconfigurable optofluidic MMI, empty, **b**, Lightvalve in its static state, empty, and **c**, Lightvalve trap, both empty (top) and filled and under optical excitation (bottom). The filling fluid for the lightvalve trap is a 3  $\mu\text{M}$  Dylight 488 solution and exhibits fluorescence when excited by 488 nm laser light, injected from the left solid-core waveguide. Note: all white scale bars represent 50  $\mu\text{m}$ .

devices are based on a combination of solid- and liquid-core waveguides, the architecture of which is presented in Fig. 7.9a.

### **7.5.1 Dynamically Reconfigurable PDMS MMI Waveguide**

In order to demonstrate the physical implementation of the PDMS waveguide platform and the ability to tune an optical device using both fluid control and pressure, we first consider a multi-mode interference (MMI) waveguide.<sup>106</sup> As seen in Section 6.2.1, MMIs create length and wavelength dependent spot patterns upon propagation of multiple waveguide modes, and have recently been used to implement spectrally multiplexed detection of single viruses flowing through intersecting fluidic channels.<sup>5</sup> The results presented in Section 6.2 demonstrate that silicon dioxide solid-core MMI waveguides work well, however, fabrication variations in the core refractive often cause irreproducible/poor multi-spot patterns. Therefore, it is desirable to create an MMI that can be tuned dynamically (to insure good quality spot patterns). Our liquid-core optofluidic MMI is schematically shown in Fig. 7.9b and is designed for active tuning by varying both pressure and core fluid. A  $5\mu\text{m}$  wide and  $7\mu\text{m}$  tall solid-core waveguide (dark grey) is used as an input for the wide liquid-core MMI section (width  $w_0$ , length  $L$ ). The MMI is surrounded laterally by  $50\mu\text{m}$  wide air channels, which enable both optical waveguiding and tuning of the MMI width through pneumatic and fluidic pressure, as is illustrated in the right side of Fig. 7.9b. The multimode interference leads to the formation of  $N$  images of the input mode for a given length,  $L$ , and pressure,  $P$ , according to



$$(L, P) = \frac{n_c w(P)^2}{\lambda} \cdot \frac{1}{L} . \quad (7.7)$$

This pattern formation is visualized in Fig. 7.9c (top) for a static MMI ( $P=0$ ;  $w_0=50\mu\text{m}$ ) filled with fluorescent dye in ethylene glycol ( $n_c=1.45$ ) and excited with  $\lambda=532\text{nm}$  laser light. Clean spot patterns are observed over a distance of several millimeters in excellent agreement with eqn. (7.7) and finite difference method simulations shown in Fig. 7.9c (bottom). Liquid-core MMIs with widths between 50 and  $200\mu\text{m}$  ( $25\mu\text{m}$  increment) were fabricated and characterized as presented in Fig. 7.9d. We were able to controllably vary the spot number from 1 to 34 images with device lengths less than 1 cm, all in excellent agreement with theory (lines). Such MMIs, therefore, provide a wide parameter space for multi-spot particle detection with high signal-to-noise ratio.<sup>5,65</sup>

Next, we turn to dynamic tuning of these optofluidic elements. The first mechanism is through replacement of guiding liquid, i.e. the waveguide core refractive index,  $n_c$ . Fig. 7.9e shows MMI tuning using different mixtures of ethylene glycol and water. Specifically, a sampling of waveguides (with various widths,  $w_0$ , and spot numbers,  $N$ ) were used to demonstrate the linear relationship between core refractive index,  $n_c$ , and image length,  $L$ . Tuning of the spot number over a very wide range from 2 to 33 was realized, and excellent agreement between theoretical and experimental results was found.

Thin sidewalls made from a pliable material (PDMS) allow for controlling a microfluidic channel's width through both inward and outward pressure. Previously,

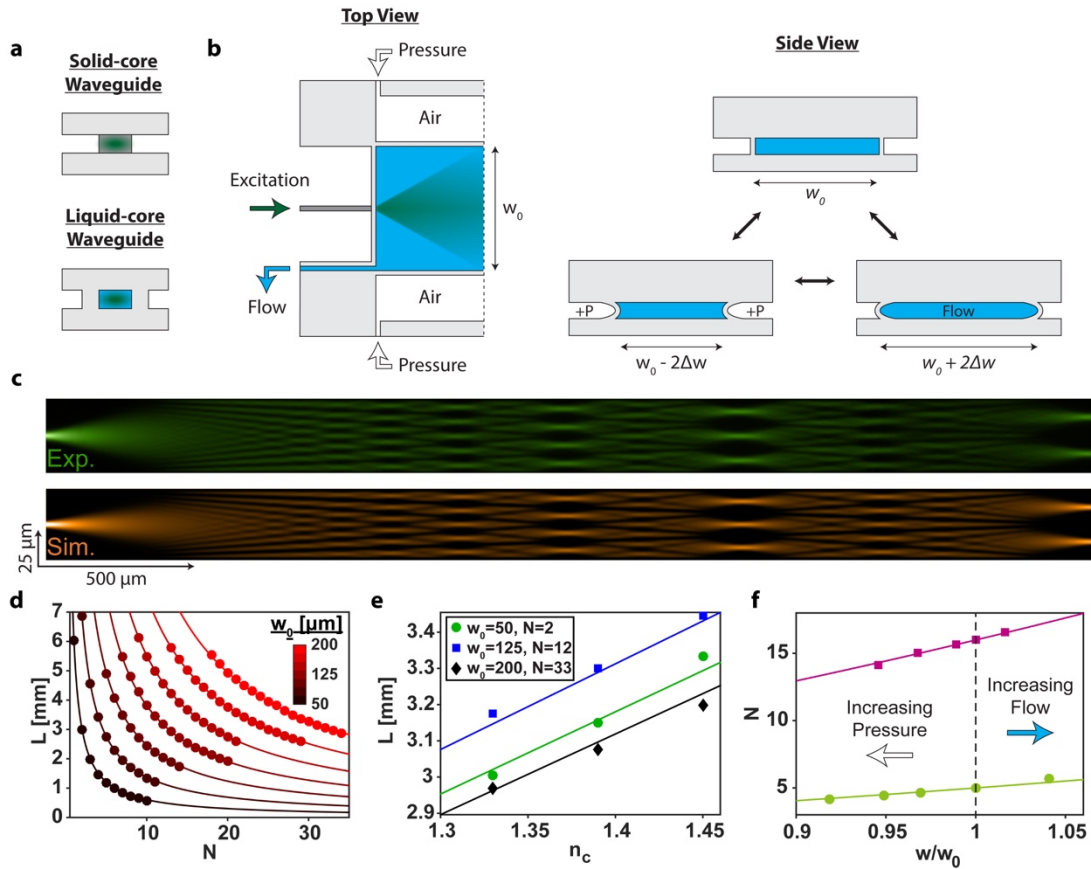


**Fig. 7.9 | Dynamically tunable multispot optofluidic waveguide.** **a**, Schematic side-view of the solid- and liquid-core waveguides. **b**, Liquid-core MMI waveguide system from top (left) and side (right) views. Fiber injected laser light propagates through the excitation solid-core waveguide and into the liquid-core waveguide with a static width of  $w_0$ . Air pressure yields a decrease in liquid-core waveguide width (bottom left, side view) while liquid flow increases waveguide width (bottom right, side view). **c**, Experimental (top, green) and simulated (bottom, orange) multispot waveguide pattern for a  $50\ \mu\text{m}$  wide liquid-core waveguide. **d**, MMI length vs. spot number for 7 fabricated liquid-core waveguide widths,  $50\text{--}200\ \mu\text{m}$ ,  $25\ \mu\text{m}$  increment. **e**, Dynamic tuning of optofluidic waveguides by varying core refractive index,  $n_c$ . **f**, Width based dynamic tuning of optofluidic waveguides,  $w_0 = 50$  and  $100\ \mu\text{m}$  for green circles and magenta squares. Positive pneumatic pressure points increase to the left, at 20, 40, and 60 PSI, while the liquid flow rate is  $1\ \text{mL}/\text{min}$ . Note: theoretical predictions using eq. (7.7) are represented as solid curves/lines in **d**, **e**, and **f**.

Abate used thin PDMS side walls for single layer membrane valves.<sup>144</sup> Here, we use this principle for pressure-based dynamic tuning of the optofluidic MMI devices.

Inward pneumatic pressure applied to the side channels causes a decrease in the MMI width, (Fig. 7.9b, right) and thus, a decreased spot number,  $N$ , at a given length,  $L$ .

Conversely, positive fluidic pressure in the core increases both  $w$  and  $N$  as seen in Fig. 7.9b and Fig. 7.9f. Note that all data points in Fig. 7.9f are at a given length  $L$  that yields an integer spot number at zero applied pressure. The data closely matches theoretical expectations (lines in Fig. 7.9f).

### **7.5.2 *Lightvalve Architecture for Simultaneous Control of Fluid and Light***

In addition to single layer reconfigurable MMIs, it is possible to incorporate multilayer lithography (seen in Fig. 7.1) to expand the PDMS optofluidic platform to more complex architectures. As such, we are able to create a fully – optically and fluidically – reconfigurable optofluidic platform. At its heart is an actuatable microvalve that simultaneously acts as an optical waveguide and actively moderates fluid flow, dubbed here as a “lightvalve”. Our implementation is based on lifting-gate microvalves that have been used in microfluidic devices for complex bioassays (see Chapters 5 and 6).<sup>61,62</sup> Fig. 7.10 shows the schematic design of the lightvalve, with the middle images showing its static architecture in cross-section and side view. It is composed of three PDMS layers, a control layer (I), a waveguide valve layer (II), and a substrate (III). The control layer, I, is designed to allow for both push-down (positive pressure, Fig. 7.10, left) and lift-up (negative pressure, Fig. 7.10, right) operation. By varying the pressure, different combinations of photonic and fluidic functions of the lightvalve can be implemented as shown in the table of Fig. 7.11a. Without pressure, light is guided across the fluid valve (green arrow) while liquid flow is blocked (cross). Alternatively, positive pressure also blocks liquid flow while enabling dynamic tuning of optical transmission by varying the pressure. Finally,

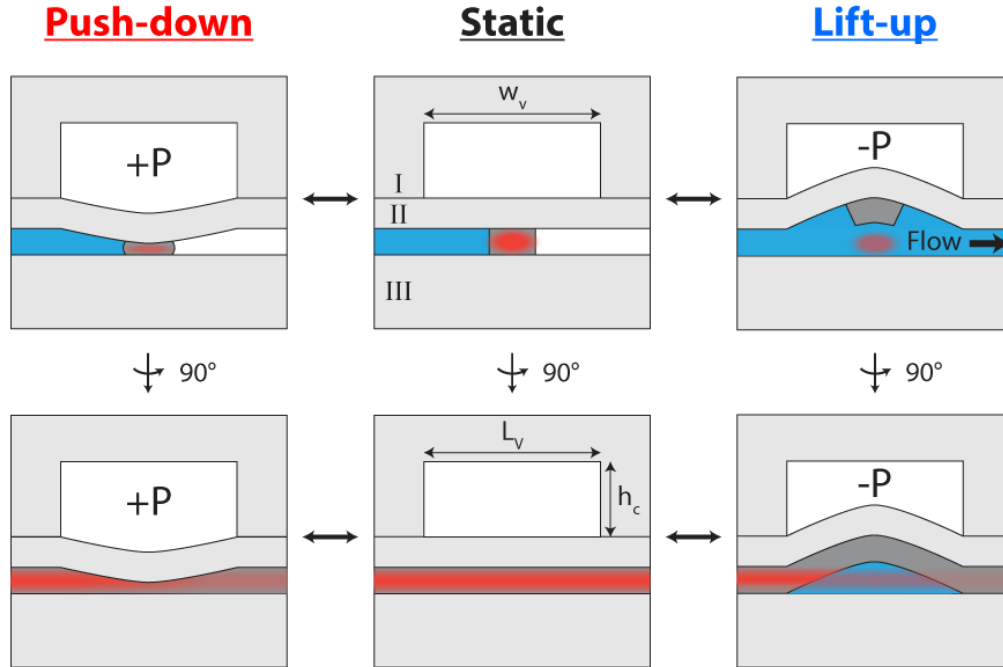


**Fig. 7.10 | Lightvalve architecture.** a, Schematic representation of the lightvalve architecture. Top-center—as fabricated lightvalve composed of three functional layers: layer I is the control layer; layer II is composed of a high refractive index waveguide core (dark grey) and a low refractive index mechanical membrane (light grey); layer III is the substrate layer. Top-left—lightvalve operated in push-down mode. Top-right—lightvalve operated in lift-up mode. The bottom row of images are respective counterparts to the upper row, rotated 90° about a vertical axis. Importantly, the control layer defines the lightvalve’s width ( $w_v$ ) and length ( $L_v$ ) as well as the maximum deflection of layer II via its height,  $h_c$ .

negative pressure results in fluid flow with tailorable optical rejection. The lightvalve can be constructed with established lifting gate valve fabrication processes, plus the addition of the waveguide core segment in layer II (dark grey) which is formed through a single added spin step of high refractive index PDMS (see Section 7.1).

The obvious Litmus test for photonic functionality of the lightvalve is operation as an on-off switch, which is reported in Fig. 7.11b for a 0.6mm long valve. The top trace shows the temporal pressure sequence for the valve and the two bottom traces show the optical transmission across the valve in push-down (middle, red) and

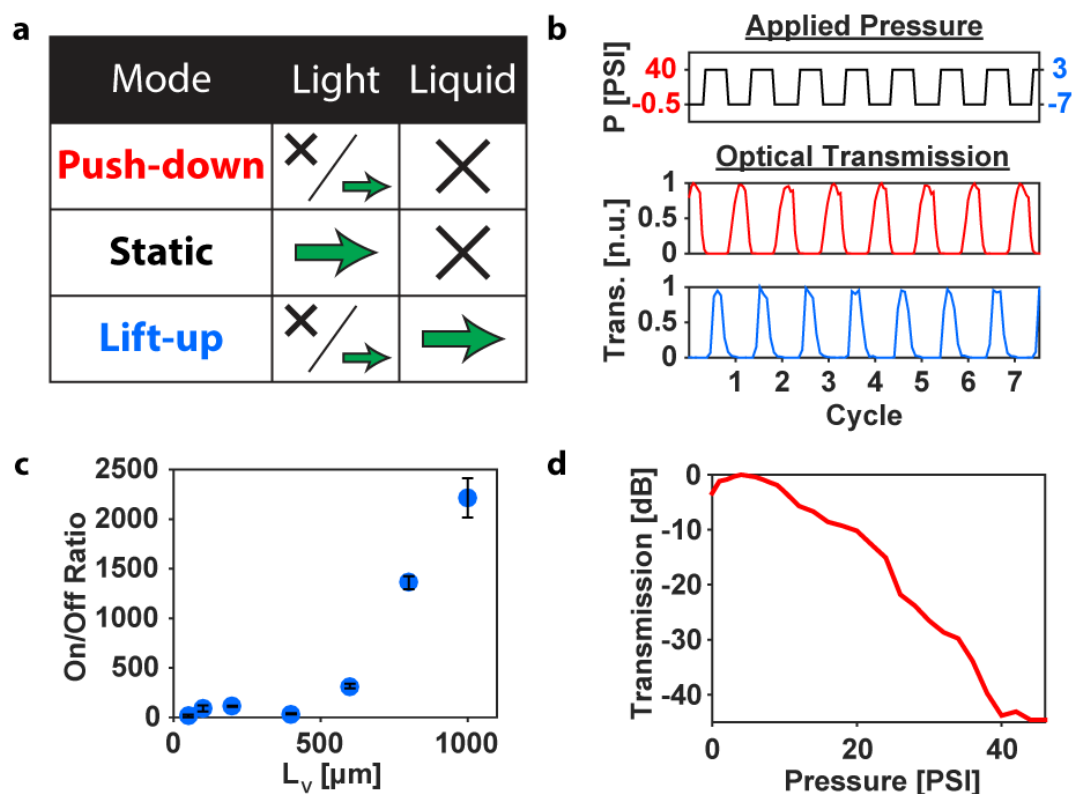


**Fig. 7.11 | Lightvalve Operation.** **a**, Lightvalve operation and respective effects on liquid and light flow. Note that light flow is tailorable/tunable in both lift-up and push-down modes (see parts **c** and **d**). **b**, Optical switching of the lightvalve operated in lift-up (bottom, blue) and push-down (red, middle). The top subplot (black) is a schematic pressure trace designating the applied control pressure at any given time. The left-hand y-axis (red labels) denotes the pressure applied during push-down operation while the right-hand y-axis (blue labels) denotes the pressures applied in lift-up mode. **c**, Optical switching efficiency of lightvalves operated in lift-up mode. The error-bars represent the standard deviation of 20 switching cycles. **d**, Optical rejection of a lightvalve operated at various push-down pressures.

lift-up (bottom, blue) modes. Successful and repeatable switching with excellent extinction is observed for both pressure modes. Cycle rates can reach  $\sim 100$  Hz and are limited by the microfluidic control system. The switches operated without degradation for over 100,000 switching cycles in both modes.

Next, we analyzed the on-off optical switching efficiency for different length lightvalves operated in lift-up mode. The results are displayed in Fig. 7.11c and show

a steep increase in performance at around 500 $\mu\text{m}$  length (with control height,  $h_c=100\mu\text{m}$ ). This is due the fact that optical switching in lift-up operation relies on bending of the entire membrane formed by layer II; as such, when the effected membrane bend is small, optical rejection is low. Fig. 7.11c shows that the lightvalve switches off for length/height ( $L_v/h_c$ ) ratios above 5 and the on-off ratio continues to improve up to  $L_v/h_c \sim 10$ . At even longer lengths, on-off ratios become inconsistent due to membrane deformations during actuation.

Push-down operation, on the other hand, is relatively length-independent as it relies only on deformation of the waveguide structure at the beginning of the lightvalve, which leads to poor mode coupling between the excitation and valve waveguides. Fig. 7.11d shows that the on-off ratio depends on the applied pressure for a short valve length,  $L_v = 300\mu\text{m}$ . After first reaching a maximum at 3psi due to optimized optical mode coupling, the transmission drops dramatically, resulting in an on-off ratio of  $\sim 45\text{dB}$  at 40psi, indicating excellent light blocking capability over short lightvalve lengths.

We also investigated the spectral dependence dependence of the lightvalve. When operated in lift-up mode, there is a clear fringe pattern when the pump wavelength is changed, as seen in Fig. 7.12a. Note that this is the visible wavelength regime (490-650 nm) plotted in frequency to linearize any free spectral ranges. Visually, the peak spacing seems to be fairly consistent, however, it is not identical throughout the spectrum ranging from 11-16 THz, thus, direct conclusions about cavity effects are difficult to draw. When the spectral dependence is considered for

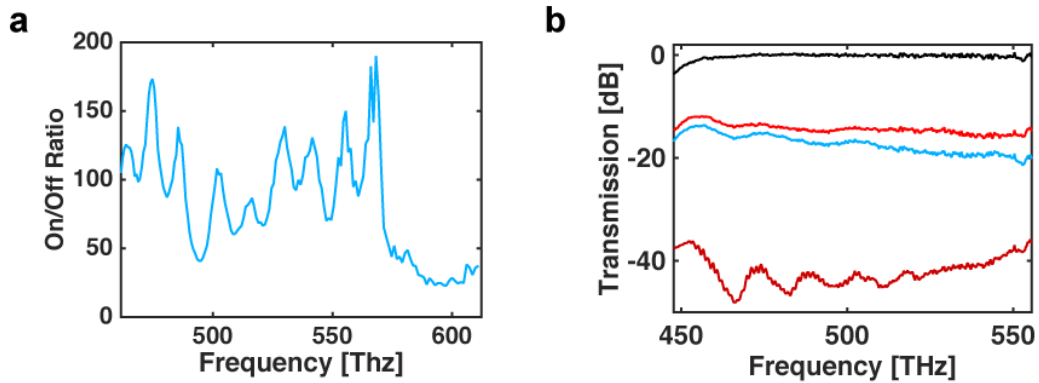


**Fig. 7.12 | Spectral dependence of lightvalve transmission. a,** Lightvalve spectral dependence operated in lift-up ( $P = -7$  PSI) mode over the visible wavelength regime using a tunable laser source and APD ( $L_v = 100 \mu\text{m}$ ,  $w_v = 160 \mu\text{m}$ ). **b,** A separate lightvalve was measured during lift-up and push-down operation using a spectrometer ( $L_v = 500 \mu\text{m}$ ,  $w_v = 500 \mu\text{m}$ ). Pressures from top to bottom are 0 (black), 20 (red), -7 (light blue), and 60 (dark red) PSI.

both negative and positive pressures (lift-up and push-down operation), the curves seen in Fig. 7.12b are observed. It is clear that there is spectral dependence in both graphs, and it seems that as the deformation of the waveguide becomes larger in Fig. 7.12b, the frequency dependence becomes more prominent. A more thorough study of this behavior is needed and could prove to be useful for future lightvalve designs such as tunable spectral filters. We note that in the case of Fig. 7.12a, the experiment was conducted by shining a variable laser source (NKT) through the waveguide onto an avalanche photodetector. The lightvalve was switched 10 times (and results were averaged) for each nanometer wavelength increment and post processing was used to achieve the plot seen in Fig. 7.12a. On the other hand, Fig. 7.12b was achieved by direct input of white laser light into the lightvalve, while the output was continuously monitored using a portable spectrometer (Ocean Optics). In this case, it was possible to monitor the fringes in time, and it was noted that the

position and spacing of the fringes changes quickly, with small increments of pressure – a property that could be useful for future lightvalve designs.

### 7.5.3 Lightvalve Trap with Single Bioparticle Analysis Capability

An even more functional version of a lightvalve can be designed and fabricated by introducing an annulus into the light propagation path as shown in Fig. 7.13a. Fluidically, the lightvalve trap can be used to mechanically trap objects within

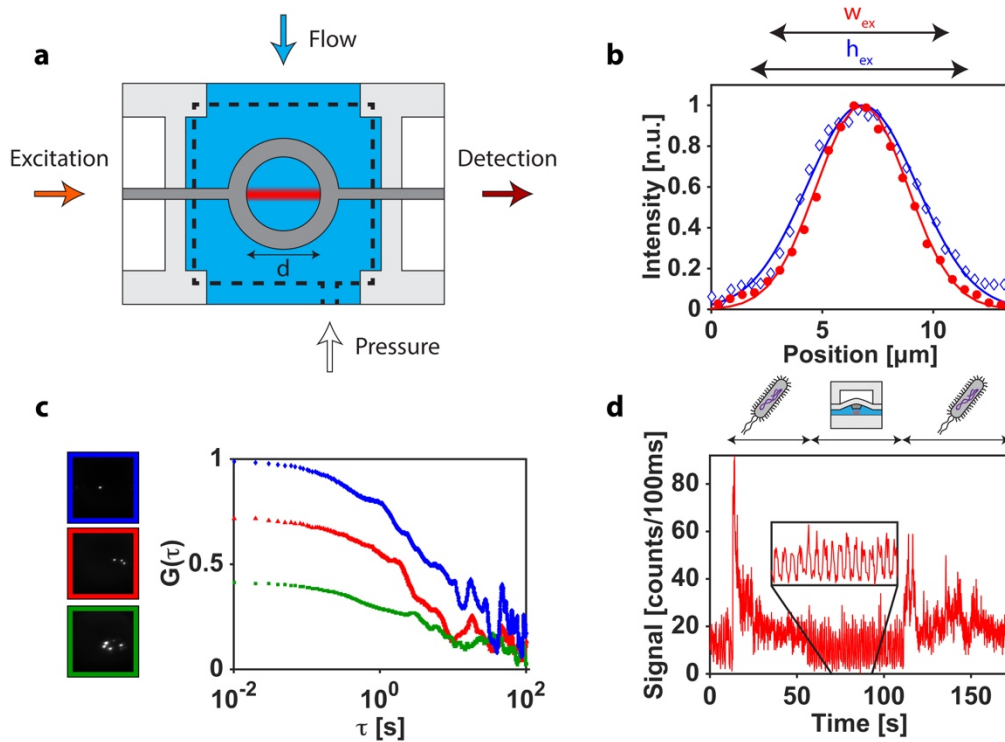


**Fig. 7.13 | Lightvalve particle trap.** **a**, Top-down schematic of lightvalve trap with excitation laser light entering the trapping region from a solid-core waveguide, while signal is collected, filtered, and detected from the opposite waveguide facet. The observation volume is indicated in the center of the lightvalve trap by a Gaussian blurred red bar and is distinctly smaller than trap volume which is characterized by the diameter ( $d$ ) of the trap. Pressure is applied to the control layer, indicated here by dashed black lines. **b**, Waveguide mode cross-sections, with the  $1/e^2$  widths in the vertical ( $h_{ex} = 9.9 \mu\text{m}$ ) and horizontal ( $w_{ex} = 8.2 \mu\text{m}$ ) directions, define the optical interrogation region. **c**, Autocorrelation curves for different numbers of particles trapped inside a lightvalve,  $d = 50 \mu\text{m}$ . Microscope images on the left are snapshots of fluorescent particles within the excitation volume for each autocorrelation trace. **d**, Fluorescence signal of trapped, single *E. coli* bacteria. Illustrations above the fluorescence trace indicate when the trap is closed, containing a cell (bacterium cartoon), and when the trap is cycling (open lightvalve cartoon).



the annulus when lowered into the channel. We fabricated annuli with 5-80 $\mu\text{m}$  diameters, enclosing volumes between 140fL and 35pL. The lightvalves also act as peristaltic pumps for refreshing fluid within the traps by connecting three or more valves in series and actuating them sequentially in lift-up mode. Optically, the annulus enables in-plane optical interrogation of trapped particles using light that traverses the valve ring along the straight waveguide path. The optical path shown in Fig. 7.13a defines the optical excitation and collection volume of the trap. The solid-core waveguides are narrow enough to create effectively single vertical and lateral optical modes as shown in Fig. 7.13b. This allows for implementing advanced optical spectroscopy methods on small numbers of particles trapped inside the annulus. We illustrate this capability using fluorescence correlation spectroscopy (FCS). Fig. 7.13c left shows top-down camera images of 3, 5, and 10 trapped, fluorescent microbeads (note that only beads within the excitation volume are fluorescing in the image). The corresponding FCS traces — acquired by in-plane fluorescence detection along the solid-core PDMS waveguides — are shown on the right. When the ratio of physical trap volume and optical excitation volume  $V_{exc}$  is taken into account, the particle concentration  $c$  obtained from the FCS curves ( $c=G(0)/V_{exc}$ ) agrees well with the value obtained by camera observation.

Lastly, we demonstrate the lightvalve trap's ability to analyze single, trapped bioparticles – here, fluorescently stained *E. coli* bacteria. Fig. 7.13d shows the time-dependent fluorescence signal collected from the trap. An initially empty trap is closed at  $t \sim 15$  sec and a single *E. coli* bacterium is trapped within the observation

volume. The detected fluorescence decreases continuously over the bacterium's 40 second residence within the trap due to photobleaching. After 55 seconds, the bacterium is released by activating the lift-up function, followed by a series of actuations (i.e. fluid pumping) in search of another bacterium. The inset of Fig. 7.13d shows high signal when the trap is up, and low signal when trap is down. After 110 seconds, the trap is locked down again because a bacterium is detected above the background optical signal threshold. Subsequently, this bacterium is diffusing in and out of the observation volume, yielding a fluctuating fluorescence signal. We note that FCS analysis of the two bacteria trapped herein yield diffusion coefficients of  $\sim 0.5 \mu\text{m}^2/\text{s}$  as expected for a particle of  $\sim 1 \mu\text{m}$  diameter.

In summary, we have introduced a new optofluidic platform that seamlessly marries optical and fluidic functions in a single chip. Based on combining solid- and liquid-core PDMS waveguides whose fabrication is compatible with purely microfluidic chips, we created devices that offer multi-modal photonic reconfigurability using core liquids, mechanical pressure and motion. The potential of this approach was illustrated using widely tunable liquid-core MMI waveguides and by the introduction of novel lightvalves that regulate both liquid and light flow. Extremely efficient optical switching and definition of physical particle traps for optical analysis were demonstrated. The fluidic valve shape and optical pathways created by the lightvalve can be designed independently and with great flexibility, making the lightvalve a powerful building block for future optofluidic devices.

## 8 Conclusions and Outlook

In conclusion, this thesis has achieved three aims—it has enhanced the ARROW platform through various means, integrated optofluidic detection chips with microfluidic processors, and created a novel, all PDMS platform for reconfigurable optofluidics and integrated optofluidic/microfluidic sensors.

Initially, the background of ARROW optofluidic chips was reduced through high temperature thermal annealing.<sup>38</sup> A chance discovering of increased throughput led to the in-depth analysis of thermal annealing of entire ARROW chips.<sup>1</sup> It was shown that through low-temperature annealing, water could be excluded from the top layer of silicon-dioxide, increasing the transmission by up to 1000x, the dye detection S/N by 100x, and particle detection efficiency by ~40x. These enhancements enabled the detection of single viruses<sup>5</sup> and clinical RNAs.<sup>4</sup> An additional modification to the ARROW platform, i.e. the MMI waveguide, was used to enhance the detection of single influenza viruses, allowing for in flow identification of different different influenza viruses.<sup>5</sup> To complement the physical change to the ARROW, a detailed analysis program was developed for post-processing of multi-peak fluorescence data. The analysis allows for shift-multiply and single-peak autocorrelation based detection and identification of particle signals.

In parallel to direct enhancement of the ARROW chip itself, additional external functionality was added to the entire platform through hybrid integration. First, passive hybrid optofluidic integration (with flow initiation off chip, no reconfigurable fluid paths) was used to label and detect single  $\lambda$ -DNAs on chip, as well as sort and

distribute microspheres for optofluidic detection.<sup>2</sup> This work was further developed through active hybrid optofluidic integration (on chip fluid pumping with reconfigurable fluid paths) where we demonstrated active, on-chip fluid control as well as the ability to extract and detect nucleic acids on chip.<sup>3</sup> This work was leveraged heavily in the detection of single clinical Ebola RNAs.<sup>4</sup>

Finally, the last portion of this thesis described a new platform technology formed entirely of PDMS.<sup>6</sup> Through the combination of monolithically fabricated solid- and liquid-core waveguides, a cheap and easily fabricated optofluidic processing and detection device was created. By adding single layer membrane valve features to the optofluidic devices, we were able to create multiply tunable MMI waveguides. Integration of valving structures in the 3<sup>rd</sup> dimension (i.e. on top of the solid-core waveguides themselves) yielded an entirely new optofluidic building block – the lightvalve. Lightvalves have the capability to control fluid and light flow, with the optical switch reaching extinction ratios beyond 40 dB. The culminating structure in this work was the lightvalve trap, that contained an annular structure simultaneously functioning as a single bioparticle trap, a fluorescence interrogation system, and microfluidic pump.

The works in this thesis have provided ARROW platforms with significantly lower detection limits and integrated sample processing. This alone opens the gate for multiple studies of point-of-care hybrid optofluidic biosensors. With the addition of an entirely new platform and optofluidic PDMS technology, work can be continued in developing new optofluidic technologies on an easily produced waveguide system.

## 9 Appendixes

### A. *T3R-Viewer – data analysis software*

The T3RViewer program is an optimized environment for viewing and analyzing time-tagged time-resolved (TTTR) fluorescence data traces. It improves upon previous programs through fast runtime, direct Matlab integration, reliable autocorrelation analysis, and multi-operating system compatibility. In addition to the basic abilities of importing .t3r files, creating histograms of photon counts over time, autocorrelating fluorescence traces, and outputting binned data, the T3RViewer adds many functionalities such as cross-correlation, peak finding, peak viewing, single peak autocorrelations, shift-multiply peak analysis, and peak statistics into a single .m Matlab file that can be run on any Matlab supported operating system. Furthermore, the program consistently excels at outputting data/analysis into an analyzable format.

#### **A.1 *T3RViewer.m Main Window***

Fig. A.1 shows a fully expanded T3RViewer.m window. However, the program has been written such that portions of the window only show up/enable when it is possible to use their functionality. For example, the data selection screen will only show up once a data file has been loaded. This should prove to be an intuitive function, as each step of the data analysis will appear when needed. For completeness, I will go through each of the panes, describing the enclosed functions in the following table.

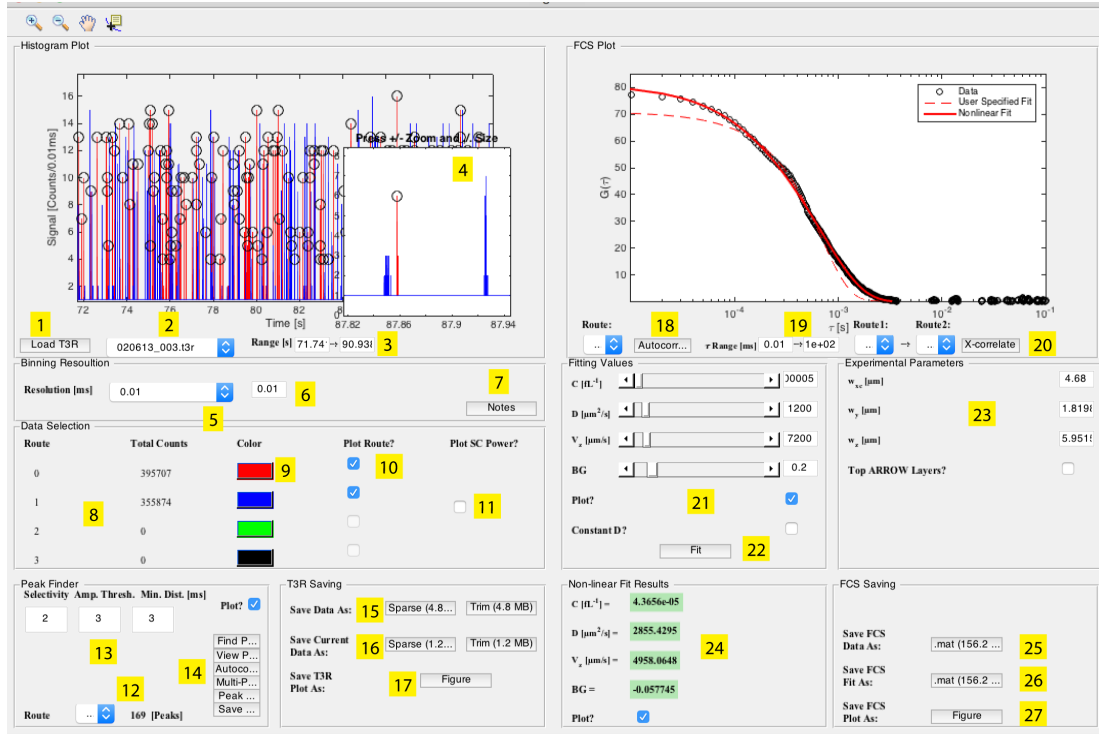


**Fig. A.1 | T3RViewer.** See description for different functions

**Table A.1 | T3RViewer graphical user interface (GUI) explanations.** See Fig. A.1 for the respective GUI image.

Number	Description
1	<b>Load button:</b> loads a T3R trace for analysis.
2	<b>File dropdown:</b> select a file from the current folder for quick viewing.
3	<b>Range:</b> time range (in seconds) to plot data histogram.
4	<b>Zoom box:</b> clicking on the plot without a tool selected zooms into that portion of the data trace, with +/- changing zoom, and ,/. changing the time range within the zoom box plot.
5	<b>Bin time selection:</b> select orders of magnitude for binning in ms.
5	<b>Custom bin time:</b> arbitrarily set histogram bin width.
7	<b>Load notes:</b> attempts to load notes.txt from current directory.
8	<b>Route information:</b> specifies route number and respective number of photons.
9	<b>Plot color:</b> changes color for each route plot in the histogram.
10	<b>Plot checkbox:</b> choose whether or not to plot the respective information (applies to other panes as well).
11	<b>Plot Power:</b> attempts to plot the .dat power trace with the same filename as the .t3r. Plots over the data histogram.

12	<b>Route choice:</b> for each data analysis pane, you must choose a Route(s) for the particular analysis (e.g. Route 0).
13	<b>Peak finding arguments:</b> arguments specifying that the peak must have a minimum “Amplitude Threshold” that is above the background by “Selectivity” times, and is located a “Minimum Distance” from nearest neighbor peaks.
14	<p><b>Peak Tools</b></p> <p><b>Find Peaks:</b> searches for peaks in the displayed histogram trace with peak finding arguments as set.</p> <p><b>View Peaks:</b> Views each found peak with respective shift-multiply analysis.</p> <p><b>Autocorrelate Peaks:</b> Correlates each found peak within the specified “Minimum Distance” window, through the <math>\tau</math> range specified in 19.</p> <p><b>Multipeak Finder:</b> Opens a new window for finding multipeaks within the histogram plot, using shift-multiply algorithm.</p> <p><b>Peak Statistics:</b> Histograms all of the found peaks in amplitude and time as well as tries to fit with Gaussian for statistics.</p> <p><b>Save Peaks:</b> Saves general peak information to a readable .mat file.</p>
15	<b>Save all data:</b> save entire histogram data trace (all times) as a sparse—only indexes non-zero points—or a trim—removes all zero points—matrix.
16	<b>Save currently displayed data:</b> see 15, saves currently displayed data in histogram plot.
17	<b>Save Figure:</b> plots and saves current histogram in a new and formatted .fig window.
18	<b>Autocorrelate:</b> performs a discrete autocorrelation of data (shown in the histogram plot) of the selected route.
19	<b>Lag range:</b> specifies the range of time lags to be used in the correlation.
20	<b>Cross-correlate:</b> performs a discrete cross correlation of the selected routes.
21	<b>Fitting Parameters:</b> concentration, diffusion coefficient, velocity of particles as well as the correlation background are specified as fitting parameters. The output of the fit with these exact parameters is plotted as a red dashed line (if the plot box is selected).
22	<b>Autocorrelation Fit:</b> performs a fit of the plotted autocorrelation trace based on the previously described model and fitting parameters in 21 and waveguide properties in 23.
23	<b>Chip properties:</b> half widths of the excitation mode profile and hollow-core waveguide profile. Specify top ARROW layers if applicable for secondary autocorrelation effect considerations. <sup>82</sup>
24	<b>Fitted Autocorrelation Values:</b> output of the non-linear fit of the plotted FCS data.
25	<b>FCS Data Save:</b> saves the plotted FCS data as a .mat file.
26	<b>FCS Fit Save:</b> saves the FCS fit and parameters.
27	<b>FCS Figure Save:</b> plots and saves current FCS trace to a .fig file.

The top left most pane is the “Histogram Plot” pane. Initially, only the load button is available **(1)**, so it is required to load a T3R file before the pane populates. Once a file is loaded, the file will plot with available photon routes over the entire time of the trace **(3)**, at the default bin size (which can be changed in the declarations in the beginning of the script, or manually after load **(5,6)**). Note that the file “020613\_003.t3r” is loaded in the drop down box **(2)**. Both available routes **(8,10)** are plotted in red and blue **(9)**.

Peaks are found in the histogram plot for Route 1 **(12)** within the designated time range **(3)** and are marked by black circles. The peak finding parameters used were set to be above background threshold **(13)**. A suite of functions **(14)** can be performed in the found peaks, and are discussed later in this appendix.

The histogram data can be saved in one of two formats: sparse or trim. Sparse is Matlab’s proprietary matrix format that only indexes data points that are non-zero, dramatically reducing the memory used to store matrixes with many “0” elements (such as those binned with small bin sizes, e.g. less than 1 ms). The data can also be saved as a trim matrix, which is a time/value pair matrix that records the data points for each non-zero data point. These data matrixes can be saved to .mat files over the entire time of the measurement **(15)** or for the currently displayed trace **(16)**. A decently formatted .fig file can also be saved for the displayed histogram plot **(17)**.

In the FCS Plot pane, an FCS trace for route 0 has been plotted **(18)** over time lags of 0.1 to 100 ms **(19)**. Although not performed in the above image, a cross-



correlation of two fluorescence routes is possible **(20)**. In order to extract important parameters from the FCS trace, a fit can be performed **(22)**. The fit is based on a number of input arguments that need to be well defined **(21)**. It is simple to define these fit parameters as one merely needs to match the dashed red line as closely to the data as possible. Note that the output of the fit depends on strictly defined system/chip parameters that are defined based on the ARROW chip's interrogation volume **(23)**. The output of the fit yields the non-linear parameters for the displayed FCS trace **(24)**. The data itself can be saved as a .mat **(25)** while the fit and its metrics can be saved in similar fashion **(26)**. Finally, an FCS figure can be plotted and saved as a .fig file **(27)**. For a more detailed explanation of the fitting parameters, equation, and process, we refer the user elsewhere.<sup>82</sup>

## ***A.2 T3RViewer.m Peak Analysis Tools***

As mentioned above, the T3RViewer has a multiple peak analysis tools built in. Designated by **(14)** in Fig. A.1, the different function and there uses will be discussed herein. First, the find peaks function is obvious and a prerequisite for other peak function except for Multi-peak finder. This is because each of the other function operates on the peaks found using this function. As such, peaks found are analyzed within a time window of “Minimum Distance”.

The second function in **(14)** is the “View Peaks” function. It can be used once peaks have been found within the data histogram based on the route number **(12)**. When pressed, a new window appears, shown in Fig. A.2. The processing is quick for this data and all information is almost immediately populated. Note that in View

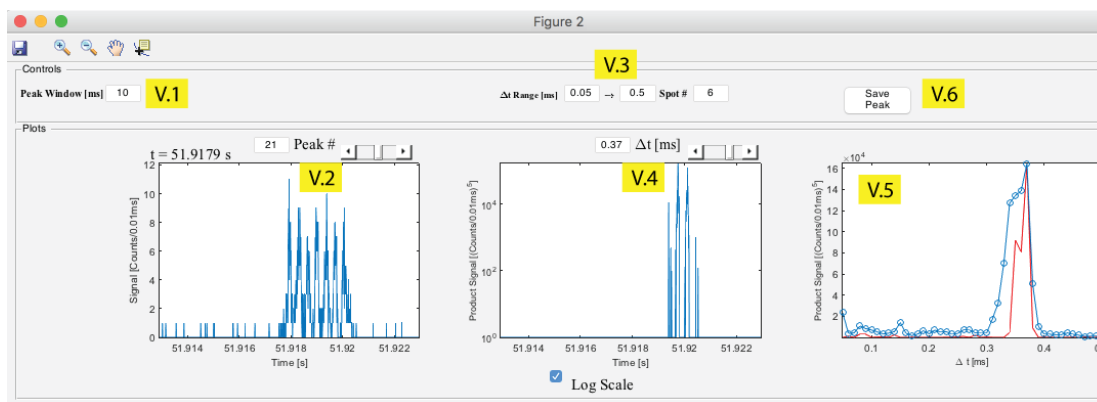


**Fig. A.2 | View peaks dialogue box.** **V.1**, The amount of space around the peak can be changed using the peak window box. **V.2**, Each peak is assigned a peak number based on its time with respect to the other peaks. The scrollbar can be used to scroll through all the peaks. The peak time is listed in the upper left and the (unprocessed) data trace for the peak is plotted here. **V.3**, Shift-multiply time range and spot number designations (note the spot number is the number of spots in an MMI/multipeak, the number of shift-multiplies is one less than this number). **V.4**, Shift-multiply signal,  $S(t)$  for the peak in **V.2** at the noted  $\Delta t$  value. The scrollbar can be used to scroll through the different  $\Delta t$ 's. **V.5**, Plot of maximum signal for given  $\Delta t$ 's, i.e.  $S(\Delta t)$ . The blue trace is  $S(\Delta t) = \max(S(t, \Delta t))$ . The red trace is  $S(\Delta t) = S(t_{\max}, \Delta t)$ , where  $t_{\max}$  is set as the time at which  $S(t)$  is at its global maximum. **V.6**, Each individual peak and its data can be saved using the noted button.

Peaks, you can change the Peak Window (**V.1**) (or the amount of time surrounding each peak), unlike the other functions which have this implicitly defined by Minimum Distance (**13**). The individual peak is plotted within its window (**V.2**), with its number and global time noted. The shift-multiply parameters can be changed on-the-fly (**V.3**) to yield the  $S(t)$  signal seen in (**V.4**). Finally, a plot of the global and local maxima  $S(\Delta t)$  (see Fig. A.2 caption for details) values are plotted (**V.5**), and all of the information can be saved using the provided button (**V.6**).

“Autocorrelate Peaks” is the third function in (**14**). Once again, the peaks must be found before this function can be used. Upon pressing the button, all peaks are autocorrelated based on the values in (**19**), the autocorrelation is smoothed, and peaks are found using an adaptation of the peak finding algorithm. Note, this is a place where the program can be improved, but is empirically set using a parameter called

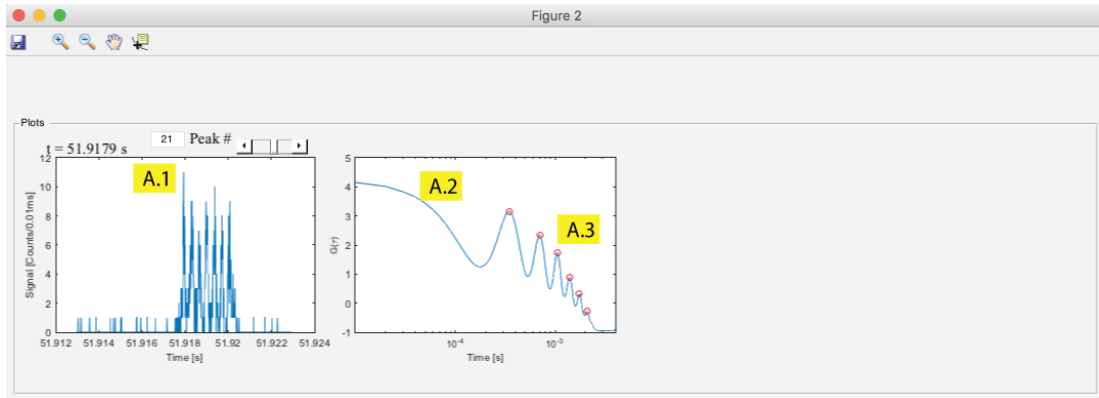


**Fig. A.3 | Autocorrelate peaks dialogue box. A.1**, The same information is plotted here as is in **V.2**, that is the single peak data trace, with time and number, unadulterated. **A.2**, Autocorrelation trace of the single peak (smoothed here), with red peaks **A.3**, marking the local secondary maxima in the trace.

“corrSelectivity” to find the secondary autocorrelation peaks with high fidelity. The user is prompted to save this data, after which the peak browser shown in Fig. A.3 is displayed. The peaks can again be browsed (**A.1**) with their respective autocorrelation traces (**A.2**) and local maxima (**A.3**) automatically plotting during browsing.

“Multi-peak Finder”, the fourth function in (14), is the only function that doesn’t require first using the peak finder algorithm. This is because all of the parameters are set within the dialogue shown in Fig. A.4 and  $S(t)$  peaks are found rather than  $F(t)$  ones. Clearly, this dialogue is similar in nature to that of Fig. A.2. We plot  $S(t)$  for the entire data trace shown in the histogram plot (**M.2**) for the specified parameters (**M.1**). A peak finding algorithm similar to the one in the main program is then used to find  $S(t)$  peaks with the given arguments (**M.3**). The globally found peaks (within the  $S(t, \Delta t)$  matrix) are plotted in their given  $\Delta t$  trace in (**M.2**) and are indicated by black circles. For example, in Fig. A.4 the first portion of the histogram trace has only blue laser light excitation, and thus the short  $\Delta t$ ’s all show up at the

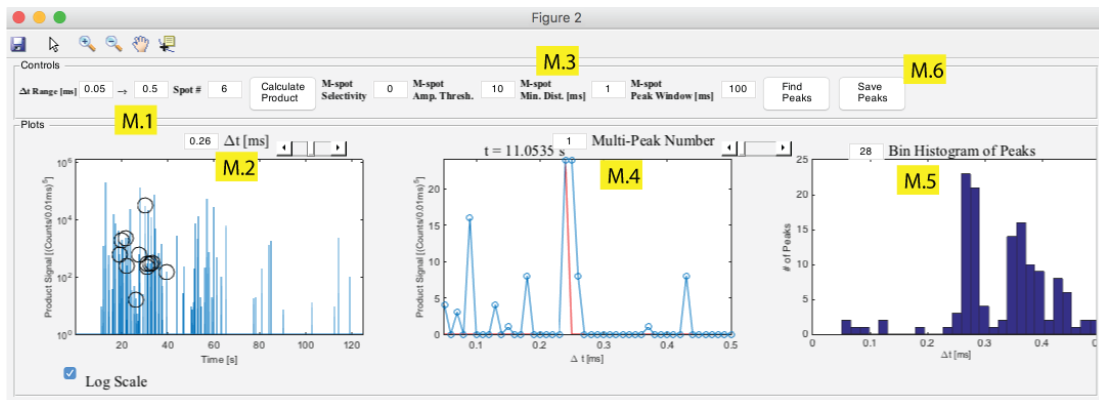


**Fig. A.4 | Multi-peak finder dialogue box.** **M.1**, Similar to **V.3**, the shift-multiply algorithm parameters can be defined here. The Calculate Product button produces a shift-multiply product matrix of the entire data trace in the histogram plot. **M.2**,  $S(t)$  plot for the entire data trace, at the specified  $\Delta t$ . The scrollbar is used to change the  $\Delta t$  slice of the matrix that is viewed. **M.3**, similar to the controls in **(13)**, the controls in the box are dictated as a shift-multiply selectivity,  $S(t)$  amplitude threshold, and peak minimum distance. The new parameter, M-spot Peak Window, designates the  $\Delta t$  range in which the program should consider all maxima as occurring from a single multi-peak shift-multiplication. **M.4**, Similar to **V.5**, the local and global maximum  $S(\Delta t)$  traces are plotted and browsable for each shift-multiply peak. **M.5**, Histogram containing each peak's  $\Delta t_{\max}$  (i.e.  $S_{\max} = S(t_{\max}, \Delta t_{\max})$ ) in the defined number of bins. **M.6**, Save the multi-peak finder processed information using this button.

beginning of the trace ( $t < 40$  s). A plot of each peak's individual  $S(\Delta t)$  traces (**M.4**), as well as the distribution of their maxima (**M.5**), can be easily saved for post-processing (**M.6**). For a more in depth consideration of these plots, see Section 6.2.7.

It is also possible to analyze the “Peak Statistics” (**14**) using the T3RViewer. After some time for peak fitting, the statistics are plotted in a separate dialogue box seen in Fig. A.5. In detail, the program does three things when calculating peak statistics – 1: it creates a histogram of all of the peaks, binning them based on their maxima (**S.1**). This allows for maxima distribution considerations, e.g. if there is no peak in the histogram, it's possible some of the peaks are below background and the system is only detecting a portion of particles. 2: the program histograms the peaks based on their times (**S.2**). This allows the user determine if there are any velocity

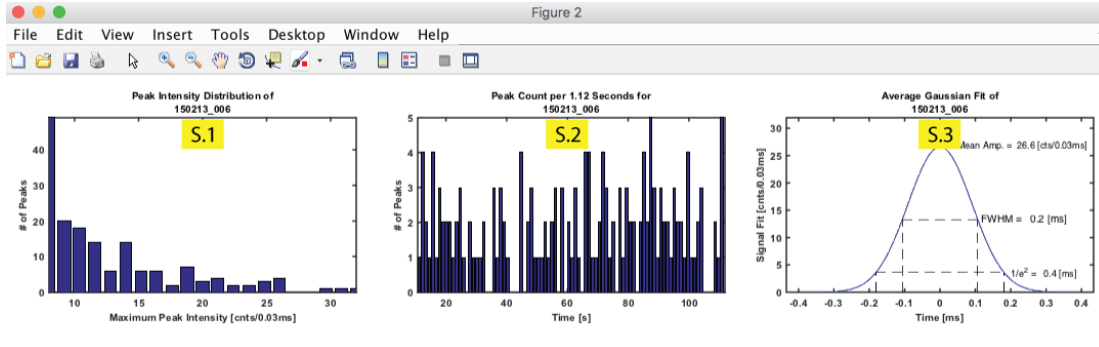


**Fig. A.5 | Peak statistics dialog box. S.1**, Histogram of peaks found in histogram plot, based on their peak intensities. **S.2**, Histogram of peaks found in histogram plot, based on their times. **S.3**, Average Gaussian fitting parameters for all peaks. Use this plot with caution.

changes/clogging events throughout the given data trace. Finally, the program attempts to fit each peak with a Gaussian, determining its FWHM and  $1/e^2$  widths, as well as the average amplitude (**S.3**). This plot should be viewed with caution as it is underdeveloped and will only work theoretically for Gaussian (non multi-peak) peak shapes.

The final button in **(14)** allows the user to save the information generated during the use of the “Find Peaks” function. Note that there is a way to save all of the information as a .mat file for each of the peak analysis functions (except “Peak Statistics” which can be saved as a figure or regenerated using the “Save Peaks” data easily). The convenience of this program should not create sloth in the user, and control analysis should be plotted independently. For a separate means of obtaining binned .t3r data for analysis in Matlab, see the scripts of the naming style “pT3R1.m”, which reads T3R data and outputs to a .mat file directly (it also contains remedial plotting options within the script header).

### A.3 T3RViewer Script Header Options

Although it is beyond the scope of this thesis to explain all 7,500 lines of code, much of the program has been commented. It does seem important to include parameters that can be easily changed by the user to alter the default functions of the program. As such, I have included the editable header in Table A.2 with detailed comments on what effect each parameter will have on program operation.

**Table A.2 | T3RViewer editable header.** Parameters are described by commented text (green).

T3RViewer Editable Header
<pre>BATCH = 1;      % Flag: if true then use batch processing PLOTSIGS = 1;  % Flag: plot signals PLOTPOWER = 0; % Flag: plot power data printParam = 0; % Flag: prints t3r record information to matlab printTXT = 0;  % Flag: prints data to separate TXT file nlinfitTF = 1; % Flag: try lmfns1q or nlinfit -----  %array size maximum for datamat if ispc == 1     maxArraySize = 4; %max array size in GB before peakfinding     algorithm uses the slower sparse version for datamat else     %for some reason mac program is handling much larger array     sizes,     %it is much quicker to not use sparse whenever possible     maxArraySize = 40; %max array size in GB before peakfinding     algorithm uses the slower sparse version for datamat end  dt = .001;      % Binningtime resolution given in seconds dtstart = dt;  %starting dt, used for reference  %default lag scale is full minLag = dt; maxLag = 1;  %default hist plot has no data so 0 histMin = 0; histMax = 0;  %manual zoom properties (don't change) startIndex = dt; lengthIndex = 0;</pre>

```

% Create and hide the GUI figure as it is being constructed.
% position vector [left bottom width height]
sr = get(0, 'ScreenSize');
windowW = sr(3)*.75;
windowH = sr(4)*.75;
if ispc == 1
    fsize = 8;
else
    fsize = 0.01*windowW-1;
end

% debug code for viewing variables in base workspace during runtime
% set to true if you want to view your variables in the matlab main
% window while T3RViewer is executing
debugVar = false;
copystr = 'c'; %string appended to variable name upon copy to avoid
if debugVar
    copyGlobalVisible = 'on'; %visiblity of copyGlobal button used
for debugging
else
    copyGlobalVisible = 'off';
end
autoload = false; %default false
autopath = '/Users/Josh/Dropbox/Research/Matlab/';
autoname = '016.t3r';
disableImpossible = true; %initial disabling of unavailable buttons,
keeps errors from happening on user improper input, default true
testingV = false; %true if you want to always see all the panes, for
GUI Building, default false

% waitbarres is a measure of how often the program calculates time
% remaining, the number specifies the number of updates over the
entire
% calculation. i.e. 100 means waitbar updates 100 times during
% computation

waitBarRes = 100;

%      %manual overrides of window size and fsize for unruly
computers
%      windowW = 1000;
%      windowH = 800;
%      fsize = 10;
f = figure('Visible', 'on', 'Position', [(sr(3)-windowW)/2, (sr(4)-
windowH)/2, windowW, windowH]);
%      %turn off uimenu
%      uimenu(f, 'visible', 'on');

%keep these menubar items, disappear the rest! unless you want them
%all!
showAllMenu = 0;
if ~showAllMenu
    keptags =

```

```

{'Exploration.Pan','Exploration.ZoomOut','Exploration.ZoomIn','Exploration.DataCursor'}; % also for figures might want
'Standard.EditPlot'
    updateToolBar(f,keepTags);
else
    enableMainMenu(f);
end

%% variable definition %%

%minCounts is the minimum number of spurious photons to ignore in a
%route. This is useful for high count rates when the experimental
SPAD
%splitter/joiner can function properly and counts are put into a
%detector that does not exist
minCounts = 100;

%turns warnings off, suppression mainly for zoom and pan callbacks
warning('off','all');

convMethod = 'conv'; %'corr' gives correlation from matlab corr
function, 'conv' gives convolution method

%core index is always assumed to be water
nc =1.33;

%change parameter to make fontsize bigger or smaller
fsizeoffPC = 3; %bigger numbers mean smaller fonts

%default values
Cc = 0.0001;
Dd = 200;
Vz = 200;
BG= 0.2;

%default sizes of saved variables
sizeFullT = 0;
sizeSparseT = 0;
sizeFullCurrT = 0;
sizeSparseCurrT = 0;
sizeFT = 0;
sizeFitFT = 0;

%parameters taken from above publication
wxc = 4.68; %um
wy = 1.8198; %um
lambda = 633e-9; %m
w0 = 4*pi*nc/lambda;
L = 12*10^-6;
wz = 5.9515; %um
constD = false; %whether fitting commenses with constant D or
fittable
r = 0;

```



```

coff = 1;

%initialization variables
plotVal = true;
plotProp = true;
fileName = '';
powerTrace = 0;
lim_xTN = true;
lim_xTOld = 0;

%maginification variables
magY = false; %magnify y axis in inset
defaultMag = 8; %times Magnification of inset
magInc = 1.4; %magnification increment, 140% - 1.4, is default

%default image save type
imtype = 'tiff';

%default colors for plots in RGB
color0 = [1 0 0];
color1 = [0 0 1];
color2 = [0 1 0];
color3 = [0 0 0];

%check box size in pixels
cbox = 15;

%set all plots to off initially
%can autoplot only certain channel by changing this value, otherwise
%all available channels are autoplotted
routePTF = [0 0 0 0];
routePTFs = routePTF;
fcsFlag = 0;
corrType = ''; %autocorr or xcorr
fastfcs = true; %defines whether to trim lag times based on ppdec
ppdec = 1000; %max number of points per decade, set in multiples of
10, i.e. 10,100,1000, smaller numbers obviously run faster

%peak finder defaults
pselectivity = 5;
pthreshold = 60;
minDist = 3; %actually a dimensionless value but user sees [ms]
input
ampVec = '';
peakVec = '';
plotPeaks = 0;
peakDensityNumBins = 100;
ampDispersionNumBins = 20;

%peak viewer starting values
vPeakWindow = 10; %ms
vPeakNum = 1;

```

```

%multispot peak finder, note: some of these variables are necessarily
%redefined in multiPeaks_Callback
deltaTMin = 20*dt*1000; %milliseconds, minimum shift value for
multipeak
deltaTMinStart = deltaTMin;
deltaTMax = 80*dt*1000; %milliseconds, maximum shift value for
multipeak
deltaTMaxStart = deltaTMax;
delT = deltaTMin/1000:dt:deltaTMax/1000; %seconds, shift vector
numSpots = 6;
mPeakNum = 1; %default plot first multipeak found
spotSelectivity = 3; %dimensionless, users sees ms, is the number of
times a multipeak must be above the average of its competitors for
inclusion
spotAmplitude = 1000*(10)^numSpots.*dt; % minimum amplitude for
multipeak detection, empirical estimate here
spotAmplitudeStart = spotAmplitude;
spotMinDist = 100; %actually a dimensionless value but user sees
[ms] input
peakWindow = 100; %max 1 multipeak per window, measured in ms
delTNum = round(((deltaTMax-
deltaTMin)/2+deltaTMin)/(dt*1000))*dt*1000; %current shift value for
multipeak
numBins = numel(delT); %number of histogram bins for plot of
multipeak lag times, redefined during callback
tracePlotX = []; %track xlim of tracePlot
maxPeaks = struct('delT',[], 'peakTime',[], 'prodAmp',[]); %struct
containing info on found multipeaks
plotMaxDelT = 0; %plot maximum delta t within peak window, or just
single time delta t trace

%find peaks in autocorrelation data, only specifier needed is
%selectivity, empirically set to 0.07
corrSelectivity = 0.07;

%all routes disabled initially, if data available on route program
will
%enable
routeEnable = {'off' 'off' 'off' 'off'};

```

## **B. ARROW Loss Calculation**

Although the group Schmidt group seems to be tending towards more biologically related projects, it still seems useful to include an analysis of the underlying ARROW technology. To this end, over the course of my first two years I created a graphical loss calculator for ARROWs. I will discuss the mathematical principles behind this program, and then I will describe the use of the program itself. Note: the program has gone through many versions and there are likely altered versions floating around the lab, however, the version that is the most updated in my possession is arrowDesignv5.m.

### **B.1 ARROW Loss Calculation**

The basic ARROW condition calculations were presented in Section 2.3.1 of this thesis. In addition, a consideration of capillary waveguide loss was considered in Section 7.2, with some applicability to ARROW waveguides. Here, I will include a detailed consideration of the matrix formalism used to define the reflection coefficients of ARROW stacks that ultimately define the ARROW loss (see Equation 7.6 and reference<sup>139</sup>). The derivation is gleaned from a useful text previously referenced.<sup>138</sup>

Maxwell's equations can be used to relate an oscillating electric field vector  $\vec{E}$  with the magnetic induction vector  $\vec{B}$ :

$$\frac{\partial \vec{B}}{\partial t} = -\nabla \times \vec{E} \quad (\text{B.1})$$

where substitution ( $\vec{B} = \mu\vec{H}$ ) and relation follow

$$\frac{\partial}{\partial t}(\mu\vec{H}) = -\nabla\times\vec{E}. \quad (\text{B.2})$$

Here the plane wave is given as

$$\vec{E} = \vec{E}_0 e^{i(\omega t - \vec{k}\cdot\vec{r})}. \quad (\text{B.3})$$

Note that here  $\vec{E}_0$  is some amplitude vector,  $\omega$  is the angular frequency of the wave and  $\vec{k}$  is the wavevector. By differentiating the magnetic field analogue with respect to time and solving for  $\vec{H}$ , Equation B.2 becomes

$$\begin{aligned} i\omega\mu\vec{H} &= -\nabla\times\vec{E} \\ \vec{H} &= -\frac{1}{i\omega\mu}\nabla\times\vec{E} \\ \vec{H} &= \frac{i}{\omega\mu}\nabla\times\vec{E}. \end{aligned} \quad (\text{B.4})$$

Now that the magnetic field vector has been solved in terms of the electric field, boundary conditions can be imposed at a dielectric interface. More specifically, application of Stoke's Theorem to Maxwell's Equation leads to the boundary conditions

$$\begin{aligned} \vec{E}_{1t} &= \vec{E}_{2t} \\ \vec{H}_{1t} &= \vec{H}_{2t} \end{aligned} \quad (\text{B.5})$$

in the absence of any surface current density. Here the subscripts indicate the medium index (i.e. 1 or 2) and the t stands for transverse. If we now assume a TE (Transverse Electric) or s-polarized wave, the electric field is perpendicular to the plane of incidence (e.g. x-z) and the relationship  $\vec{E} = \vec{E}_y$  holds as seen in Fig. B.1.<sup>138</sup>

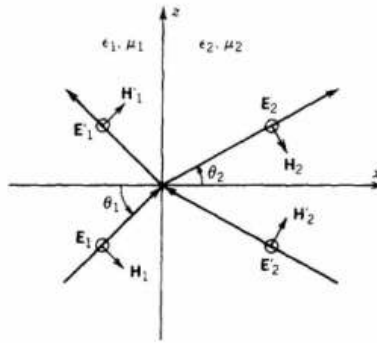


**Fig. B.1 | Reflection of an S polarized (TE) wave at a dielectric interface.**

Furthermore, because the electric field is oscillating in the transverse direction, it is entirely tangential so that incident the total electric field must be continuous across the boundary. In the case of the s-polarized wave, solving for the boundary conditions of the magnetic field is not so trivial. Luckily we have already solved for the magnetic field in terms of the electric field and further manipulation results as follows

$$\vec{H} = \frac{i}{\omega\mu} \nabla \times \vec{E}$$

$$\vec{H} = \frac{i}{\omega\mu} \begin{vmatrix} \hat{i} & \hat{j} & \hat{k} \\ \frac{\partial}{\partial x} & \frac{\partial}{\partial y} & \frac{\partial}{\partial z} \\ 0 & E_y & 0 \end{vmatrix}$$

$$\vec{H} = \frac{i}{\omega\mu} \left( \frac{\partial}{\partial x} E_y \hat{k} - \frac{\partial}{\partial z} E_y \hat{i} \right) \tag{B.6}$$

$$\vec{H}_z = \frac{i}{\omega\mu} (-ik_x \vec{E})$$

$$\vec{H}_z = \frac{k_x}{\omega\mu} (\vec{E}) \quad \left( k_x = \frac{\omega n}{c} \cos(\theta) \right)$$

$$\vec{H}_z = \frac{n \cos(\theta)}{c\mu} (\vec{E}) \quad \left( n = \sqrt{\frac{\mu\epsilon}{\mu_0\epsilon_0}} \quad c = \sqrt{\frac{1}{\mu_0\epsilon_0}} \right)$$

$$\vec{H}_z = \sqrt{\frac{\epsilon}{\mu}} \vec{E} \cos(\theta)$$

Note that the cross product yields a z and x component for the electric field, however the  $\vec{H}_z$  component (tangential component) is the only quantity conserved across the interface and thus is the only one considered. Upon derivation, the x component of the propagation vector  $\vec{k}$  is revealed that the dependence of the transverse magnetic field on the incidence angle  $\theta$  is deduced. Reduction of terms yield the final equation and the boundary relations for a TE wave can finally be written

$$\vec{E}_{1s} + \vec{E}'_{1s} = \vec{E}_{2s} + \vec{E}'_{2s} \quad (\text{B.7})$$

$$\sqrt{\frac{\epsilon_1}{\mu_1}} (\vec{E}_{1s} - \vec{E}'_{1s}) \cos(\theta_1) = \sqrt{\frac{\epsilon_2}{\mu_2}} (\vec{E}_{2s} - \vec{E}'_{2s}) \cos(\theta_2).$$

Note that the numerical indexes represent the medium number (incident from medium 1 to 2), and ' indicates a reflected wave. Also,  $\theta_1$  is the angle of incidence and  $\theta_2$  is

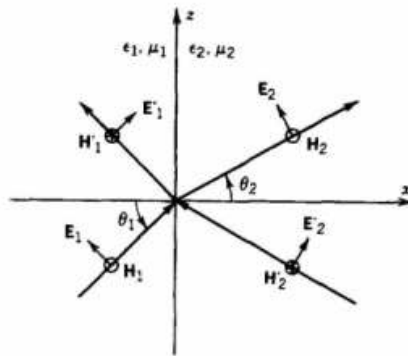


**Fig. B.2 | Reflection of an S polarized (TE) wave at a dielectric interface.**

derived from Snell's Law. Note that similar expressions are similarly derived for a TM, or p (as seen in Fig. B.2<sup>138</sup>), wave to be

$$(\vec{E}_{1p} + \vec{E}'_{1p}) \cos(\theta_1) = (\vec{E}_{2p} + \vec{E}'_{2p}) \cos(\theta_2) \quad (\text{B.8})$$

$$\sqrt{\frac{\epsilon_1}{\mu_1}} (\vec{E}_{1p} - \vec{E}'_{1p}) = \sqrt{\frac{\epsilon_2}{\mu_2}} (\vec{E}_{2p} - \vec{E}'_{2p}).$$

In order to characterize layered media, developing a formalism that scales well with a large number of layers is extremely important. Thus, the Equations B.7 and B.8 in can be rewritten as 2x2 matrix equations:

$$D_s(1) \begin{pmatrix} E_{1s} \\ E'_{1s} \end{pmatrix} = D_s(2) \begin{pmatrix} E_{2s} \\ E'_{2s} \end{pmatrix} \quad (\text{B.9})$$

$$D_p(1) \begin{pmatrix} E_{1p} \\ E'_{1p} \end{pmatrix} = D_p(2) \begin{pmatrix} E_{2p} \\ E'_{2p} \end{pmatrix}$$

where  $D_s(i)$  and  $D_p(i)$  are described by

$$D_s(i) = \begin{pmatrix} 1 & 1 \\ \sqrt{\frac{\epsilon_i}{\mu_i}} \cos(\theta_i) & -\sqrt{\frac{\epsilon_i}{\mu_i}} \cos(\theta_i) \end{pmatrix} \quad (\text{B.10})$$

$$D_p(i) = \begin{pmatrix} \cos(\theta_i) & \cos(\theta_i) \\ \sqrt{\frac{\epsilon_i}{\mu_i}} & -\sqrt{\frac{\epsilon_i}{\mu_i}} \end{pmatrix}$$

Now that the matrix formalism has been developed, it can be employed to treat propagation through layered media. Take, for example, the propagation of a right (A) and left (B) traveling wave seen in Fig. B.3.<sup>138</sup> This is simply one more layer of complexity as compared to the above analysis as it is reflection and refraction

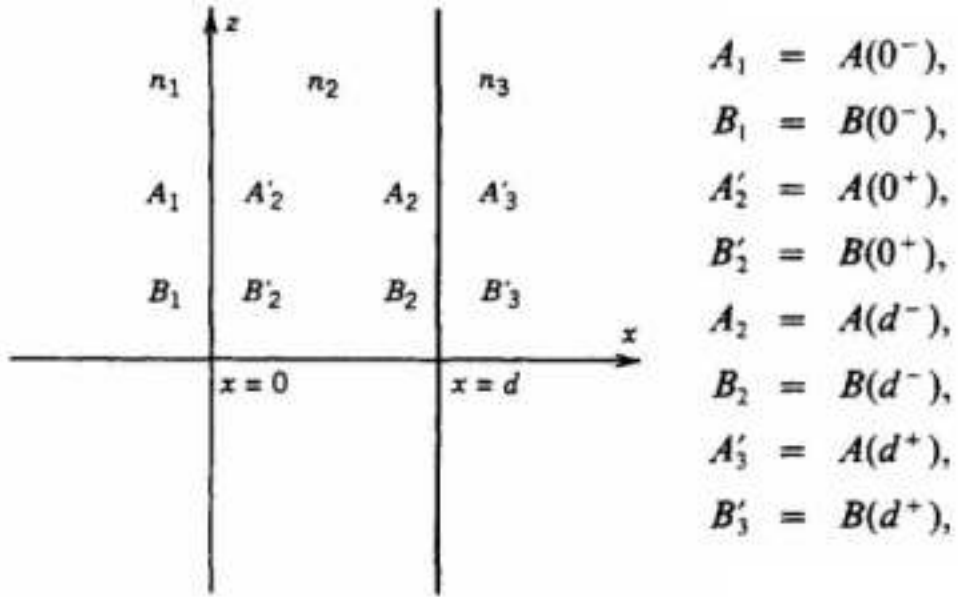


**Fig. B.3 | Electric field propagation across two interfaces.**

through two isotropic interfaces instead of one. Note that  $A(x)$  and  $B(x)$  are electric field amplitudes at  $x$ . Using Equations B.9 for the boundary conditions, the electric field amplitudes  $A_1$  and  $B_1$  can be solved for in terms of their respective matrixes and the vector containing  $A_2'$  and  $B_2'$  as seen in the below Equation set

$$\begin{pmatrix} A_1 \\ B_1 \end{pmatrix} = D_1^{-1} D_2 \begin{pmatrix} A_2' \\ B_2' \end{pmatrix} = D_{12} \begin{pmatrix} A_2' \\ B_2' \end{pmatrix} \quad (\text{B.11})$$

$$\begin{pmatrix} A_2' \\ B_2' \end{pmatrix} = P_2 \begin{pmatrix} A_2 \\ B_2 \end{pmatrix} = \begin{pmatrix} e^{-i\phi_2} & 0 \\ 0 & e^{-i\phi_2} \end{pmatrix} \begin{pmatrix} A_2 \\ B_2 \end{pmatrix}$$

$$\begin{pmatrix} A_2 \\ B_2 \end{pmatrix} = D_2^{-1} D_3 \begin{pmatrix} A_3' \\ B_3' \end{pmatrix} = D_{23} \begin{pmatrix} A_3' \\ B_3' \end{pmatrix}$$

Note that  $A_2$  and  $B_2$  can similarly be solved in terms of  $A_3'$  and  $B_3'$ . The middle Equation in B.11 denotes the propagation of the wave through a layer where the phase factor is given by  $\phi_2 = k_{2x}d$  (the right hand side of the equation is the product



of the (x component) wave vector in medium two and the respective thickness of layer 2). The equation relating the field amplitudes at  $A_3'$  and  $B_3'$  to  $A_1$  and  $B_1$  is

$$\begin{pmatrix} A_1 \\ B_1 \end{pmatrix} = D_1^{-1} D_2 P_2 D_2^{-1} D_3 \begin{pmatrix} A_3' \\ B_3' \end{pmatrix} \quad (\text{B.12})$$

It is clear that the multiplication of the matrixes will give a single 2x2 matrix that can be written in the general form

$$\begin{pmatrix} A_0 \\ B_0 \end{pmatrix} = \begin{pmatrix} M_{11} & M_{12} \\ M_{21} & M_{22} \end{pmatrix} \begin{pmatrix} A_s' \\ B_s' \end{pmatrix} \quad (\text{B.13})$$

where, once again, the coefficients of this matrix are defined by the product of the individual boundary conditions and propagation matrixes. Writing this in general form we have

$$\begin{pmatrix} M_{11} & M_{12} \\ M_{21} & M_{22} \end{pmatrix} = D_0^{-1} \left[ \prod_{l=1}^N D_l P_l D_l^{-1} \right] D_s \quad (\text{B.14})$$

Note the inner matrix product is a nice simplification of the matrix formalism and N is the number of layers. By simple expansion of Equation B.13, we find

$$\begin{pmatrix} A_0 \\ B_0 \end{pmatrix} = \begin{pmatrix} M_{11}A_s' + M_{12}B_s' \\ M_{21}A_s' + M_{22}B_s' \end{pmatrix} \quad (\text{B.15})$$

Since  $B_s'$  is the left propagating, right incident wave, it can be set to 0 as electric field intensity is assumed to be only incident from the left (or due to reflections, which don't happen at the Nth layer). We can note that general reflection (coefficient) from any surface is given by

$$r = \frac{E_{ref}}{E_{inc}} \quad (\text{B.16})$$

which is simply the ratio of reflected amplitude in comparison to incident amplitude. Applying this general theorem to the current problem (while setting right incident intensity  $B_s'$  to 0), we retrieve from Equation B.15 and B.16

$$R = |r|^2 = \left| \frac{B_0}{A_0} \right|_{B_s'=0}^2 = \left| \frac{M_{21}A_s'}{M_{11}A_s'} \right|_{B_s'=0}^2 = \left| \frac{M_{21}}{M_{11}} \right|_{B_s'=0}^2 \quad (\text{B.17})$$

Note that the reflectivity  $R$  is simply the squared magnitude of the reflection coefficient. The value of  $R$  can clearly be substituted into Equation 7.6 to find the loss of a generic ARROW. The benefit of the matrix formalism can now be seen as the reflectance (or transmittance) of a periodic dielectric mirror can be given by simple matrix multiplication, something computers are extremely efficient at; a process that has been programmed into a graphical user interface in the following section.

## ***B.2 arrowDesignv5.m ARROW Loss Calculator***

First and foremost, I would like to thank Kaelyn Leake and Jennifer Black for their help in the development of this application. Kaelyn's work on unifying the GUI and Jennifer's help on the "Custom" ARROW calculator saved me countless hours of toil. An image of the general GUI window, fully expanded, is shown in Fig. B.4. Similar to the T3RViewer in Section A.1, the filling options only appear as they are useful to input. We can see that the beginning point of the program is ARROW condition equation (1). While it is possible to input desired fabrication parameters directly into the input boxes (2), it is advisable to check example inputs by pressing the "Example" button first (3). Note that the inputs can be easily cleared using the "Clear" button (4). Using the ARROW equation (1), arrowDesign can also calculate

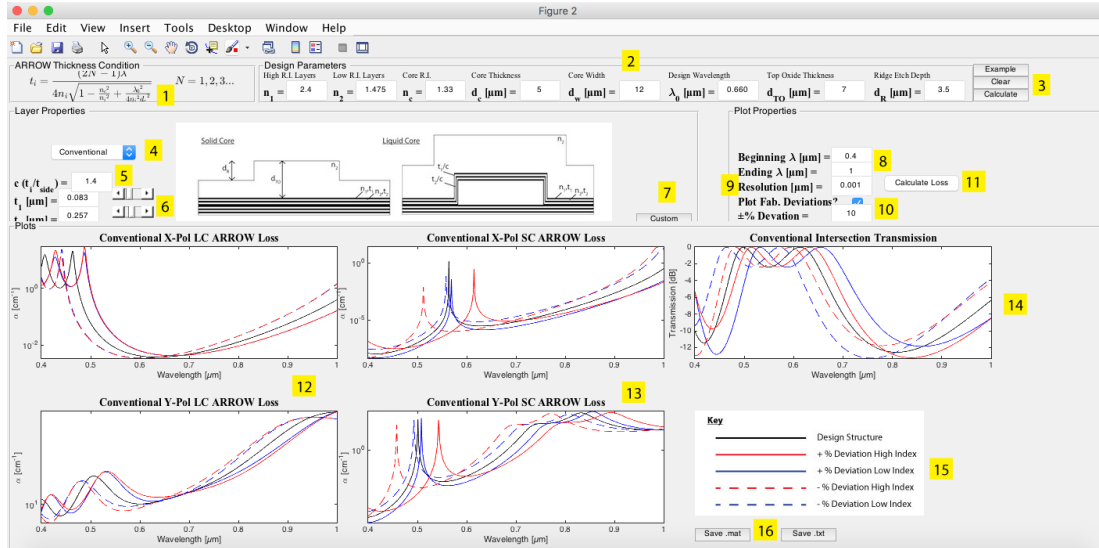


**Fig. B.4 | arrowDesignv5.m main window.** Numbers are described throughout the textual explanation.

the antiresonant thickness for input parameters (3), populating the thickness boxes  $t_1$  and  $t_2$  (6). By default, the designer is set for conventional ARROW waveguide design, with bottom and top layers (4). In the case of conventional devices, it is necessary to input a conformality ratio  $c = t_{//}/t_{\perp}$  (i.e. the deposition thickness for sputtered films on surfaces parallel to the wafer surface divided by the thickness of the films deposited on surfaces perpendicular to wafer surface—e.g. side walls) (5). Instead of using the generic ARROW structures from (4), it is also possible to use a custom dialogue to create arbitrary structures (7) (this function will be described separately, later).

The plot properties define the computational window for the loss calculation. It is possible to define a beginning and ending wavelength (8), a resolution for the calculation (9) (note this can dramatically increase calculation times if set too low), and a fabrication deviation (10). Note that this last input is an option, and will

recalculate the typical loss calculation with  $\pm$  the input percentage deviation applied to the different layer thicknesses. Once the “Calculate Loss” button is pressed **(11)**, the entire calculation will complete in one process. Plots will be displayed according to the selections of ARROW type (e.g. “Conventional”) and deviation options. Liquid-core **(12)** and solid-core waveguide losses **(13)** are plotted in addition to intersection transmission **(14)**. A key is present to demonstrate the different deviation plot line styles **(15)**. Finally, the data can be saved in .mat or .txt file formats for future use.

In addition to the generic calculations, it is also possible to solve losses for custom waveguide structures **(7)**. Shown in Fig. B.5, five vectors must be input for custom calculations. The “Top Index” and “Bottom Index” vectors define the

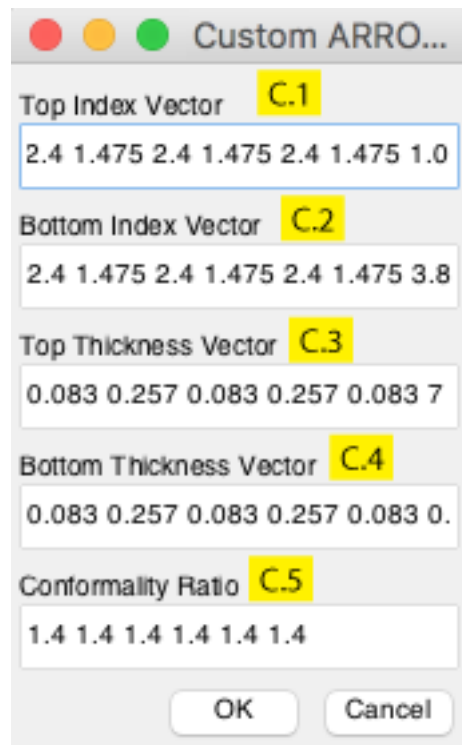


Fig. B.5 | Custom ARROW calculation dialogue box.

refractive index sequence of the layers, and can be of arbitrary lengths  $N$  and  $M$ , respectively **(C.1, C.2)**. The “Top Thickness” and “Bottom Thickness” vectors define the layer thickness sequences, and of arbitrary lengths  $N-1$  and  $M-1$ , respectively **(C.3, C.4)**. Note, decrements from  $N$  and  $M$  come from the fact that the terminal index is considered infinite in the matrix calculations. Finally, the conformality ratio, similarly to **(5)**, is defined for each individual top layer, at an arbitrary length of  $N-1$  **(C.5)**. Note that this dialogue uses the core parameters defined in **(2)**.

## **C. PDMS Waveguide Fabrication**

The fabrication of PDMS waveguides differs from generic automaton fabrication only by a single step – the spin deposition of 5:1 PDMS to form a high refractive index solid core. However, in this section I will provide a thorough consideration of PDMS fabrication techniques, especially as they pertain to PDMS waveguide manufacture. I will outline the steps of the fabrication and follow this with notes from an example fabrication run. I would like to thank GM Meena for his help in honing the fabrication process and procedures.

### **C.1 SU-8 Master Fabrication**

SU-8 lithography is a standard procedure involving steps that vary from cleanroom to cleanroom. While the minute details of the procedure are beyond the scope of this thesis, a general fabrication workflow for the University of California Santa Cruz cleanroom will be presented below.

#### **Silicon Wafer Preparation**

- 1) Spray blank Si with IPA, blow dry with Nitrogen
- 2) Bake in 60 °C oven for >1 hour (overnight if possible)
- 3) Reactive ion etch in oxygen plasma at 80% power for 10 min (recipe: "80p\_10min")

#### **SU8 2005 Spin procedure**

- 1) 500 RPM 10 sec @ 100 RPM/s ramp
- 2) 3500 RPM 60 sec @ 300 RPM/s ramp
- 3) 0 RPM 0 sec @ 500 RPM/s ramp

### **Soft Bake**

- 1) Bake @ 65 °C 1 min
- 2) Bake @ 95 °C 6 min
- 3) Bake @ 65 °C 1 min
- 4) 3 min rest at room temperature (can be ~3 min rest, until wafer is cool)

### **Edge Bead Removal (Acetone)**

- 1) Spin at 700 RPM after baking procedures
- 2) Use a 30-gauge syringe to squirt edge of wafer with acetone for 5-10 seconds, i.e. until clearly a contrasted edge appears. Note: initiate the stream of acetone by pressing hard on the plunger before the needle is over the wafer. Slowly bring the needle towards the edge of the wafer, with the stream perpendicular to the tangent of the edge. The needle should be angled at 30 ° from horizontal. Continue spraying until the edge bead is removed and slowly move stream off of the wafer. Only once the stream is no longer over the wafer is the flow stopped.
- 3) Ramp to 1500 RPM @ 300 RPM/s, 5 seconds
- 4) Ramp to 2500 RPM @ 1000 RPM/s, 10 sec

### **Exposure**

Expose with mask aligner for 4.5 sec @ 8.0 mW/cm<sup>2</sup>

### **Post Exposure Bake (PEB)**

- 1) 6 min @ 65 °C
- 2) 6 min @ 95 °C

3) 7 min @ 65 °C

4) 5 min rest at RT

### **Development**

8 seconds developer spray + 10 sec IPA

NOTE: If white residue remains on wafer after development, spray with developer for a couple more seconds followed by 10 seconds of IPA. Repeat this process until all residue is removed while being careful not to lift off features.

### **Hard Bake**

200 °C 5 min

NOTE: if cracks do not disappear, repeat 200 °C bake for another 5 minutes.

### **Flood Exposure**

Expose 30 sec @ 8.0 mW/cm<sup>2</sup> (not sure if this step does anything, but could increase mask sturdiness).

### **Common Pitfalls for SU-8 Master Fabrication:**

Below is a list of common pitfalls to avoid during fabrication of SU-8 master wafers:

- If the wafer is improperly cleaned, contaminant dust will destroy features and reduce lithography effectiveness.
- SU-8 should be poured onto the wafer directly after plasma cleaning. If delayed, the adhesion of the photoresist is dramatically reduced (on the order of minutes).
- Hard contact should always be used for best feature resolution.



- Bath development of SU-8 is inconsistent and should be avoided, i.e. use of a spray bottle of SU-8 developer over a waste container is advised.
- It is possible that partially lifted-off features can be melted back onto the wafer during the hard bake step, so it is advised to delay destruction of a master wafer until after this step.

## ***C.2 PDMS Waveguide Fabrication Overview***

Mix 5:1 and 10:1 PDMS (10 g and 50 g, respectively, for one wafer set). Use an IPA cleaned glass rod to mix the precursor and base together in plastic cup. Mix slowly in the beginning so as not to spill the curing agent. Next, thoroughly mix the PDMS until it is saturated with bubbles, i.e. it becomes opaque from the presence of many small bubbles, the process should take about 5 minutes. It should be noted that if too much PDMS is mixed in a single cup, it becomes difficult to pour with reproducible rates and bubbles can occur. As such a maximum of 60-80 g of PDMS should be mixed in one cup. Degas both PDMS mixtures for 2 hours in a vacuum desiccator. Keep the plastic lid on top of the cups containing PDMS (this reduces the infiltration of dust when opening the chamber) but do not close it all the way (as the lids will burst off when sufficient vacuum has been reached).

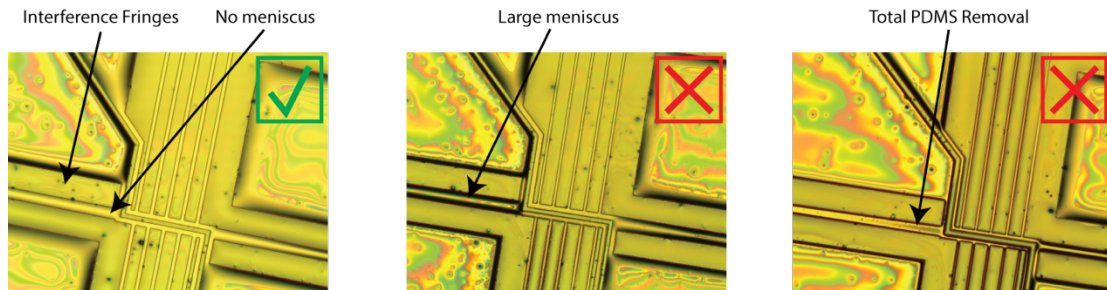
While degassing the PDMS, clean the SU-8 masters by peeling any residual PDMS and then spray with IPA. Prepare a vacuum desiccator for silanization by placing 3-4 drops of trichloro(1*H*,1*H*,2*H*,2*H*-perfluorooctyl)silane onto a glass slide inside the chamber using a clean Pasteur pipette (note: this chemical should always be opened/handled in a fume hood). Silanize the waveguide and control masters for 40

minutes in the vacuum desiccator. Keep the wafers as far away from the silane source as possible. After removing from wafers from the silanization chamber, pass a stream of nitrogen over them to remove any dust particles.

Once the PDMS is sufficiently degassed (approximately 2 hours), hold the waveguide master wafer in one hand and pour 5:1 PDMS in the center of the wafer. Pouring should occur with the edge of the cup as close to the wafer as possible without touching, and at a very slow rate. Continue pouring until approximately  $2/3^{\text{rds}}$  of the wafer is covered. Tilt the cup and while twisting it to stop pouring the PDMS. Slowly tilt/rotate the wafer so as to cover all the features with 5:1 PDMS. Place the wafer inside the spin coater and use the following spin recipe to coat it:

### 5:1 PDMS spin procedure

- 1) 500rpm for 10sec @ 100rpm/s ramp



Spin time / Spin speed / 5:1 Dilution

**Fig. C.1 | 5:1 PDMS spinning characteristics.** Note that as the spin time, spin speed, or dilution is increased, the results are achieved from left to right.

- 2) 5000rpm for 900sec @ 600rpm/sec ramp (after completion, check for meniscus formation/thin layer interference fringes and repeat as necessary, see Fig. C.1 for details).

3) 0rpm for 0sec @ 500rpm/sec ramp

Note that this spin step is crucially important as it defines the core of the PDMS waveguide. In Step 2 of the spin procedure, it is mentioned that waveguide features should be checked under a microscope to ensure that waveguide indentations are filled with 5:1 PDMS without meniscus formation – see Fig. C.1. This insures a homogeneously defined rectangular waveguide core. Furthermore, the PDMS layer on top of the SU-8 features should be thin enough to show interference fringes under a microscope – this insures that there is little to no waveguide “pedestal” formation. Note: pedestal is used here to define a thin layer of 5:1 PDMS on top of and outside of the core waveguide region. Such a feature creates lateral divergence of light and poor waveguiding. Pedestal can be removed in multiple ways, including increasing the 5:1 spin speed, increases the 5:1 spin time, or diluting the 5:1 PDMS with solvents to reduce its viscosity.<sup>145,146</sup> Here, we have opted away from solvent dilution as it created somewhat irreproducible refractive index effects. Once an optical profile of 5:1 PDMS such as that seen in the left of Fig. C.1 is achieved, place the waveguide master in oven for 2 hours at 60 °C for curing.

While the 5:1 PDMS is curing on the master, clean the acrylic molding plates with H<sub>2</sub>O, Alconox, and IPA for casting the control master wafer. Also remove previous residual PDMS from the screws used to clamp the plates.

Once the 5:1 PDMS is fully cured (2 hours), spin 10:1 PDMS onto the waveguide master mold. Use the same procedure for pouring 10:1 PDMS as used for 5:1. The

following spin recipe is used to create a uniform  $\sim 50 \mu\text{m}$  continuous PDMS membrane that allows for valve actuation:

**10:1 PDMS Spin Procedure**

- 1) 500rpm for 10sec @ 100rpm/sec ramp
- 2) 2000rpm for 600sec @ 600rpm/sec ramp
- 3) 0rpm for 0sec @ 500rpm/sec ramp

During the 10:1 spin coating, begin preparing the control master for 10:1 drop casting using the following steps:

- I. Place the control master wafer between acrylic plates 1 and 2 with clamping screws in place.
- II. Arrange the wafer such that PDMS won't seep between the acrylic plates.
- III. Pour 10:1 PDMS on the center of the control wafer very slowly (using similar technique for the spin pouring procedures). Pour enough PDMS such that it slightly over flows around the topmost ring acrylic. Acrylic plates are to be used in order and are illustrated in Fig. C.2:
  1. Rectangular plate: acrylic plate with no ring. Control master wafer is placed on top of this plate.
  2. Rectangular wafer window plate: 1/8" thickness with wafer shaped ring in the center and holes in the corners.
  3. Rectangular polygon plate: 3/8" thickness with polygon shaped cutouts for PDMS extrusion and holes in the corners. Note: it should be assured that this plate will fit onto the alignment stage's posts before casting PDMS.

When assembling this plate with the others, it should be placed very gently on the PDMS meniscus such that the air bubbles escape through the polygons. This plate is used as the mechanical base for the PDMS mold during alignment and bonding.

- IV. Carefully tighten nuts onto the screws, clamping the plates 1-3 together with the control master in the center.

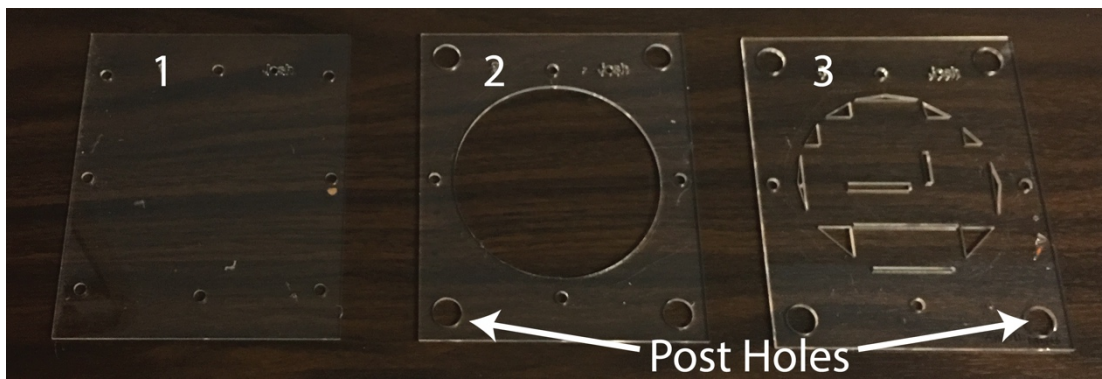


**Fig. C.2 | Control master mold casting assembly.** Plate 1 is the base rectangular plate that the master wafer sits on, plate 2 is the rectangular wafer window plate, allowing for PDMS pouring, and plate 3 is the rectangular polygon plate that is used for mechanical stability to prevent PDMS shrinkage during alignment/bonding.

Finish the casting procedure by placing both the waveguide and control masters (with uncured 10:1 PDMS on each) into the 60 °C oven for a 2-hour cure.

After curing, remove both the waveguide and control master molds from the oven. Gently remove the clamping screws from control master mold assembly so as not to disturb the 10:1 PDMS mold. Slowly remove the bottom (1) acrylic plate. The control master wafer will be stuck to the 10:1 PDMS. Use a razor blade to create a wedge between the wafer and the PDMS near a featureless region. Pour IPA in between the gap created and slowly remove the wafer while maintaining constant supply of IPA between wafer and PDMS. Next remove the wafer window plate (2). Only the PDMS

mold attached to the topmost polygon plate (due to deliberate PDMS overfilling) will remain. Clean the PDMS mold with IPA after removing the control master wafer. Blow dry thoroughly with a stream of nitrogen. Protect the bonding surface by covering it with overlaying Scotch Magic Tape (note: the brand is important to insure no residual adhesive is introduced into the device).

Place the waveguide master mold/wafer onto the alignment stage such that it is

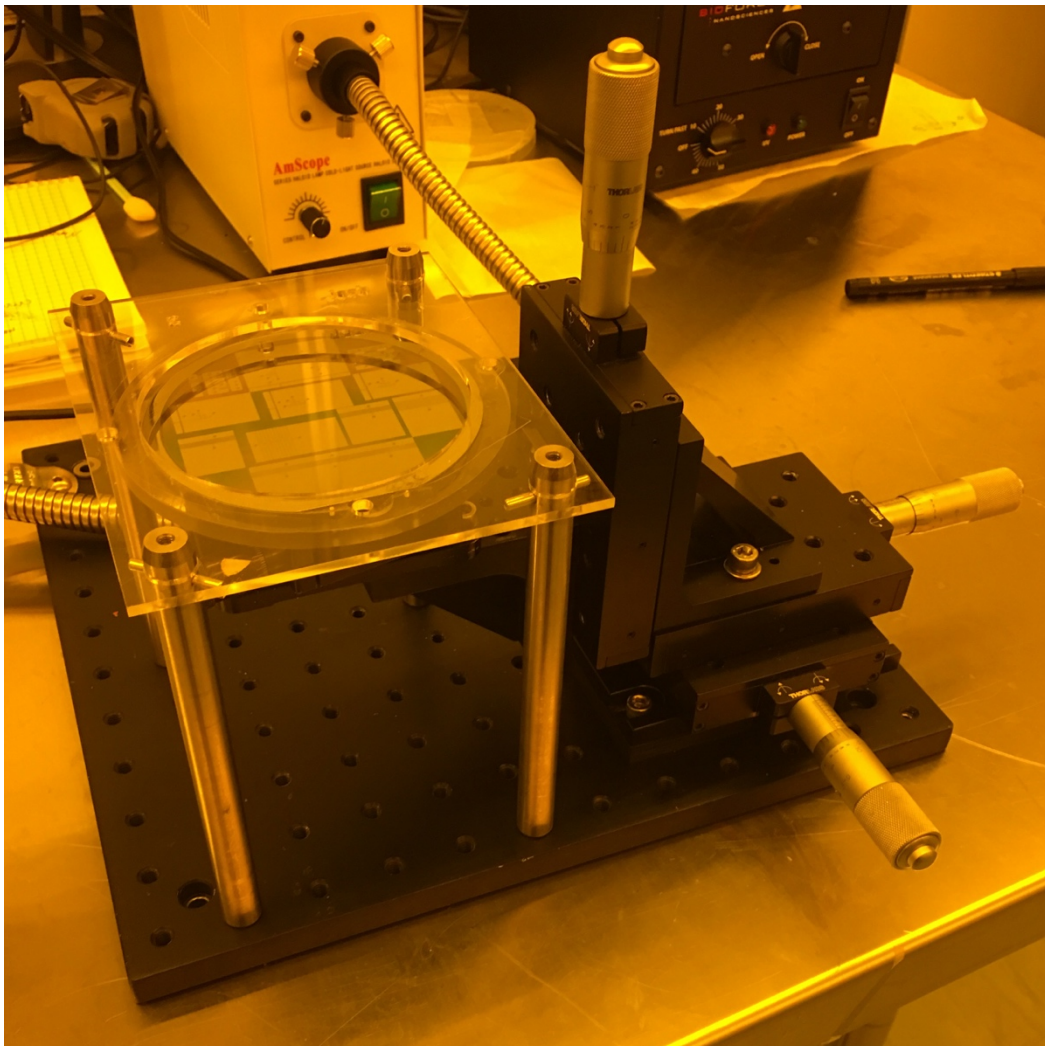


**Fig. C.3 | PDMS alignment stage.** Note that the acrylic plate will be a polygon plate (3) during the actual procedure.

flat and it is at the bottom of the custom acrylic holder. Make sure of this using a level scale on the stage itself before placing the wafer onto it. Fit the control PDMS master mold/polygon plate onto the alignment posts after removing the protective tape. The alignment setup is shown in Fig. C.3. Note that there the plate in the image is a wafer window plate (used here so that the wafer is in view), however, during an actual fabrication, a polygon plate with attached control mold will be in its place.

Slowly bring the waveguide master mold/wafer close to the control mold. Due to reflections, there will be a secondary virtual image during the alignment process. It is important to use the top (upper most vertical focused) image for the alignment. Choose a feature and align it using the x-y movement of the translational stage (preferably these are alignment features near the center of the wafer). Next, use the rotational stage to align a feature near the edge of the wafer. Repeat this process iteratively, until an optimal alignment is achieved.

Remove both molds from the assembly and place them into the reactive ion etcher for plasma activation of the surfaces (both bond surfaces should be facing up during the activation). Replace the molds into their respective positions in the alignment setup and do a final quick alignment step, finally bringing the two surfaces into contact for bonding. Retain contact overnight in a 60 °C oven.

Remove the bonded molds from the oven and cut the polygon extrusions using a razor blade. Carefully remove the bonded devices from the plate and then the waveguide master wafer, using techniques described above. Again, protect the device surface using Scotch Magic Tape. Mark punch holes with a Sharpie, and punch

control inlets using a 500  $\mu\text{m}$  diameter punch, and fluidic inlets using a 1 mm diameter punch. Dice the devices using a razorblade and store them in a petri dish.

To prepare for device completion, insure that a setup is available for applying vacuum to the control inlets of the devices to be bonded. Cast a 10:1 blank master mold for use as the fourth wall of the PDMS waveguide devices. Once complete, cut a piece slightly larger than the device to be bonded. Note that the bonding surface should be the wafer side of the blank mold, to insure superior flatness. Treat both surfaces (waveguide and blank) with oxygen plasma activation. Quickly remove the

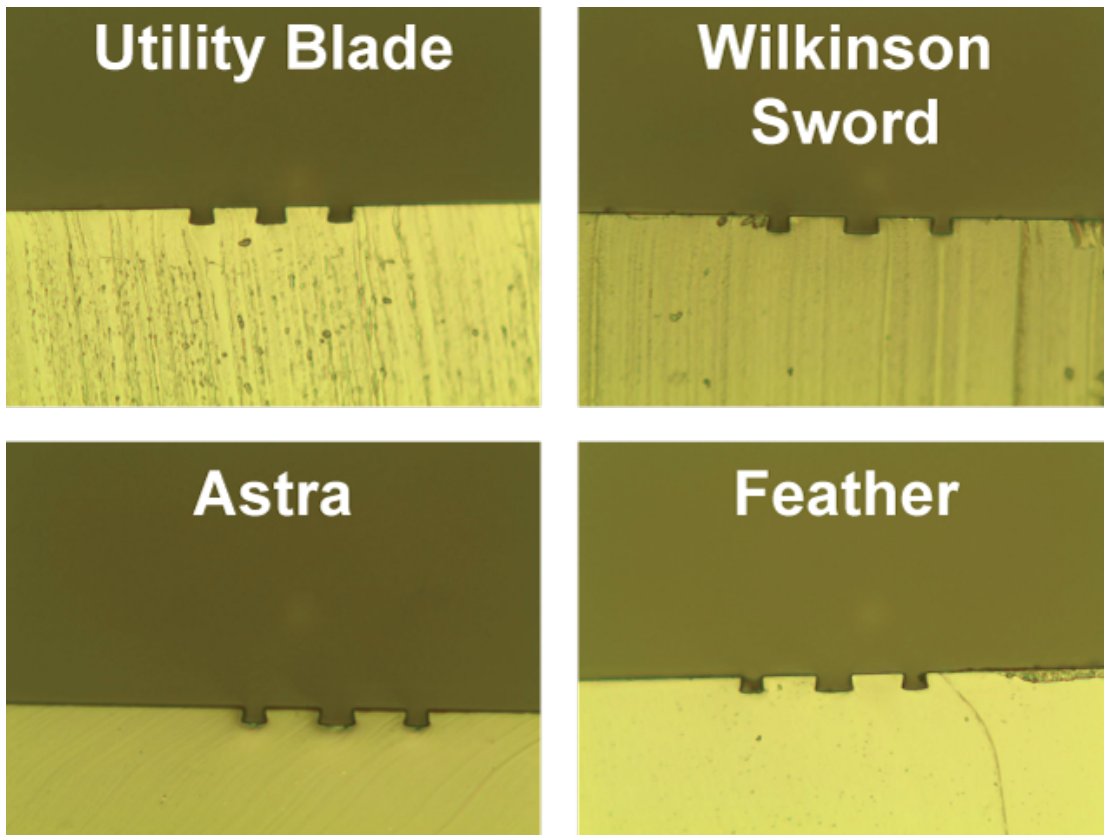


**Fig. C.4 | PDMS surface images after dicing with different razor blades.** The utility blade is a thick blade made for general purpose cutting while the other blades are commercial razor blades designed for shaving.



pieces from the chamber and place the devices onto the vacuum system, applying negative pressure to the control inlets and lifting the valves into the up position. This process insures the valve seats aren't bonded to the substrate. Gently bring the activated, blank PDMS surface into contact with the waveguide surface, attempting to mitigate any bubble formation. Allow the devices to bond overnight. The bonding can occur at room temperature, however, to create a stronger bond, it is advisable to bond the fourth wall of the device on a 60 °C hotplate.

The final step of device fabrication is waveguide facet exposure. As mentioned in the body of the thesis, using a commercial razor blade is important to insure facets with optical grade surface smoothness. Testing clearly shows that commercial utility razor blades are tooth thick/dull for this purpose. Using commercial razor blades designed for shaving<sup>135</sup>, it is possible to create much cleaner facets, as shown in Fig. C.4. Clearly, the Feather (product name: New Hi-Stainless Double Edged Blade, supplier: Amazon) blade performed the best and is currently the best option. Before dicing the PDMS, the blade should be inserted into the custom blade holder, and used to cut cleaned (using Scotch Magic Tape) pieces of blank PDMS. A microscope should be used to inspect the quality of the test cuts for both sides of the reversible blade, and the sharper side should be used for dicing. Clean the top side of the device with Scotch Magic Tape, place the device ontop of a recycled piece of blank PDMS, and align the blue to the cutting point. Press the blade down in a directly perpendicular fashion, swiftly cutting through the entire device and partially into the

recycled PDMS. After inspecting the optical facets under the microscope to insure proper dicing, any dirt/dust can be removed from the facet using Scotch Magic Tape.

**Common Pitfalls for PDMS Waveguide Fabrication:**

Below is a list of common pitfalls to avoid during fabrication of PDMS waveguide chips:

- Quick degassing (via centrifugation) and pouring of PDMS leads to a lower viscosity polymer mixture, which in turn results in trapped air bubbles during pouring. It is advisable to wait at least 2 hours before pouring degassed PDMS mixtures.
- Over-spinning of 5:1 PDMS layers will result in poor fill factors for features with width/height ratios greater than 1. Similarly, under-spinning of 5:1 PDMS layers will result in a continuous layer of high refractive index PDMS leading to poor optical confinement and high scattering backgrounds.
- Poor refractive index contrast results from under-curing or over-curing of 5:1 PDMS (i.e. use 2 hour cure time at 65 °C).
- After curing control master molds, it is important that the mold stays in contact with the acrylic molding foundation plate. If the mold delaminates/removes from the plate, PDMS will shrink and wafer scale alignment is no longer possible.
- Substrate 10:1 PDMS pieces should be cut larger than the chip that it will be bonded with. This is to allow for a clean facet/edge after cutting.

- If dicing PDMS before bonding to non-PDMS substrates, it is important to make sure the PDMS is larger than substrate itself such that the waveguide facets will be accessible via fiber. Furthermore, it is important to cut the chip starting from the top (opposite of the waveguide side) to ensure quality facets.
- Razor blades should be checked and refreshed often (~10 cuts per blade) in order to mitigate poor facet creation.
- Bonding should always be conducted using gentle contact, otherwise feature deformation often occurs.
- Once activated PDMS surfaces have contacted one another, they should not be repositioned as it destroys the bonding potential.
- After completion of fabrication, there should be no residual PDMS on the master wafers. If there is, it is likely that there is damage within the fabricated chips.

### ***C.3 Fabrication Characterization Worksheet***

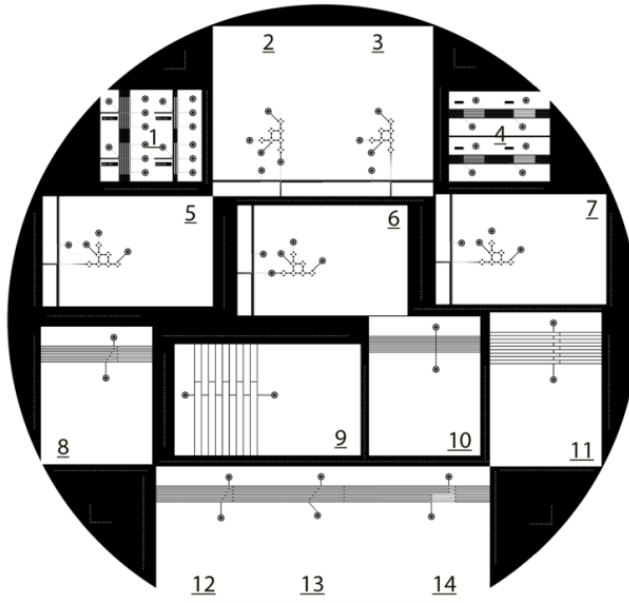
Master wafers, master molds, and PDMS chips should be monitored throughout the fabrication workflow. An example characterization sheet used for recording optical inspection of masters/samples is presented on the following two pages. The file is accessible with the following name: AWG\_PDMSWG\_InspectionSheet\_2.ai. Note that defects are marked on the wafer images themselves while overall chip quality is denoted symbolically (e.g. ++).

AW \_\_\_\_\_ - AWC \_\_\_\_\_  
 (Master<sub>Casting</sub>) (Master<sub>Casting</sub>)

Name: \_\_\_\_\_

**Waveguide Master Inspection**

Inspection of actual SU8 master for defects



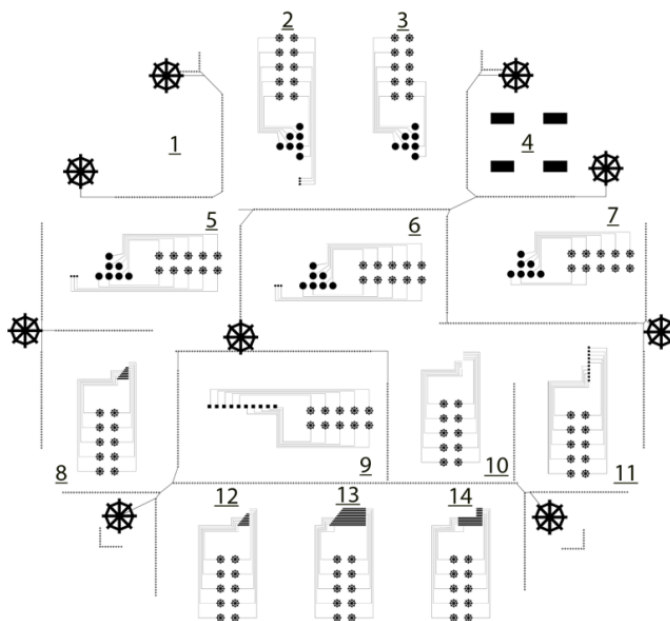
**Inspection Standards**

- ++ Excellent (likely working)
- + Good with minor defects (probably working)
- Many defects (possibly working)
- Major defects (probably not working)
- x Unusable

- 1 \_\_\_\_\_
- 2 \_\_\_\_\_
- 3 \_\_\_\_\_
- 4 \_\_\_\_\_
- 5 \_\_\_\_\_
- 6 \_\_\_\_\_
- 7 \_\_\_\_\_
- 8 \_\_\_\_\_
- 9 \_\_\_\_\_
- 10 \_\_\_\_\_
- 11 \_\_\_\_\_
- 12 \_\_\_\_\_
- 13 \_\_\_\_\_
- 14 \_\_\_\_\_

**Control Master Inspection**

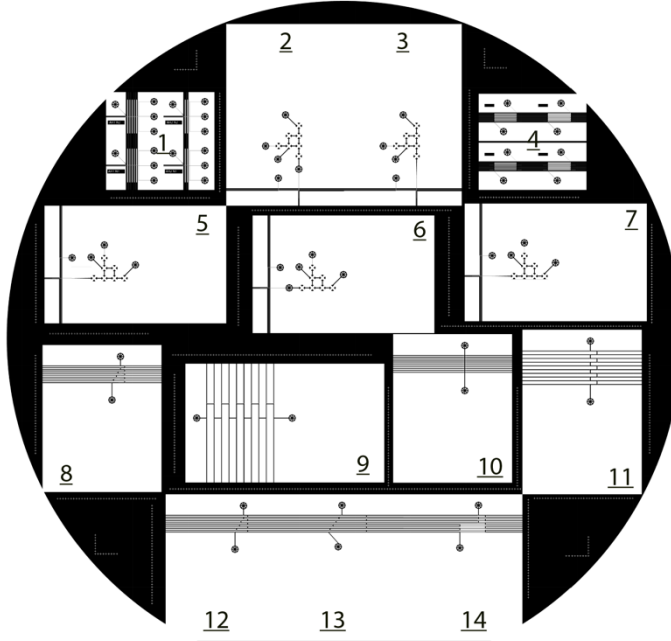
Inspection of actual SU8 master for defects



- 1 \_\_\_\_\_
- 2 \_\_\_\_\_
- 3 \_\_\_\_\_
- 4 \_\_\_\_\_
- 5 \_\_\_\_\_
- 6 \_\_\_\_\_
- 7 \_\_\_\_\_
- 8 \_\_\_\_\_
- 9 \_\_\_\_\_
- 10 \_\_\_\_\_
- 11 \_\_\_\_\_
- 12 \_\_\_\_\_
- 13 \_\_\_\_\_
- 14 \_\_\_\_\_

### Waveguide Casting Inspection

Inspection of SU8 Master after removing casting, checking for implied waveguide damage  
(Also note any problems with spin of base layer here)



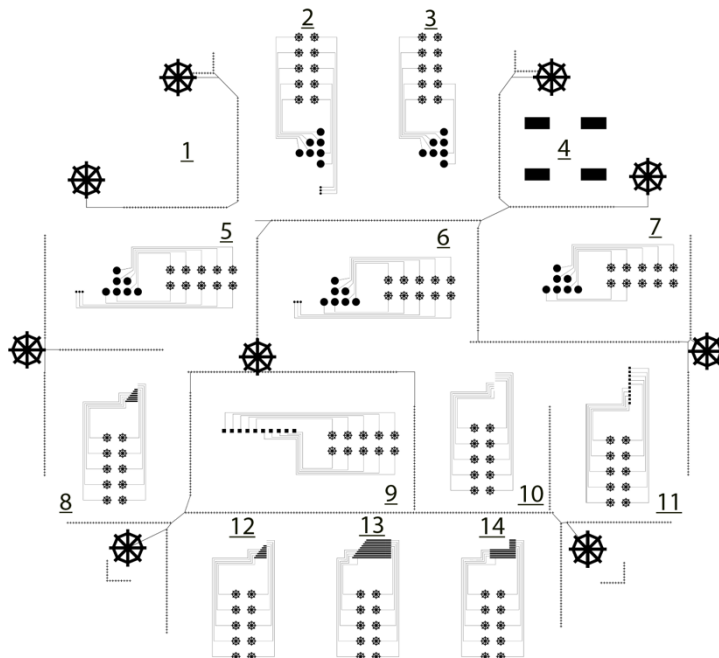
### Inspection Standards

- ++ Excellent (likely working)
- + Good with minor defects (probably working)
- Many defects (possibly working)
- Major defects (probably not working)
- x Unusable

- 1 \_\_\_\_\_
- 2 \_\_\_\_\_
- 3 \_\_\_\_\_
- 4 \_\_\_\_\_
- 5 \_\_\_\_\_
- 6 \_\_\_\_\_
- 7 \_\_\_\_\_
- 8 \_\_\_\_\_
- 9 \_\_\_\_\_
- 10 \_\_\_\_\_
- 11 \_\_\_\_\_
- 12 \_\_\_\_\_
- 13 \_\_\_\_\_
- 14 \_\_\_\_\_

### Control Casting/Bonding Inspection

Inspection of casting including punches and bonding to membrane layer,



- 1 \_\_\_\_\_
- 2 \_\_\_\_\_
- 3 \_\_\_\_\_
- 4 \_\_\_\_\_
- 5 \_\_\_\_\_
- 6 \_\_\_\_\_
- 7 \_\_\_\_\_
- 8 \_\_\_\_\_
- 9 \_\_\_\_\_
- 10 \_\_\_\_\_
- 11 \_\_\_\_\_
- 12 \_\_\_\_\_
- 13 \_\_\_\_\_
- 14 \_\_\_\_\_

## 10 Bibliography

1. Parks, J. W., Wall, T. A., Cai, H., Hawkins, A. R. & Schmidt, H. Enhancement of ARROW Photonic Device Performance via Thermal Annealing of PECVD-Based SiO<sub>2</sub> Waveguides. *IEEE J. Sel. Top. Quantum Electron.* **22**, 1–6 (2016).
2. Parks, J. W. *et al.* Hybrid optofluidic integration. *Lab. Chip* **13**, 4118–4123 (2013).
3. Parks, J. W. *et al.* Integration of programmable microfluidics and on-chip fluorescence detection for biosensing applications. *Biomicrofluidics* **8**, 54111 (2014).
4. Cai, H. *et al.* Optofluidic analysis system for amplification-free, direct detection of Ebola infection. *Sci. Rep.* **5**, 14494 (2015).
5. Ozcelik, D. *et al.* Optofluidic wavelength division multiplexing for single-virus detection. *Proc. Natl. Acad. Sci.* **112**, 12933–12937 (2015).
6. Parks, J. W. & Schmidt, H. Flexible optofluidic waveguide platform with multi-dimensional reconfigurability. *Sci. Rep.* **6**, 33008 (2016).
7. Nathanson, H. C., Newell, W. E., Wickstrom, R. A. & Davis, J. R. The resonant gate transistor. *IEEE Trans. Electron Devices* **14**, 117–133 (1967).
8. Roylance, L. M. & Angell, J. B. A batch-fabricated silicon accelerometer. *IEEE Trans. Electron Devices* **26**, 1911–1917 (1979).
9. Hornbeck, L. J. Deformable-Mirror Spatial Light Modulators. in **1150**, 86–103 (1990).

10. Peeters, E. & Verdonckt-Vandebroek, S. Thermal ink jet technology. *IEEE Circuits Devices Mag.* **13**, 19–23 (1997).
11. Whitesides, G. M. The origins and the future of microfluidics. *Nature* **442**, 368–373 (2006).
12. Duffy, D. C., McDonald, J. C., Schueller, O. J. & Whitesides, G. M. Rapid Prototyping of Microfluidic Systems in Poly(dimethylsiloxane). *Anal. Chem.* **70**, 4974–84 (1998).
13. Anderson, J. R. *et al.* Fabrication of topologically complex three-dimensional microfluidic systems in PDMS by rapid prototyping. *Anal. Chem.* **72**, 3158–64 (2000).
14. Oh, K. W. & Ahn, C. H. A review of microvalves. *J. Micromechanics Microengineering* **16**, R13 (2006).
15. Tan, Y.-C., Fisher, J. S., Lee, A. I., Cristini, V. & Lee, A. P. Design of microfluidic channel geometries for the control of droplet volume, chemical concentration, and sorting. *Lab. Chip* **4**, 292–298 (2004).
16. Cho, Y.-K. *et al.* One-step pathogen specific DNA extraction from whole blood on a centrifugal microfluidic device. *Lab. Chip* **7**, 565–73 (2007).
17. Zare, R. N. & Kim, S. Microfluidic platforms for single-cell analysis. *Annu. Rev. Biomed. Eng.* **12**, 187–201 (2010).
18. Manz, A., Graber, N. & Widmer, H. M. Miniaturized total chemical analysis systems: A novel concept for chemical sensing. *Sens. Actuators B Chem.* **1**, 244–248 (1990).

19. Psaltis, D., Quake, S. R. & Yang, C. Developing optofluidic technology through the fusion of microfluidics and optics. *Nature* **442**, 381–6 (2006).
20. Wolfe, D. B. *et al.* Dynamic control of liquid-core/liquid-cladding optical waveguides. *Proc. Natl. Acad. Sci. U. S. A.* **101**, 12434–8 (2004).
21. Xi, J.-Q., Kim, J. K. & Schubert, E. F. Silica Nanorod-Array Films with Very Low Refractive Indices. *Nano Lett.* **5**, 1385–1387 (2005).
22. Datta, A. *et al.* Microfabrication and characterization of Teflon AF-coated liquid core waveguide channels in silicon. *IEEE Sens. J.* **3**, 788–795 (2003).
23. Bernini, R., Campopiano, S. & Zeni, L. Silicon micromachined hollow optical waveguides for sensing applications. *IEEE J. Sel. Top. Quantum Electron.* **8**, 106–110 (2002).
24. Schmidt, H., Barber, J. P. & Hawkins, A. R. Hollow-core waveguides and 2-D waveguide arrays for integrated optics of gases and liquids. *IEEE J. Sel. Top. Quantum Electron.* **11**, 519–527 (2005).
25. Bernini, R. *et al.* Development and characterization of an integrated silicon micro flow cytometer. *Anal. Bioanal. Chem.* **386**, 1267–72 (2006).
26. Yin, D., Barber, J. P., Hawkins, A. R. & Schmidt, H. Highly efficient fluorescence detection in picoliter volume liquid-core waveguides. *Appl. Phys. Lett.* **87**, 211111 (2005).
27. Kühn, S., Phillips, B. S., Lunt, E. J., Hawkins, A. R. & Schmidt, H. Ultralow power trapping and fluorescence detection of single particles on an optofluidic chip. *Lab. Chip* **10**, 189–94 (2010).



28. Measor, P., Phillips, B. S., Chen, A., Hawkins, A. R. & Schmidt, H. Tailorable integrated optofluidic filters for biomolecular detection. *Lab. Chip* **11**, 899–904 (2011).
29. Nucleic Acid Stains—Section 8.1 | Thermo Fisher Scientific. Available at: <https://www.thermofisher.com/us/en/home/references/molecular-probes-the-handbook/nucleic-acid-detection-and-genomics-technology/nucleic-acid-stains.html>. (Accessed: 27th June 2016)
30. Rye, H. S. *et al.* Stable fluorescent complexes of double-stranded DNA with bis-intercalating asymmetric cyanine dyes: properties and applications. *Nucleic Acids Res.* **20**, 2803–2812 (1992).
31. Fürstenberg, A., Deligeorgiev, T. G., Gadjev, N. I., Vasilev, A. A. & Vauthey, E. Structure–fluorescence contrast relationship in cyanine DNA intercalators: toward rational dye design. *Chem. Eur. J.* **13**, 8600–8609 (2007).
32. Tyagi, S. & Kramer, F. Molecular Beacons : Probes that Fluoresce upon Hybridization. *Nat. Biotechnol.* (1996).
33. Marras, S. E. in *Fluorescent Energy Transfer Nucleic Acid Probes* (eds. Didenko, V. & MD, V. V. D.) 3–16 (Humana Press, 2006). doi:10.1385/1-59745-069-3:3
34. Duguay, M., Kokubun, Y., Koch, T. & Pfeiffer, L. Antiresonant reflecting optical waveguides in SiO<sub>2</sub>-Si multilayer structures. *Appl. Phys. Lett.* **49**, 13–15 (1986).

35. Yin, D., Schmidt, H., Barber, J. & Hawkins, A. R. Integrated ARROW waveguides with hollow cores. *Opt. Express* **12**, 2710–5 (2004).
36. Holmes, M., Liu, S. & Keeley, J. Hollow Waveguides with Low Intrinsic Photoluminescence Fabricated with PECVD Silicon Nitride and Silicon Dioxide Films. *IEEE Photonics Technol. Lett.* **23**, 1466–1468 (2011).
37. Zhao, Y. *et al.* Hollow waveguides with low intrinsic photoluminescence fabricated with Ta(2)O(5) and SiO(2) films. *Appl. Phys. Lett.* **98**, 91104 (2011).
38. Zhao, Y. *et al.* Tailoring the spectral response of liquid waveguide diagnostic platforms. *J. Biophotonics* **5**, 703–711 (2012).
39. Soref, R. A., Schmidtchen, J. & Petermann, K. Large single-mode rib waveguides in GeSi-Si and Si-on-SiO<sub>2</sub>. *IEEE J. Quantum Electron.* **27**, 1971–1974 (1991).
40. Measor, P. *et al.* Multi-mode mitigation in an optofluidic chip for particle manipulation and sensing. *Opt. Express* **17**, 24342–8 (2009).
41. Lunt, E. J. *et al.* Hollow ARROW Waveguides on Self-Aligned Pedestals for Improved Geometry and Transmission. *IEEE Photonic Technol. Lett.* **22**, 1147–1149 (2010).
42. Yin, D., Barber, J., Hawkins, A. R. & Schmidt, H. Waveguide loss optimization in hollow-core ARROW waveguides. *Opt. Express* **13**, 9331–6 (2005).
43. Zhao, Y., Leake, K., Measor, P., Jenkins, M. & Keeley, J. Optimization of Interface Transmission between Integrated Solid Core and Optofluidic Waveguides. *IEEE Photonics Technol. Lett.* **24**, 46–48 (2012).

44. Holmes, M., Keeley, J., Hurd, K., Schmidt, H. & Hawkins, A. R. Optimized piranha etching process for SU8-based MEMS and MOEMS construction. *J. Micromechanics Microengineering Struct. Devices Syst.* **20**, 1–8 (2010).
45. Measor, P. *et al.* Hollow-core waveguide characterization by optically induced particle transport. *Opt. Lett.* **33**, 672 (2008).
46. Kühn, S. *et al.* Loss-based optical trap for on-chip particle analysis. *Lab. Chip* **9**, 2212–6 (2009).
47. Measor, P. *et al.* On-chip surface-enhanced Raman scattering detection using integrated liquid-core waveguides. *Appl. Phys. Lett.* **90**, 211107 (2007).
48. Schmidt, H. *et al.* Rubidium spectroscopy on a chip. *Proc. SPIE* **6482**, 64820P–64820P–11 (2007).
49. Yang, W. *et al.* Atomic spectroscopy on a chip. *Nat. Photonics* **1**, 331–335 (2007).
50. Slow light on a chip. *Nat. Photonics* **4**, 798–798 (2010).
51. Phillips, B., Measor, P. & Zhao, Y. Optofluidic notch filter integration by lift-off of thin films. *Opt. Express* **18**, 2595–2597 (2010).
52. Ozcelik, D. *et al.* Dual-core optofluidic chip for independent particle detection and tunable spectral filtering. *Lab. Chip* **12**, 3728–33 (2012).
53. Rudenko, M. I. *et al.* Controlled gating and electrical detection of single 50S ribosomal subunits through a solid-state nanopore in a microfluidic chip. *Biosens. Bioelectron.* **29**, 34–9 (2011).

54. Liu, S. *et al.* Correlated electrical and optical analysis of single nanoparticles and biomolecules on a nanopore-gated optofluidic chip. *Nano Lett.* **14**, 4816–20 (2014).
55. Liu, S. *et al.* Electro-optical detection of single  $\lambda$ -DNA. *Chem Commun* **16**, 2084–2087 (2014).
56. Xia, Y. & Whitesides, G. Soft lithography. *Annu. Rev. Mater. Sci.* **37**, 550–575 (1998).
57. Sollier, E., Murray, C., Maoddi, P. & Di Carlo, D. Rapid prototyping polymers for microfluidic devices and high pressure injections. *Lab. Chip* **11**, 3752 (2011).
58. Mukhopadhyay, R. When PDMS isn't the best. *Am. Chem. Soc. Anal. Chemistry* 3249–3253 (2007). doi:10.1021/ac071903e
59. Unger, M., Chou, H., Thorsen, T., Scherer, A. & Quake, S. Monolithic microfabricated valves and pumps by multilayer soft lithography. *Science* **288**, 113–6 (2000).
60. Grover, W. H., Skelley, A. M., Liu, C. N., Lagally, E. T. & Mathies, R. A. Monolithic membrane valves and diaphragm pumps for practical large-scale integration into glass microfluidic devices. *Sens. Actuators B Chem.* **89**, 315–323 (2003).
61. Schudel, B. R., Choi, C. J., Cunningham, B. T. & Kenis, P. J. A. Microfluidic chip for combinatorial mixing and screening of assays. *Lab. Chip* **9**, 1676–80 (2009).

62. Kim, J., Kang, M., Jensen, E. C. & Mathies, R. A. Lifting gate polydimethylsiloxane microvalves and pumps for microfluidic control. *Anal. Chem.* **84**, 2067–71 (2012).
63. Kim, J., Jensen, E. C., Megens, M., Boser, B. & Mathies, R. A. Integrated microfluidic bioprocessor for solid phase capture immunoassays. *Lab. Chip* **11**, 3106–12 (2011).
64. Lunt, E. J. *et al.* Improving solid to hollow core transmission for integrated ARROW waveguides. *Opt. Express* **16**, 20981–6 (2008).
65. Ozcelik, D. *et al.* Signal-to-noise enhancement in optical detection of single viruses with multi-spot excitation. *IEEE J. Sel. Top. Quantum Electron.* **22**, 1–1 (2015).
66. Chongsawangvirod, S., Irene, E. A., Kalnitsky, A., Tay, S. P. & Ellul, J. P. Refractive Index Profiles of Thermally Grown and Chemically Vapor Deposited Films on Silicon. *J. Electrochem. Soc.* **137**, 3536 (1990).
67. Measor, P., Phillips, B. S., Chen, A., Hawkins, A. R. & Schmidt, H. Tailorable integrated optofluidic filters for biomolecular detection. *Lab. Chip* **11**, 899–904 (2011).
68. Zhao, Y., Leake, K., Measor, P., Jenkins, M. & Keeley, J. Optimization of Interface Transmission between Integrated Solid Core and Optofluidic Waveguides. *IEEE Photonics Technol. Lett.* **24**, 46–48 (2012).
69. Measor, P. *et al.* Multi-mode mitigation in an optofluidic chip for particle manipulation and sensing. *Opt. Express* **17**, 24342–8 (2009).

70. Yin, D., Deamer, D. W., Schmidt, H., Barber, J. P. & Hawkins, A. R. Single-molecule detection sensitivity using planar integrated optics on a chip. *Opt. Lett.* **31**, 2136–8 (2006).
71. Liu, S. *et al.* Electro-optical detection of single  $\lambda$ -DNA. *Chem Commun* **16**, 2084–2087 (2014).
72. Manz, A., Graber, N. & Widmer, H. M. Miniaturized total chemical analysis systems: A novel concept for chemical sensing. *Sens. Actuators B Chem.* **1**, 244–248 (1990).
73. Huang, B. *et al.* Counting low-copy number proteins in a single cell. *Science* **315**, 81–4 (2007).
74. Fan, X. & White, I. M. Optofluidic Microsystems for Chemical and Biological Analysis. *Nat. Photonics* **5**, 591–597 (2011).
75. Schmidt, H. & Hawkins, A. R. The photonic integration of non-solid media using optofluidics. *Nat. Photonics* **5**, 598–604 (2011).
76. Erickson, D., Rockwood, T., Emery, T., Scherer, A. & Psaltis, D. Nanofluidic tuning of photonic crystal circuits. *Opt. Lett.* **31**, 59–61 (2006).
77. Yin, D., Deamer, D. W., Schmidt, H., Barber, J. P. & Hawkins, A. R. Integrated optical waveguides with liquid cores. *Appl. Phys. Lett.* **85**, 3477 (2004).
78. Yin, D., Lunt, E. J., Barman, A., Hawkins, A. R. & Schmidt, H. Microphotonic control of single molecule fluorescence correlation spectroscopy using planar optofluidics. *Opt. Express* **15**, 7290–5 (2007).

79. Yin, D. *et al.* Planar optofluidic chip for single particle detection, manipulation, and analysis. *Lab. Chip* **7**, 1171–5 (2007).
80. Lee, K. S. & Ram, R. J. Plastic-PDMS bonding for high pressure hydrolytically stable active microfluidics. *Lab. Chip* **9**, 1618–24 (2009).
81. Bruus, H. *Theoretical Microfluidics*. (Oxford University Press, 2007).
82. Rudenko, M. I. *et al.* Ultrasensitive Qbeta phage analysis using fluorescence correlation spectroscopy on an optofluidic chip. *Biosens. Bioelectron.* **24**, 3258–63 (2009).
83. Fernandez, J. G., Mills, C. a., Rodríguez, R., Gomila, G. & Samitier, J. All-polymer microfluidic particle size sorter for biomedical applications. *Phys. Status Solidi A* **203**, 1476–1480 (2006).
84. Jensen, E. C., Bhat, B. P. & Mathies, R. A. A digital microfluidic platform for the automation of quantitative biomolecular assays. *Lab. Chip* **10**, 685–91 (2010).
85. Kim, J., Jensen, E., Stockton, A. & Mathies, R. Universal microfluidic automaton for autonomous sample processing: application to the Mars organic analyzer. *Anal. Chem.* **85**, 7682–8 (2013).
86. Bhattacharyya, A. & Klapperich, C. M. Mechanical and chemical analysis of plasma and ultraviolet-ozone surface treatments for thermal bonding of polymeric microfluidic devices. *Lab. Chip* **7**, 876–82 (2007).

87. Jensen, E. C., Bhat, B. P. & Mathies, R. A. A digital microfluidic platform for the automation of quantitative biomolecular assays. *Lab. Chip* **10**, 685–91 (2010).
88. Karlinsey, J. M., Monahan, J., Marchiarullo, D. J., Ferrance, J. P. & Landers, J. P. Pressure injection on a valved microdevice for electrophoretic analysis of submicroliter samples. *Anal. Chem.* **77**, 3637–43 (2005).
89. Jensen, E. C. *et al.* Digitally programmable microfluidic automaton for multiscale combinatorial mixing and sample processing. *Lab. Chip* **13**, 288–96 (2013).
90. Schallhorn, K., Kim, M. & Ke, P. C. A single-molecule study on the structural damage of ultraviolet radiated DNA. *Int. J. Mol. Sci.* **9**, 662–7 (2008).
91. Jungell-Nortamo, A., Syvänen, A. C., Luoma, P. & Söderlund, H. Nucleic acid sandwich hybridization: enhanced reaction rate with magnetic microparticles as carriers. *Mol. Cell. Probes* **2**, 281–8 (1988).
92. Day, P. J., Flora, P. S., Fox, J. E. & Walker, M. R. Immobilization of polynucleotides on magnetic particles. Factors influencing hybridization efficiency. *Biochem. J.* **278 (Pt 3)**, 735–40 (1991).
93. Klamp, T. *et al.* Highly rapid amplification-free and quantitative DNA imaging assay. *Sci. Rep.* **3**, 1852 (2013).
94. Kim, J., Johnson, M., Hill, P. & Gale, B. K. Microfluidic sample preparation: cell lysis and nucleic acid purification. *Integr. Biol.* **1**, 574 (2009).



95. Thorsen, T., Maerkl, S. J. & Quake, S. R. Microfluidic large-scale integration. *Science* **298**, 580–4 (2002).
96. Outbreaks Chronology: Ebola Virus Disease | Ebola Hemorrhagic Fever | CDC. Available at: <http://www.cdc.gov/vhf/ebola/outbreaks/history/chronology.html>. (Accessed: 20th October 2016)
97. *First Antigen Rapid Test for Ebola through Emergency Assessment and Eligible for Procurement.*
98. Liu, S. *et al.* Electro-optical detection of single  $\lambda$ -DNA. *Chem. Commun.* **51**, 2084–2087 (2015).
99. Trombley, A. R. *et al.* Short report: Comprehensive panel of real-time TaqMan<sup>®</sup> polymerase chain reaction assays for detection and absolute quantification of filoviruses, arenaviruses, and new world hantaviruses. *Am. J. Trop. Med. Hyg.* **82**, 954–960 (2010).
100. Towner, J. S. *et al.* Rapid diagnosis of Ebola hemorrhagic fever by reverse transcription-PCR in an outbreak setting and assessment of patient viral load as a predictor of outcome. *J. Virol.* **78**, 4330–4341 (2004).
101. Daaboul, G. G. *et al.* Digital Sensing and Sizing of Vesicular Stomatitis Virus Pseudotypes in Complex Media: A Model for Ebola and Marburg Detection. *ACS Nano* **8**, 6047–6055 (2014).
102. Zhou, J., Ellis, A. V. & Voelcker, N. H. Recent developments in PDMS surface modification for microfluidic devices. *Electrophoresis* **31**, 2–16 (2010).

103. Brackett, C. A. Dense wavelength division multiplexing networks: principles and applications. *IEEE J. Sel. Areas Commun.* **8**, 948–964 (1990).
104. Murthy, C. S. R. & Gurusamy, M. *WDM Optical Networks: Concepts, Design, and Algorithms*. (Prentice Hall., 2001).
105. Agrawal, G. P. *Fiber-Optic Communication Systems*. (Wiley, 2010).
106. Soldano, L. B. & Pennings, E. C. M. Optical multi-mode interference devices based on self-imaging: principles and applications. *J. Light. Technol.* **13**, 615–627 (1995).
107. Schmidt, H. & Hawkins, A. R. Optofluidic waveguides: I. Concepts and implementations. *Microfluid. Nanofluidics* **4**, 3–16 (2007).
108. Martini, J. *et al.* Time encoded multicolor fluorescence detection in a microfluidic flow cytometer. *Lab. Chip* **12**, 5057–62 (2012).
109. Lien, V. & Berdichevsky, Y. High-sensitivity cytometric detection using fluidic-photonic integrated circuits with array waveguides. *IEEE J. Sel. Top. Quantum Electron.* **11**, 827–834 (2005).
110. Leake, K. D., Olson, M. A. B., Ozelik, D., Hawkins, A. R. & Schmidt, H. Spectrally Reconfigurable Multi-Spot Trap on Optofluidic ARROW Chip. **1**, 3–4 (2015).
111. *Molecular Probes Handbook, A Guide to Fluorescent Probes and Labeling Technologies, 11th Edition*. (Invitrogen, 2010).
112. Rigler, R. & Elson, E. S. *Fluorescence Correlation Spectroscopy*. **65**, (Springer Berlin Heidelberg, 2001).

113. Watzinger, F., Ebner, K. & Lion, T. Detection and monitoring of virus infections by real-time PCR. *Mol. Aspects Med.* **27**, 254–298 (2006).
114. Ratcliff, R. M., Chang, G., Kok, T. & Sloots, T. P. Molecular diagnosis of medical viruses. *Mol. Diagn. Curr. Technol. Appl.* 269 (2006).
115. Baccam, P., Beauchemin, C., Macken, C. A., Hayden, F. G. & Perelson, A. S. Kinetics of Influenza A Virus Infection in Humans. *J. Virol.* **80**, 7590–7599 (2006).
116. Suess, T. *et al.* Comparison of Shedding Characteristics of Seasonal Influenza Virus (Sub)Types and Influenza A(H1N1)pdm09; Germany, 2007–2011. *PLOS ONE* **7**, e51653 (2012).
117. Monat, C., Domachuk, P. & Eggleton, B. J. Integrated optofluidics: A new river of light. *Nat. Photonics* **1**, 106–114 (2007).
118. Li, Z. & Psaltis, D. Optofluidic Distributed Feedback Dye Lasers. *IEEE J. Sel. Top. Quantum Electron.* **13**, 185–193 (2007).
119. Tang, S. K. Y. *et al.* A multi-color fast-switching microfluidic droplet dye laser. *Lab. Chip* **9**, 2767 (2009).
120. Song, W. & Psaltis, D. Pneumatically tunable optofluidic dye laser. *Appl. Phys. Lett.* **96**, 3–5 (2010).
121. Bakal, A., Vannahme, C., Kristensen, A. & Levy, U. Tunable on chip optofluidic laser. *Appl. Phys. Lett.* **107**, 211105 (2015).
122. Bedoya, A. C. *et al.* Reconfigurable photonic crystal waveguides created by selective liquid infiltration. *Opt. Express* **20**, 11046–11056 (2012).

123. Cuennet, J. G., Vasdekis, A. E. & Psaltis, D. Optofluidic-tunable color filters and spectroscopy based on liquid-crystal microflows. *Lab. Chip* **13**, 2721–6 (2013).
124. Mao, X. *et al.* Tunable Liquid Gradient Refractive Index (L-GRIN) lens with two degrees of freedom. *Lab. Chip* **9**, 2050–8 (2009).
125. Bernini, R., Testa, G., Zeni, L. & Sarro, P. M. Integrated optofluidic Mach–Zehnder interferometer based on liquid core waveguides. *Appl. Phys. Lett.* **93**, 11106 (2008).
126. Chin, L. K., Liu, A. Q., Soh, Y. C., Lim, C. S. & Lin, C. L. A reconfigurable optofluidic Michelson interferometer using tunable droplet grating. *Lab. Chip* **10**, 1072–1078 (2010).
127. Campbell, K. *et al.* A microfluidic 2x2 optical switch. *Appl. Phys. Lett.* **85**, 6119–6121 (2004).
128. Groisman, A. *et al.* Optofluidic 1x4 switch. *Opt. Express* **16**, 13499–13508 (2008).
129. Song, W. & Psaltis, D. Pneumatically tunable optofluidic  $2 \times 2$  switch for reconfigurable optical circuit. *Lab. Chip* **11**, 2397–2402 (2011).
130. Yang, A. H. J. *et al.* Optical manipulation of nanoparticles and biomolecules in sub-wavelength slot waveguides. *Nature* **457**, 71–75 (2009).
131. Vollmer, F., Arnold, S. & Keng, D. Single virus detection from the reactive shift of a whispering-gallery mode. *Proc. Natl. Acad. Sci. U. S. A.* **105**, 20701–4 (2008).

132. Testa, G., Persichetti, G., Sarro, P. M. & Bernini, R. A hybrid silicon-PDMS optofluidic platform for sensing applications. *Biomed. Opt. Express* **5**, 417–26 (2014).
133. Cai, Z., Qiu, W., Shao, G. & Wang, W. A new fabrication method for all-PDMS waveguides. *Sens. Actuators Phys.* **204**, 44–47 (2013).
134. Cai, D. K., Neyer, A., Kuckuk, R. & Heise, H. M. Optical absorption in transparent PDMS materials applied for multimode waveguides fabrication. *Opt. Mater.* **30**, 1157–1161 (2008).
135. Valouch, S. *et al.* Direct fabrication of PDMS waveguides via low-cost DUV irradiation for optical sensing. *Opt. Express* **20**, 28855–61 (2012).
136. Rugeland, P., Sterner, C. & Margulis, W. Visible light guidance in silica capillaries by antiresonant reflection. *Opt. Express* **21**, 29217 (2013).
137. Archambault, J. L., Black, R. J., Lacroix, S. & Bures, J. Loss calculations for antiresonant waveguides. *J. Light. Technol.* **11**, 416–423 (1993).
138. Yeh, P. *Optical Waves in Layered Media*. (John Wiley & Sons Inc., 1998).
139. Haus, H. & Miller, D. Attenuation of cutoff modes and leaky modes of dielectric slab structures. *IEEE J. Quantum Electron.* **22**, 310–318 (1986).
140. Huang, W., Shubair, R. & Nathan, A. The Modal Characteristics of ARROW Structures. *J. Light. Technol.* **10**, 1015–1022 (1992).
141. Hidrovo, C. H., Brau, R. R. & Hart, D. P. Excitation nonlinearities in emission reabsorption laser-induced fluorescence techniques. *Appl. Opt.* **43**, 894 (2004).

142. Crimaldi, J. P. Planar laser induced fluorescence in aqueous flows. *Exp. Fluids* **44**, 851–863 (2008).
143. Eckbreth, A. C. *Laser diagnostics for combustion temperature and species*. **3**, (CRC Press, 1996).
144. Abate, A. R. & Weitz, D. A. Single-layer membrane valves for elastomeric microfluidic devices. *Appl. Phys. Lett.* **92**, 243509 (2008).
145. Thangawng, A. L., Swartz, M. a, Glucksberg, M. R. & Ruoff, R. S. Bond-detach lithography: a method for micro/nanolithography by precision PDMS patterning. *Small Weinh. Bergstr. Ger.* **3**, 132–8 (2007).
146. Koschwanez, J. H., Carlson, R. H. & Meldrum, D. R. Thin PDMS films using long spin times or tert-butyl alcohol as a solvent. *PloS One* **4**, e4572 (2009).